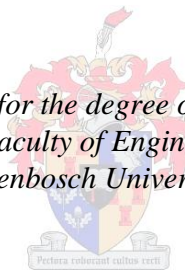


# Thermal energy storage in metallic phase change materials

by

Johannes Paulus Kotzé

*Dissertation presented for the degree of Doctor of Philosophy  
in the Faculty of Engineering at  
Stellenbosch University*



Promoter: Prof. Theodor Willem Von Backström

Co-Promoter: Dr. Paul Johan Erens

December 2014

The financial assistance of the National Research Foundation (NRF) towards this research is hereby acknowledged. Opinions expressed and conclusions arrived at are those of the author and are not necessarily to be attributed to the NRF.

***Declaration***

By submitting this dissertation electronically, I declare that the entirety of the work contained therein is my own, original work, that I am the sole author thereof (save to the extent explicitly otherwise stated), that reproduction and publication thereof by Stellenbosch University will not infringe any third party rights and that I have not previously in its entirety or in part submitted it for obtaining any qualification.

This dissertation includes one original paper published in a peer-reviewed journal, two peer reviewed conference papers, three conference papers and one unpublished publication. The development and writing of these papers (published and unpublished) were the principal responsibility of myself and, for each of the cases where this is not the case, a declaration is included in the dissertation indicating the nature and extent of the contributions of co-authors.

Date: \_\_\_\_\_

Copyright © 2014 Stellenbosch University

All rights reserved

## ***Abstract***

Currently the reduction of the levelised cost of electricity (LCOE) is the main goal of concentrating solar power (CSP) research. Central to a cost reduction strategy proposed by the American Department of Energy is the use of advanced power cycles like supercritical steam Rankine cycles to increase the efficiency of the CSP plant. A supercritical steam cycle requires source temperatures in excess of 620°C, which is above the maximum storage temperature of the current two-tank molten nitrate salt storage, which stores thermal energy at 565°C. Metallic phase change materials (PCM) can store thermal energy at higher temperatures, and do not have the drawbacks of salt based PCMs. A thermal energy storage (TES) concept is developed that uses both metallic PCMs and liquid metal heat transfer fluids (HTF). The concept was proposed in two iterations, one where steam is generated directly from the PCM – direct steam generation (DSG), and another where a separate liquid metal/water heat exchanger is used – indirect steam generation, (ISG). Eutectic aluminium-silicon alloy (AlSi12) was selected as the ideal metallic PCM for research, and eutectic sodium-potassium alloy (NaK) as the most suitable heat transfer fluid.

Thermal energy storage in PCMs results in moving boundary heat transfer problems, which has design implications. The heat transfer analysis of the heat transfer surfaces is significantly simplified if quasi-steady state heat transfer analysis can be assumed, and this is true if the Stefan condition is met. To validate the simplifying assumptions and to prove the concept, a prototype heat storage unit was built. During testing, it was shown that the simplifying assumptions are valid, and that the prototype worked, validating the concept. Unfortunately unexpected corrosion issues limited the experimental work, but highlighted an important aspect of metallic PCM TES. Liquid aluminium based alloys are highly corrosive to most materials and this is a topic for future investigation.

To demonstrate the practicality of the concept and to come to terms with the control strategy of both proposed concepts, a storage unit was designed for a 100 MW power plant with 15 hours of thermal storage. Only AlSi12 was used in the design, limiting the power cycle to a subcritical power block. This demonstrated some practicalities about the concept and shed some light on control issues regarding the DSG concept.

A techno-economic evaluation of metallic PCM storage concluded that metallic PCMs can be used in conjunction with liquid metal heat transfer fluids to achieve high temperature storage and it should be economically viable if the corrosion issues of aluminium alloys can be resolved. The use of advanced power cycles, metallic PCM storage and liquid metal heat transfer is only merited if significant reduction in LCOE in the whole plant is achieved and only forms part of the solution. Cascading of multiple PCMs across a range of temperatures is required to minimize entropy generation. Two-tank molten salt storage can also be used in conjunction with cascaded metallic PCM storage to minimize cost, but this also needs further investigation.

### *Opsomming*

Tans is die minimering van die gemiddelde leeftydskoste van elektrisiteit (GLVE) die hoofdoel van gekonsentreerde son-energie navorsing. In die kostevermindingsplan wat voorgestel is deur die Amerikaanse Departement van Energie, word die gebruik van gevorderde kragstelsels aanbeveel. 'n Superkritiese stoom-siklus vereis 'n bron temperatuur hoër as 620 °C, wat bo die 565 °C maksimum stoor temperatuur van die huidige twee-tenk gesmelte natriumsout termiese energiestoor (TES) is. Metaal fase veranderingsmateriale (FVMe) kan termiese energie stoor by hoër temperature, en het nie die nadele van soutgebaseerde FVMe nie. 'n TES konsep word ontwikkel wat gebruik maak van metaal FVM en vloeibare metaal warmteoordrag vloeistof. Die konsep is voorgestel in twee iterasies; een waar stoom direk gegenereer word uit die FVM (direkte stoomopwekking (DSO)), en 'n ander waar 'n afsonderlike vloeibare metaal/water warmteruiler gebruik word (indirekte stoomopwekking (ISO)). Eutektiese aluminium-silikon aliooi (AlSi12) is gekies as die mees geskikte metaal FVM vir navorsingsdoeleindes, en eutektiese natrium – kalium aliooi (NaK) as die mees geskikte warmteoordrag vloeistof.

Termiese energie stoor in FVMe lei tot bewegende grens warmteoordrag berekening, wat ontwerp-implikasies het. Die warmteoordrag ontleding van die warmteruilers word aansienlik vereenvoudig indien kwasi-bestendige toestand warmteoordrag ontledings gebruik kan word en dit is geldig indien daar aan die Stefan toestand voldoen word. Om vereenvoudigende aannames te bevestig en om die konsep te bewys is 'n prototipe warmte stoor eenheid gebou. Gedurende toetse is daar bewys dat die vereenvoudigende aannames geldig is, dat die prototipe werk en dien as 'n bevestiging van die konsep. Ongelukkig het onverwagte korrosie die eksperimentele werk kortgeknip, maar dit het klem op 'n belangrike aspek van metaal FVM TES geplaas. Vloeibare aluminium aliooi is hoogs korrosief en dit is 'n onderwerp vir toekomstige navorsing.

Om die praktiese uitvoerbaarheid van die konsep te demonstreer en om die beheerstrategie van beide voorgestelde konsepte te bevestig is 'n stoor-eenheid ontwerp vir 'n 100 MW kragstasie met 15 uur van 'n TES. Slegs AlSi12 is gebruik in die ontwerp, wat die kragstelsel beperk het tot 'n subkritiese stoomsiklus. Dit het praktiese aspekte van die konsep onderteken, en beheerkwessies rakende die DSO konsep in die kollig geplaas.

In 'n tegno-ekonomiese analise van metaal FVM TES word die gevolgtrekking gemaak dat metaal FVMe gebruik kan word in samewerking met 'n vloeibare metaal warmteoordrag vloeistof om hoër temperature stoor moontlik te maak en dat dit ekonomies lewensvatbaar is indien die korrosie kwessies van aluminium aliooi opgelos kan word. Die gebruik van gevorderde kragstelsel, metaal FVM stoor en vloeibare metaal warmteoordrag word net geregverdig indien beduidende vermindering in GLVE van die hele kragstelsel bereik is, en dit vorm slegs 'n deel van die oplossing. 'n Kaskade van verskeie FVMe oor 'n reeks van temperature word vereis om entropie generasie te minimeer. Twee-tenk gesmelte soutstoor kan ook gebruik word in samewerking met kaskade metaal FVM stoor om koste te verminder, maar dit moet ook verder ondersoek word.

### *Acknowledgements*

I would like to acknowledge the following people:

My promoters: Prof. T.W von Backström and Dr. P.J. Erens, for your time and for supervising me throughout this project.

My siblings, Ilze, Pieter, Hannetjie, Koot and Alwyn who always supported me with love and incredible friendship, you are my best friends.

My parents Koot and Marianne, whose unconditional love and support are never-ending, which really is a base of stability in my life. Dad, you are truly my mentor and the greatest engineer I know. Mom, you are like a cool breeze on a hot summer's day.

Alexandra, your friendship, love and endless prayers carried me more than you know.

The staff of the Mechanical and Mechatronic Department.

All the members of STERG.

The NRF/DST, CRSES and STERG for funding.

ESTEIQ for making FLOWNEX available free of charge.

Mrs. Banks, you gave me a second chance, and without your experience and knowledge, none of this would be possible.

The late Prof. Detlev Kröger, you were an inspiration to all of us.

*“My grace is sufficient for thee: for my strength is made perfect in weakness.”*

*2 Cor 12:9*

**Table of contents**

	<b>Page</b>
<i>List of figures</i> .....	ix
<i>List of tables</i> .....	xiv
<i>Nomenclature</i> .....	xvi
<i>Important dimensionless numbers</i> .....	xx
1 Introduction .....	1
2 Literature review and project goals .....	3
2.1 Cost breakdown of CSP and strategies for cost reduction.....	4
2.2 Factors determining thermal efficiency .....	5
2.3 Power cycles .....	9
2.4 Overview of thermal energy storage and current technical limitations	10
2.4.1 Current state of the art.....	11
2.4.2 High temperature storage concepts .....	14
2.5 Thermal energy storage in phase change materials .....	17
2.5.1 Eutectic materials .....	18
2.5.2 Comparison of some PCMs .....	19
2.6 AlSi12 as a PCM in literature.....	21
2.7 Heat transfer fluids and current technical limitations.....	27
2.7.1 Thermal oil .....	28
2.7.2 Molten salt.....	29
2.7.3 Direct steam .....	30
2.7.4 Air or gas.....	30
2.7.5 Sodium .....	30
2.7.6 NaK .....	31
2.7.7 Conclusion .....	32
2.8 Conclusion and project scope .....	33
3 Thermal energy storage concept.....	35
3.1 Direct steam generator .....	35
3.2 Indirect steam generator .....	37
4 Material properties .....	39
4.1 The properties and characteristics of AlSi12.....	39

4.1.1	Thermal and physical properties of eutectic Aluminium silicon alloy .....	40
4.2	The properties and characteristics of NaK .....	42
4.2.1	Physical properties .....	43
4.2.2	Safety .....	46
4.2.3	Steam generator design .....	47
4.3	Other materials .....	48
5	Flownex .....	49
6	Heat transfer mechanisms .....	51
6.1	Liquid metal heat transfer.....	51
6.2	Convective boiling heat transfer inside plain tubes.....	52
7	Moving boundary heat transfer around vertical heat transfer tubes.....	53
7.1	Analysis of the moving boundary system and transient analysis .....	54
7.2	Instantaneous heat transfer .....	58
7.3	Numerical solution to the moving boundary problem for transient analysis .....	60
7.4	Prototype and experimental setup.....	66
7.4.1	Heating elements.....	71
7.4.2	Cooling system.....	72
7.4.3	Thermal insulation and losses .....	75
7.4.4	Measurements and data acquisition .....	76
7.5	Experiment .....	78
7.6	Numerical simulation .....	80
7.7	Comparison and conclusions .....	81
8	Preliminary plant design and simulation .....	85
8.1	Power generating cycle.....	85
8.2	Primary heat transfer loop .....	89
8.2.1	Primary loop heat transfer requirements.....	90
8.2.2	Receiver sizing.....	95
8.3	Storage sizing .....	99
8.4	Heat exchanger sizing and modelling.....	101
8.4.1	Steam/water Heat exchangers for the DSG concept .....	104
8.4.2	NaK heat exchangers for the DSG concept .....	107



8.4.3	Heat exchangers for the ISG concept.....	108
8.5	Overall model .....	111
8.6	Conclusion and practical considerations .....	114
8.6.1	Feasibility of the DSG concept .....	114
8.6.2	Thermodynamic considerations and cascaded thermal energy storage. ....	114
9	High temperature corrosion of AlSi12 .....	118
10	Techno-economic feasibility .....	121
11	Future work .....	128
11.1	Axial conduction and CFD models .....	128
11.2	Material testing .....	128
11.3	More alloys and investigation into hyper-eutectics.....	129
11.4	High temperature corrosion resistance, heat exchangers and containment .....	129
11.5	The use of liquid metals in CSP .....	129
11.6	Analysis of a combined molten salt storage system with metallic PCM storage .....	130
11.7	Optimisation through entropy minimization .....	130
12	Conclusion.....	131
13	References .....	134
Appendix A	Candidate phase change materials .....	140
Appendix B	Properties of NaK.....	144
Appendix C	Derivation of the Stefan number .....	147
Appendix D	Experimental design.....	150
D.1	Certificates of analysis and calibration.....	150
D.2	Laminar flow meter design detail.....	153
Appendix E	Prediction of thermal losses of the test section.....	158
Appendix F	Heat transfer measurements .....	160
F.1	Measurement of heat transfer from PCM to Oil .....	160
F.2	Measurement of heat transfer from Oil to Water .....	161
Appendix G	Simulation Code.....	162
Appendix H	Thermodynamic analysis of the steam cycle .....	166
Appendix I	Flownex model.....	171

**List of figures**

	<b>Page</b>
Figure 1 - Efficiency of a receiver at various concentration ratios.....	7
Figure 2 – Approximate thermal efficiency of a steam cycle at increasing source temperatures for a sink temperature of 40°C .....	7
Figure 3 - Thermal efficiency of a CSP plant at different concentration ratios for a sink temperature of 40°C .....	8
Figure 4 - Modes of thermal energy storage.....	10
Figure 5 – Classification of TES concepts.....	11
Figure 6 - Two tank molten salt TES for central receivers (Direct system).....	13
Figure 7 - Two tank molten salt TES system for parabolic trough (Indirect) (Herrmann, et al., 2006).....	13
Figure 8 - Graphite heat transfer enhancements for low thermal diffusivity in PCMs (Tamme, 2007).....	16
Figure 9 - Concrete storage with heat exchanger pipes visible at the end (Tamme, 2007).....	16
Figure 10 - Generic phase diagram for a binary eutectic system.....	19
Figure 11 - Comparison of high temperature PCMs found in literature (Latent heat of fusion against temperature) .....	20
Figure 12 - Metallic phase change materials found in literature (Birchenall, et al., 1979).....	21
Figure 13 - Analytical comparison of the charging rate of a metallic PCM versus a salt PCM (Hoshi, et al., 2005 ) .....	22
Figure 14 - Steam generator as proposed by Adinberg <i>et al.</i> (2010).....	22
Figure 15 - Thermal storage around a catalyst to reduce the light-up time for a catalytic converter.....	23
Figure 16 - Catalytic converter with PCM TES system .....	23
Figure 17 - Test results from catalytic converter tests.....	24
Figure 18 - Waste heat recovery unit using AlSi12 as PCM .....	24
Figure 19 - Temperature readouts for thermocouples in the storage unit through discharge .....	25
Figure 20 - Space heater with latent heat storage (Wang, et al., 2004) .....	25
Figure 21 - Sectioned view of the space heater (Wang, et al., 2004) .....	26
Figure 22 - Section through the space heater (Wang, et al., 2004).....	26
Figure 23 - Test results for 1540 W heating power (Wang, et al., 2004) .....	27

Figure 24 - Sodium-Potassium eutectic system (Liquid metal engineering center, 1972) .....	32
Figure 25 - Comparison of HTF operative temperatures.....	33
Figure 26 - Direct steam generator concept.....	36
Figure 27 - Power cycle with the direct steam generation concept .....	37
Figure 28 - Indirect steam generation concept.....	38
Figure 29 - Power cycle with the indirect steam generation concept .....	38
Figure 30 - Aluminium-Silicon eutectic system (Murray, et al., 1984).....	40
Figure 31 - Thermal diffusivity of eutectic NaK .....	45
Figure 32 - Prandtl number of eutectic NaK.....	45
Figure 33 – Flownex model of a Rankine cycle .....	49
Figure 34 – Discretization and two dimensional models for charging and discharging.....	53
Figure 35 - Hexagonal elements showing solidified PCM cylinders touching .....	54
Figure 36 - Problem description .....	55
Figure 37 - Stefan number as a function of wall temperature .....	58
Figure 38 - Resistance heat transfer model for charging and discharging.....	59
Figure 39 - Discretisation of the heat transfer problem .....	60
Figure 40 - Resistances between elements .....	61
Figure 41 - T-H diagram for a eutectic or pure metal.....	63
Figure 42 - Enthalpy method algorithm.....	65
Figure 43 - Cross section of the test section .....	66
Figure 44 – Test section.....	67
Figure 45 – Empty test section .....	69
Figure 46 - Casting of AlSi12 into test section.....	69
Figure 47 - Test section suspended in frame with heating elements and cladding (cladding still open) .....	70
Figure 48 - Ceramic band heater.....	71
Figure 49 - Wiring of the three band heaters .....	72
Figure 50 – Band heaters installed around the storage vessel .....	72
Figure 51 – Test rig process diagram.....	73
Figure 52 - Flownex model used to design the experiment.....	74
Figure 53 – The experimental setup .....	76

Figure 54 - Heat transfer measurements .....	79
Figure 55 - Thermocouple readouts throughout discharge of the storage system .	80
Figure 56 - Simulation results of the phase change problem based on the experimental.....	81
Figure 57 - Experimental data and simulation data plotted over each other for comparison.....	82
Figure 58 - Comparison between the positions of solidification front as predicted by the simulation and measured in the prototype .....	83
Figure 59 - Quasi steady conduction problem .....	83
Figure 60 - Temperature distribution through melt as the solidification front passes thermocouple #5 .....	84
Figure 61 - Overview of the model.....	85
Figure 62 - Power generation cycle .....	86
Figure 63 - T-s diagram for the power cycle .....	87
Figure 64 - Flownex model of the Rankine Cycle.....	89
Figure 65 - Heat exchanger configuration for the DSG concept .....	90
Figure 66 - Annual DNI for South Africa (Geosun).....	91
Figure 67 - Clear sky DNI for Upington.....	91
Figure 68 - Normalized DNI for the summer solstice, winter solstice and the southward equinox (spring) for Upington .....	92
Figure 69 - Energy balance to storage .....	93
Figure 70 - Power to and from storage .....	94
Figure 71 - External receiver .....	95
Figure 72 - Liquid sodium receiver tested at PSA (Schiel, 1988) .....	96
Figure 73 - Pressure drop over receiver versus outer diameter for various B36.19 tubes .....	98
Figure 74 – Receiver model.....	99
Figure 75 – Heat transfer sizing.....	102
Figure 76 - Boiler arrangement.....	104
Figure 77 – Boiler model .....	105
Figure 78 - Re-heater and super-heater arrangement.....	105
Figure 79 – Re-heater and super-heater model .....	106
Figure 80 – ISG heat transfer and storage .....	109
Figure 81 - Primary cooling loop for the ISG concept .....	109

Figure 82 – Calculation of charge state and moving boundary position .....	111
Figure 83 – Screenshot of the overall Flownex model for the DSG concept .....	112
Figure 84 – Screenshot of the overall Flownex model for the ISG concept.....	113
Figure 85 - Entropy generation between the primary cooling loop and the PCM .....	116
Figure 86 – Single PCM storage in the DSG concept .....	116
Figure 87 – Single PCM storage in the ISG concept.....	117
Figure 88 – Cascaded PCMs for the DSG concept.....	117
Figure 89 - Microstructure of inter-metallic zone (Bouayad, et al., 2003).....	118
Figure 90 - Aluminium-iron eutectic system.....	119
Figure 91 - Electron-micrograph of a surface treated steel sample after corrosion testing. (Deqing, et al., 2003).....	120
Figure 92 – Material cost of metallic PCMs versus melting temperature. ....	123
Figure 93 – Single metallic PCM storage to enable supercritical steam .....	126
Figure 94 – T-s diagram of a supercritical steam cycle for combined storage....	126
Figure 95 - Density of eutectic NaK .....	144
Figure 96 - Dynamic viscosity of NaK.....	144
Figure 97 - Kinematic viscosity of eutectic NaK .....	145
Figure 98 - Thermal conductivity of eutectic NaK.....	145
Figure 99 - Specific heat of eutectic NaK.....	146
Figure 100 - Temperature profiles during one-dimensional freezing of a liquid initially at $T_{\infty}$ .....	147
Figure 101 - Chemical analysis of aluminium alloy cast into the test section....	150
Figure 102 - Certification of compliance for K-type thermocouples .....	152
Figure 103 - Calibration certificate - water flow meter .....	152
Figure 104 - Laminar flow meter drawing.....	154
Figure 105 - Calibration curve for the Endress+Hauser Deltabar S PMD75 pressure transducer .....	154
Figure 106 - Kinematic viscosity of the ISO 100 heat transfer oil .....	155
Figure 107 - Kinematic viscosity of ISO 100 oil as a function of temperature...	156
Figure 108 - Dynamic viscosity of ISO100 oil as a function of temperature.....	156
Figure 109 - Calibration curve for the flow meter at 42.5°C.....	157
Figure 110 - Heat transfer rates from PCM to oil.....	160

Figure 111 - Heat transfer from oil to water .....	161
Figure 112 - Steam Rankine cycle .....	166
Figure 113 - T-S diagram for the Rankine steam cycle .....	167
Figure 114 - Flownex model of the steam Rankine cycle .....	171
Figure 115 - HP turbine settings .....	172
Figure 116 - LP turbine settings .....	172
Figure 117 - LP Pump chart.....	173
Figure 118 - HP pump chart .....	173

**List of tables**

	<b>Page</b>
Table 1 - Cost breakdown of CSP (Kolb, et al., 2011) .....	4
Table 2 - Notable examples of thermal energy storage (Medrano, et al., 2010) ...	12
Table 3 - Thermal properties of nitrate salts .....	14
Table 4 - Candidate materials for sensible thermal energy storage (Gil, et al., 2010) .....	15
Table 5 - Properties of heat transfer fluids .....	28
Table 6 - Composition specifications of LM6 alloy (BS 1490:1988 LM6) .....	39
Table 7 - General material properties of eutectic AlSi12 alloy (Matbase) .....	41
Table 8 - Thermal properties used by He <i>et al.</i> (He, et al., 2001) .....	41
Table 9 - Thermophysical properties of AlSi12 as used by Wang <i>et al.</i> .....	41
Table 10 - Properties of AlSi12 .....	42
Table 11 – Thermal properties of low carbon steel and stainless steel 304 .....	48
Table 12 - Test section geometry .....	68
Table 13 - Chemical analysis of the cast aluminium alloy .....	70
Table 14 - Properties of ISO 100 quenching oil (Kopeliovich, 2013) .....	73
Table 15 - Cooling loop component details .....	75
Table 16 - Thermal resistance of insulating layers around the storage unit .....	75
Table 17 - Measurement errors on the test section thermocouples .....	77
Table 18 - Measurement devices and calibration points .....	78
Table 19 - Energy balance during latent heat discharge .....	79
Table 20 - Energy balance of a hypothetical power cycle .....	88
Table 21 - Boundary conditions and heat transfer requirements of the steam generator .....	88
Table 22 - Heat transfer requirements for the primary heat transfer loop .....	94
Table 23 – Typical receiver peak flux design values (Battleon, 1981) .....	96
Table 24 - Pressure drop for various heat transfer tube diameters for the receiver .....	98
Table 25 - Receiver geometry and performance parameters .....	99
Table 26 - Mass and volume required for 15h of thermal energy storage .....	100
Table 27 - Size of the storage tanks .....	100

Table 28 - ISG storage sizing .....	100
Table 29 – Summary of material property databases used in Flownex .....	102
Table 30 – Summary of correlations used in the Flownex simulations.....	103
Table 31 – Steam water heat exchanger geometry .....	106
Table 32 – Steam/water heat exchanger control strategy .....	107
Table 33 – NaK flow distribution .....	107
Table 34 – NaK heat exchanger geometry for the DSG concept.....	108
Table 35 – NaK heat exchanger geometry, storage tank dimensions and operational parameters .....	110
Table 36 – Material cost of eutectic nitrate salt.....	121
Table 37 – Constituent metal prices .....	122
Table 38 – Material cost of a select number of metallic PCMs.....	122
Table 39 – Overall cost estimates of metallic PCMs.....	123
Table 40 – Predicted reduction in LCOE.....	125
Table 41 – Enthalpy of steam in a supercritical steam generator .....	127
Table 42 – Carbonates (Kenisarin, 2009) .....	140
Table 43 – Hydroxides (Kenisarin, 2009) .....	140
Table 44 – Chlorides (Kenisarin, 2009).....	141
Table 45 – Fluorides (Kenisarin, 2009) .....	142
Table 46 – Metals (Kenisarin, 2009) .....	143
Table 47 – Nitrates (Kenisarin, 2009) .....	143
Table 48 - Design parameters of the laminar flow meter .....	153
Table 49 - Laminar flow meter critical geometry .....	153
Table 50 – Geometry, properties and conditions for heat loss estimation.....	158
Table 51 – Air properties at 121°C .....	158
Table 52 - Component efficiencies for the steam Rankine cycle .....	167
Table 53 - Energy balance of hypothetical power cycle.....	170
Table 54 - Boundary conditions and heat transfer requirements of the steam generator .....	170



***Nomenclature****Acronyms:*

AES	Alkaline earth silicate
AlSi12	Eutectic aluminium-silicon alloy
ASME	American society of mechanical engineers
CAD	Computer aided drawing
CFD	Computational fluid dynamics
CSP	Concentrating solar power
DNI	Direct normal irradiation
DOE	US Department of energy
DSC	Differential scanning calorimeter
DSG	Direct steam generation
HP	High pressure
HSU	Heat storage unit
HTF	Heat transfer fluids
IAPWS97'	International association for the properties of water and steam
ID	Inside diameter
IEA	International energy agency
ISG	Indirect steam generation
ISO	International standards organization
LBE	Lead-bismuth eutectic
LCOE	Levelised cost of electricity
LM6	Eutectic aluminium-silicon alloy (British designation)
LMFBR	Liquid metal fast breeder reactor
LP	Low pressure
NaK	Eutectic sodium-potassium alloy
NNR	National nuclear regulator
O&M	Operations and maintenance
OD	Outer diameter
PBMR	Pebble bed modular reactor
PCM	Phase change material
PID	Proportional-Integral-Differential
PSA	Plataforma Solar de Almeria
PTC	Parabolic trough collector
S-CO <sub>2</sub>	Supercritical carbon dioxide
SM	Solar multiple
TES	Thermal energy storage
V&V	Verification and validation

*Symbols:*

A	Area	(m <sup>2</sup> )
C	Optical concentration ratio	
C <sub>p</sub>	Specific heat	(J/kgK)
D	Diameter	(m)
D <sub>H</sub>	Hydraulic diameter	(m)
g	Gravitational constant	(m/s <sup>2</sup> )
h	Enthalpy	(kJ/kg)
I	Incident radiation	(W.m <sup>2</sup> )
k	thermal conductivity	(W/mK)
L	Length	(m)
N	Mole fraction	
Q	Heat transfer (energy)	(J)
$\dot{Q}$	Heat transfer rate	(W)
$\dot{q}$	Heat transfer rate per unit area	(W/m <sup>2</sup> )
R	Thermal resistance	(K/W)
r	Radius	(m)
s	Entropy	(J/K)
T	Temperature	(°C/K)
T <sub>m</sub>	Melting temperature	(°C/K)
t	Time	(s)
v	Velocity	(m/s)

*Greek letters:*

$\alpha$	Thermal diffusivity	$\alpha = k/\rho C_p$ (m <sup>2</sup> /s)
or		
$\alpha$	Absorptivity	
or		
$\alpha_{cb}$	Convective boiling heat transfer coefficient	(W/K.m <sup>2</sup> )
$\alpha_{tp}$	Two phase heat transfer coefficient	(W/K.m <sup>2</sup> )
$\alpha_{nb}$	Nucleate boiling heat transfer coefficient	(W/K.m <sup>2</sup> )
$\beta$	Volumetric thermal expansion coefficient	
$\varepsilon$	Emissivity	
$\eta$	Efficiency	
$\lambda$	Heat of fusion	(kJ/kg)
$\mu$	Dynamic viscosity	(kg/m.s)
$\nu$	Kinematic viscosity	$\nu = \mu/\rho$ (m <sup>2</sup> /s)
$\rho$	Density	(kg/m <sup>3</sup> )
$\sigma$	Stefan Boltzmann constant	

*Subscripts:*

e	Electrical
H	High
i	Inner diameter of PCM/outer diameter of heat transfer tube
K	Potassium
L	Low
m	Solidification front
Na	Sodium
NaK	Eutectic sodium-potassium alloy
o	Outer diameter of PCM volume
p	Pipe
pi	Pipe inner diameter
PCM	Phase change material
PCM <sub>s</sub>	PCM in solid state
PCM <sub>l</sub>	PCM in liquid state
S	Surface
th	Thermal
$\infty$	Infinity

***Important dimensionless numbers***

Boussinesq number:  $Bo = (Gr)(Pr)^2 = (Ra)(Pr)$

Grashof number:  $Gr_L = \frac{g\beta(T_s - T_\infty)L^3}{\nu^2}$

Prandtl number:  $Pr = \frac{\nu}{\alpha}$

Rayleigh number:  $Ra_L = Gr_L Pr = \frac{g\beta}{\nu\alpha}(T_s - T_\infty)L^3$

Reynolds number:  $Re = \frac{\rho\nu D_h}{\mu} = \frac{\nu D_h}{\nu}$

Stefan number:  $Ste = \frac{C_p \Delta T}{\lambda} = \frac{C_p(T_s - T_m)}{\lambda}$

## 1 INTRODUCTION

Solar power is becoming a more prominent source of renewable energy. Due to the intermittent and variable nature of the solar resource, an energy storage system is required to match electrical supply to demand. Energy can be stored in a number of ways, but thermal energy storage (TES) proves to be the most economical option for large-scale use. In principle more energy needs to be stored in thermal energy than would be necessary in electrical or kinetic energy storage because of the thermodynamic limitations of the power generating cycle, but the cost of electrical, kinetic and potential energy storage is prohibitive. Concentrating solar power (CSP) directly generates thermal energy that can be stored, making it inherently suitable for TES.

Thermal energy is accumulated in a storage medium, the storage mechanism being either sensible heat, latent heat, or chemical storage. Considering a review paper by Medrano *et al.* (2010) it is clear that almost all operational solar thermal power stations use sensible heat thermal storage. The most popular sensible thermal storage systems use molten salts in a two tank storage system.

Currently the cost of CSP is the highest of all renewables (U.S. Energy Information Administration, 2012); therefore cost reduction is the greatest priority of the CSP community. The use of higher efficiency power cycles is essential for cost reduction (Kolb, et al., 2011). Advanced high efficiency power cycles (e.g. ultra-supercritical steam and supercritical CO<sub>2</sub>) require thermal sources in excess of 600°C. This is above the temperature limits of current state of the art thermal energy storage and heat transfer fluids (HTF).

Not only is the upper working temperature of current HTFs limited, but they solidify at temperatures above ambient. This is an issue that needs to be addressed by either using parasitic heating or a method of clearing the heat transfer pipes, which increases the operational and maintenance cost of the plant.

Latent heat storage materials or phase change materials (PCM) can store relatively large amounts of energy in small volumes at temperatures not possible with sensible TES. Most PCMs operate between solid-liquid transitions and are therefore most suitable as indirect storage concepts (Gil, et al., 2010). According to review papers (Gil, et al., 2010) (Kenisarin, 2009) most of the potential salt-based PCMs have low thermal conductivity and extensive material or heat exchanger modifications must be performed to yield feasible storage systems. This negates the cost savings through material reduction and makes them difficult to implement. Birchenall *et al.* (1979) proposed that eutectic metals may be used to store thermal energy in industrial processes; a concept that has been investigated by:

- He *et al.* (2001), who developed a waste heat storage device using an eutectic alloy of silicon and aluminium (AlSi12);
- Wang *et al.* (2004), who developed a space heater that stores thermal energy in AlSi12; and
- Sun *et al.* (2007), who explored the use of AlMg34Zn6 as a storage material.

The application of these storage devices was not aimed at TES in CSP, nor did it give answers regarding the application of metallic PCMs and the value which it could add to CSP. The value addition may be two fold;

- Cost reduction of thermal energy storage; and
- Decreasing the levelised cost of electricity (LCOE) of CSP by making it possible to use advanced power cycles through high temperature TES.

To investigate the feasibility of metallic PCMs for TES, a concept was developed for a TES system using metallic PCMs. Eutectic aluminium-silicon alloy (AlSi12) was chosen as a good candidate PCM for research and a eutectic sodium-potassium alloy (NaK) was identified as an ideal heat transfer fluid for CSP. The concept was further developed and investigated using these two materials as a basis, but the work is applicable to other metallic PCMs that would be better suited for supercritical steam power cycles, like pure aluminium.

The heat transfer mechanisms of a latent heat TES system using metallic PCMs was identified as a Stefan problem, which merited simplifying assumptions to aid in concept evaluation and analysis. A Stefan problem is a moving boundary heat transfer problem that occurs if a PCM with a high heat of fusion discharges across a small temperature range. This is called the Stefan condition, where the assumption could be made that the sensible heat of the storage material has little effect on the heat transfer problem. A prototype was built and tested to validate the concept and to validate the assumptions made. The practicality of the use of AlSi12 as a PCM was evaluated using Flownex (Flownex, 2011) to highlight some design aspects of a TES system using metallic PCMs. This aided in the techno-economic feasibility study which was done to determine the economic feasibility of metallic PCMs and the role it could play in the reduction of the LCOE.

The scope of this project includes:

- The development of a TES concept that utilizes metallic PCMs
- Explore and evaluate the appropriate analytical tools necessary for evaluation of metallic PCM TES systems and metallic HTFs.
- Build a prototype to evaluate the concept and analytical tools.
- Use these analytical tools to prove the concept and to determine operational parameters.
- Perform a techno-economic feasibility study and highlight the role of metallic PCMs as a method to LCOE reduction.
- Determine what future research is required for further development of these storage concepts.

## 2 LITERATURE REVIEW AND PROJECT GOALS

The growing awareness of the need for renewable energy and the urgency for change led the International Energy Agency (IEA) to develop a set of roadmaps (International Energy Agency, 2010) for those technologies that are crucial for the development of a renewable energy plan. These roadmaps are intended to help turn political statements and analytical work into real-world solutions for renewable energy.

CSP is one of these key technologies for a renewable energy future and the IEA's objectives are that CSP should be able to provide 11.3 % of the global energy needs by 2050 (International Energy Agency, 2010). CSP has the inherent ability to store thermal energy, which makes this a key technology to achieve a renewable energy future. This will enable CSP to produce electricity to meet demands after sunset, through cloud cover, and even enable base load electrical power generation. The bulk of the electrical power generation by CSP will be from large grid coupled power plants, but CSP will also be used to produce industrial heat, which can be used in applications like desalination or the production of solar fuels. It is expected that CSP can become a competitive source of large scale power generation by 2020 for intermediate loads, and be able to provide base-load power somewhere between 2025 and 2030 (International Energy Agency, 2010). A reduction in the levelised cost of electricity is required to make CSP competitive.

Currently CSP is one of the most expensive renewable energy sources (U.S. Energy Information Administration, 2012). The cost of CSP consists of capital investment and operational and maintenance (O&M) costs and is currently estimated to be about 16.5 US\$ cents per kWh (Kolb, et al., 2011). Naturally the research objectives for CSP are aimed at the reduction of the LCOE. The power tower receiver concept offers the potential for higher thermal efficiencies and therefore there is much interest in developing technology that can increase thermal efficiency and reduce the LCOE (Kolb, et al., 2011). The overall goal is to drive down CSP costs to a level where it is competitive with other energy sources without subsidy. The goal has been set to 6 US\$ cents per kWh to make CSP competitive with coal and nuclear (Kolb, et al., 2011). For the time being, governments have to incentivise CSP and other renewables to allow investors to invest into the renewable energy market. The IEA roadmap for CSP outlines work that needs to be done on key technologies to facilitate these cost reductions. Cost reduction can be achieved by:

- Reduction in component cost
- Increase in thermal efficiency
- Reduction in O&M costs

Currently the majority of CSP plants are funded by investors, which means that the technology needs to be proven in the field before an investment can be made. The security of the investment is also dependent on the security of the feed-in tariff structure guaranteed by the government, energy regulators and utility companies.



## 2.1 Cost breakdown of CSP and strategies for cost reduction

It is important to understand what makes up the LCOE of a technology in order to effectively address the right aspects of the technology to effectively reduce the LCOE. Sandia National Laboratories and the U.S. Department of Energy compiled a report with the aim of providing direction regarding the cost reduction of power tower technology (Kolb, et al., 2011). The report is focused on power tower technology in an American context, and the cost breakdown is presented in Table 1 for a plant with the following specifications:

- 100 MWe
- Solar multiple of 2.1
- Heliostat field of 1000 000 m<sup>2</sup>
- 540 MW<sub>t</sub> peak surround receiver
- 9 hours of thermal storage

**Table 1 - Cost breakdown of CSP (Kolb, et al., 2011)**

Cost breakdown of LCOE (All costs)		
Heliostat cost	22.1	%
Indirect costs	20.8	%
Operations and maintenance	12.1	%
Power plant cost	12.1	%
Receiver cost	10.1	%
Tax	8.1	%
Storage cost	7.4	%
Balance of plant cost	4.0	%
Site cost	2.0	%
Tower cost	1.3	%

It must be noted that indirect costs and tax are very specific of the legislative and economic environment where the development is considered. The total LCOE for power towers was calculated to be 15 US\$ cents/kWh. The indirect costs of a CSP plant accounts for nearly 41 % (6.2 US\$ cents/kWh) of the overall costs of a power tower CSP plant in the USA. This includes tax, O&M and other more diverse costs. The rests of the costs are direct costs of the physical CSP plant, which is 59 % (8.8 US\$ cents/kWh) of the LCOE.

The cost breakdowns in Table 1 are arranged in descending order where it is clear that the cost of the heliostat field is the most expensive part of the power tower CSP plant. Cost reduction in the heliostat field has been identified as a key technology improvement opportunity. The focus is placed on reducing the cost of heliostats, and increasing the thermal efficiency of the whole plant. The increase in thermal efficiency does not only reduce the size of the heliostat field but also reduces the size of the thermal energy storage and requires less land.

Currently the highest efficiency power cycles used in CSP are subcritical water cycles that have overall thermal efficiencies between 38 and 40 %. Using advanced power cycles with a higher efficiency (like Helium and supercritical CO<sub>2</sub> cycles) may increase the thermal efficiency to above 50 %. For argument's sake, consider a 7 % increase in thermal efficiency from 38 %. This relates to 15.56 % input energy savings. This means that there will be 15.56 % less heliostats. A 15.56 % saving on heliostats relates to a 3.44 % reduction of the LCOE based on heliostats and storage alone. However, it is estimated that the use of an advanced power cycle could provide even greater cost reductions. This is discussed in detail in section 10.

The key to increased thermal efficiency is to increase the temperature at which energy is introduced to the power cycle. Apart from the thermodynamic cycle limitations (discussed in section 2.3) the current operational temperatures of the storage and heat transfer systems are limited (discussed in sections 2.4 and 2.7). The argument can be made that an increase of the thermal efficiency is essential to a reduction in LCOE. This would require higher operational temperatures of the heat transfer and thermal energy storage system.

## 2.2 Factors determining thermal efficiency

When considering the overall thermal efficiency of a CSP plant there are many factors to consider. If thermal energy storage comes into play the energy balance is more complicated because the storage decouples the receiver from the power cycle. For argument's sake, take a simple scenario where the energy absorbed by the receiver is used directly by the thermodynamic power cycle.

The overall thermal efficiency ( $\eta_{th(CSP)}$ ) is primarily dependent on the thermal efficiency of the power cycle ( $\eta_{th}$ ), and the thermal efficiency of the receiver ( $\eta_{receiver}$ ). Thus,

$$\eta_{th(CSP)} = \eta_{receiver} \cdot \eta_{th} \quad (2.1)$$

The thermal efficiency of the power cycle ( $\eta_{th}$ ) can be approximated by the Chambadal-Novikov efficiency correlation (Novikov, 1958) (Chambadal, 1957):

$$\eta_{th} = 1 - \sqrt{\frac{T_L}{T_H}} \quad (2.2)$$

Where  $T_L$  is the sink temperature, and  $T_H$  is the source temperature.

The thermal efficiency of the receiver is highly dependent on its design, but generally radiation is the greatest loss in high temperature receivers. The efficiency of the receiver can be expressed as:

$$\eta_{receiver} = \frac{Q_{absorbed} - Q_{lost}}{Q_{rad}} \quad (2.3)$$

Where  $Q_{rad}$  is the radiation incident on the receiver,  $Q_{absorbed}$  is the solar radiation absorbed by the receiver and  $Q_{lost}$  is the thermal losses from the receiver.:

$$Q_{rad} = \eta_{optics} ICA \quad (2.4)$$

$$Q_{absorbed} = \alpha Q_{solar} \quad (2.5)$$

Here I is the incident radiation, C the concentration ratio of the collector, and A the surface area of the receiver.

For  $Q_{lost}$  it is assumed that the convective losses of the receiver are negligible, and by applying the Stefan-Boltzmann law:

$$Q_{lost} = A\varepsilon\sigma T_s^4 \quad (2.6)$$

The following simplifications can be made:

- $\alpha = 1$  and  $\varepsilon = 1$  (blackbody)
- $\sigma = 5.670373 \times 10^{-8} \text{ W/m}^2 \cdot \text{K}^4$
- $T_H = T_s$
- $\eta_{optics} = 1$
- $I = 1000 \text{ W/m}^2$

Substituting equations 2.4, 2.5 and 2.6 into equation 2.3, and substituting the simplified result and equation 2.2 into equation 2.1 yields:

$$\eta_{th(CSP)} = \left(1 - \frac{\sigma T_H^4}{IC}\right) \cdot \left(1 - \sqrt{\frac{T_L}{T_H}}\right) \quad (2.7)$$

Assuming that the sink temperature is constant at 40°C, Figure 1 and Figure 2 show the efficiency of the receiver and the thermodynamic cycle respectively. The overall thermal efficiency of the plant is presented in Figure 3, where the overall thermal efficiency is plotted against receiver temperature for various concentration ratios.

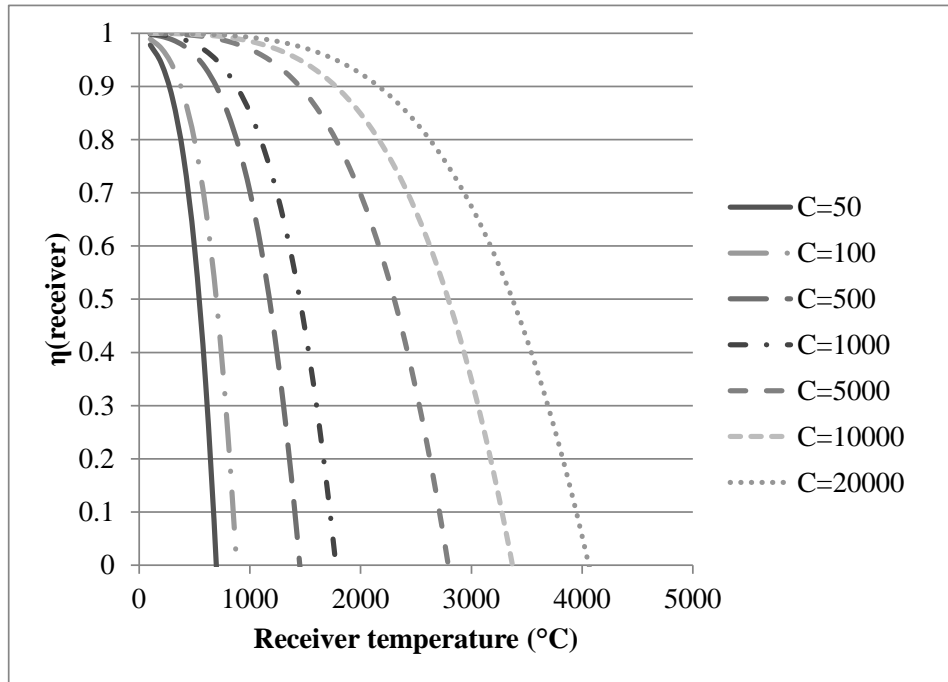


**Figure 1 - Efficiency of a receiver at various concentration ratios**

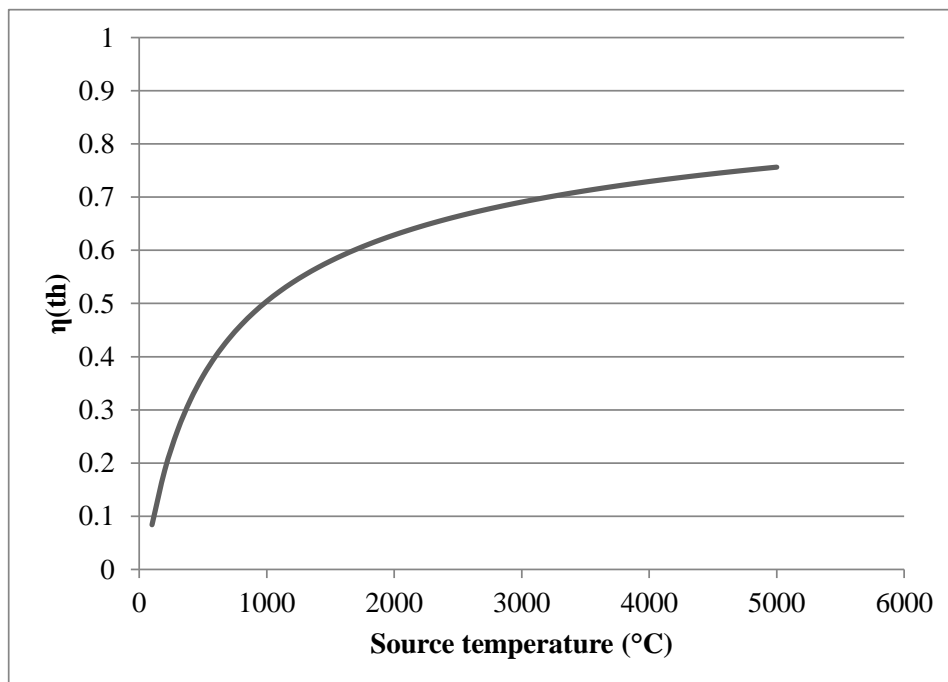


**Figure 2 – Approximate thermal efficiency of a steam cycle at increasing source temperatures for a sink temperature of 40°C**

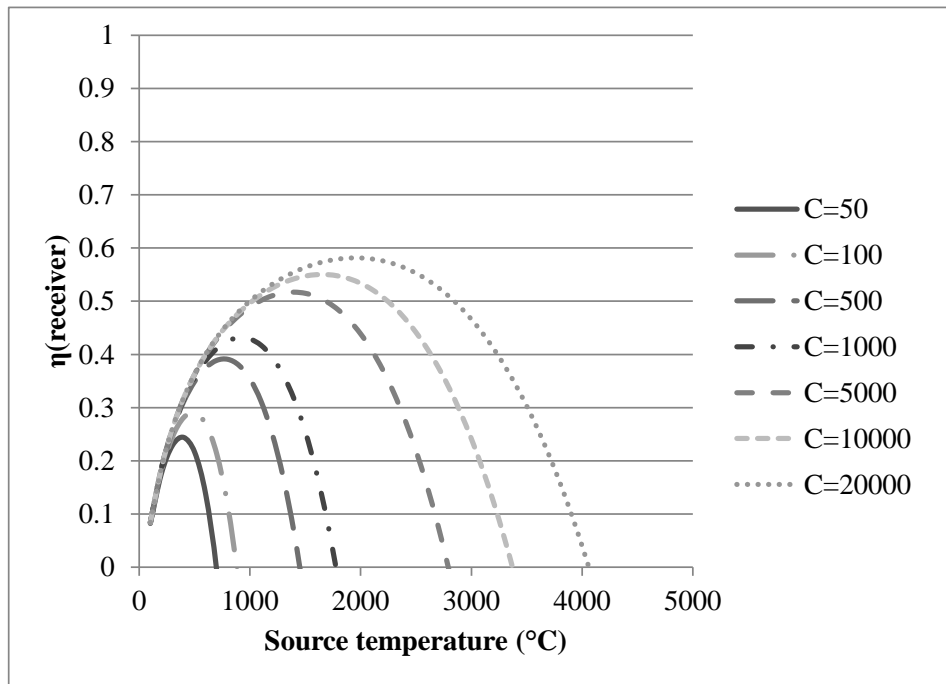


**Figure 3 - Thermal efficiency of a CSP plant at different concentration ratios for a sink temperature of 40°C**

For each concentration ratio there is an optimum receiver temperature.

Even though the specifics of any given power plant are distinctly different, this analysis highlights the following key concepts:

- A receiver's thermal efficiency decreases at elevated temperatures due to radiation losses.
- The larger the surface area of the receiver, the greater the losses (equation 2.6).
- Higher source temperature for a thermodynamic power cycle increases the thermal efficiency of the CSP plant.
- Because of these two counteracting effects there is an optimum receiver temperature for any given concentration ratio.
- At higher concentration ratios, radiation losses are less prominent.

Point focus collectors have the highest possible concentration ratio, and accordingly, the highest possible thermal efficiency. Furthermore, because the dish concept does not lend it to the use of one central power block, and therefore the power tower collector is theoretically the CSP concept that has the highest possible overall thermal efficiency. The higher the maximum flux density of the receiver, the higher the concentration ratio of the collector will be. Therefore a high flux density receiver is important in cost reduction; this is discussed in section 8.

## 2.3 Power cycles

High efficiency power generation is crucial for the reduction of LCOE. The most common and versatile power cycle is the steam Rankine cycle. Through years of development the efficiency of these cycles have improved as the metallurgical limits of newer, more advanced alloys allow higher temperatures and pressures. Subcritical steam technology is mature, and power cycles running at live steam conditions (the steam conditions at the turbine entrance) of 540 °C, 14 MPa are commonplace. It is possible to obtain thermal efficiencies between 36 and 40 % with these subcritical power blocks. Most current CSP plants use subcritical steam power cycles.

Advanced metal alloys have enabled the development of supercritical and ultra-supercritical power blocks that can achieve thermal efficiencies in the range of 45 to 49 %. Currently there are a number of power plants that are operating at temperatures above 600 °C, at pressures between 25.5 MPa and 30 MPa, having practical thermal efficiencies as high as 49 % when cooled with sea water. It has been shown that these power blocks are not only technically feasible, but also economical (Bugge, et al., 2006).

In the 1998 the European Union launched a project for the development of ultra-supercritical steam power plants operating at 700 °C. With the high price of chrome, the development of high performance austenitic and nickel based alloys is crucial to the realisation of economic power blocks that can operate above 700 °C (Bugge, et al., 2006).

Air Brayton cycles are under investigation. One of the primary limitations in CSP is the upper temperature limit of HTFs used in a CSP plant. To overcome this, air Brayton cycles have been proposed. The overall thermal efficiency of an air Brayton cycle is not as high as an S-CO<sub>2</sub> or a steam cycle, but it can be used in conjunction with a steam cycle to form a more efficient combined cycle (as a topping cycle). By using thermal energy storage, the thermal energy of the hot exhaust gasses of the Brayton cycle can be stored, and then used at night in the steam cycle. This will also increase the thermal efficiency of the entire cycle (Allen, et al., 2009).

A number of technical difficulties arise if an air Brayton cycle is applied in CSP. Because air is a gas, the volume flow rate of the air is high resulting in large pressure losses in a receiver or an intermediate heat exchanger, and this will have a significant impact on the thermal efficiency. Furthermore, air is a poor heat transfer medium and requires large heat exchange surfaces. In normal air Brayton cycle applications heat is added to the air through combustion. There are numerous concepts to try and mitigate these issues, but each with drawbacks.

Much work is being done on supercritical CO<sub>2</sub> Brayton cycles (S-CO<sub>2</sub>). Above 500 °C and 20 MPa S-CO<sub>2</sub> has properties that enable thermal efficiencies exceeding 45 % at source temperatures as low as 550°C. Because of the high density and non-ideal gas properties of S-CO<sub>2</sub> it results in exceptionally compact turbo machinery and heat exchangers. Unfortunately S-CO<sub>2</sub> thermodynamic

cycles are not well suited for dry cooling, which limits the use of such cycles in CSP. Another obstacle is the high pressures, but due to metallurgical advances and the compact nature of S-CO<sub>2</sub> power cycles, S-CO<sub>2</sub> cycles are considered technically and economically feasible (Dostal, et al., 2004).

Since supercritical steam, ultra-supercritical steam and S-CO<sub>2</sub> power cycles can utilise higher source temperatures to increase thermal efficiency, higher temperature TES and HTFs are needed.

#### 2.4 Overview of thermal energy storage and current technical limitations

Thermal energy storage is the main advantage that CSP has over other renewables. It is important that the thermal energy storage system matches the operational parameters of the power cycle. Since the goal is to investigate higher thermal efficiency power cycles, only TES systems that can deliver thermal energy at temperatures higher than 500°C will be discussed. Currently the two tank molten nitrate salt system is considered as state of the art and is well suited for subcritical steam generation, but it is currently at its upper temperature limit (Gil, et al., 2010).

Thermal energy can be stored in a thermal energy storage material. Thermal energy storage materials can be either solid or liquid and the storage mechanism can be classified as either sensible, latent or chemical. In sensible thermal energy storage the energy is stored by raising the temperature of a material. On the other hand, latent energy storage refers to thermal storage by adding energy to a material that is undergoing phase change (this is an isothermal process). This is illustrated in Figure 4 below. In thermal chemical energy storage the thermal energy is stored in a reversible chemical reaction.

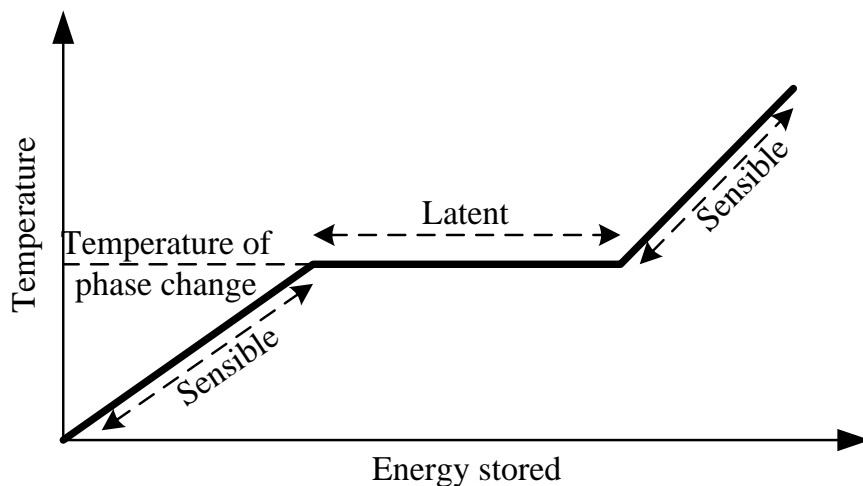


**Figure 4 - Modes of thermal energy storage**

Liquid thermal energy storage media lend themselves to active storage concepts. In active storage concepts the storage medium is pumped through heat

exchangers. In some instances the liquid storage medium is used as HTF in both the steam generator and the receiver. These are called direct systems. In other TES systems an intermediate heat transfer fluid is needed to transfer heat from the receivers to the storage media (known as indirect systems).

Solid thermal energy storage materials generally yield passive storage concepts where the storage media is contained and heat is added to or taken from the storage material using a heat transfer fluid. Most latent heat thermal energy storage and solid sensible concepts are passive, indirect concepts. The classification is illustrated in Figure 5.

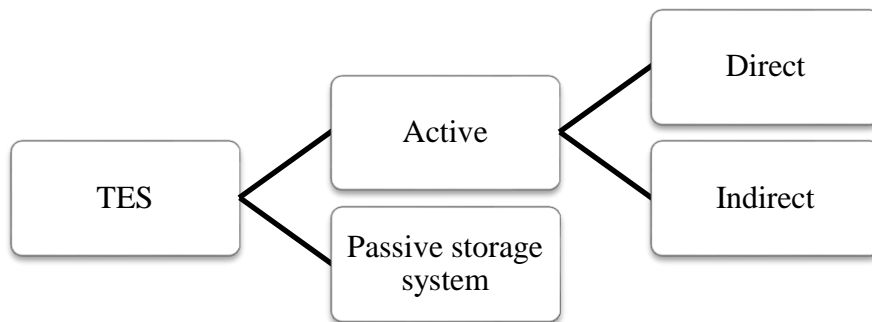


**Figure 5 – Classification of TES concepts**

Since cost reduction is the greatest factor in CSP, the most important factors for sensible thermal energy storage are that the storage medium has a large specific heat, and that the operational temperature of the PCM is as high as possible. Similarly, for latent heat thermal energy storage, the phase change material (PCM) needs to have a large heat of fusion. The maximum operational temperature of the storage system is also extremely important since the storage temperature is the source temperature of the power cycle.

#### 2.4.1 Current state of the art

Table 2 shows some of the more notable TES systems built for CSP (Medrano, et al., 2010). There are numerous concepts, some more successful than others. Notably all of the commercial TES systems are of the active type. The state of the art is two tank molten salt storage. The specifics of the plant layout depend on the receiver technology, but the general concept remains the same.



**Table 2 - Notable examples of thermal energy storage (Medrano, et al., 2010)**

Storage concept			Storage media	Mode	HTF	Plant	Collector type	Operating temperature range (°C)	Thermal capacity (MWhth)	Total capacity (MWe)
Active Storage	Direct storage	Direct steam generation	Steam	Sensible	Steam	PS10	Central receiver	n.a.	15(50min)	11
			Steam	Sensible		PS20	Central receiver	n.a.	n.a.	20
		Two tanks	Oil	Sensible	Mineral Oil (CALORIA)	SEGS I	Parabolic trough	307-240	115	14
			Oil	Sensible	Mineral Oil (ESSO 500)	SEGS II	Parabolic trough	316-240	n.a.	30
			Molten salts	Sensible	Molten salts	THEMIS	Central receiver	450-250	40	2.5
			Molten salts	Sensible	Molten salts	Solar Two	Central receiver	565-275	105	10
			Molten salts	Sensible	Molten salts	Gemasolar	Central receiver	565-288	15h	20
	Indirect storage	One Tank (Thermocline)	Oil	Sensible	Mineral Oil (Santotherm 55)	SSPS DCS (PSA)	Central receiver	290-180	588 (16 h)	17
				Molten salts, Rock, Sand	Sensible	Steam	Solar one	Central receiver	304-224	182
		Two tanks	Molten salts	Sensible	Molten salts	SSPS CESA1 (PSA)	Central receiver	340-220	7	1.2
			Molten salts	Sensible	Molten salts	SSPS CERS (PSA)	Central receiver	n.a.	2.7	0.5
			Molten salts	Sensible	Steam	ANDASOL I	Parabolic trough	381-291	1010	50
			Molten salts	Sensible	Steam	ANDASOL II	Parabolic trough	n.a.	n.a.	50

Molten nitrate salt is used as the storage medium and it is held in two tanks, one hot, and the other cold. The cold tank holds molten nitrate salt at a temperature of about 230°C. The salt is pumped to either the receiver (direct system, Figure 6) where the salt is heated up to the salt's maximum operational temperature, or a heat exchanger (indirect system, Figure 7). The hot salt is then piped to the hot tank where it will stay in storage.

For steam generation, hot salt is taken from the hot tank and pumped through either the steam generator (direct system) or to a heat exchanger (indirect). The thermal energy of the salt is then used to generate steam, which powers the turbines. The cooled salt returns to the cold tank.

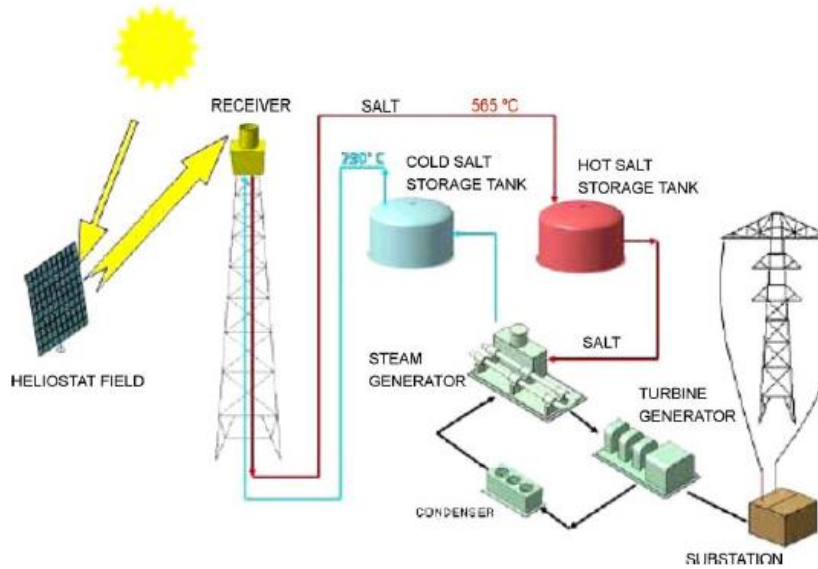


**Figure 6 - Two tank molten salt TES for central receivers (Direct system)**

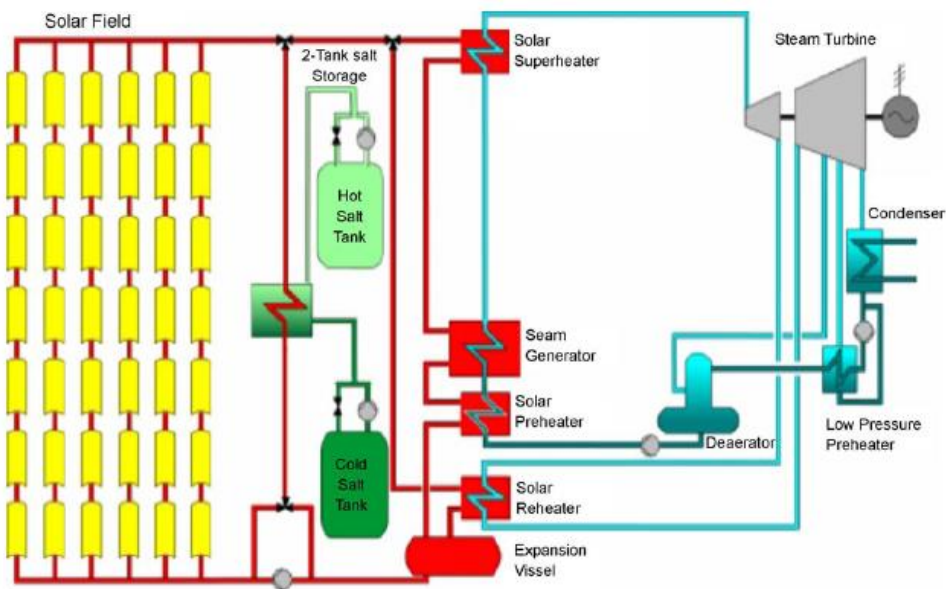


**Figure 7 - Two tank molten salt TES system for parabolic trough (Indirect) (Herrmann, et al., 2006)**

The salts used are typically a binary or a ternary eutectic mixture of nitrate and nitrite salts. The key issues with molten salt storage are: high melting point (120 to 240°C), and limited upper operational temperature (565°C).

The properties of various nitrate salts are listed in Table 3. There are three prominent salt mixtures, Hitec, Hitec XL and Hitec solar salt. Hitec, and Hitec XL are better suited for parabolic trough applications because of their lower melting

points. Hitec solar salt is better suited for use in a central receiver system because of its higher maximum operational temperature.

The highest storage temperature in commercial thermal energy storage systems is 565°C, and is due to the upper temperature limit of Hitec solar salt. Because of the temperature limitations on nitrate salts and the risk of solidification, a number of other thermal energy storage concepts had been proposed and researched. There are very few of these storage concepts that enable high enough storage temperatures to enable the use of high thermal efficiency thermodynamic cycles (Gil, et al., 2010).

**Table 3 - Thermal properties of nitrate salts**

	Unit	Hitec XL	Hitec	Hitec solar salt
Melting point	°C	120	142	240
Maximum operating temperature	°C	500	538	567
Density	kg/m <sup>3</sup>	1640	1762	1794
Specific heat capacity	kJ/kg.K	1.9	1.56	1.214
Volumetric heat capacity	kJ/m <sup>3</sup> .K	3116	2748	2177
Viscosity	Pa.s	0.0063	0.003	0.0022
Thermal conductivity	W/(m.K)	na.	0.363	0.536
Prandtl number			12.89	4.98

#### 2.4.2 High temperature storage concepts

Currently there is much research being done on higher temperature thermal energy storage. Sensible thermal energy storage can use either solid or liquid storage media. The advantage of a liquid sensible storage medium is that it can be pumped through a heat exchanger and can be stored in separate hot and cold tanks. This is a very efficient and elegant form of thermal energy storage. For this reason the two tank molten salt thermal energy storage is state of the art, and is a tried and tested system, an important factor when bankability is a foremost consideration. A number of liquid sensible storage materials have been investigated in the past (listed in Table 4), but nitrate and nitrite salts have been found to be the most favourable because of a combination of a manageable melting point, low cost, high operational temperature and acceptable heat transfer characteristics.

The current aim is to increase the maximum operational temperature and to decrease the melting point of salt storage. Thus far a breakthrough has not been made in a suitable heat transfer salt, and researchers have been investigating other storage concepts (Gil, et al., 2010).

**Table 4 - Candidate materials for sensible thermal energy storage (Gil, et al., 2010)<sup>1</sup>**

Storage medium	Temperature		Average density (kg/m <sup>3</sup> )	Thermal conductivity (W/mK)	Heat capacity (kJ/kgK)	Volume specific heat capacity (kWh <sub>th</sub> /m <sup>3</sup> )	Cost (US\$/kg)	Cost (US\$/KWth)
	Cold (°C)	Hot (°C)						
Solid								
NaCl (solid)	200	500	2160	7	0.85	150	0.15	1
Cast steel	200	700	7800	40	0.6	450	5	60
Cast iron	200	400	7200	37	0.56	160	1	32
Silica fire bricks	200	700	1820	1.5	1	150	1	7
Magnesia fire bricks	200	120	3000	5	1.15	600	2	6
Sand-rock-mineral oil	200	300	1700	1	1.3	60	0.15	4.2
Reinforced concrete	200	400	2200	1.5	0.85	100	0.5	1
Liquid								
Mineral Oil	200	300	770	0.12	2.6	55	0.3	4.2
Synthetic Oil	250	350	900	0.11	2.3	57	3	43
Silicone oil	300	400	900	0.1	2.1	52	5	80
Nitrite salts	250	450	1825	0.57	1.5	152	1	12
Nitrate salts	265	565	1870	0.52	1.6	250	0.5	3.7
Carbonate salts	450	850	2100	2	1.8	430	2.4	11
Liquid sodium	270	530	850	71	1.3	80	2	21

Most of the solid TES materials that have been investigated (Table 4) have very low thermal diffusivity, requiring large heat exchange surfaces. Some of these can be used in a packed bed, but others need a large heat exchanger that is embedded in the material. Two notable examples of this are shown in Figure 8 and Figure 9. These heat transfer modifications make up a significant portion of the capital cost needed for the thermal energy storage unit and have a significant impact on the economic viability for these concepts.

Among the various TES materials only PCMs and sensible thermal energy storage in solids show potential for higher temperature thermal energy storage. Both PCM and solid sensible TES result in passive storage systems, and this requires HTFs that can charge and discharge the storage material.

<sup>1</sup> Cost was calculated in 2010, and only to be used for comparison.



**Figure 8 - Graphite heat transfer enhancements for low thermal diffusivity in PCMs (Tamme, 2007)**



**Figure 9 - Concrete storage with heat exchanger pipes visible at the end (Tamme, 2007)**

Most research on PCMs and solid sensible TES focussed on lower temperature storage that is more suited for direct steam solar application (Kenisarin, 2009). Solid sensible thermal energy storage has been investigated for high temperature applications, but very few solid storage materials show long term stability through thermal cycling or prove to be economically viable. Some of the more viable solid TES materials are shown in Table 4.

Since the temperature of a sensible TES material decreases as it discharges, it is a technical challenge to design a system that can yield constant thermal output. Consequently PCMs offer an attractive solution to high temperature TES. PCMs store thermal energy isothermally, which is significantly easier to design for from a heat transfer and process control point of view.

Unfortunately isothermal storage has a thermodynamic penalty as it can act as a large entropy generator (this is discussed in section 8.6.2). To overcome the shortcomings of PCM storage and solid sensible TES, a combination of both may be used, or various PCMs can be cascaded to match the heat transfer of the power cycle.

## 2.5 Thermal energy storage in phase change materials

Thermal energy storage in the latent heat of phase change materials has the advantage that a great amount of energy can be stored across a small temperature difference. The higher the heat of fusion of a PCM, the more energy can be stored in it per unit mass. Therefore a high heat of fusion ( $\lambda$ ) is preferable. Other than the heat of fusion, there are a number of important properties that must be considered in PCM selection (Kenisarin, 2009):

- Melting temperature ( $T_m$ )
- Low or no sub-cooling
- Thermal stability
- Chemical stability
- Cyclic stability
- Thermal conductivity
- Specific thermal capacity
- Low cost
- Availability
- Low toxicity
- Compatibility with construction materials

The melting temperature of the material is one of the most important considerations, and it limits the use of the material. The melting point will be the operational temperature at which the TES system will operate. When designing a latent TES system, it is important that the melting point of the PCM matches the input temperature of the power block. Thermodynamically it makes sense to use multiple PCMs with different melting temperatures in a cascaded fashion to minimize entropy generation (Michels, et al., 2007). This is discussed in more detail in section 8.6.2.

Thermal conductivity is probably the most important thermal property other than heat of fusion and melting temperature. Hoshi, et al. (2005) investigated the charging and discharging rate between a low conductivity salt and a metallic phase change material. The results showed that thermal conductivity has a very large role in the performance of the thermal storage unit. In thermal energy storage, energy needs to be added and removed from the PCM. Because nearly all of the feasible PCMs operate between the solid-liquid phase transition, these storage solutions will be passive thermal storage concepts. Thus, a heat transfer fluid must transfer thermal energy to and from the heat storage unit (HSU). If the thermal conductivity of the PCM itself is too low, the size of the heat exchange surfaces embedded into the PCM will have to be very large or material modifications will be needed in the PCM (Agyenim, et al., 2009). Most of these material modifications involve embedding metal or graphite structures into the PCM to enhance the thermal diffusivity of the bulk material. This might result in uneconomic storage concepts. If the thermal conductivity of the PCM is high, sufficient heat transfer rates can be achieved with no material modification or elaborate heat exchange surfaces.

Ideally a PCM should accumulate and release its energy at the same temperature, but in practice some materials must cool down to substantially lower temperatures than the melting point before the crystal structure of the material will form in the absence of crystallization centres. This effect is called subcooling. This is a very unfavourable phenomenon because energy that has been stored at one temperature will now be “re-claimed” at a lower temperature. Thus the energy is returned with more entropy (lower quality).

Naturally the long term stability, safety and general feasibility of the PCM is also very important. The PCM should not corrode its container, be chemically reactive, toxic or be a potential fire hazard. It should be chemically stable in its operational temperature range, and it should be able to go through multiple phase changes without a change in its thermal properties. This is one of the reasons pure substances or eutectic mixtures and alloys are considered as candidate PCMs.

### 2.5.1 Eutectic materials

A eutectic system is a homogeneous mixture of substances that solidifies at a temperature lower than that of the individual components. The eutectic composition is the ratio of the constituent substances that has a lower melting point than any other composition of those substances. The associated melting temperature is called the eutectic temperature, and the intersection of the eutectic temperature and the eutectic composition is called the eutectic point. A eutectic system may comprise of a number of substances, but due to the complexity associated in investigating these systems, most known eutectic systems are either binary or ternary. A generic binary eutectic system is shown in Figure 10, where L denotes liquid phase,  $\alpha$  denotes the solid phase of constituent A, and  $\beta$  denotes the solid phase of constituent B.

A eutectic mixture that is towards the right of the eutectic system is called a hyper-eutectic composition and to the left is called a hypo-eutectic composition. As either in a hypo- or hyper-eutectic system, either the  $\alpha$  or  $\beta$  phases solidify first, and cause the material to change phase over a range of temperatures. This also causes “clumps” of either  $\alpha$  or  $\beta$  phase material to form throughout the material. This causes a non-homogeneous microstructure through the material. In a eutectic composition, both the  $\alpha$  and  $\beta$  phases solidify in a homogeneous manner with both phases dispersed evenly through the microstructure. The homogeneous dispersion of the two solid phases aids in material stability, as the “clumps” of  $\alpha$  or  $\beta$  phases in the hypo- and hyper-eutectic compositions have a tendency to drift out of solution through multiple heating and cooling cycles (Li, et al., 2011).

Thus, eutectic compositions and pure substances are preferred as PCMs because of thermal stability and very small temperature range for phase change.



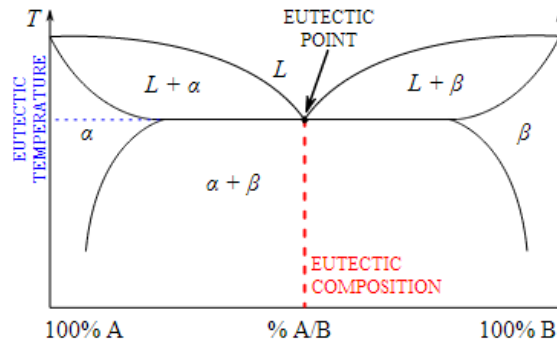


**Figure 10 - Generic phase diagram for a binary eutectic system**

### 2.5.2 Comparison of some PCMs

Through the last three decades the need for thermal energy storage spurred investigation into various PCMs. Nearly all of the investigated PCMs are binary and ternary compositions of salts and metals. They can be classified under:

- Eutectic salt compositions
  - Fluorides
  - Chlorides
  - Hydroxides
  - Nitrates
  - Carbonates
- Eutectic metal alloys

To compare the classes of the various PCMs that can be found in literature, a plot of the heat of fusion against the melting point of each candidate PCM is shown in Figure 11. The data used in this graph is presented and referenced in Appendix A. It is clear that the metallic PCMs and fluoride salts have melting temperatures that are very well suited for high efficiency power blocks.

Generally the thermal conductivity of the salts is extremely low, in the order of  $1 \text{ W/m}^2\text{K}$  (Kenisarin, 2009). This is in stark contrast with metal alloys that have thermal conductivities a factor of more than a hundred higher than those of salts. This is a very significant factor when it comes to the design of a heat storage unit (HSU). Hoshi, et al. (2005) showed that the thermal conductivity of a PCM is crucial for charge and discharge rates. The lower the thermal conductivity, the larger the heat transfer area of the heat exchanger needs to be to achieve adequate charge and discharge rates. To decrease the size and cost of the heat exchangers, some researchers attempt to effectively increase the thermal conductivity of the PCM by modifying the material through the inclusion of high conductivity conductive elements like graphite flakes (Tamme, et al., 2004).



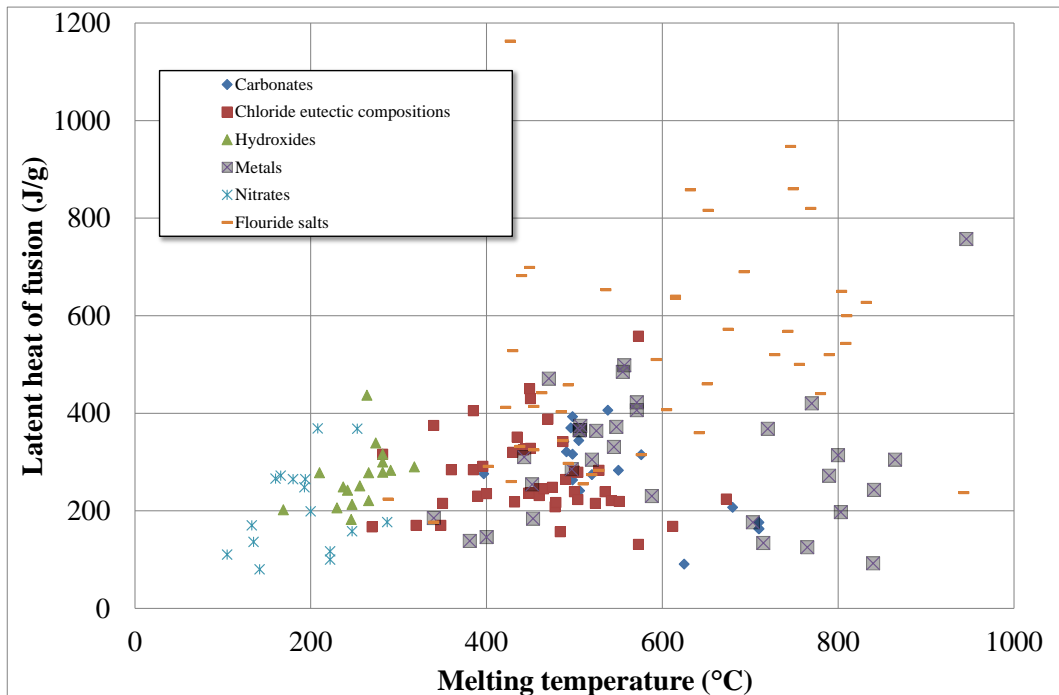


**Figure 11 - Comparison of high temperature PCMs found in literature (Latent heat of fusion against temperature)**

Salts have a significant set of drawbacks that metallic PCMs generally do not exhibit:

- Salts are prone to subcooling, where metals generally have no or little subcooling.
- Salts have a large volume change over phase change.

Thus, metallic phase change materials pose a set of significant advantages over that of salts. Figure 12 shows only the metallic phase change materials that could be found in literature. Notably, AlSi12, a eutectic alloy of aluminium and silicon has an exceptionally high heat of fusion, and a fairly moderate melting point. For this reason, AlSi12 is the only metallic PCM with a melting point over 500 °C that has been investigated to date (Gil, et al., 2010) (Kenisarin, 2009) (Herrmann, et al., 2006). Therefore, AlSi12 will be used in this project, even though it will be pointed out in chapter 10 that a pure aluminium or eutectic silicon-magnesium alloy is better suited in practice.

AlSi12 is commercially available as LM6 casting alloy, and its metallurgy and thermal properties are very well known in literature. It is inexpensive, commonly available and it has a very high thermal conductivity. This makes AlSi12 an ideal candidate metallic phase change material for both research and commercial purposes. AlSi12 is discussed in more detail in section 4.1.

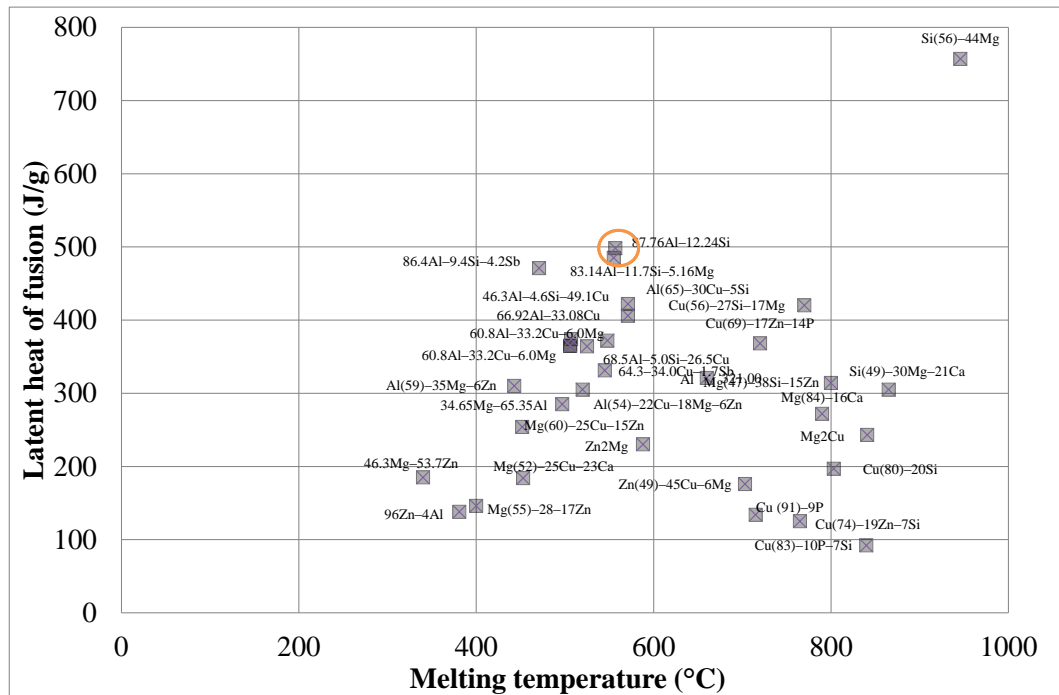


**Figure 12 - Metallic phase change materials found in literature (Birchenall, et al., 1979)**

## 2.6 AlSi12 as a PCM in literature

The first mention of AlSi12 as a PCM was made by Birchenall and Reichmann (1979) in a paper that proposed thermal energy storage in eutectic metals. The core of the research was the prediction of the composition, melting temperature and heat of fusion of eutectic substances by using molecular thermodynamics. In their text a large list of potential PCMs had been listed. The metallic PCMs that were listed in their paper are presented in Figure 12. Until recently most research efforts focussed on TES at temperatures lower than 400 °C due to focus on parabolic through technology (Kenisarin, 2009). With increased interest in central receiver technology, the emphasis of storage technology shifted to higher storage temperatures, making high temperature phase change TES a more relevant field of research.

Considering PCM research as a whole, a lot of research has gone into the simulation, testing and modification of low conductivity PCMs. Most of the work has gone into artificially increasing the thermal conductivity of the PCM material by including high conductivity material into the bulk of the PCM. These analysis methods are not of particular importance to metallic PCMs. This will be discussed in greater detail in chapter 7 (Agyenim, et al., 2009).

The importance of high thermal conductivity is emphasised clearly by Hoshi, et al. (2005), who compared the effect of thermal conductivity on the discharge rate of a PCM. In their study they used computational methods to study the discharge rate of lead and potassium nitrate as PCMs. They found that lead's inherently high

thermal conductivity enabled far higher discharge rates. This comes as no surprise, but underlines the advantage of using a metallic PCM in thermal energy storage. Figure 13 shows the results of the analysis done by Hoshi, et al. (2005).

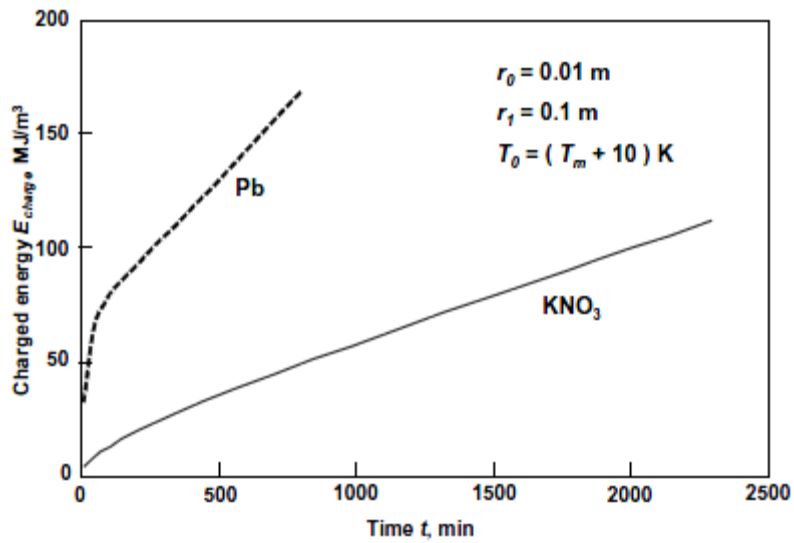


**Figure 13 - Analytical comparison of the charging rate of a metallic PCM versus a salt PCM (Hoshi, et al., 2005 )**

Adinberg, Zvegilsky and Epstein (2010) investigated the use of eutectic Zinc-Tin alloy as a PCM in a “heat pipe” type steam generator (shown in Figure 14). The system was evaluated analytically, and shows that steam could be delivered at 340-360 °C. The applicability of the concept to higher temperatures is limited to lower temperatures due to the heat transfer arrangement. This concept lends itself well to direct steam systems due to its operational temperature range.

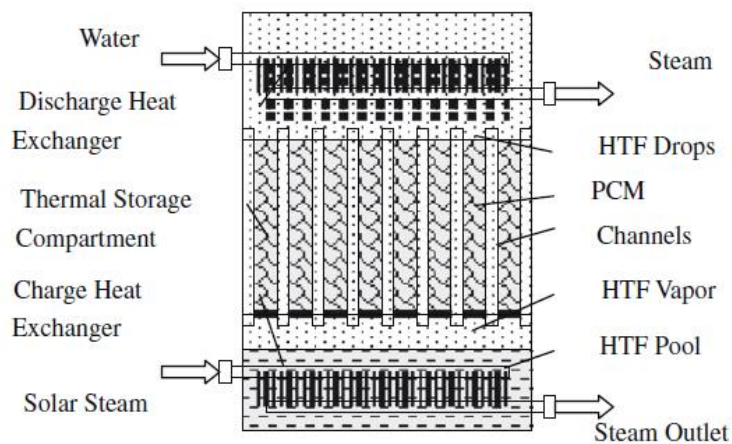


**Figure 14 - Steam generator as proposed by Adinberg *et al.* (2010)**

Otherwise there is limited published information on metallic PCMs researched in CSP. A number of authors have investigated PCM TES concepts for applications not directly associated to solar.

Burch, *et al.* (1996) presented a concept where two PCMs are used to store thermal energy around the catalytic converter in a car's exhaust system to reduce light up time and reduce emissions. Figure 15 and Figure 16 shows the physical setup. The paper does not divulge what PCM is used, but one of the PCMs used in the prototype is definitely AlSi12 (PCM #1). Figure 17 demonstrates the ability of the storage unit to keep the catalytic converter warm.

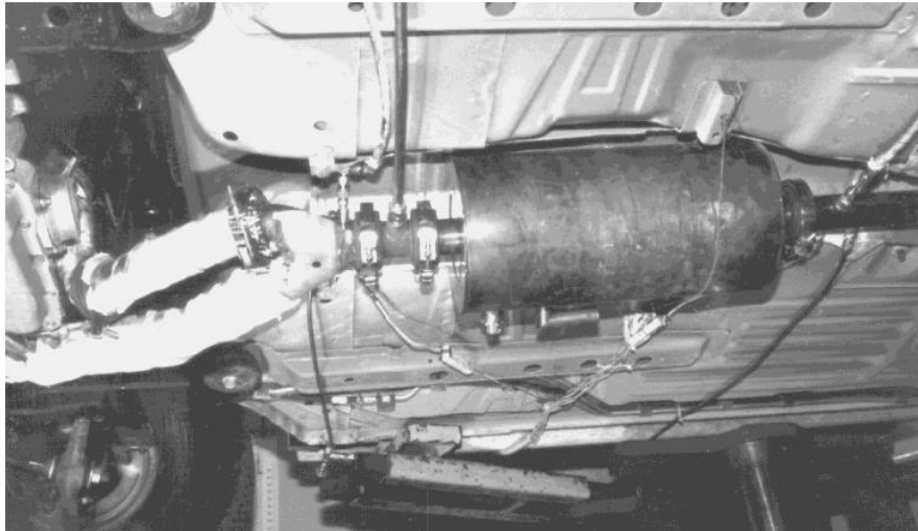


**Figure 15 - Thermal storage around a catalyst to reduce the light-up time for a catalytic converter**

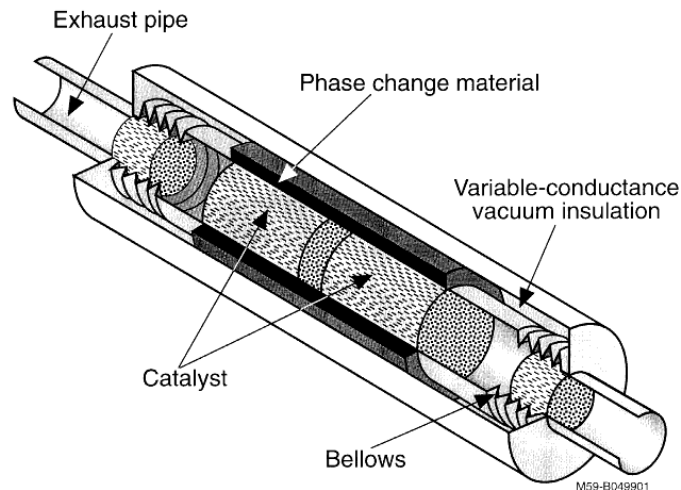


**Figure 16 - Catalytic converter with PCM TES system**

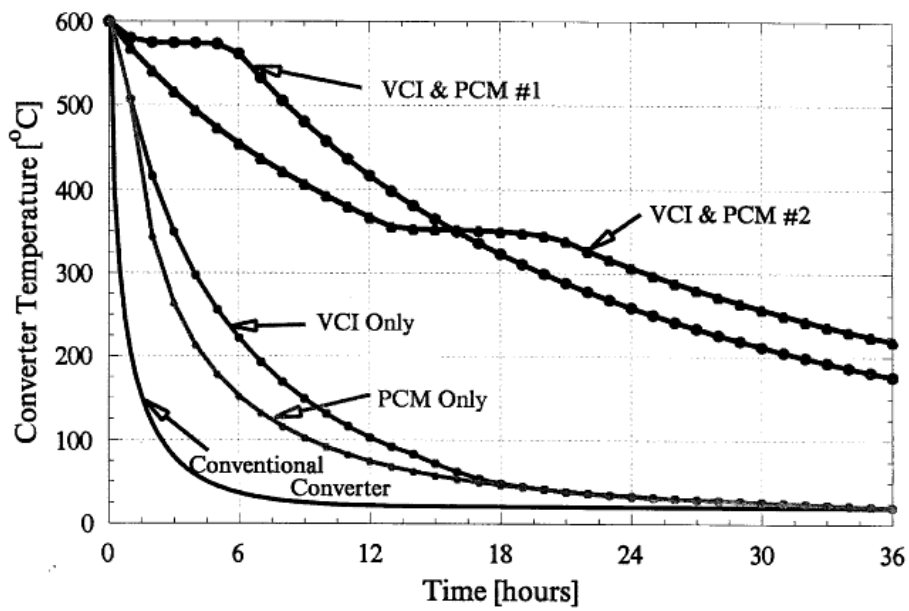


**Figure 17 - Test results from catalytic converter tests**

He and Zhang (2001) investigated a concept intended to capture waste heat from industrial furnaces for recovery at a later stage. It consists out of a shell and tube heat exchanger, filled with AlSi12 alloy on the shell side. It has eighteen 20mm ID tubes running the 400mm length of the heat exchanger. The tubes are configured in a double pass configuration and air is used as a heat transfer medium. For the experiment the storage unit is heated up using electrical heating elements. Figure 18 shows a conceptual drawing of the heat recovery unit, and Figure 19 shows the temperature readouts of the thermocouples at the positions indicated in Figure 18 through discharge.

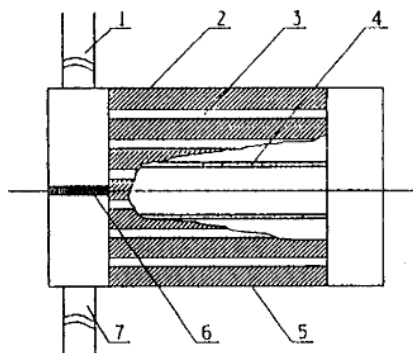


**Figure 18 - Waste heat recovery unit using AlSi12 as PCM**

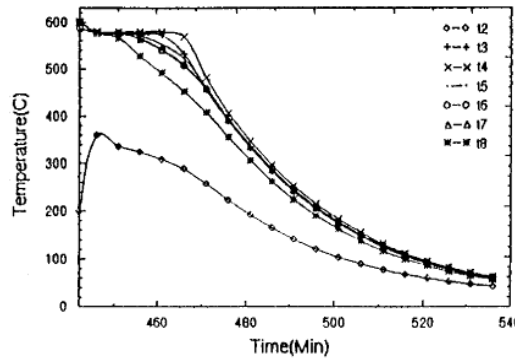


**Figure 19 - Temperature readouts for thermocouples in the storage unit through discharge**

The mass of AlSi12 in the storage unit is not stated explicitly in the paper (just one of many shortcomings in the paper) making it hard to follow exactly what the operational parameters of the experiment were. The test is supplemented by a simulation that does not seem to follow the experimental data particularly well, nor is it possible to determine exactly where the thermocouples were placed relative to the heat exchange surfaces.

Wang, *et al.* (2004) investigated a novel space heater concept (Figure 20). The idea is to offset electrical usage by charging a mass of AlSi12 as a PCM during times of the day when electricity is cheaper, and to allow the PCM to bridge the high cost times of the day through discharge. It consists of a 31 kg block of AlSi12 alloy encased in insulation with one side open to the atmosphere (Figure 21 and Figure 22). Thermal energy is added to the space heater using long cartridge heating elements embedded into the PCM.



**Figure 20 - Space heater with latent heat storage (Wang, et al., 2004)**

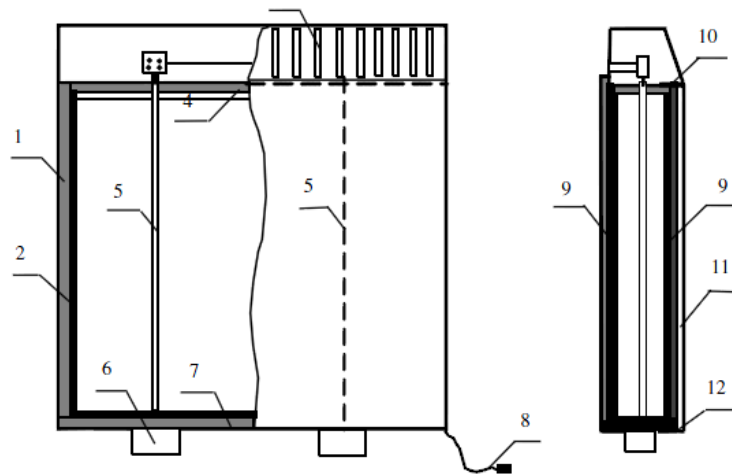


**Figure 21 - Sectioned view of the space heater (Wang, et al., 2004)**

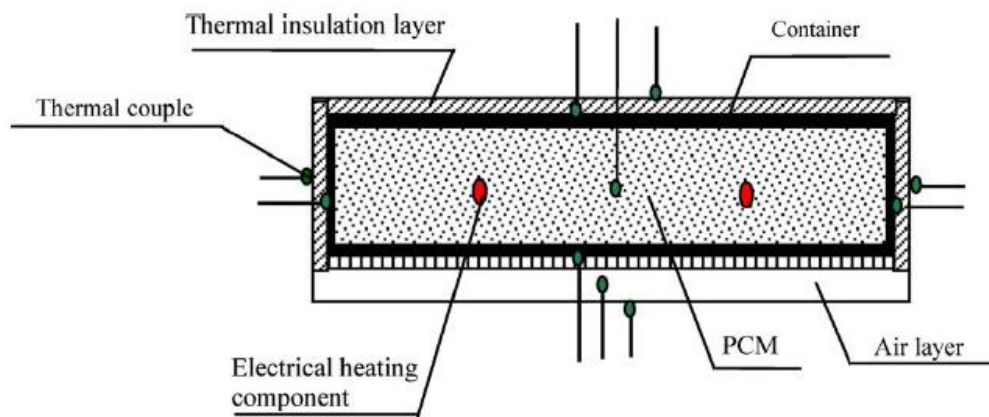


**Figure 22 - Section through the space heater (Wang, et al., 2004)**

The positions of various thermocouples are visible in Figure 22. The heater was tested and compared against a simple model. The model was simply an energy balance for the mass of PCM, with appropriate convective heat transfer coefficients applied to each of its surfaces. The heater was tested at two power levels, yielding similar results in both cases. The results of one of the tests are shown in Figure 23. The input power was 1540W and it had a charge time of 8 hours, where it was in latent charge mode for about 3.41 hours. The latent discharge time was 4.32 hours after the power was switched off. This demonstrates the phase change material's ability to charge and discharge isothermally.



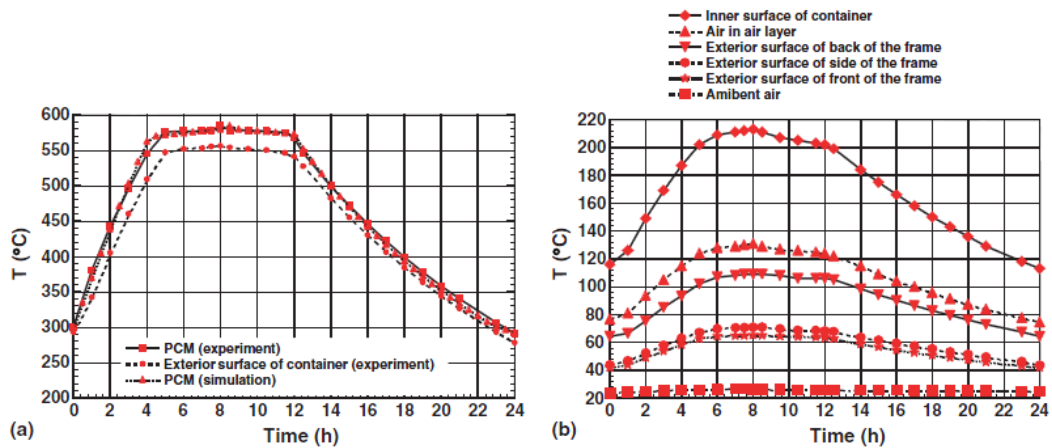


**Figure 23 - Test results for 1540 W heating power (Wang, et al., 2004)**

It must be noted that the corrosive properties of aluminium alloys were not mentioned in any of the papers dealing with AlSi12 as a storage material. This is dealt with in section 9.

## 2.7 Heat transfer fluids and current technical limitations

Since phase change materials lend themselves to passive TES concepts, HTFs must transfer thermal energy between the receiver, storage and power block. The three primary HTFs used in CSP are:

- Thermal oil
- Molten salt
- Direct steam

These HTFs have limitations that inhibit CSP plant performance which are discussed below along with other proposed HTFs that may offer superior heat transfer performance which will enable the use of high temperature thermal energy storage. The properties of these HTFs are listed in Table 5 for comparison.



**Table 5 - Properties of heat transfer fluids**

	Unit	Sodium (atm)	NaK78 (atm)	Potassium	Hitec XL	Hitec	Hitec solar salt	Dowtherm A
Melting point	°C	97.82	-12.6	63.2	120	142	240	15
Maximum operating temperature	°C	881.4	785	756.5	500	538	567	400
Density	kg/m <sup>3</sup>	820	749	715	1640	1762	1794	1056
Specific heat capacity	kJ/kg.K	1.256	0.937	0.782	1.9	1.56	1.214	2.5
Viscosity	Pa.s	0.00015	0.00018	0.00017	0.0063	0.003	0.0022	0.0002
Thermal conductivity	W/(m.K)	119.3	26.2	30.7	na.	0.363	0.536	0.093
Prandtl number		0.0016	0.0063	0.0043		12.89	4.98	5.38
Reference (see footnotes):		2	2	2	3	3	4	5

### 2.7.1 Thermal oil<sup>6</sup>

Some parabolic trough collector (PTC) type solar plants use synthetic oil as a primary heat transfer fluid. There are various brands of synthetic oil HTFs. Synthetic heat transfer oils such as Dowtherm A are stable at higher temperatures than mineral oil. Synthetic oils start to decompose at 400°C. At the maximum operating temperature the vapour pressure of Dowtherm A is 11 bars, which means that all the pipes, joints and receiver tubes must be pressurised. Thermal oil is highly flammable, especially at high temperature. It is also hazardous to the environment if it should leak out of the system.

<sup>2</sup> (Liquid metal engineering center, 1972)

<sup>3</sup> (Coastal Chemical, 2012)

<sup>4</sup> (Kearney, et al., 2003),

<sup>5</sup> (Dow chemical company, 2001)

<sup>6</sup> (Dow chemical company, 2001)

### 2.7.2 Molten salt<sup>7</sup>

Sensible heat storage in molten nitrate salt is one of the most prominent thermal storage mediums today. The high melting point of eutectic nitrate salts means that special precautions are needed to prevent freezing. This may be done with either trace heating or by circulating hot salt through the receiver, which is an energy loss. Trace heating is where the HTF is heated throughout the system using heating elements. For this reason it is preferable to use the salt as a primary HTF in a central receiver system where piping is contained within the tower and the power block.

Different molten salt mixtures are available but they generally have similar heat transfer characteristics. The most prominent high temperature salt is known as solar salt. It is a eutectic mixture of sodium nitrate (60 % by weight) and potassium nitrate (40 % by weight). It has a melting point of 238°C, and an operative temperature range of between 260 and 567 °C. It is non-toxic, non-flammable and has a low vapour pressure.

For lower temperature applications ternary eutectic products like Hitec and Hitec XL are used. These salt mixtures have melting points of about 100 °C lower than that of solar salt, but their maximum operational temperature is between 500 and 538°C. These salts are more applicable for parabolic trough collector (PTC) applications. Table 5 shows the operative temperatures of some molten salts. Solar salt is better suited for high temperature applications.

There is some incentive to use molten salt as a primary HTF in PTC plants (Kearney, et al., 2003): Parabolic trough plants represent the most mature CSP concept; the increased maximum operational temperature (from 400 °C to 450-500°C) means higher thermal efficiency.

The use of molten salt as HTF in a PTC system needs innovative designs to prevent the solidification of salt in the receiver tubes. The high melting temperature of molten salt poses a potential reliability issue in CSP installations, but the risk is substantially mitigated in central receiver plants. The power consumption of a trace heating system depends on the specific plant, and figures may vary extensively. In a study done on a 55 MW<sub>e</sub> PTC system using molten salt as a primary HTF, the night time thermal power loss of the solar field was 10.7 MW<sub>th</sub> (Kearney, et al., 2003).

In central receiver plants with molten salt storage it is possible to perform thermal storage and operate at a maximum temperature of 567 °C. The risk of frozen salt blockage is still present but because the heat transfer pipes are centralized and substantially shorter, freeze protection is more manageable.

---

<sup>7</sup> (Coastal Chemical, 2011 ) (Coastal Chemical, 2012)

### 2.7.3 Direct steam

Direct steam allows higher operational temperatures than possible with either molten salt or thermal oil. Theoretically it is possible to achieve superheated temperatures, but the high operating pressures are a limiting factor. While it is possible to build a regular steam cycle running at supercritical pressures, it is a technical challenge to create receiver equipment that can handle high pressures.

Currently the maximum operational steam conditions for a PTC are 500 °C and 120 bar in an experimental setup at the REAL-DISS test facility at the Endesa Litoral power plant in Carboneras (Spain). This technology is still in development but the main challenges are (Eck, et al., 2011):

- Availability in large numbers of high pressure components such as flexible connector hoses and high pressure receiver tubes.
- Suitable thermal energy storage
- Process management of direct steam generation within a large parallel field.

In central receiver systems the pressure limitations are far lower, and process control is much simpler, but thermal storage remains an issue.

Another limiting factor is the trade-off between receiver tube performance and maximum operating pressure. Higher pressures mean that the receiver tubes must be made of thicker walled tube. The thicker walls impede the heat transfer performance of the receiver tubes.

### 2.7.4 Air or gas

In an attempt to achieve higher thermal efficiencies it has been proposed that compressed air or gas be used in a Brayton cycle. Since both the HTF and the working fluid is a gas, the maximum temperature is no longer limited by the HTF or working fluid. But there are a number of drawbacks:

- The low density of the gas/air requires large heat transfer areas for efficient heat exchange to occur
- Since the gas or air is at high pressure, a closed volumetric receiver is needed. This is a major technical challenge for two reasons; the surface area needed for effective heat exchange is large, and the aperture needs to be covered by a completely transparent lens that can withstand high temperature and pressure (Achenbach, 2011).
- Thermal storage is difficult and needs a large surface area for heat exchange.

One example of proposed CSP concepts using air as a HTF is the SUNSPOT (Allen, et al., 2009) project.

### 2.7.5 Sodium

Sodium is a well-known HTF in fast neutron reactors. It has a melting point of 97.8 °C and boiling point of 881.4 °C<sub>@atm</sub>. It has a very high thermal conductivity

and relatively high heat capacity, making it a good HTF, but it is very reactive with water. In the 1950s the United States of America began the development of liquid metal fast breeder reactors (LMFBR). Sodium was chosen as the coolant because of its good heat transfer and nuclear characteristics. The program outcomes were very stringent and they had to satisfy guidelines and standards that ensured reliable operation of sodium cooled power plants, and the ability for operators to live with sodium on a routine basis. All data, guidelines and experience gained over this program were published in the Sodium-NaK Engineering Handbook by the Liquid Metals Engineering Centre (Liquid metal engineering center, 1972)

In the 1980s a consortium funded by the IEA investigated the use of sodium as a coolant in CSP applications. Testing was done at the Plataforma Solar de Almería (PSA) as the IEA-SSPS High Flux Experiment (Schiel, 1988). In August 1985 a sodium fire broke out during a maintenance procedure and caused extensive damage to the sodium system and the PSA. This event emphasised the importance of safe liquid metal design practices.

Sodium solidifies at 97.8°C. In a system where the primary source of thermal energy is intermittent the possibility exists that the sodium could solidify somewhere in the system. This causes a hazard and some measures will have to be taken to unblock the system to prevent a sodium spill. This situation is avoided at all costs in the nuclear industry, and Eutectic NaK alloy is used instead (Liquid metal engineering center, 1972).

#### 2.7.6 NaK

In LMFBRs that must be operated intermittently, the solidification of sodium causes an inherent reliability issue. Therefore NaK is used in these reactors (Liquid metal engineering center, 1972). Similarly one can argue that the use of sodium in a CSP application causes an inherent risk of blockage since the energy source is intermittent, thus NaK is more suitable for CSP applications.

NaK is a eutectic alloy of sodium and potassium that melts at  $-12.8^{\circ}\text{C}_{@ \text{atm}}$  and boils at  $785^{\circ}_{@ \text{atm}}$ . It has heat transfer properties inferior to those of sodium (see Table 5), and a relatively low specific heat capacity compared to other HTFs, but it is still considered an excellent heat transfer medium. The NaK eutectic system (shown in Figure 24) also allows for different compositions of sodium and potassium. Eutectic NaK has composition of 77.8 % potassium by weight and 22.2 % sodium. It is possible to use NaK46 (46 % potassium), which has a melting point of  $20^{\circ}\text{C}$ , and has higher thermal conductivity and greater specific heat capacity than eutectic NaK (Liquid metal engineering center, 1972). The properties of sodium, potassium and NaK are shown in Table 5. The properties for NaK (in Table 5) is that of eutectic NaK alloy, even though it is acknowledged that NaK alloy with higher sodium content is better suited for CSP applications because of its superior heat transfer characteristics and acceptable melting point.

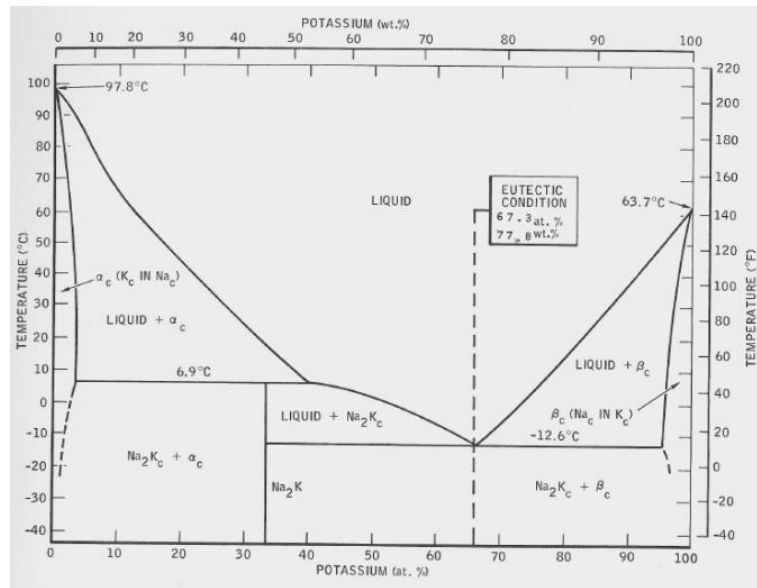


**Figure 24 - Sodium-Potassium eutectic system (Liquid metal engineering center, 1972)**

The biggest risk involving NaK and sodium is that they react violently with water. This becomes a problem during routine maintenance and when parts need to be replaced. In a system using NaK it is possible to clear the piping using high pressure inert gas when the system has cooled down. This is inherently safer than a situation where there is a risk of pipe blockage during maintenance.

By pressurising eutectic NaK to a pressure of 10 bar, the operational temperature of liquid NaK can be increased to over 1100 °C (Liquid metal engineering center, 1972).

### 2.7.7 Conclusion

Considering all the current HTF solutions in CSP, limitations on the maximum operational temperature is the most prominent. Liquid metals pose an elegant but risky solution to the problem, capable of maximum operational temperatures between 785 °C (NaK) and 881 °C (Sodium) at atmospheric pressure, which can be increased to temperatures exceeding 1100 °C with moderate pressurisation. A comparison between the temperature ranges of the HTFs is shown in Figure 25. Note that pressurised NaK46 has an operational temperature range exceeding all of the other HTFs.

Both NaK and sodium are highly reactive with water, and both pose a serious safety risk. Experience with NaK and sodium as HTFs in LMFBRs yielded an extensive database of regulations, design codes and handling instructions that can be used to create a safe design that use either NaK or sodium as an HTF. Furthermore, NaK's low melting point is more suited for use in CSP than sodium because it does not pose an inherent risk for pipe blockage. Accordingly, it is possible to design a CSP system where personnel can work with the NaK system without danger, and have the advantage of high operating temperatures. The fact

that NaK needs no freeze protection means that the entire primary loop can be shut down at night with no risk of damage to the receiver, pumps or heat exchangers. This means that the primary heat transfer system can be designed to be much more robust.

It should also be noted that other NaK compositions can also be used to increase the thermal conductivity, maximum operative temperature and to increase the specific heat capacity. By using a NaK composition of 48 % potassium by weight, the NaK alloy still melts at 20 °C but the heat transfer properties are improved. This translates to savings in pumping power for the primary cooling loop.

Because all literature on NaK is based on the eutectic composition, the eutectic composition will be considered from here on unless otherwise specified. The properties of NaK will be discussed in more detail in section 4.2.

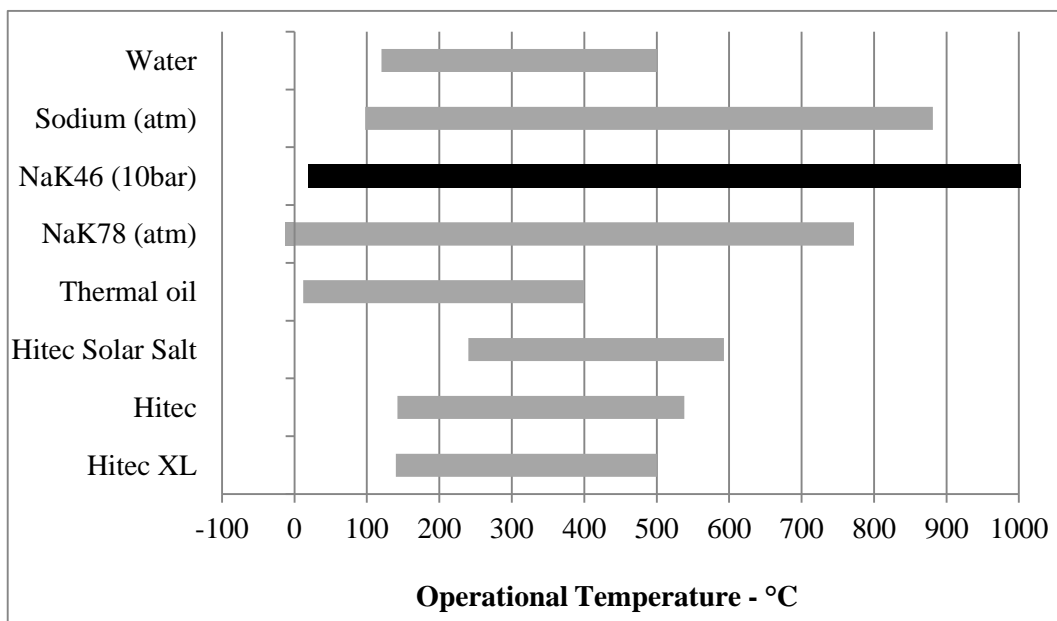


**Figure 25 - Comparison of HTF operative temperatures**

## 2.8 Conclusion and project scope

Currently the main objective for research and development in CSP is the reduction of LCOE. One of the most direct paths to cost reduction is to increase the thermal efficiency of the power block. This requires a higher source temperature than possible with two-tank molten salt storage. Unfortunately the maximum storage temperatures of molten salts are limited to 565 °C. It is possible to store thermal energy isothermally at higher temperatures in PCMs. The operational temperature of a PCM is its melting temperature, and at temperatures higher than 565 °C only fluoride salts, chloride salts and eutectic metal alloys can be used. Metallic PCMs have properties that make them a more viable class of storage material than salt based PCMs.

Looking at the known metallic PCMs, there is a number of pure metals and eutectic metal alloy that are suitable characteristics for high temperature TES. AlSi12 has an exceptionally high heat of fusion at a reasonably manageable melting temperature, making it an ideal candidate metallic PCM for research purposes. Furthermore it is affordable, readily available and has very favourable thermophysical properties.

Because thermal energy storage in PCMs result in passive storage concepts, a heat transfer fluid is needed that can operate at temperatures exceeding that of metallic PCMs. Considering all available HTFs, NaK is the heat transfer fluid best suited for CSP applications due to its low melting point (-12.8 °C), high boiling point, low vapour pressure and high thermal conductivity.

The scope of this project is limited to:

- The development of a TES concept that utilizes metallic PCMs to demonstrate the implementation of advanced power cycles.
- Explore and evaluate the appropriate analytical tools necessary for evaluation of metallic PCM TES systems and metallic HTFs.
- Build a prototype to evaluate the concept and analytical tools that may be used for design.
- Use these analytical tools to prove the concept and to determine operational parameters.
- Perform a techno-economic feasibility study and highlight the role of metallic PCMs as a method to LCOE reduction.
- Determine what future research is required for further development of these storage concepts.

### 3 THERMAL ENERGY STORAGE CONCEPT

In chapter 2 it has been established that metallic PCMs will enable the use of higher efficiency power cycles through high temperature storage. The specific PCM used depends on the application and the melting point of the PCM. This is primarily a techno-economic consideration and is discussed in chapter 10. AlSi12 is a metallic PCM which has been identified as a good PCM with a high heat of fusion, high thermal conductivity and a reasonably high melting point. It is readily available and is inexpensive which makes AlSi12 an excellent candidate PCM for this project. Furthermore, NaK has been identified as an ideal HTF for high temperature applications. AlSi12 melts at 577°C, and is well suited for a subcritical steam cycle. The concept will be developed to apply AlSi12 to a subcritical steam cycle, but it must be kept in mind that the concepts are also applicable for higher temperature storage.

NaK is extremely reactive with water, and has serious safety implications. In the nuclear industry NaK-water steam generators are common, but the application of liquid metal cooling in CSP is still under development and the feasibility of a NaK-water steam generator in CSP is still not clear. Consequently, two storage concepts are developed. The one is called the direct steam generator (DSG) concept, where the steam is generated directly from the PCM (section 3.1). The key here is to separate the NaK and water heat exchangers from each other using the PCM as a buffer. The other is the indirect steam generator (ISG) concept (section 3.2) where the steam is generated in a steam generator separate from the storage unit like in a nuclear power plant.

Each of these concepts has to be evaluated using a preliminary design that is representative of what might be a real world implementation. For AlSi12, a subcritical steam cycle is the most applicable power cycle, and the concepts are developed accordingly. This is discussed in greater detail in chapter 8. The two concepts are presented in the subsequent sections along with a power cycle in which it is implemented.

The power cycle is specified as follows:

- 100 MW electrical output;
- Base load operation;
- 540 °C, 140 bar superheat;
- 540 °C, 30 bar re-heat;
- one open-feed water heater supplied from the high-pressure turbine outlet;  
and
- air-cooled condenser.

#### 3.1 Direct steam generator

In the direct steam generator, both the steam pipes and the liquid metal heat transfer pipes are imbedded into the bulk of the storage media as illustrated in Figure 26. Heat is added to the PCM using the liquid metal heat exchanger, and



heat is removed using the water/steam heat exchanger. As illustrated in Figure 26, the water/steam and liquid metal heat transfer pipes are arranged regularly through the whole melt. Therefore, steam is generated with heat directly from the PCM.

As the PCM charges and discharges, the PCM will melt or solidify in a radial fashion around the pipes of the heat exchangers. This is discussed in more detail in chapter 7.

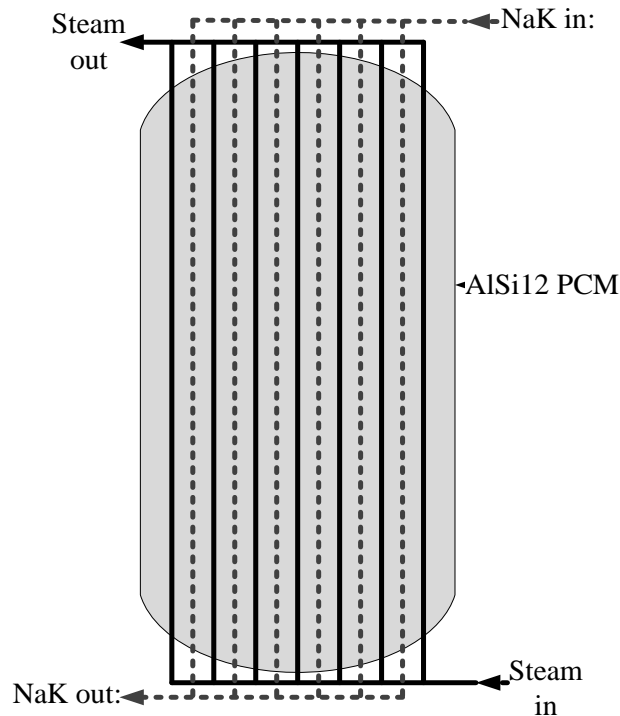


**Figure 26 - Direct steam generator concept**

In a subcritical steam power cycle three heat exchangers are needed:

- Boiler
- Super-heater
- Re-heater

All three parts of the steam generation system are conceptually the same as in Figure 26. The layout of the subcritical power cycle is shown in Figure 27. The boundary conditions of these subsections of the steam generator are presented in section 8.1.

The specifications and boundary conditions of the liquid metal heat exchanger in the storage system is determined by nature of the field, the location of the plant and the capabilities of the receiver. This is discussed in section 8.2

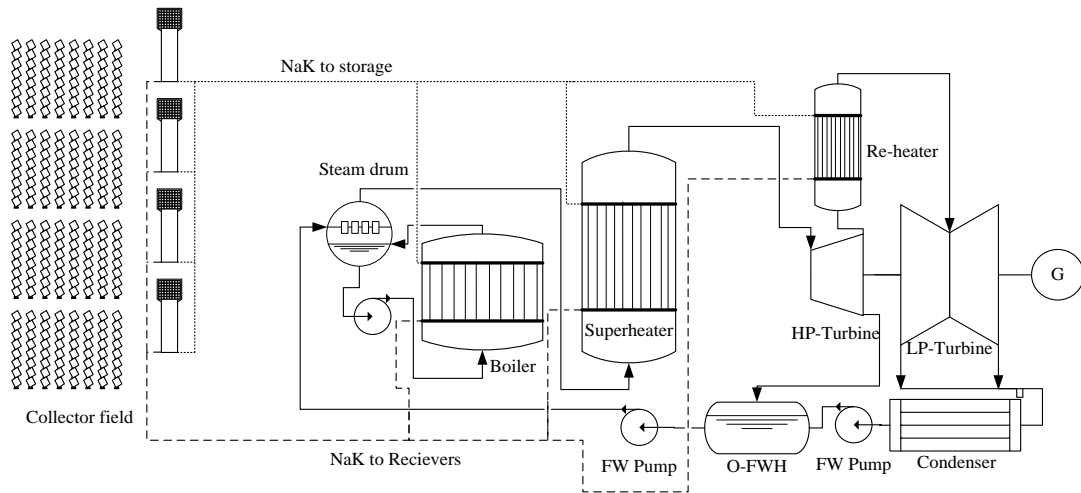


**Figure 27 - Power cycle with the direct steam generation concept**

### 3.2 Indirect steam generator

In the ISG concept, only NaK heat transfer pipes will be imbedded into the PCM as illustrated in Figure 28. A separate steam generator will be used, and the plant layout is shown in Figure 29 where it can be seen that the steam generator is separate from the storage unit. Because the PCM charges and discharges isothermally, the NaK will always exit the storage system at a temperature close to the melting point of the PCM whether it is charging or discharging.

In this case the steam generator is a separate and specially built unit that is beyond the scope of this project. Similarly to the DSG concept, the sizing of the liquid metal heat exchanger in the heat storage unit is primarily dictated by the factors affecting the energy input into the storage system. This is discussed in section 8.2

During charging, NaK passes from the receivers, through the storage system and to the steam generator and then back to the receivers. During discharge the receivers will be bypassed, and the NaK will only cycle between the steam generator and the storage unit.

Similarly to the DSG concept the PCM will melt or solidify in a radial fashion around the pipes of the heat exchangers. This is discussed in more detail in chapter 7.

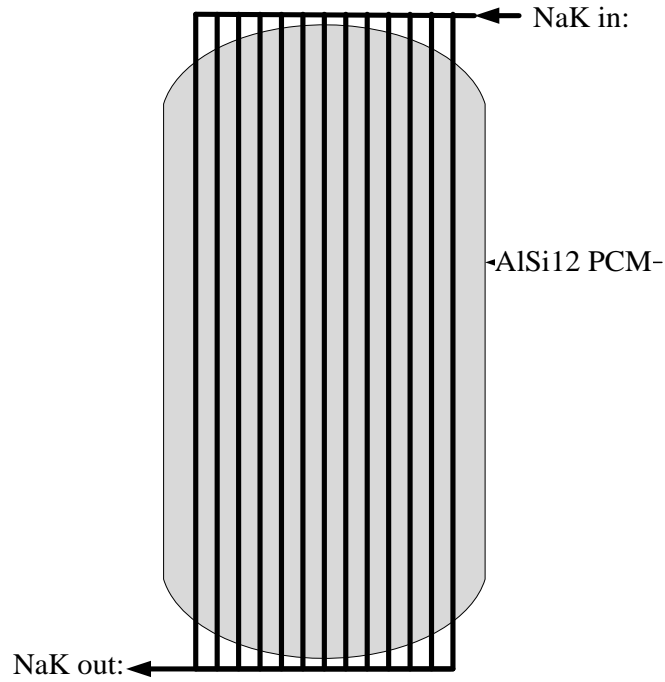


**Figure 28 - Indirect steam generation concept**

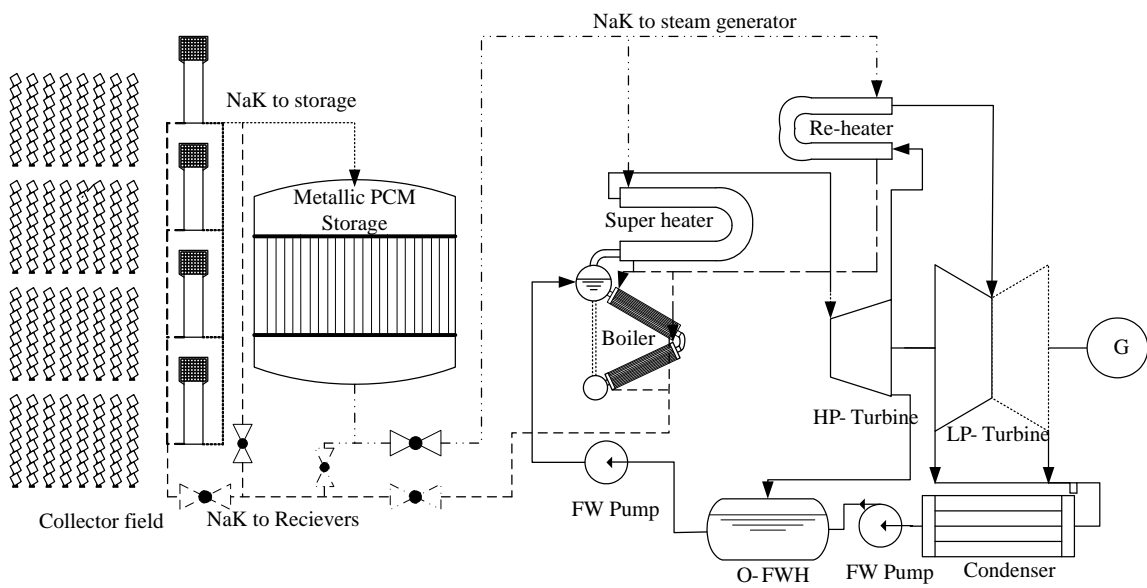


**Figure 29 - Power cycle with the indirect steam generation concept**

## 4 MATERIAL PROPERTIES

### 4.1 The properties and characteristics of AlSi12

Eutectic Aluminium Silicon alloy is well known for having a high heat of fusion, low melting point, high fluidity, low thermal expansion coefficient and low shrinkage during solidification. For this reason it is popular in the casting industry for the production of cast parts with thin sections and work pieces with fine detail. AlSi12 is known in the casting industry by many names depending on region, but in the commonwealth it is known by its British standards designation: LM6. The composition of LM6 is standardised in the BS 1490:1988 LM6 standard, and can be regularly purchased as a master alloy. The composition of LM6 is listed in Table 6.

**Table 6 - Composition specifications of LM6 alloy (BS 1490:1988 LM6)**

<b>Element</b>	<b>wt.%</b>
Copper	0.1 max
Magnesium	0.10 max
Silicon	10.0-13.0
Iron	0.6 max
Manganese	0.5 max
Nickel	0.1 max
Zinc	0.1 max
Lead	0.1 max
Tin	0.05 max
Titanium	0.2 max
Aluminium	Remainder

The phase diagram of the Al-Si eutectic system is shown in Figure 30 on the next page. One thing to notice is that it is a very simple phase system. It only has two solid solution phases, a face centered cubic aluminium  $\alpha$ -phase, and a diamond cubic silicon  $\beta$ -phase. These phases crystallize out of solution in hyper- and hypoeutectic solutions affecting the microstructure of the alloy. The effect of the microstructure might have effects on the cyclic stability of the alloy. This is discussed later in this section.

At the eutectic point (12.2 at.% silicon) the phase change occurs at 577 °C. Master alloys are manufactured within specifications will be close to the eutectic point, but will still have  $\alpha$ - and  $\beta$ -phase inclusions depending on the exact composition.

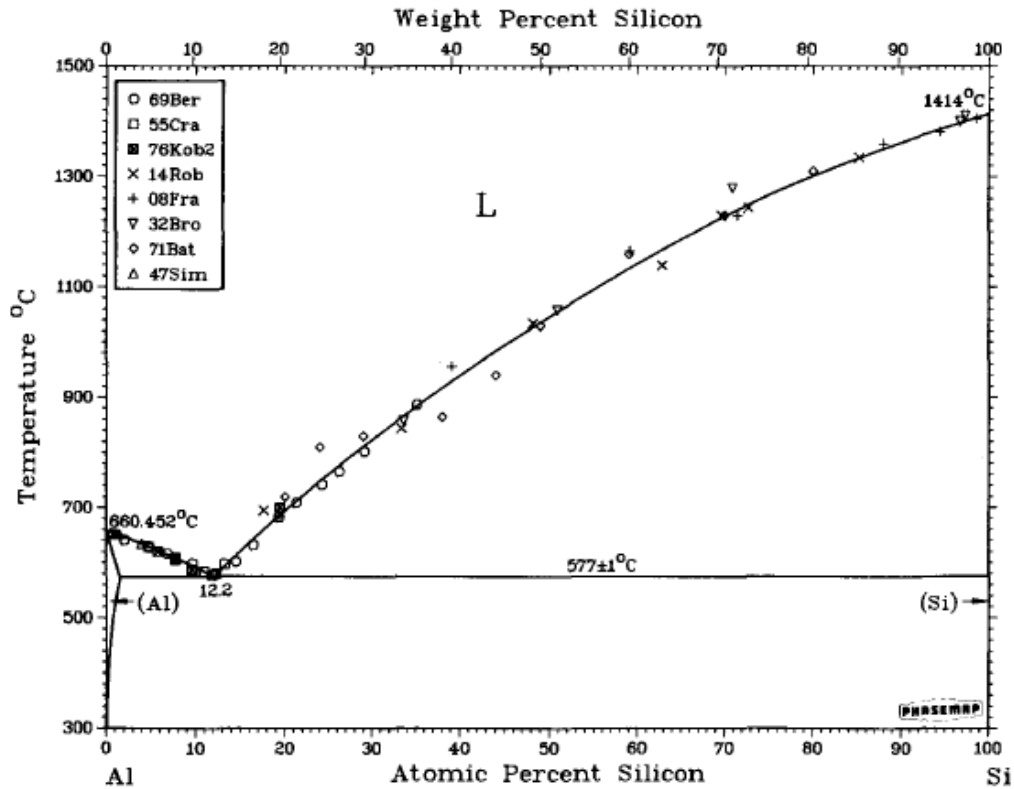


**Figure 30 - Aluminium-Silicon eutectic system (Murray, et al., 1984)**

#### 4.1.1 Thermal and physical properties of eutectic Aluminium silicon alloy

To perform thermal analysis, sizing and mechanical design, knowledge of the thermophysical properties of AlSi12 is important. Because AlSi12 is just one of a large family of alloys, the exact properties of AlSi12 are not as commonly available as one would expect. Various manufacturers do in-house testing for the required properties. This data is considered a company asset and is not divulged into the public domain. This means that there is no central database for AlSi12 properties over a large range of temperatures like there is for water and NaK.

Because the nature of this work is to evaluate the feasibility of using metallic PCMs as high temperature thermal storage materials, detailed high temperature materials testing on AlSi12 is not possible due to the high costs associated with it. Only some of the most critical properties like heat of fusion and melting temperature will be measured using a Scanning Differential Calorimeter (DSC).

The required accuracy of the properties depends on the application. Because the storage system will operate around the melting point of the system, it is important that the properties are representative of AlSi12 around the melting point in either the solid or liquid state.

The general properties of eutectic AlSi12 are presented in Table 7 as quoted on an online materials database. The temperature range of these properties was not listed.

**Table 7 - General material properties of eutectic AlSi12 alloy (Matbase)**

<b>Mechanical properties</b>		
Solidification shrinkage	0.5	%
Density	2650	kg/m <sup>2</sup>
Fatigue failure	55-60	MPa
Shear modulus	27500-28000	MPa
Tensile strength	150	MPa
Yield strength	70	MPa
Young's modulus	72000-75000	MPa
<b>Thermal properties</b>		
Melting temperature	577	degC
Specific heat	970	J/kg.K
Thermal conductivity	130-190	W/m.K
Thermal expansion	21	e-6/K
Heat of fusion	460	kJ/kg

To date a limited number of authors have published on the practical use of AlSi12 as a PCM (see section 2.6), and because of this, their analytical work had to be based on some assumptions. Both of the authors who did a practical investigation into AlSi12 as a PCM did not reference the property set that they used. He *et al.* used the following values (Table 8):

**Table 8 - Thermal properties used by He *et al.* (He, et al., 2001)**

<b>Mechanical properties</b>		
Density	2661	kg/m <sup>2</sup>
<b>Thermal properties</b>		
Melting temperature	577	degC
Specific heat	939	J/kg.K
Latent heat of fusion	515	kJ/kg

Curiously, the thermal conductivity of the material is not mentioned in the paper, which is a very important factor in modelling PCM systems. Wang *et al.* (Wang, et al., 2004) used the values presented in Table 9:

**Table 9 - Thermophysical properties of AlSi12 as used by Wang *et al.***

<b>Mechanical properties</b>		
Density	2700	kg/m <sup>2</sup>
<b>Thermal properties</b>		
Melting temperature	576	degC
Specific heat (solid)	1038	J/kg.K
Specific heat (liquid)	1741	J/kg.K
Thermal conductivity	160	W/m.K
Heat of fusion	560	kJ/kg

Since there is some inconsistency between the values found in literature (Wang, et al., 2004) (He, et al., 2001) other sources had to be used. The values for specific heat and heat of fusion stated by Wang *et al.* are considered correct because they were measured using a differential scanning calorimeter. The rest of the values used in this text have been taken from a selection of text books and were recommended by a metallurgist specializing in aluminium alloys (Munn, 2013). Unfortunately the values of thermal conductivity for liquid AlSi12 could not be found, and the value for solid AlSi12 around the melting point is used as recommended by a metallurgist (Munn, 2013). The physical properties used in this text are presented in Table 10.

**Table 10 - Properties of AlSi12**

<b>Mechanical properties</b>		<b>Temperature</b>		<b>Reference</b>
Solidification shrinkage	0.5 %	n.a.		(Matbase) (Mondolfo, 1976)
Thermal expansion (solid)	21.6 $10^{-6}$ m/m.K	27-327°C		(Mondolfo, 1976)
Thermal expansion (liquid)	10			(Mondolfo, 1976)
Dynamic Viscosity	2.96 mPa.s	577°C-580°C		(Brandes, et al., 1998)
Density	2560 kg/m <sup>3</sup>	577°C		(Mondolfo, 1976)
<b>Thermal properties</b>				
Melting temperature	577 degC	n.a.		Measured & (Mondolfo, 1976)
Specific heat (solid)	1038 J/kg.K	577°C		(Wang, et al., 2004)
Specific heat (liquid)	1741 J/kg.K	577°C		(Wang, et al., 2004)
Thermal conductivity	160 W/m.K	577°C		(Wang, et al., 2004) & (Mondolfo, 1976)
Heat of fusion	560 kJ/kg	n.a.		(Tenekedjiev, et al., 1995) Measured

#### 4.2 The properties and characteristics of NaK

In section 2.7 it has been established that NaK is an ideal heat transfer fluid for high temperature CSP applications. It has distinct advantages and shares some heat transfer properties with potassium and sodium that make high heat transfer rates possible at temperatures not possible with other HTFs, whilst not requiring trace heating due to its low melting point. It has two drawbacks: the first being that, it has a relatively low specific heat; and the second, but most important drawback is that it is extremely reactive with water.

Because sodium and NaK are difficult materials to work with the Liquid Metals Engineering Centre summarised all data on Sodium and NaK in the Sodium-NaK Engineering Handbook. This is the most comprehensive resource on liquid metal engineering.

The following sections will give an overview of some of the more significant properties of NaK (and sodium) and some findings that are significant to liquid metals in CSP.

#### 4.2.1 Physical properties

NaK-78 is a eutectic alloy of sodium and potassium, containing 78 wt.% potassium, simply referred to as NaK. It has a melting point of  $-12.6\text{ }^{\circ}\text{C}$  but the compositions NaK-46 and NaK-89 are liquid at or below room temperature ( $20^{\circ}\text{C}$ ). This is the only advantage that NaK has over pure sodium; otherwise sodium is a superior heat transfer fluid to NaK.

All of the physical and thermal properties of NaK have been correlated and those most applicable in this text are presented in the following paragraphs. They have been taken from the Sodium-NaK engineering handbook (Liquid metal engineering center, 1972), and graphs of these properties are presented in Appendix B.

##### **Density:**

The density of NaK can be calculated depending on the composition using the relation:

$$v_{NaK} = N_K v_K + N_{Na} v_{Na} \quad (4.1)$$

Where :

$$v_{NaK} \equiv \text{Specific volume of the alloy} = 1/\rho_{NaK}.$$

$v_K, v_{Na} \equiv$  Specific volume of potassium and sodium respectively

$N_K, N_{Na} \equiv$  Mole fractions of potassium and sodium respectively

The density of sodium can be taken from the correlation:

$$\rho_{Na} (g/cm^3) = 0.9591 - 2.2976 \times 10^{-4}T - 1.460 \times 10^{-8}T^2 + 5.638 \times 10^{-12}T^3 \quad (4.2)$$

$$98 \leq T \leq 1370^{\circ}\text{C}$$

And the density of potassium can be taken from the correlation:

$$\rho_K (g/cm^3) = 0.8415 - 2.172 \times 10^{-4}T - 2.70 \times 10^{-8}T^2 + 4.77 \times 10^{-12}T^3 \quad (4.3)$$

$$63 \leq T \leq 1250^{\circ}\text{C}$$

With T in  $^{\circ}\text{C}$ .

##### **Dynamic viscosity:**

Liquid eutectic NaK's viscosity can be obtained using the following correlations:



$$\mu(\text{centipose}) = 0.116\rho^{\frac{1}{3}} \exp\left[\frac{688\rho}{T}\right] \quad (4.4)$$

$T \leq 400^\circ\text{C}$

$$\mu(\text{centipose}) = 0.082\rho^{\frac{1}{3}} \exp\left[\frac{979\rho}{T}\right] \quad (4.5)$$

$T > 400^\circ\text{C}$

Where  $\mu$  is measured in centipoise,  $\rho$  in  $\text{g/cm}^3$  and T in K.

**Thermal conductivity:**

The thermal conductivity of eutectic NaK can be taken from the correlation:

$$k(W/cm^\circ\text{C}) = 0.214 \pm 0.002 + 2.07 \times 10^{-4}T - 2.2 \times 10^{-7}T^2 \quad (4.6)$$

$50 \leq T \leq 900^\circ\text{C}$

With T in  $^\circ\text{C}$ .

**Specific heat:**

The specific heat of eutectic NaK can be calculated from the correlation:\

$$p(\text{cal/g} \cdot ^\circ\text{C}) = 0.232 - 8.82 \times 10^{-5}T + 8.2 \times 10^{-8}T^2 \quad (4.7)$$

$0 \leq T \leq 800^\circ\text{C}$

With T in  $^\circ\text{C}$ .

The specific heat of eutectic NaK is presented in Figure 99 as a function of temperature (presented in SI units)

The thermal diffusivity and Prandtl number of eutectic NaK are presented in Figure 31 and Figure 32 respectively to give quick reference in subsequent subsections

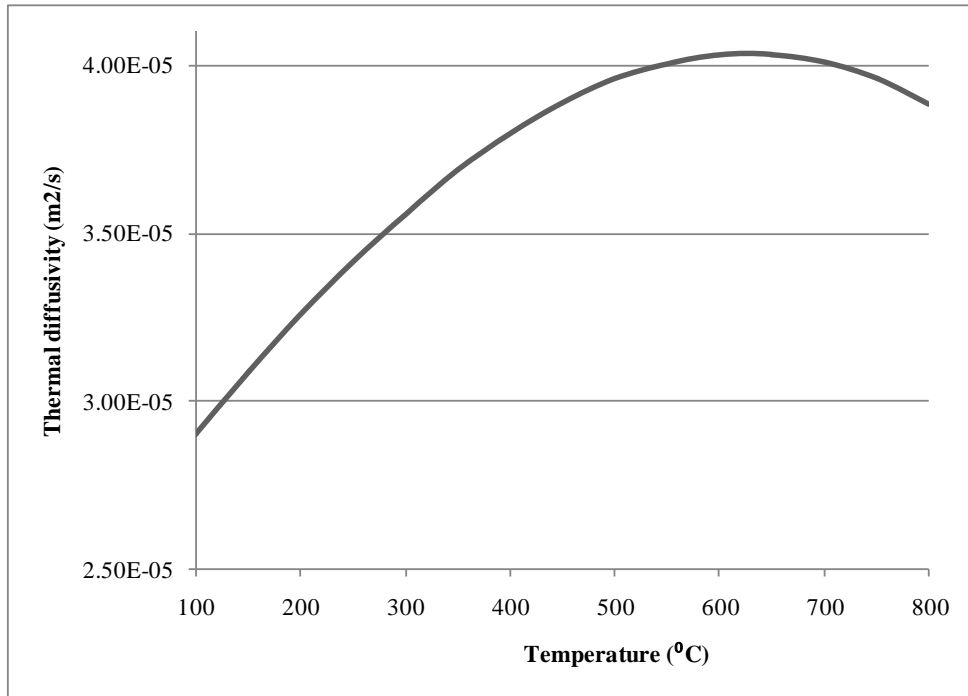


**Figure 31 - Thermal diffusivity of eutectic NaK**

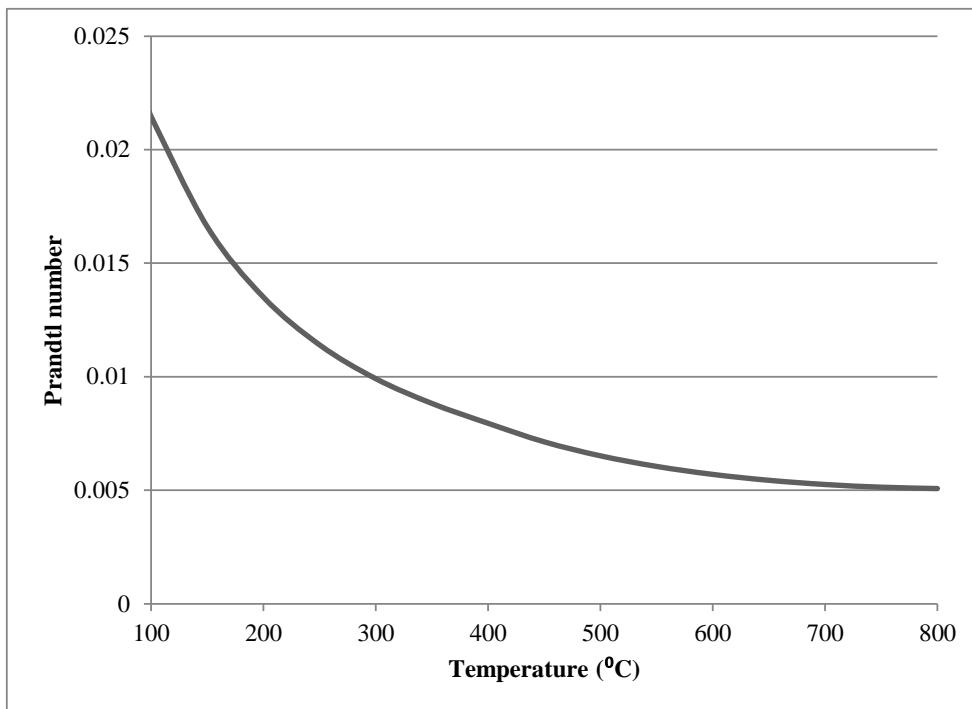


**Figure 32 - Prandtl number of eutectic NaK**

#### 4.2.2 Safety

One of the key issues when it comes to liquid metals is safety. Throughout the liquid metal heat transfer programmes, a key consideration was to establish design, handling and operational protocols to allow engineers, technicians and operators to work with liquid metals on a routine basis in a safe manner.

Unlike lead-bismuth and mercury, sodium and NaK are not toxic, but the most prominent concerns are:

- Corrosion
- Leakage (from pumps and valves)
- Maintenance procedures

Of which the major issue underpinning all of these is a fire hazard. Alkali metals react exothermically with water, producing hydrogen, and forming a strong base. It can be described with the following equation:



And



Where sodium hydroxide is a very strong base and the hydrogen burns off during the reaction. Sodium and potassium's affinity for water is so strong, that the reaction can occur with the moisture from the air. If NaK is exposed to air, a yellow potassium superoxide is formed, that reacts explosively with organic compounds. Thus, NaK should be kept away from air and water at all times. In practice NaK is stored under dry argon or nitrogen.

In the mid-1980s the IEA – SSPS High flux experiment investigated the performance of a sodium cooled receiver (discussed in section 8.2.2). During a maintenance procedure, technicians had to remove a pipe which was blocked with solidified sodium. A section that was mistaken to be solidified actually contained a vacuum which made it appear to be cool and when the pipe was removed, liquid sodium leaked out of the system. The moisture in the air started a fire that destroyed the facility. This could have prevented if proper design protocol was followed.

The Sodium-NaK engineering handbook stipulates all factors of liquid metal engineering, and addresses all matters from handling to equipment design. Following these established guidelines, it is possible to build a heat transfer system that is safe and reliable, offering superior heat transfer solutions for CSP applications.

An intermittent power input is a key reliability issue in CSP. Nitrate salts must be kept in a molten state throughout the night and during maintenance. Trace heating is used to keep pipes warm at night and during down time and the molten salt must be continually pumped through these pipes to prevent solidification in cold

spots like the receiver. A similar situation would exist if sodium is used, and this would present a significant safety risk during maintenance.

For this reason NaK's low melting point has two advantages. The first is that there is no need for trace heating, and secondly, maintenance and repairs can be done in a safe manner, because it is possible to purge the pipes and equipment at room temperature. This is the reason NaK is used in experimental LMFBRs.

A convenient attribute of NaK is that it is electrically conductive, making electromagnetic pumping possible. This further adds to safety, as the seals on a conventional pump is a great concern.

#### 4.2.3 Steam generator design

Because NaK's great reactivity with water, the steam generator is a great safety concern. For the success of any CSP plant, the risk to the investor needs to be minimized and proven through demonstration. If NaK is to be implemented into a CSP plant, one of the main concerns would be that of a NaK steam generator, where NaK and water would come into close proximity with each other. This requires that the heat exchangers should have a high structural integrity and be capable of handling the worst possible accidents.

The high heat transfer capability of NaK means that the heat exchanger will experience high thermal stresses during transient conditions. In the past sodium heated steam generators have failed due to thermal stress, and lessons learnt from these failures have been used to establish design guidelines to ensure safe and reliable designs in the future. Some of these problems include:

- Tube-to-tube-sheet joints
- Differential expansion
- Flow distribution
- Vibration
- Thermal transient stress

Other issues like corrosion from the water side and material compatibility are some design aspects that had to be resolved. NaK/sodium is not as corrosive as lead-bismuth, and proper material selection is sufficient to ensure lasting corrosion protection in the steam generator as well as the whole system from the NaK side. The central material related issues that must be taken into account can be summarised as:

- Material compatibility
- Corrosion
- Erosion
- Material processes

Throughout the life of the steam generator, some key issues must be addressed. These might be the hardest to implement, because of human error. For this reason a certain level of robustness must be designed into the steam generator. Some of the more prominent problems that must be considered are:

- Flow misedistribution
- Excessive thermal transients
- Feed water purity
- Sodium purity

Through years of experience and a number of failures, the design criteria for NaK/sodium steam generators have been built up to design for all of these problems. Along with good design protocol, leak detection systems enable the plant to stop and clear the steam generator in the event of a leak. Generally this involves the detection of hydrogen, and then clearing the heat exchanger using high pressure inert gas. In the nuclear industry double redundancy is a requirement, but other techniques of risk dissipation can be implemented in CSP, since the field can be defocused in the event of an emergency.

A number of successful experimental and commercial LMFBRs has been built and is still in use to this day proving the technical viability of NaK and sodium heated steam generators. The only factor that may prohibit the use of such a steam generator may be cost, and a detailed economic feasibility study may shed some light on the implications on LCOE.

### 4.3 Other materials

Some of the more standard materials used in this project include:

- Water
- Stainless steel
- Mild steel

The properties of water are taken from the IAPWS industrial formulation 1997 for the thermodynamic properties of water and steam (Wagner, et al., 2011). This is known to be the most comprehensive and accurate model for water and steam properties.

The construction material of choice for the experimental rig is low carbon steel, and the material proposed for use for the NaK heat exchanger is austenitic stainless steel as prescribed for the use in the Liquid metals engineering handbook (Liquid metal engineering center, 1972). The thermal properties presented in Table 11 are used throughout this text.

**Table 11 – Thermal properties of low carbon steel and stainless steel 304**

	Low carbon steel	Stainless steel (AISI 304)
Density (kg/m <sup>3</sup> )	7854	7900
Specific heat (J/kg.K)	685	482
Thermal conductivity (W/m.K)	36.2	22.6
Thermal expansion (10 <sup>-6</sup> m/m.K)	16.6	18.7

## 5 FLOWNEX

The simulation and modelling will be done in Flownex<sup>®</sup> SE throughout this project. Flownex<sup>®</sup> is a simulation environment that has been developed and validated within an ISO 9001 and ASME NQA1 accredited system and has seen extensive validation and verification within these systems. Flownex has also been validated in the nuclear industry, and holds the following accreditations:

- In 2007 the National Nuclear Regulator (NNR) of South Africa reviewed the Flownex<sup>®</sup> Software Verification & Validation (V&V) status and found it to be acceptable to be used to support the design and safety case for the PBMR.
- NQA1:2008 (Westinghouse EC USA)
- 2009: ISO 9001 (audited and approved)

Flownex uses nodes connected by components to analyse thermal-fluid networks. Each component is a mathematical model; mostly comprising partial differential equations (PDE) for mass, momentum and energy conservation. Flownex solves these networks of PDEs to yield the temperature, pressure and mass flow rates through the network. These networks can either be solved as steady state or transient state problems. Additional equations are also solved to describe other aspects such as shaft dynamics, electrical networks and control systems. The solution procedure is well documented in the Flownex theory help files supplied with the program. The Flownex model of a Rankine cycle is shown in Figure 33.

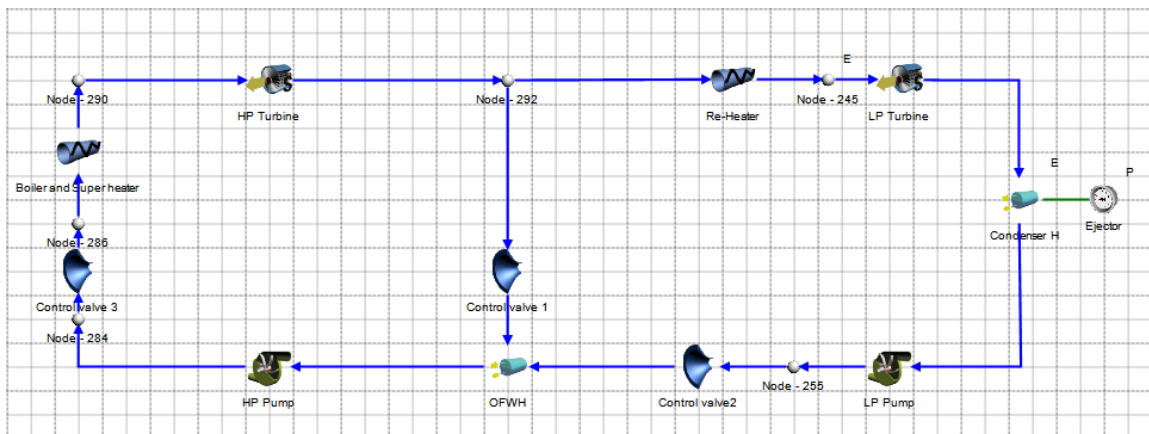


**Figure 33 – Flownex model of a Rankine cycle**

Flownex can deal with single and multiphase flow, and has built-in heat transfer and pressure drop correlations which are automatically chosen to yield the most accurate results possible. It is also possible to manually program new correlations into Flownex using a C# user interface.

An extensive component, fluid and material database makes it possible to build up network models of varying complexity. It is also possible to add components, fluids and materials to the database using a specialized tool set. The database is

well documented and enables the user to evaluate every component and determine the applicability of the results.

A number of built-in tools in the Flownex package proved to be very helpful in this project. The design and optimization tools were key to the sizing of heat exchangers and the sensitivity analysis tool helped with the discretization of the heat transfer and flow problems.

## 6 HEAT TRANSFER MECHANISMS

To evaluate and establish design guidelines, heat transfer predictions for the heat exchangers are needed. Both liquid metal heat transfer and forced convective boiling are considered specialist fields of heat transfer, and the methods used in this text are described here.

### 6.1 Liquid metal heat transfer<sup>8</sup>

Liquid metals have unique thermal properties that make them very efficient HTFs. Low viscosity and high thermal conductivity means that NaK and sodium have very low Prandtl numbers as discussed in section 4.2. This means that conductive heat transfer is dominant. For this reason, extremely high flux densities can be achieved in a NaK heat exchanger, this is especially important in the receiver, where it leads to a smaller heat exchanger, and higher overall efficiency. Because of the application of NaK in this study, only single phase heat transfer in tubes will be dealt with.

A property of heavy metals such as lead-bismuth and mercury is that they tend not to properly wet iron and iron alloy surfaces because of thin layers of oxides that form. This is only of concern with NaK in the presence of an abundance of gasses in the system. Otherwise there is enough reason to assume perfect wetting between NaK and the heat exchange surfaces and that there is no contact resistance that have to be considered.

In the case of normal liquids in forced convective heat transfer, the greatest temperature variation is found in the laminar sub-layer at the channel wall, where molecular thermal conduction is the primary mode of heat transfer in this layer. In the turbulent core of the tube eddy conduction is the primary heat transfer mode. In stark contrast, the thermal conductivity in liquid metals is so high that molecular thermal conductivity is competing with eddy conductivity in the turbulent core. The result is that it is possible to get very high heat transfer rates into the fluid without boiling.

According to the Sodium-NaK engineering handbook, the recommended heat transfer correlations:

$$Nu_t = 5.0 + 0.025Pe^{0.8} \quad (6.1)$$

for uniform heat flux, and

$$Nu_t = 4.0 + 0.025Pe^{0.8} \quad (6.2)$$

for uniform wall temperature. Pe is the Péclet number, which is the product of the Reynolds and the Prandtl numbers. These correlations are accurate for  $0.003 < Pr < 0.06$

---

<sup>8</sup> (Liquid metal engineering center, 1972)



## 6.2 Convective boiling heat transfer inside plain tubes

Convective boiling yields extremely high heat transfer rates, but it is difficult to predict the local heat transfer coefficients for a fluid flowing within a pipe because of the complex hydrodynamic behaviour of a two phase fluid. A number of correlations have been developed to predict heat transfer and pressure drop of an evaporating fluid in a closed channel. Generally these correlations have limited accuracy, but some perform better than others depending on application.

All of these correlations assume a homogeneous model. In the homogeneous model, the fluid properties of the fluid at any given position of the pipe are taken as a weighted average between the properties of the liquid and gaseous phases. The gas-liquid composition (otherwise known as the steam quality, and represented by  $x$ ) is predicted by the model itself.

The local two phase flow boiling heat transfer coefficient ( $\alpha_{tp}$ ) is defined as:

$$\alpha_{tp} = \frac{\dot{q}}{(T_{wall} - T_{sat})} \quad (6.3)$$

Where  $\dot{q}$  is the local heat flux from the tube wall into the fluid,  $T_{sat}$  is the local saturation pressure, and  $T_{wall}$  is the local, uniform wall temperature along the evaporator tube.

There are two mechanisms at work with forced convective boiling:

- Nucleate boiling heat transfer ( $\alpha_{nb}$ )
- Convective boiling heat transfer ( $\alpha_{cb}$ )

Using a power law format, the flow boiling heat transfer can be expressed as:

$$\alpha_{tp} = [(\alpha_{nb})^n + (\alpha_{cb})^n]^{1/n} \quad (6.4)$$

Most of the models use this expression as a basis, and use various methods to predict the nucleate and convective boiling heat transfer. Nucleate boiling heat transfer ( $\alpha_{nb}$ ) is considered to be a function of heat flux and convective boiling heat transfer ( $\alpha_{cb}$ ) is considered to be a function of mass velocity. This is an important factor that needs consideration for process control.

There are many correlations, but the two recommended heat transfer correlations for flow boiling are the Steiner-Taborek asymptotic model (Steiner, et al., 1992) for vertical tubes, and the updated version of the Kattan-Thome-Favrat model (Thome, et al., 2002) for horizontal tubes. Only vertical tubes will be considered in this text due to the geometry of the concept. The models were incorporated into the Flownex heat transfer models discussed in chapter 8.

## 7 MOVING BOUNDARY HEAT TRANSFER AROUND VERTICAL HEAT TRANSFER TUBES

As shown in chapter 3, the heat storage unit concept consists of heat transfer tubes embedded at regular intervals throughout a pool of phase change materials (PCM). There are two variations of the concept, the indirect steam generation (ISG) and the direct steam generation (DSG).

In the DSG concept the liquid metal heat transfer pipes (heat input) and the steam/water heat transfer pipes (heat output) are all embedded at regular intervals throughout the melt. This may lead to a very complex thermal distribution throughout the PCM which is highly dependent on the exact geometry of both the liquid metal and the steam/water heat exchange pipes. To simplify the analysis, only discharge conditions will be considered for the DSG concept, since a computational fluid dynamics (CFD) solution is necessary for charge conditions. On the other hand, in the ISG concept, the same heat exchange surface is used to charge and discharge the heat storage unit (HSU), resulting in a fairly simple heat transfer problem from a geometrical point of view.

Axial conduction is ignored to simplify the heat transfer problem. If there is a significant temperature gradient along the length of a heat transfer pipe, the chances are that the cylinder will not grow out evenly along the length of the pipe, but like a cone. This phenomenon must be analysed using a CFD analysis, and it is outside the scope of this project. The assumption makes this a one dimensional heat transfer problem around each heat transfer pipe.

For simplification, the entire volume of PCM is discretized into hexagonal cylinders around each heat exchange pipes as illustrated in Figure 34. As the HSU discharges, the PCM solidifies in cylinders around the heat transfer pipes known as a moving boundary problem.

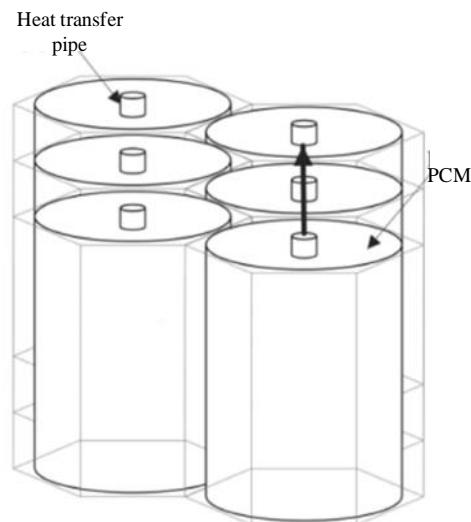


**Figure 34 – Discretization and two dimensional models for charging and discharging**

Eventually the cylinders will grow into each other (Figure 35). This will create a situation where the heat transfer characteristics of the heat exchange surfaces are nonlinear, and heat transfer rates will decrease rapidly and therefore the volume between the cylinders is treated as a dead volume. It can be geometrically proven that if the cylinders expand to the point where they touch each other, 9.3 % of the total volume of PCM is still liquid. This volume is ignored in the analysis and is considered to be construction material

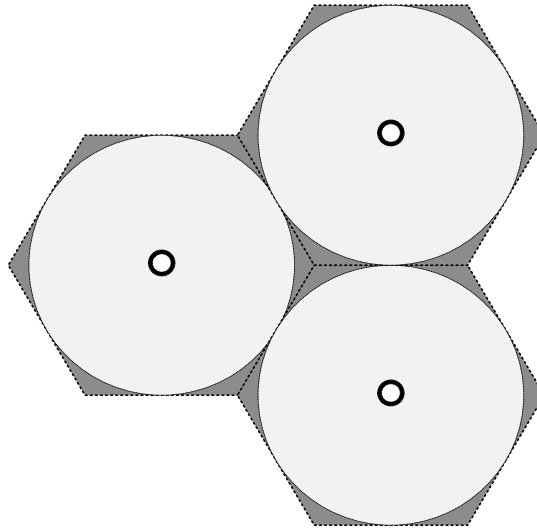


**Figure 35 - Hexagonal elements showing solidified PCM cylinders touching**

The central theme of this study is to evaluate the feasibility of the concepts presented in chapter 3. Part of this is to understand the nature of a moving boundary problem and how this will affect the functionality of the heat transfer surfaces. This is especially true during discharge, when the solidified PCM around the heat transfer surfaces increase the thermal resistance between the molten PCM and the HTF.

### **7.1 Analysis of the moving boundary system and transient analysis**

The charging and discharging states of a hexagonal element are described in Figure 36 below. The heat transfer problem is essentially three concentric cylinders, with a moving boundary,  $r_m$  separating the solid and the liquid phase. As the HSU charge or discharge, the boundary moves. The temperature at this boundary is equal to the melting point of the PCM,  $T_m$ .

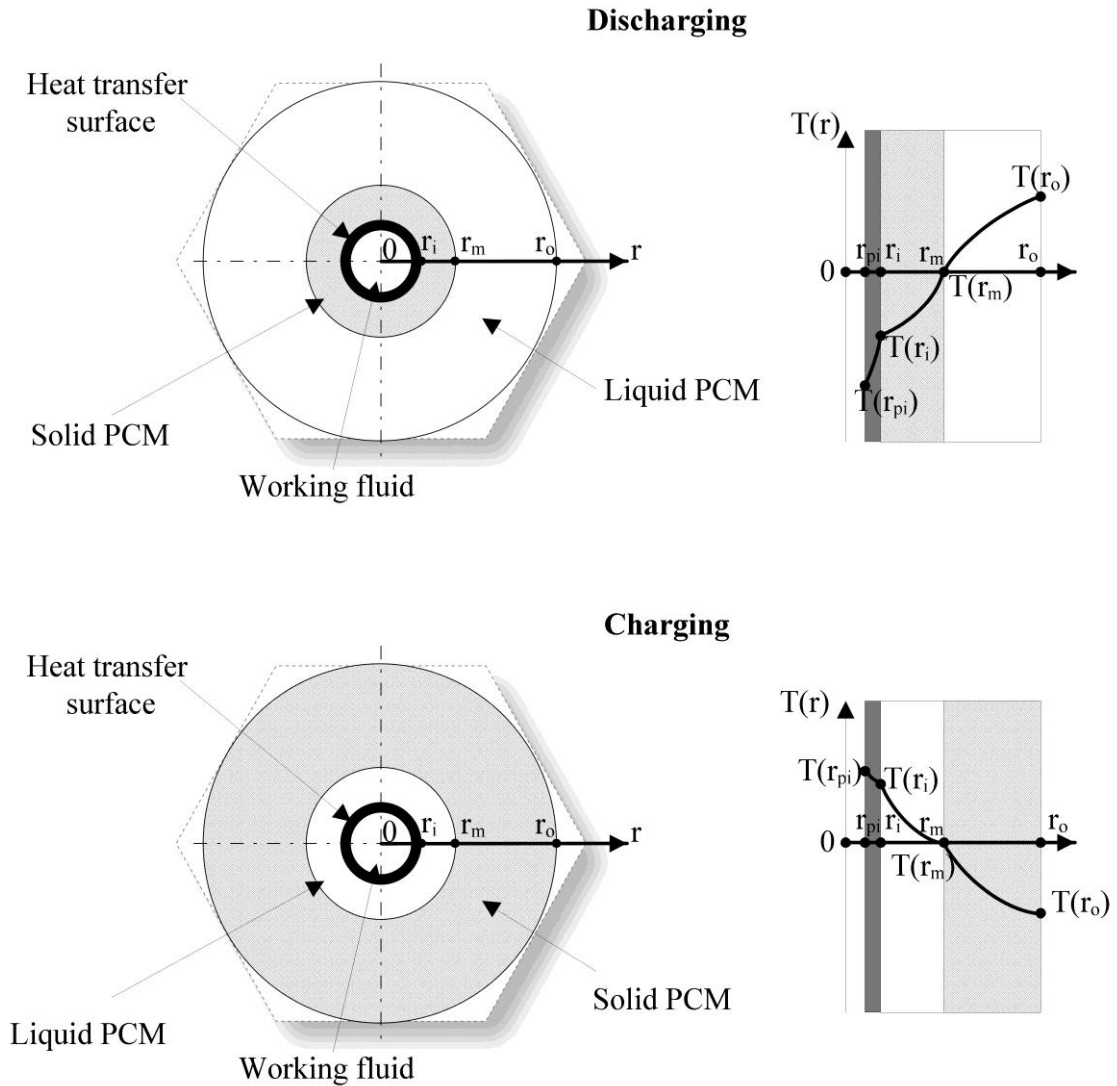


**Figure 36 - Problem description**

As described in Figure 36, there are three material zones in both the discharge and charging cases:

- Heat transfer pipe – Designated by subscript P
- Solidified PCM – Designated by subscript S-PCM
- Liquid PCM – Designated by subscript L-PCM

A key consideration is the dominating heat transfer mechanism in all of these regions. It is clear that conduction is dominant in the two solid regions, but either Rayleigh-Bénard convective mixing (Getling, 1998) or conductive heat transfer can be dominant in the liquid region. The low Prandtl number of liquid AlSi12 (0.032209) and the isothermal nature of the storage concept suggests that conduction is the dominating heat transfer mechanism in the liquid phase (Getling, 1998). Furthermore, the high thermal conductivity of liquid AlSi12

suggest that the temperature gradient of the liquid AlSi12 would be low, which has implications for the heat transfer between the solid and liquid phase.

Thus, the heat transfer mechanism throughout the entire problem is considered to be conductive. The one dimensional conduction equation for a cylinder is:

$$\frac{\delta T}{\delta t} = \alpha \frac{\delta^2 T}{\delta r^2} + \frac{\alpha}{r} \frac{\delta T}{\delta r} \quad (7.1)$$

Perfect thermal contact between the heat transfer pipe and the PCM is assumed:

$$T_p(r_i) = T_{PCM}(r_i) \quad (7.2)$$

And:

$$-k_p \frac{\partial T_p(r_i, t)}{\partial r} = k_{PCM,S} \frac{\partial T_{PCM}(r_i, t)}{\partial r} \quad (7.3)$$

The Rayleigh number is a dimensionless number used to determine the significance of buoyancy driven flow in liquid metals. The Boussinesq number is in turn used to calculate the Nusselt number for the convective heat transfer in liquid metals, and it is defined as:

$$Bo = (Gr)(Pr)^2 = (Ra)(Pr) \quad (7.4)$$

If the Rayleigh number for a liquid is below its critical number, the heat transfer mechanism is primarily conductive. Unfortunately the critical Rayleigh number is dependent on the fluid, and no published critical Rayleigh number could be found for AlSi12 specifically. If it is assumed that the bulk of the liquid, ( $T_\infty$ ) is close to the melting point of the PCM ( $T_m$ ), the Rayleigh number will be low, and conductive heat transfer between the solid-liquid interface is the dominant heat transfer mechanism. This assumption is based on the high thermal conductivity of the AlSi12, but was verified in the experiment presented in section 7.4 and is discussed in section 7.7.

Therefore the energy balance on the solidification front yields:

$$\rho \lambda \frac{dr_m(t)}{dt} = k_{PCM,S} \frac{\partial T(r_m, t)}{\partial r} - k_{PCM,L} \frac{\partial T(r_m, t)}{\partial r} \quad (7.5)$$

And the temperature of the solidification front is the melting temperature of the PCM:

$$T(r_m) = T_m$$

The internal convection boundary layer at  $r_{pi}$  and the outer boundary condition at  $r_o$  depend on the specific problem, and will be specified accordingly.

The low Rayleigh number dominating conductive heat transfer implies that the PCM will solidify uniformly along the length of the pipe given uniform cooling along the length of the heat transfer pipe.

Accordingly, the assumptions made in this model are:

- Conductive heat transfer is dominant in the liquid PCM
  - Valid for low Prandtl numbers
- Only conductive heat transfer at the solid-liquid PCM interface and no convective currents along the length of the heat transfer pipe resulting in uniform solidification if the pipe has uniform cooling along its length.
  - Valid for low Rayleigh numbers – to be confirmed in the experiment
- Perfect thermal contact between the heat transfer pipe and the PCM
  - Valid for metal casting

A moving boundary heat transfer problem can either be solved as a Stefan problem (Lock, 1996) or with the Neumann method (Lock, 1996). Unfortunately the Neumann method is limited to simple temperature boundary conditions applied to the free surface of semi-infinite domains (Lock, 1996). This makes the Neumann method unsuitable for investigating transient systems. The Stefan solution is also limited in that it is an analytical solution, and the exact solutions do not yield the flexibility needed to analyse a system with a time dependent thermal energy input.

The Stefan problem is formulated in Appendix C, where the implications of the Stefan condition are justified. The Stefan number is the ratio between the sensible versus latent heat in the forming phase (solidifying phase in discharge and melting phase in charge). The Stefan value is expressed as:

$$Ste = \frac{C_p(T_m - T_i)}{\lambda} \quad (7.6)$$

Where  $T_m$  is the melting front interface temperature and  $T_i$  is the heat transfer surface temperature. If the  $Ste \ll 1$ , then the problem can be approximated as a quasi-steady state problem. Figure 37 presents the Stefan number for AlSi12 plotted against free surface temperatures. From Figure 37 it can be seen that the Stefan condition holds true from about 450 °C to 700 °C.

The lack of flexibility of both the Neumann and Stefan solutions merits the use of a numerical model that will be able to simulate the movement of the solidification front and predict heat transfer rates at various stages of discharge that can be used to evaluate the heat exchangers imbedded into the PCM.

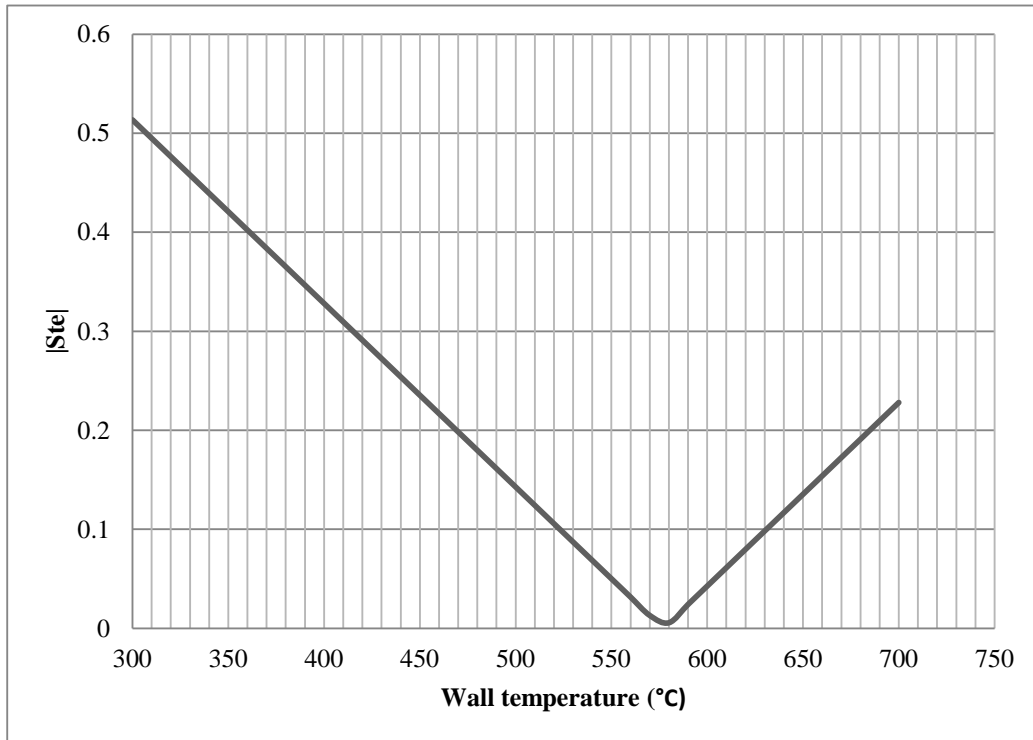


**Figure 37 - Stefan number as a function of wall temperature**

## 7.2 Instantaneous heat transfer

Because the system can be approximated as quasi-steady at low Stefan numbers, the instantaneous heat transfer for any charge state can be calculated using the resistance model given that the Stefan number remains low. Thus, if the thermal resistance of the solidified PCM is high enough, then the Stefan number will rise, making the quasi-steady assumption invalid, and the enthalpy method for transient analysis needs to be applied to the problem. As established in section 7.1, heat transfer in both the liquid and the solid phases can be considered purely conductive, simplifying the analysis considerably.

The same assumptions and conclusions that were established in section 7.1 holds for the instantaneous heat transfer analysis. The model for both charging and discharging is shown in Figure 38.

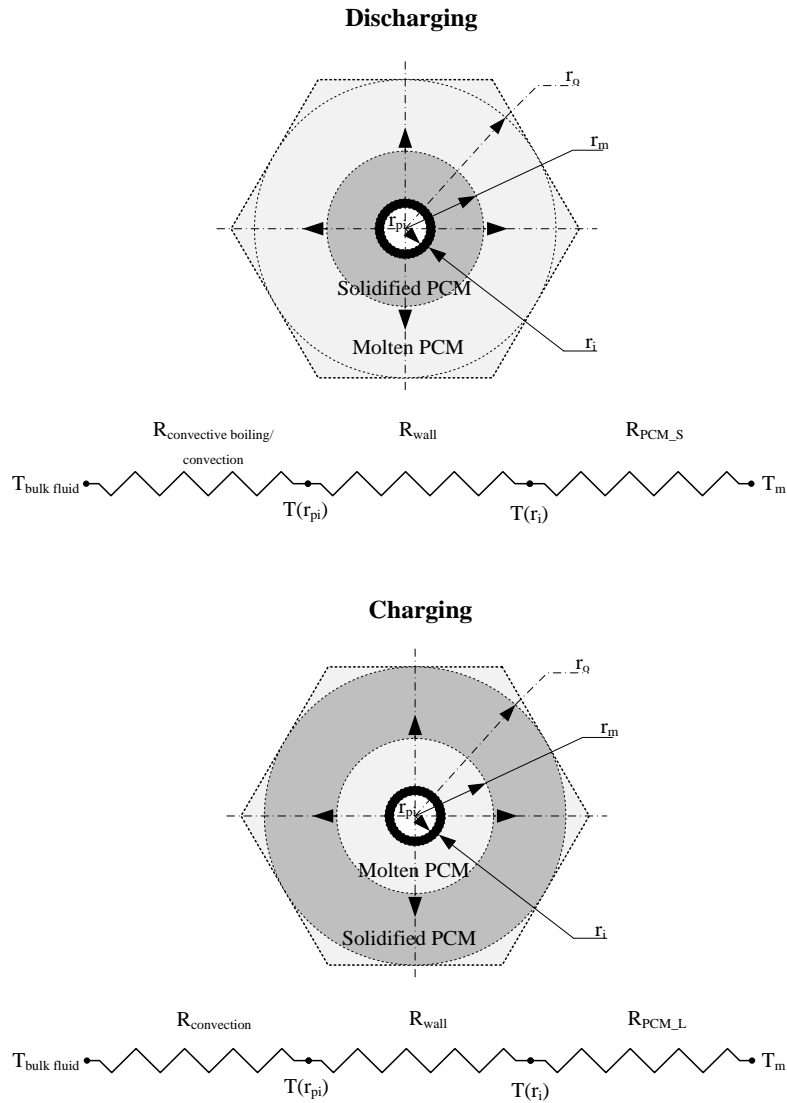


**Figure 38 - Resistance heat transfer model for charging and discharging**

The resistances are calculated using equations 7.7 and 7.8. In these equations  $r_2$  is the outer radius and  $r_1$  is the inner radius. The values for the physical properties are taken as close to the melting point,  $T_m$ , this is possible due to the isothermal nature of the storage system and lack of thermal properties at high temperatures (see section 4.1)

$$R = \frac{\log\left(\frac{r_2}{r_1}\right)}{2\pi Lk} \quad (7.7)$$

$$R_{conv} = \frac{1}{2\pi hr} \quad (7.8)$$



The heat rates transfer is calculated using equation 7.9:

$$\dot{Q} = \frac{T_m - T_{bulk\ fluid}}{\sum R} \quad (7.9)$$

### 7.3 Numerical solution to the moving boundary problem for transient analysis

The best way to implement a numerical solution of a moving boundary problem is the enthalpy method (Voller, et al., 1980). In the enthalpy method, the enthalpy of each node is used to determine its temperature using enthalpy-temperature relations. The heat transfer between nodes is calculated based on the conduction equation (Eqn. 7.1) and the temperature of the nodes. Thus, the conservation of energy will be applied directly rather than indirectly as in the finite difference method (Kakac, et al., 1993).

The enthalpy method will be discussed in the form of an algorithm. Referring to Figure 39, the entire domain ( $r_{pi} < r < r_o$ ) is discretised into cylindrical shell elements of thickness  $\Delta r$ . The position of the element is denoted by variable  $j$ , and the radial position ( $r_j$ ) is taken in the centre of the element, with its boundaries at  $r_{j+} \Delta r/2$  and  $r_{j-} \Delta r/2$  respectively.

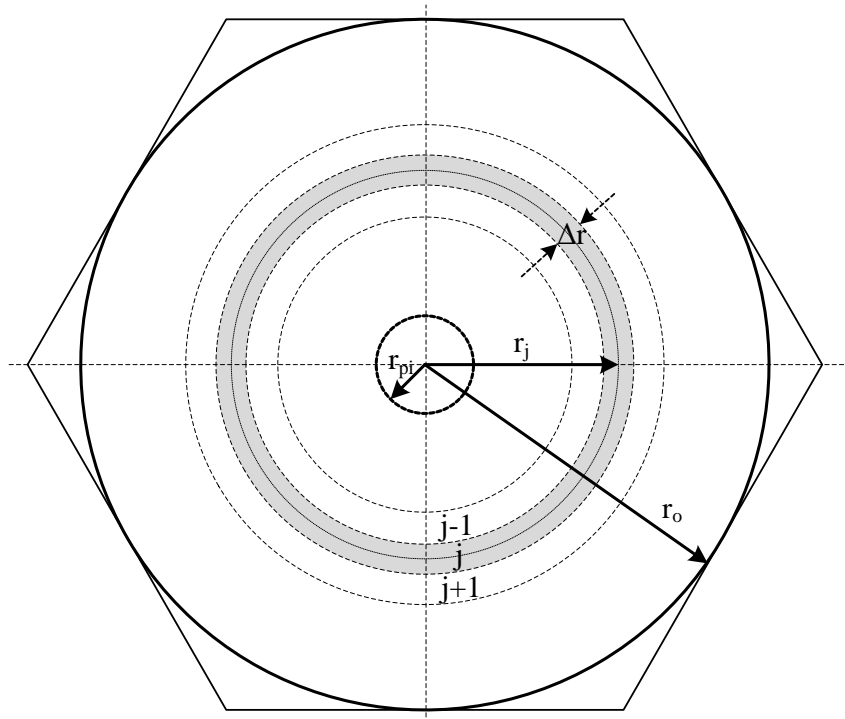


**Figure 39 - Discretisation of the heat transfer problem**

**Step 1 – Calculate position, volume and mass of each node**

The first step is to calculate the position, volume and mass constants for each element, which are stored in vectors  $r(j)$ ,  $V(j)$  and  $M(j)$  respectively. The density of the element is taken as that of the solid AlSi12 at the melting point. The  $r(j)$ ,  $V(j)$  and  $M(j)$  is calculated by equations 7.10, 7.11 and 7.12 respectively.

$$r(j) = r_{pi} + (j - 1)\Delta r \quad (7.10)$$

$$V(j) = L\pi((r(j) + \Delta r/2)^2 - (r(j) - \Delta r/2)^2) \quad (7.11)$$

$$M(j) = \rho V(j) \quad (7.12)$$

**Step 2 – Calculate the thermal resistance between each node**

In section 7.1 it has been established that the heat transfer through the entire problem is conductive. The steady state analytical solution for equation 7.1 can be implemented using the resistance method (Kakac, et al., 1993). In this sense, the heat transfer between elements is treated as quasi-steady within each time step. The thermal resistances between the nodes (Figure 40) are stored in vector  $R(j)$ , and are calculated using equation 7.13.

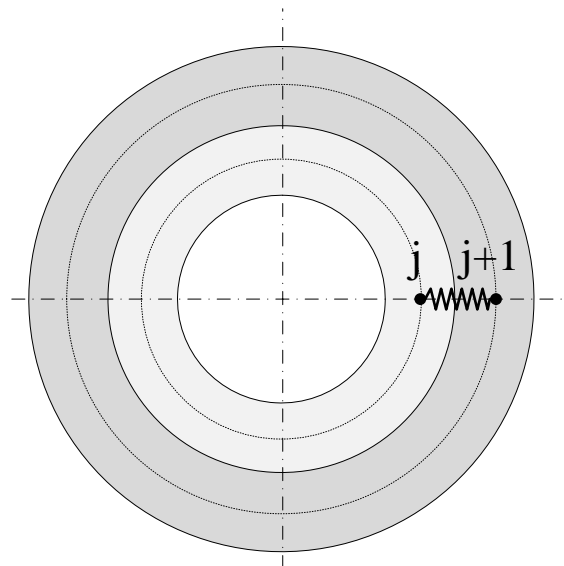


**Figure 40 - Resistances between elements**

$$R(j) = \frac{\log\left(\frac{r^{(j+1)}}{r^{(j)}}\right)}{2\pi Lk} \quad (7.13)$$

**Step 3 – Define boundary and initial conditions**

The boundary conditions of the problem can also be represented using the resistance model for heat transfer. Generally the heat transfer at the inner pipe at  $r_{pi}$  depends on the heat transfer mechanism on that boundary, and similarly on the outside,  $r_o$ , either way, the heat transfer coefficient of this boundary condition can be calculated with the appropriate heat transfer correlation which will be discussed along with the analysis. Convective boundary conditions are generally represented by equation 7.14 where  $h$  represents the heat transfer coefficient.

$$R_{conv} = \frac{1}{2\pi hr(j)} \quad (7.14)$$

The initial conditions can be initialized by using the temperature vector,  $T(j)$ , which is simply the temperature of each node, or by using the internal energy vector,  $E(j)$ . The internal energy vector can be used to describe an initial condition with a solid-liquid interface somewhere within the domain to represent a partial charge or discharge.

If the initial temperature,  $T_i$ , is given, then:

$$T(j) = T_i \quad (7.15)$$

If  $T_i$  is above or below the melting point, the internal energy is calculated as:

$$E(j) = M(j) \int_0^{T_i} Cp(T) dT \quad (7.16)$$

if

$$T_i < T_m$$

$$E(j) = M(j) \left( \int_0^{T_m} Cp(T) dT + \lambda + \int_{T_m}^{T_i} Cp(T) dT \right) \quad (7.17)$$

if

$$T_i > T_m$$

The initial enthalpy matrix  $H(j)$ , is calculated by

$$H(j) = E(j)/H(j) \quad (7.18)$$

#### ***Step 4 – Calculate the temperature of each node***

Essential to the enthalpy method is the temperature-enthalpy (T-H) relationships. The enthalpy-temperature relationships can be derived using a DSC machine, yielding complex T-H curves. Fortunately, eutectic materials such as AlSi12, have a very sharp melting temperature, which results in a fairly simple, linear T-H relations (Voller, et al., 1992). The T-H diagram for a eutectic of pure substance is shown in Figure 41.

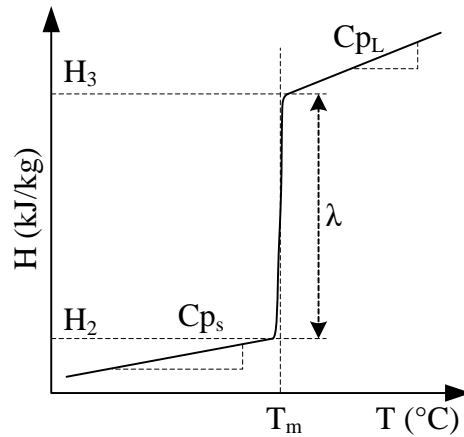


**Figure 41 - T-H diagram for a eutectic or pure metal**

The T-H relations for the eutectic system are defined in equations 7.19 through 7.24.

$$H_1 = 0 \quad (7.19)$$

$$H_2 = \int_0^{T_m} C_p(T) dT \quad (7.20)$$

$$H_3 = H_2 + \lambda \quad (7.21)$$

$$T(j) = \frac{H(j)}{C_{p_s}} \quad (7.22)$$

if

$$H(j) < H_2$$

$$T(j) = T_m$$

if

$$H_2 < H(j) < H_3$$

$$T(j) = T_m + \frac{(H(j) - H_3)}{C_{p_L}} \quad (7.24)$$

if

$$H_3 < H(j)$$

Because the whole system is essentially on the melting point, the specific heat will be taken as close to the melting temperature a possible and will be treated as a constant.

**Step 5 – Re-evaluate resistances for new temperatures**

If the thermal conductivity of the PCM varies significantly within the temperature range of the model, it might be necessary to re-evaluate the thermal resistances at the newly calculated temperatures.

**Step 6 – Calculate the heat transfer between elements**

The heat transfer between the nodes is calculated using the resistance model. The heat transfer between the elements is calculated using equation 7.25.

$$\dot{Q}(j) = \frac{T(j) - T(j - 1)}{R(j - 1)} \quad (7.25)$$

**Step 7 – Calculate new internal energy and enthalpy for each node**

The internal energy of each node is calculated using an energy balance on the node. The internal energy of each node is calculated using equation 7.26.

$$E(j) = E(j)_{t-\Delta t} + \Delta t(\dot{Q}(j + 1) - \dot{Q}(j)) \quad (7.26)$$

**Step 8 – Repeat steps 5 to 7 for each time step until maximum time steps is complete.**

The entire algorithm is presented in Figure 42.

**Step 9 – Print results**

Because equation 7.26 implies the explicit method, stability needs to be checked using equation 7.27.

$$\Delta t < \frac{\Delta r^2}{2\alpha} \quad (7.27)$$

The enthalpy method is used and validated in section 7.4.

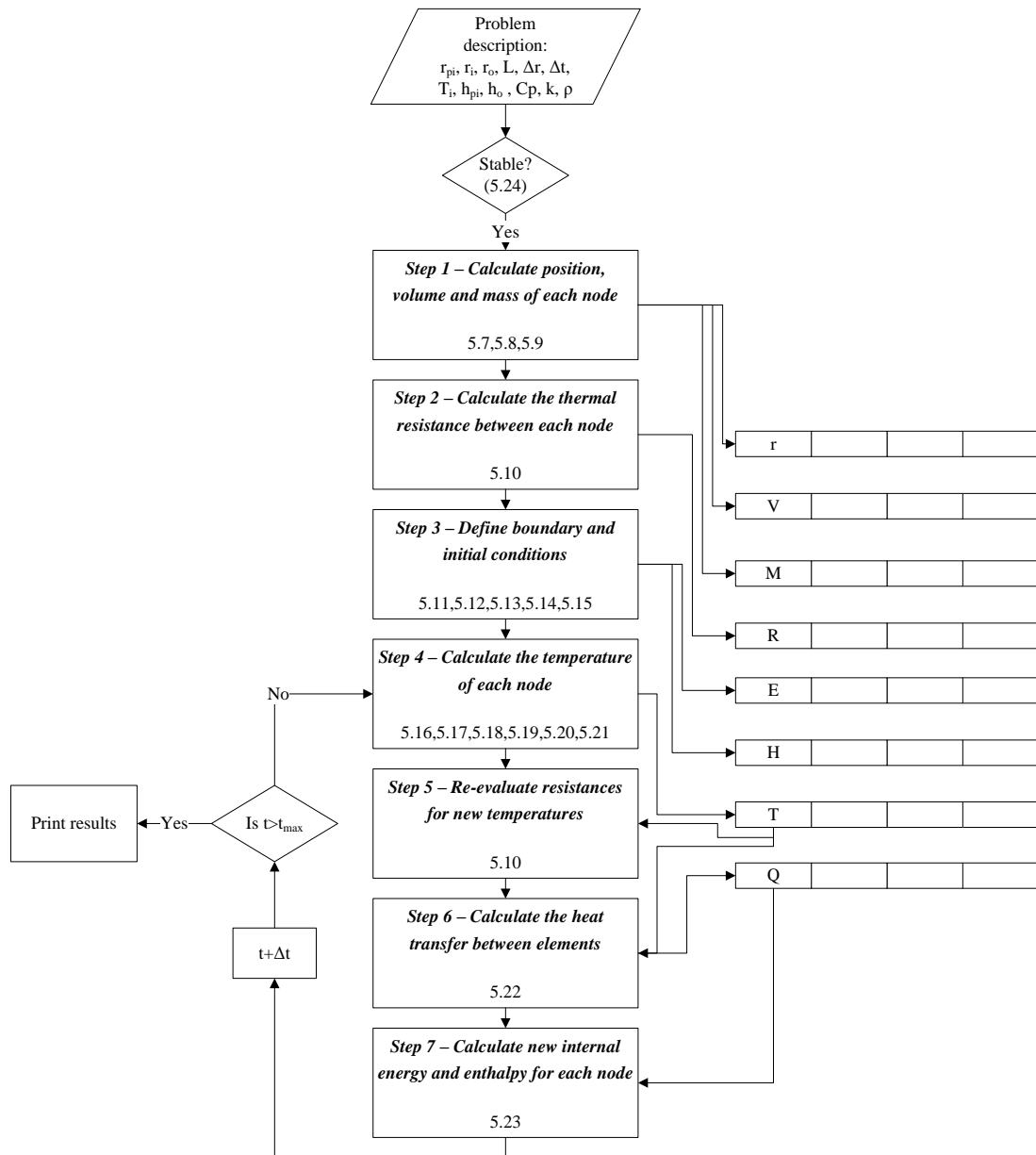
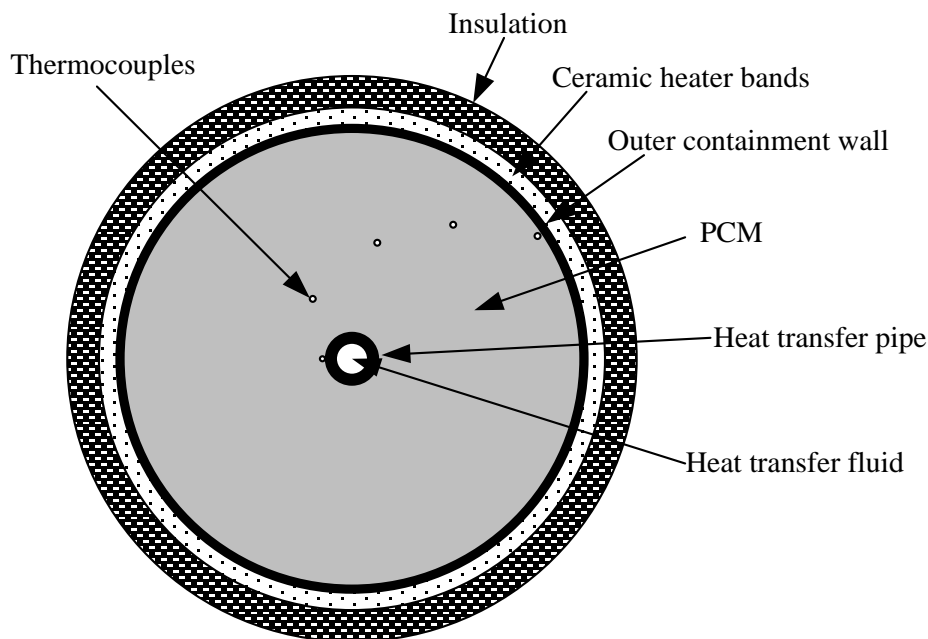


Figure 42 - Enthalpy method algorithm

#### 7.4 Prototype and experimental setup

To serve as a proof of concept and to validate the analytical methods developed in sections 7.1, 7.2 and 7.2, an experiment was devised. Liquid metals posed a serious safety risk, and as alternative heat transfer fluid had to be used. For this reason the storage system could not be heated up through the central heat transfer pipe, but has to be heated with external ceramic band heaters. A single storage element is approximated by the arrangement shown in Figure 43. It consists out of a steel cylinder filled with AlSi12 alloy and a thick walled steel pipe running through the centre that will act as a cooling pipe. The steel containment vessel is heated using ceramic band heaters, and the whole assembly is wrapped in ceramic wool for insulation. A set of five thermocouples is imbedded at various distances from the centre of the vessel, which measure the temperature of the melt and will enable the measurement of charge state.



**Figure 43 - Cross section of the test section**

The diameter of the outer containment shell was determined by the limitations of the laboratory power supply. The 240V, 100A 3-phase power supply permitted the use of three 406.4mm diameter, 330mm long ceramic band heaters, making the outside diameter of the containment vessel 406.4mm and the length of the vessel to 990mm excluding end caps.

Because the use of liquid metal was not permitted for safety reasons, another heat transfer fluid had to be used. The following HTFs were considered:

- Air
- Water
- Quenching oil

Preliminary heat transfer calculations revealed that the heat transfer rates using air would be too low, and no distinct solid-liquid interface would form. On the other hand, water also proved unfeasible because it either needs a high pressure cooling system that resulted in an excessively expensive test rig, or the heat transfer rates would result in two phase flow, which would complicate the measurement of heat transfer rates. Quenching oil was considered the only viable heat transfer fluid.

A drawing of the test section is presented in Figure 44 with some of the more important dimensions listed in Table 12. The entire test section was manufactured from carbon steel. The internal pipe was chosen to be a BSP 1 inch S80 seamless carbon steel pipe. It was only later discovered that molten aluminium is corrosive to steel, which is discussed in chapter 9.

The thermocouples were placed into open ended thermocouple guide tubes to keep them straight and in position. These were in turn held in place with a baffle plate with location holes for the thermocouple sleeves. Unfortunately the second thermocouple tube was accidentally installed at an angle due to a mistake during assembly, and ended up missing the guide hole in the baffle. This was only discovered on inspection at the foundry, and could not be fixed due to logistical reasons. The radial position of this thermocouple tube had to be re-measured using a calliper, and is not considered accurate.

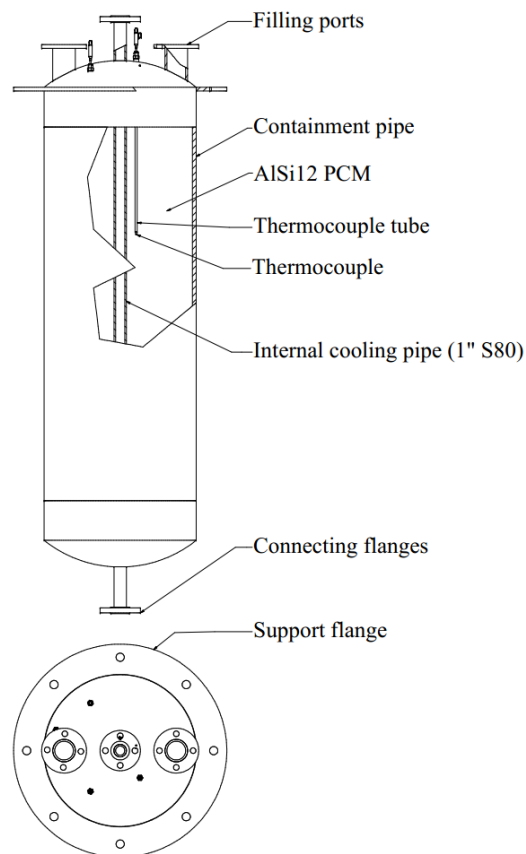


**Figure 44 – Test section**



**Table 12 - Test section geometry**

<b>Cylinder geometry</b>		
<b>Outer cylinder</b>		
Inside diameter	398	mm
Outside diameter	408	mm
<b>Heat transfer pipe</b>		
Inside diameter	24.4	mm
Outside diameter	33	mm
Length in contact with AlSi12	1289	mm
<b>Volume of AlSi12</b>	0.1533	m <sup>3</sup>
<b>Mass of AlSi12</b>	408	kg
<b>Thermocouple placement from the centre</b>		
Probe 1	30	mm
Probe 2	82	mm
Probe 3	90	mm
Probe 4	135	mm
Probe 5	180	mm

Figure 45 shows the empty test section just after production. The test section was filled up from a single furnace at Zimalco Aluminium Company in Johannesburg. The filling process is shown in Figure 46. By using a single furnace it was possible to fine-tune the composition of the alloy to exactly that which was required. The exact composition of the AlSi12 is presented in Table 13 alongside the specification for LM6 alloy. It is clear that the cast alloy is not only within specification, but of a high purity and has a very precise composition. The certificate of analysis is shown in Appendix D.

408 kg of AlSi12 alloy was cast into the test section, where the last 10 kg was cast in slowly when the bulk of the alloy has solidified to ensure that the top level of the AlSi12 is flat and without sink holes. To determine the length of the internal cooling pipe that was in contact with the AlSi12, a measuring tape was used to measure the top level of the AlSi12 from the edge of the filling port. It was determined that 1289mm of the heat transfer pipe was in contact with the AlSi12.

The test section is suspended upright in a frame by the top support flange upon a steel deck bolted to the top of the frame as pictured in Figure 47.



**Figure 45 – Empty test section**



**Figure 46 - Casting of AlSi12 into test section**

**Table 13 - Chemical analysis of the cast aluminium alloy**

<b>Element</b>	Spec	Measured
	<b>wt.%</b>	<b>wt.%</b>
Copper	0.1 max	0.01
Magnesium	0.10 max	0.01
Silicon	10.0-13.0	12.89
Iron	0.6 max	0.54
Manganese	0.5 max	0.08
Nickel	0.1 max	0.01
Zink	0.1 max	0.02
Lead	0.1 max	<0.01
Tin	0.05 max	<0.01
Titanium	0.2 max	0.09
Strontium	na.	293 ppm
Aluminium	Remainder	86.33

**Figure 47 - Test section suspended in frame with heating elements and cladding (cladding still open)**

#### 7.4.1 Heating elements

The heating elements around the storage unit are ceramic band heaters (pictured in Figure 48). The size of the heaters was determined by the limitations on the electrical supply. The properties of the heaters are as follows:

- Power: 23kW max
- Voltage: 3-phase 230V each
- Current: 33A
- Inside diameter: 406mm
- Height: 330mm
- Maximum operational temperature: 600°C



**Figure 48 - Ceramic band heater**

The band heaters is wired through an electrical panel which controls the power delivery of the band heaters using solid state relays controlled by GEFTRAN 450 PID temperature controllers. This is depicted in Figure 49. Safety features include:

- Isolator on the main distribution board
- Isolator in the electrical panel
- A main circuit breaker
- Safety interlock toward the heater bands
- 300 mA earth leakage
- 100A ultra rapid fuses

The installed band heaters are shown in Figure 50 along with the orange electrical panel in the background.

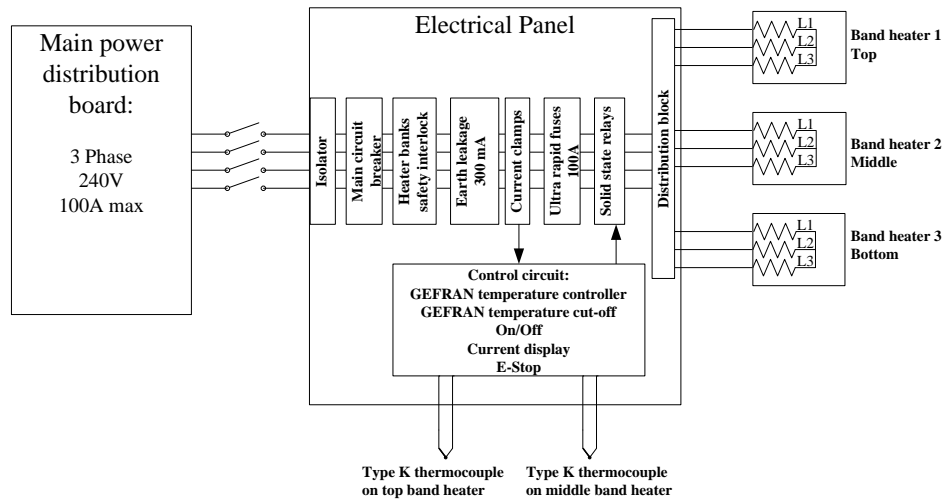


**Figure 49 - Wiring of the three band heaters**



**Figure 50 – Band heaters installed around the storage vessel**

#### 7.4.2 Cooling system

The cooling of the test section was a particularly challenging design because of the high temperature at which the AlSi12 PCM stores energy and the limitations of regular HTFs. ISO 100 quenching oil was selected as a coolant because of its high temperature stability and moderate heat transfer rates at high temperature gradients. Quenching oil has the following characteristics:

- High flash point
- Oxidation stability
- Controlled volatility
- Thermal stability at high temperatures



The quenching oils generally come in three grades, ISO 22, ISO 32 and ISO 100. The number indicates the oil’s viscosity index. The higher the viscosity index, the lower the quenching oil’s cooling rate. The properties of ISO 100 quenching oil is presented in Table 14.

**Table 14 - Properties of ISO 100 quenching oil (Kopeliovich, 2013)**

Density at 60°F (15.6°C)	890	kg/m <sup>3</sup>
Kinematic viscosity at 104°F (40°C)	90.2	cSt
Kinematic viscosity at 212°F (100°C)	10.6	cSt
Viscosity index	100	
Flash point	267	°C
Pour Point	-9	°C
Thermal conductivity at 104°F (40°C)	0.0106	W/m.K
Specific heat capacity at 104°F (40°C)	1950	J/(kg.K)

The oil is then cooled using water in a plate heat exchanger. The water is cooled using a cooling tower. The cooling arrangement is illustrated in Figure 51. The oil flow through the test section is controlled using a bypass line that is controlled using a gate valve. All the oil piping is 1½ inch high temperature rubber hose, piping through and close to the test section is 1 inch S40 carbon steel pipe. The water piping is 1¼ inch Polyethylene irrigation pipe throughout.

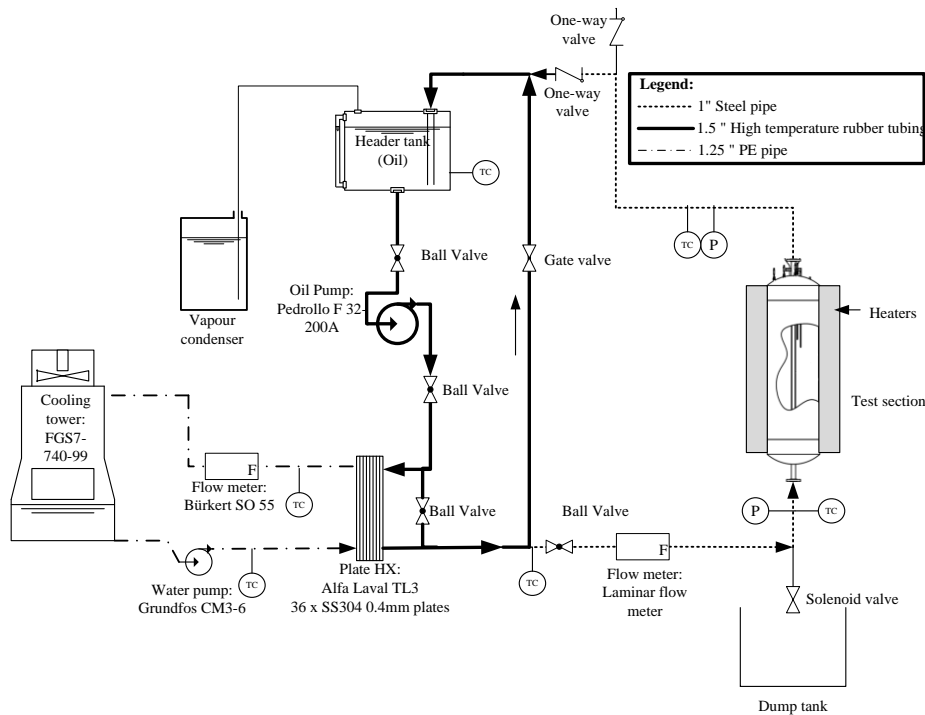


**Figure 51 – Test rig process diagram**

The components of the system were sized with the help of the Flownex model shown in Figure 52. It is difficult to predict the heat transfer to the quenching oil because there is no two-phase data for ISO 100 quenching oil, and a constant approximate heat transfer coefficient of  $800 \text{ W/m}^2\text{K}$  (Herring, 2010) was used for the design phase. A steady state heat transfer model was used as discussed in section 7.2, where the diameter of the solidified aluminium could be altered in the Flownex model.

The temperature of the water supplied by the cooling tower was taken to be  $20^\circ\text{C}$ .

The data used in the model was obtained and integrated with the model in the following ways:

- The pump charts for both pumps were imported from the appropriate catalogues.
- Pipe geometry was obtained from a CAD drawing
- Valve and fitting characteristics were taken from the Flownex library
- Material roughness was taken from the Flownex library
- Heat exchanger pressure drop and heat transfer characteristics were imported from Alfa Laval design software.

The most relevant components are listed in Table 15 along with the manufacturer and model number.

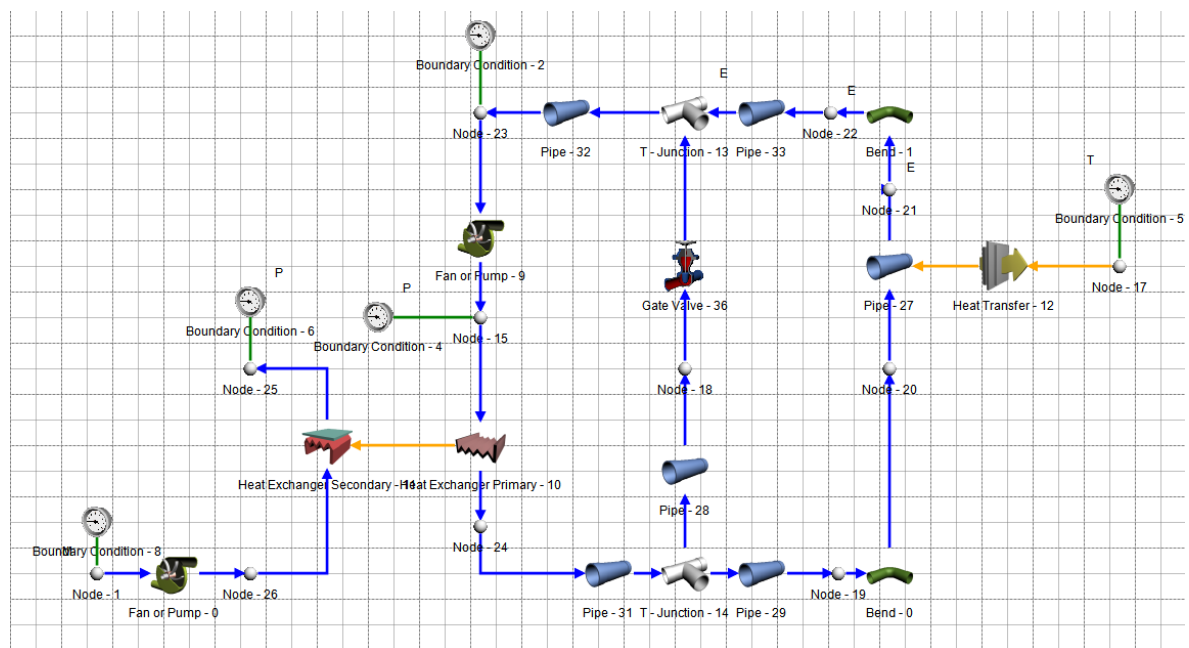


**Figure 52 - Flownex model used to design the experiment**

**Table 15 - Cooling loop component details**

Component:	Manufacturer	Model number
Cooling tower	IWC	FGS7-740-99
Water pump	Grundfos	CM3-6
Plate Heat Exchanger	Alfa Laval	TL3 -36 x SS304 0.4mm
Oil pump	Pedrollo	F 32-200A

The heat transfer from the test section was predicted to be about 35kW at an oil flow rate of 0.22 kg/s.

#### 7.4.3 Thermal insulation and losses

Insulation for the system was challenging since the band heaters had to be operated at their upper temperature and power delivery limits, and band heater failure meant the constant replacement of the cladding. For this reason removable cladding bands had to be devised. The solution was to build cladding bands that would go around each heater which could be removed individually. Because of manufacturing limitations, the thickness of the cladding was limited to 22mm of alkaline earth silicate wool (AES wool).

The conductive thermal resistance between the outer layer of the AlSi12 PCM and the outside is summarised in Table 16.

**Table 16 - Thermal resistance of insulating layers around the storage unit**

	Thermal conductivity $\gamma$ (W/mK)	Thickness (mm)	Resistance ( $^{\circ}$ C/W)	Source
Steel wall	22.6	5	0.00015	(Cengel, 2003)
Ceramic heating element	1.5	13	0.00572	(Technical ceramics, 2013)
AES wool	0.14	22	0.09588	(Technical Glass , 2011)

The surface temperature of the cladding was measured during the experiment using an infrared temperature probe and was later verified using a K-type thermocouple. The temperature was determined to be 224 $^{\circ}$ C. This translates to a thermal loss of 3462W as presented in Appendix E. This is well in agreement with radiation and convective heat transfer predictions based on a surface temperature of 224 $^{\circ}$ C, an emissivity of 0.17 and an ambient temperature of 18 $^{\circ}$ C.

The completed experimental setup is shown in Figure 53.



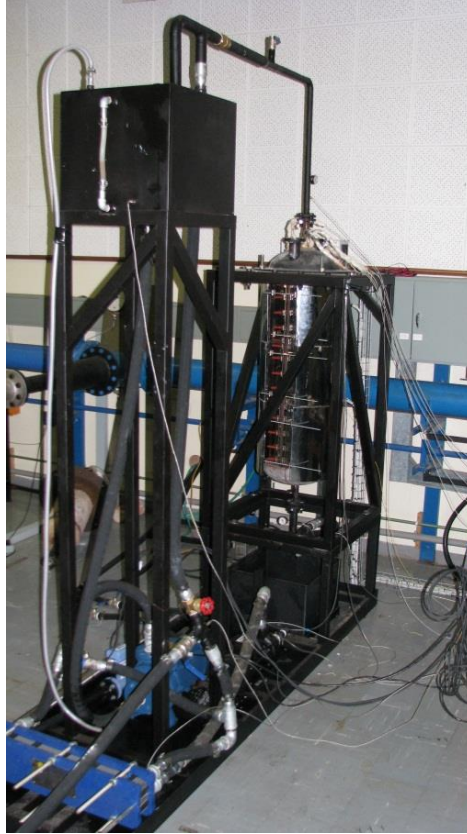


**Figure 53 – The experimental setup**

#### 7.4.4 Measurements and data acquisition

The two aspects of the experiment that had to be monitored were the temperature distribution in the melt, and the heat transfer from the test section. Data was collected using an Agilent 34972A data logger.

All temperatures were measured using K-type thermocouples. The certification of compliance of the thermocouples is included in Appendix D. The thermocouples were connected to the Agilent before installation and checked at 0 and 100 °C using ice water and boiling water. All of the thermocouples measured correctly, passing the initial calibration. K-type thermocouples have an accuracy of  $\pm 0.75\%$  (based on a 0 °C reference junction), which relates to an expected offset of approximately 4.33 °C at 577 °C. Fortunately, the melting point of AlSi12 alloy is fixed at 577 °C, which serves as a reference point for calibration. During the test, the phase change is very distinct in the data set because during both the charge and discharge the thermocouples measure a constant temperature for a fair amount of time. By averaging the isothermal readings of each thermocouple, it could be seen that all the thermocouples had an average offset of 4.21 °C. The readings of the thermocouples imbedded into the molten AlSi12 were then adapted accordingly.

**Table 17 - Measurement errors on the test section thermocouples**

	Measurement	Error
Probe 1	572.78 °C	4.22 °C
Probe 2	572.81 °C	4.19 °C
Probe 3	572.80 °C	4.20 °C
Probe 4	572.79 °C	4.21 °C
Probe 5	572.73 °C	4.27 °C
Average	572.78 °C	4.21 °C

To measure the heat transfer rates from the test sections, two measurement arrangements were made. The first measured the oil flow rate and the entrance and exit temperatures, and the other measuring the heat transfer from the oil to the water using the water flow rate and the inlet and exit temperatures of the heat exchanger.

Measuring oil flow rate is difficult since it has laminar flow and oil is not conductive. For that reason a laminar flow meter had to be devised. In preliminary design stages of the experimental setup, oil flow rates between 0.1 and 2 kg/s were considered. The Hagen-Poiseuille equation (7.28) can be used to calculate the flow rate of the fluid (Johnson, 1998).  $\dot{V}$  Is the volumetric flow rate, D is the diameter of the pipe, L is the length and  $\mu$  is the dynamic viscosity.

$$\Delta P = \frac{128\mu L \dot{V}}{\pi D^4} \quad 7.28$$

For equation 7.28 to be valid, the flow needs to be fully developed. The length of the pipe ( $L_h$ ) required for laminar flow can be calculated using equation 7.29 (Johnson, 1998).

$$\frac{L_h}{D} \cong 0.05 Re \quad 7.29$$

Using the properties of the thermal oil listed in Table 14 and equations 7.28 and 7.29, it was possible to design a laminar flow meter consisting of a long pipe with two pressure taps a meter apart and 4.5m of entrance region to allow for developed flow. The flow meter is constructed as an annulus, of which the air in the annulus is evacuated, preventing heat transfer from the oil inside the pipe, which could seriously affect measurements because a temperature variation in the oil greatly affects the viscosity of the oil. The pressure is measured using an Endress+Hauser Deltabar S PMD75 pressure transducer, which has been calibrated using a Betz water micromanometer, of which the calibration curve is presented in Appendix D. The details of this flow-meter are included in Appendix D. The water flow rate is measured with a Bürkert SO 55 electromagnetic flow meter. The calibration certificate is available in Appendix D.

All the information of the sensors and calibration information are presented in Table 18.

**Table 18 - Measurement devices and calibration points**

<b>Measurement</b>	<b>Sensor</b>	<b>Calibration range/point</b>
<b><i>Temperature probes</i></b>		
<b>Test section</b>		
Probe 1	K-Type thermocouple	Zero, 100 & 577 °C
Probe 2	K-Type thermocouple	Zero, 100 & 577 °C
Probe 3	K-Type thermocouple	Zero, 100 & 577 °C
Probe 4	K-Type thermocouple	Zero, 100 & 577 °C
Probe 5	K-Type thermocouple	Zero, 100 & 577 °C
<b>Oil loop</b>		
Header tank	K-Type thermocouple	Zero & 100 °C
Distribution manifold	K-Type thermocouple	Zero & 100 °C
Test section inlet	K-Type thermocouple	Zero & 100 °C
Test section Outlet	K-Type thermocouple	Zero & 100 °C
<b>Water loop</b>		
Heat exchanger inlet	K-Type thermocouple	Zero & 100 °C
Heat exchanger outlet	K-Type thermocouple	Zero & 100 °C
<b><i>Flow meters</i></b>		
<b>Oil loop</b>		
Laminar flow meter		1.12E-04 to 2.25E-03 m <sup>3</sup> /s
<b>Water loop</b>		
Bürkert SO55 Electromagnetic flow meter		1 to 10 m/s

## 7.5 Experiment

The test section was first heated using the band heaters to a uniform temperature of 630°C. During the heating of the test section, the oil is pre-heated to 40 °C by simply passing the oil through the bypass loop with a partially closed ball valve giving flow resistance. When the test section reached a steady and uniform temperature of 630 °C through all the embedded thermocouples, the band heaters were switched off and the cooling oil was re-directed through the test section and the water cooling loop was switched on. The cooling loop was kept on until the entire test section was cooled down to 200 °C.

The heat transfer through the cooling system could not be accurately predicted due to the lack of two phase heat transfer data of the ISO100 oil, and therefore it had to be measured and a correlation had to be fed back to the simulation for the validation. The heat transfer rates from PCM to oil and from oil to water are presented in Figure 54. The details of the heat transfer measurements are presented in Appendix F.

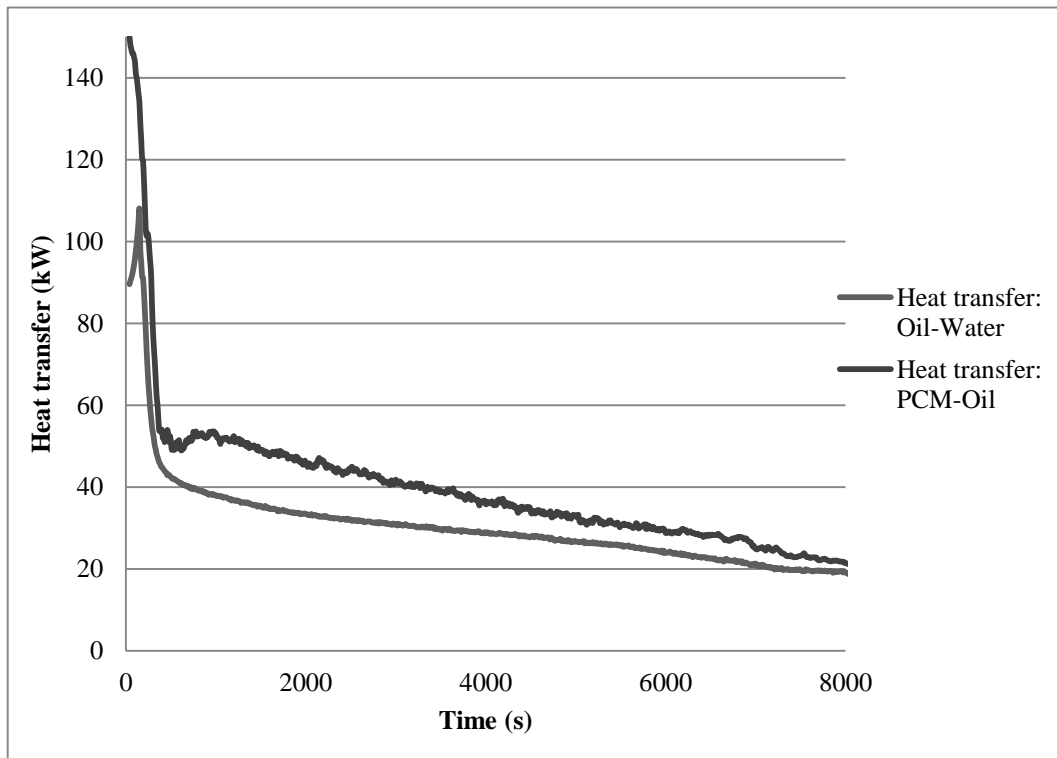


**Figure 54 - Heat transfer measurements**

It was possible to do an energy balance on the storage system during latent heat discharge by numerically integrating the heat transfer data from the beginning to the end of latent heat discharge. The energy balance is presented in Table 19. 95.95 % of the energy that was discharged from the storage system was accounted for by the heat transfer to the oil and calculated losses.

**Table 19 - Energy balance during latent heat discharge**

Heat of fusion	560	kJ/kg	
Mass of AISI12	408	kg	
Latent energy stored	228.48	MJ	100 %
Losses through cladding (calculated)	16.86	MJ	7.38 %
Discharge through coolant (measured)	202.36	MJ	88.57 %
Total heat out	219.22	MJ	95.95 %
Energy unaccounted for	9.26	MJ	4.05 %

The thermocouple readouts throughout the discharge are presented in Figure 55, where isothermal storage is very evident, and the movement of the solidification front is very clear where the temperature of the thermocouples drops below the melting point of the PCM.

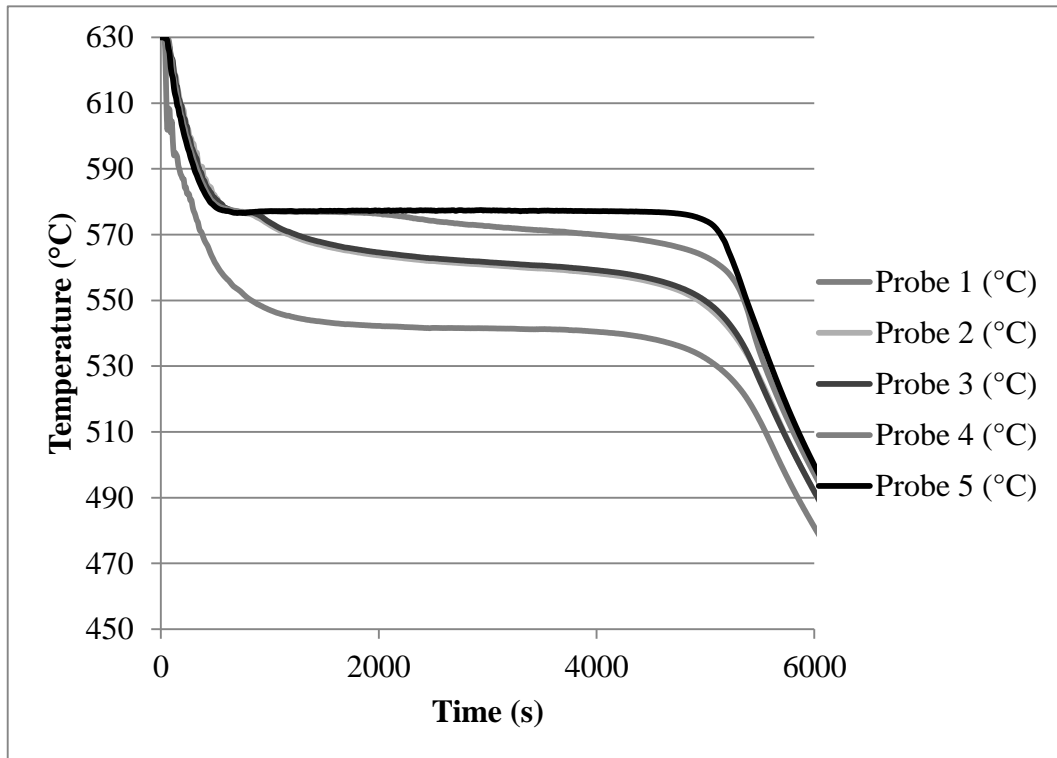


**Figure 55 - Thermocouple readouts throughout discharge of the storage system**

Unfortunately, this experiment could only be run once, as an unexpected corrosion issue was uncovered during high temperature testing of steel samples immersed into AlSi12. This posed significant safety risks. It was discovered that molten AlSi12 is highly corrosive to most steels through mass transfer, as iron is highly soluble into aluminium. This was unexpected, and is not readily documented in literature. This is discussed in more detail in chapter 9.

For this reason, the data presented here is all that is available, and a replacement test section was not possible due to budget constraints.

## 7.6 Numerical simulation

The entire test section was modelled as a cylinder and discretised into cylindrical shells as discussed in section 7.2. Material properties for steel and AlSi12 was used as presented in chapter 4 and geometry as presented in section 7.4 was used.

The inner boundary conditions for the numerical model could be expressed as:

$$\dot{Q}(r_{pi}) = PP(t) \quad 7.30$$

Where  $PP(t)$  is a spline which is fitted through the measured heat transfer data presented in Figure 54.  $PP(t)$  is a result of the built in spline function in Matlab.

The thermal losses towards the outside were dealt with by including the resistances of the heating elements and cladding to the model and giving the outer node a constant temperature as discussed in section 7.4.3.

The discretization,  $\Delta r$ , was chosen to be 1 mm because one of the aspects of the moving boundary problem that must be investigated is the energy distribution around the solidification front, and a resolution of 1mm was considered small enough. Based on this, and the material properties listed in chapter 4, stability criterion (equation 7.27) requires that the time step should be smaller than 9.1 ms. The time step was made 1 ms since computational time was still within acceptable limits.

The resulting Matlab code is presented in Appendix G.

The simulation was started with an initial temperature of 630 °C throughout. The cooling boundary condition on the inside of the heat transfer pipe is only started after 40 s. The temperatures of the nodes corresponding to the probes in the experiment is plotted every 10 s, and the results is shown in Figure 56.

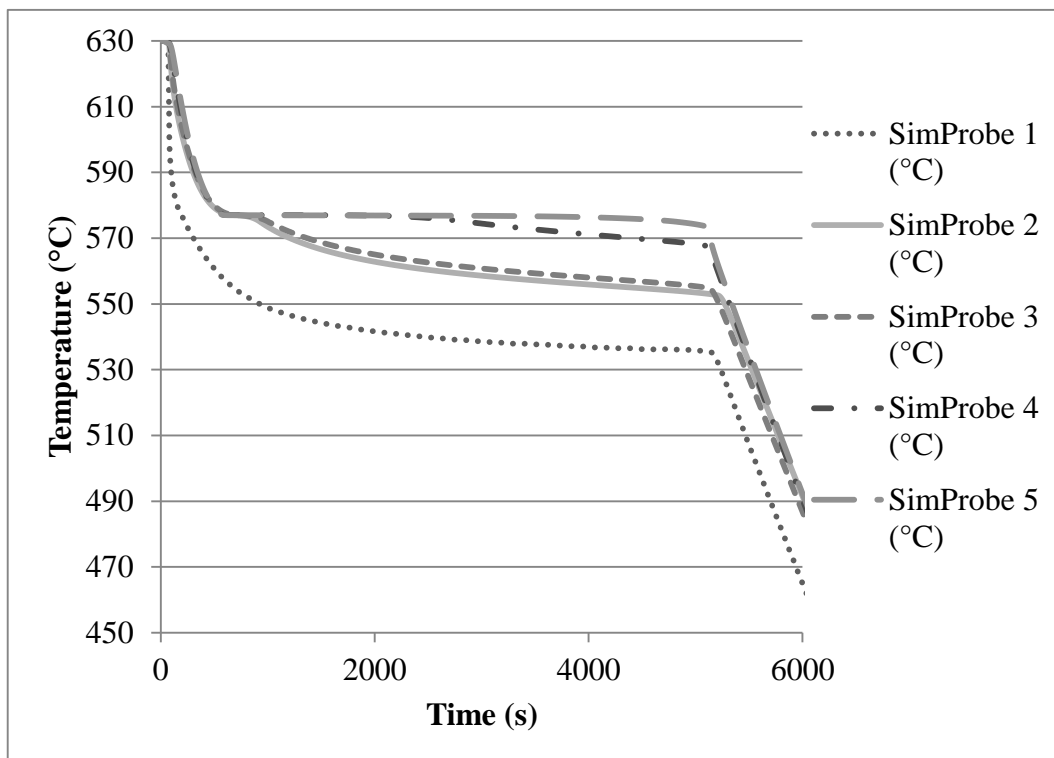


**Figure 56 - Simulation results of the phase change problem based on the experimental**

## 7.7 Comparison and conclusions

The first very obvious observation that can be made from the experimental data is that the molten part of the PCM is isothermal at the melting temperature of AlSi12, 577 °C, confirming one of the core simplifying assumptions made. This

means that there are no convective currents in the melt, and heat transfer can be considered as purely conductive.

By simply plotting the experimental and the simulation data over each other, as in Figure 57, it is possible to see that the model simulates the general trends very well apart from the transition towards the end of the discharge which is more abrupt in the simulation than in the experiment. This can be attributed to the constant specific heat used. The specific heat capacity of AlSi12 will have to be determined using a differential scanning calorimeter.

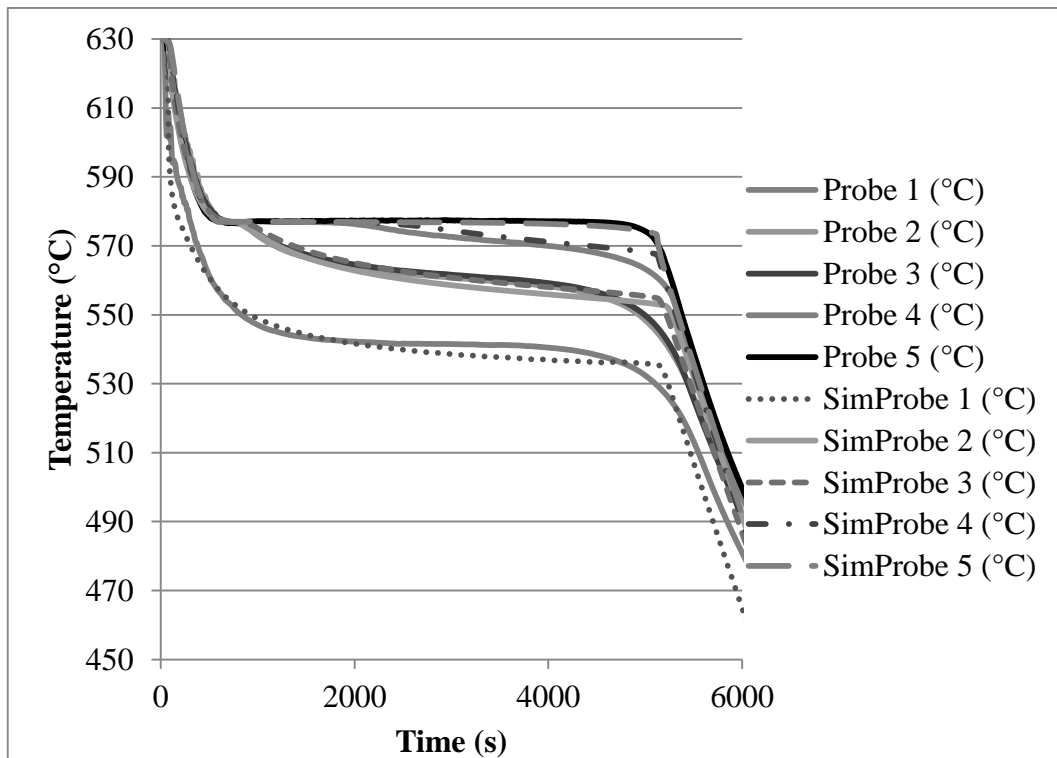


**Figure 57 - Experimental data and simulation data plotted over each other for comparison**

One of the key questions is if the numerical model accurately predicts the movement of the solidification front through discharge. Figure 58 shows the position of the thermocouples against the time when the thermocouple readout drops below the melting point. The position of the melting point, as calculated by the simulation, is also plotted in Figure 58 and shows good correlation with the experimental data.

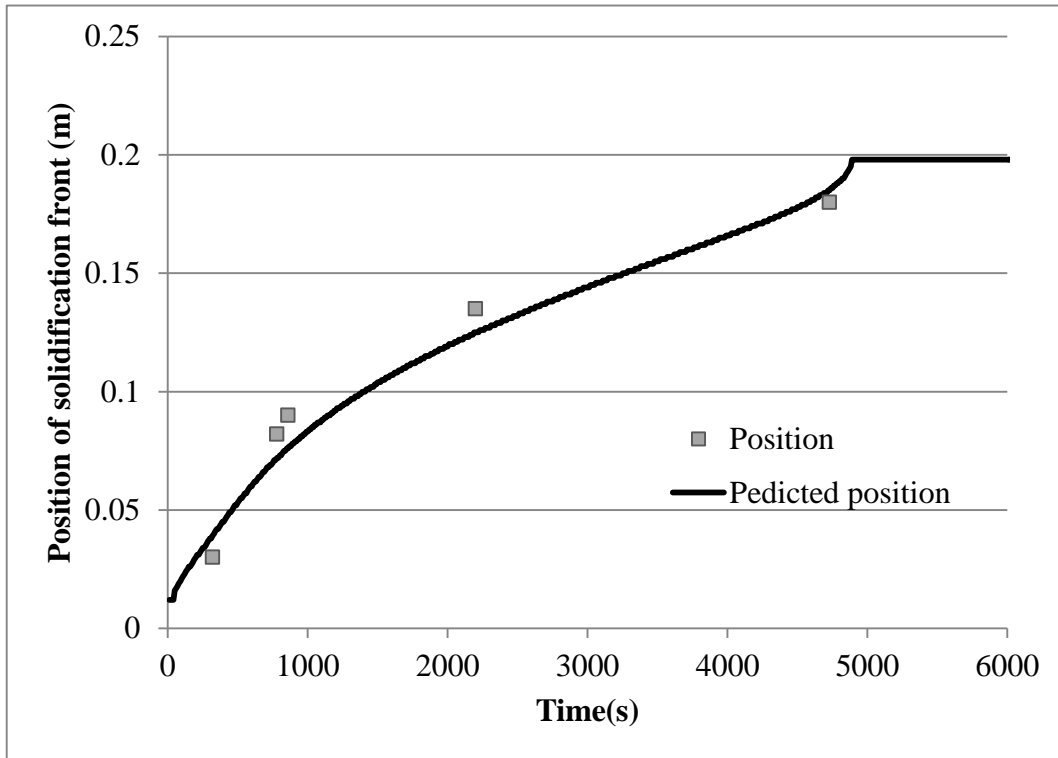


**Figure 58 - Comparison between the positions of solidification front as predicted by the simulation and measured in the prototype**

The assumption that quasi steady assumptions are valid is the basis for using the resistance model for instantaneous heat transfer calculations for heat exchanger sizing. From Figure 55 and Figure 56 it is clear that after discharge, the temperature of the solidified mass of PCM is upheld by the discharge process and the thermal resistance “downstream” from that location in the melt, as illustrated in Figure 59.

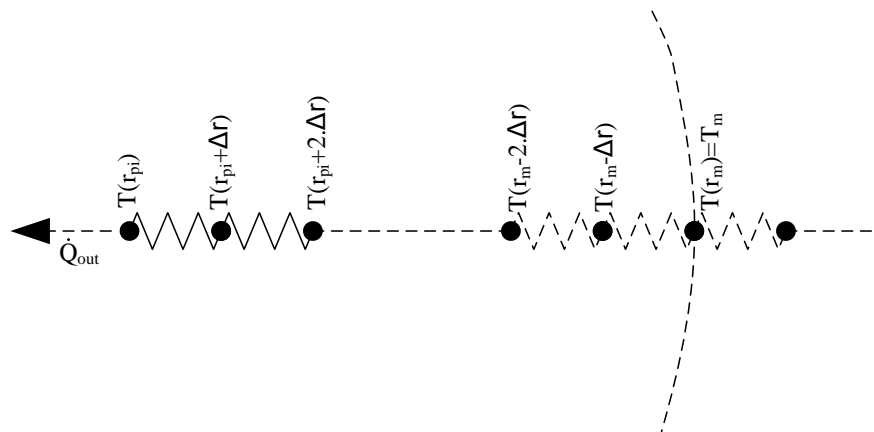


**Figure 59 - Quasi steady conduction problem**



According to the Stefan condition, quasi steady analysis is only valid if the Stefan number is much lower than 1. The closest measurement to the inside of the steam pipe is the first thermocouple. When the solidification front moved past thermocouple #5, thermocouple #1 read 536.2 °C. Considering a melting point of 577 °C, a heat of fusion of 560 kJ/kg, and a specific heat of 1.038 kJ/kg.K, the Stefan number is 0.07. Thus, the Stefan assumption for quasi steady analysis is valid.

This is clear when the temperature distribution through the melt at the moment the solidification front moved past thermocouple #5, is plotted against the simulation data. This is presented in Figure 60.

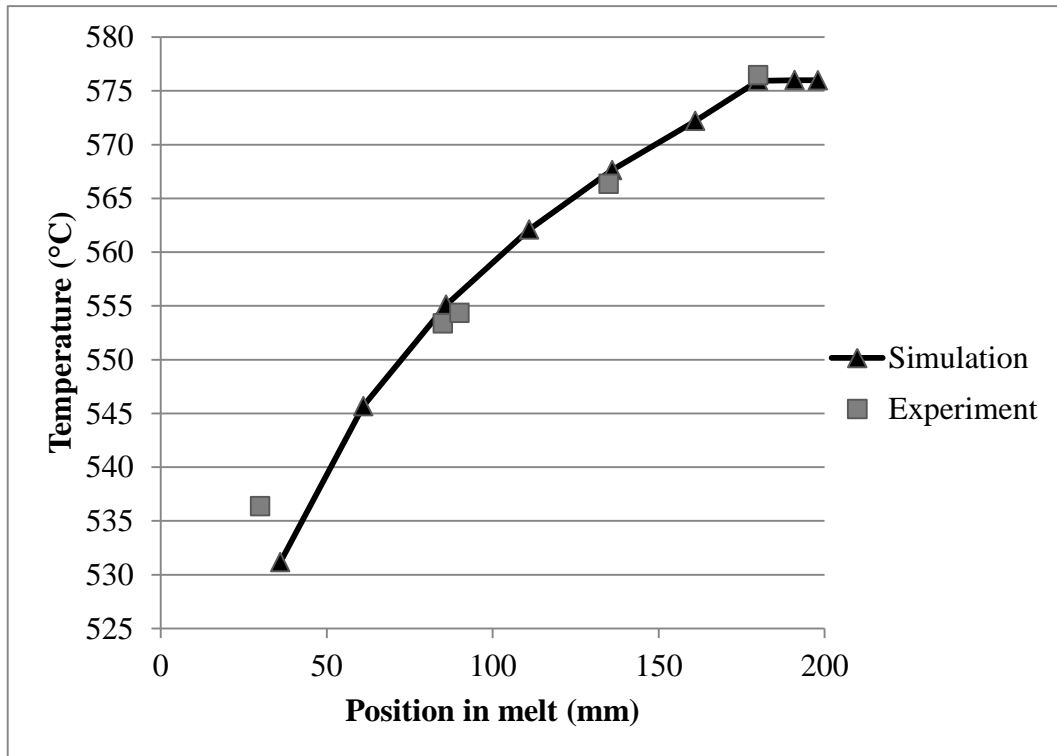


**Figure 60 - Temperature distribution through melt as the solidification front passes thermocouple #5**

## 8 PRELIMINARY PLANT DESIGN AND SIMULATION

For concept evaluation a preliminary design is needed along with a simulation and design evaluation for both concepts and a basic analysis for process control. To obtain representative boundary conditions for the steam generators and proper sizing, a hypothetical steam Rankine cycle is considered. In simulation and evaluation of the concept, the entire plant is divided up into models that are outlined in Figure 61. The entire system was designed and modelled in Flownex.

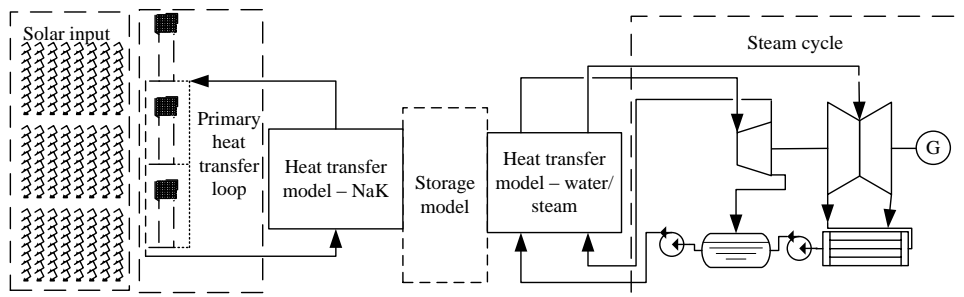


**Figure 61 - Overview of the model**

The sizing of a CSP plant's capacity and storage capability is mainly a financial consideration and is a function of:

- Feed in tariff and incentive plan to which the plant will deliver
- Weather patterns
- Location

This is a complex financial consideration, where the return on investment depends on these factors. Most studies suggest that the current value proposition of CSP is not necessarily base load power production, but peaking (Hummon, et al., 2012). This falls outside the scope of this project.

Because this study is on the evaluation of a storage mechanism, a base load implementation poses a more challenging scenario. Currently Gemasolar is the only central receiver power plant that delivers base load electricity, and it has 15 hours of storage (Torresol Energy, 2013). For this reason, 15 hours of storage is selected for the hypothetical plant. The turbine size of 100 MW is chosen based on the sizing of the Siemens SST turbines recommended for solar thermal applications (Siemens, 2010).

### 8.1 Power generating cycle

To derive the boundary conditions for the rest of the plant, the boundary conditions of the power generating cycle are required. The power generating cycle for both concepts will be a subcritical steam cycle with the following properties:

- 100 MW electrical output;
- 540 °C, 140 bar superheat;
- 540 °C, 30 bar re-heat;
- one open-feed water heater supplied from the high-pressure turbine outlet; and
- Air-cooled condenser (ACC) with a condenser pressure of 0.15 bar.

A process diagram of the Rankine cycle is shown in Figure 62 and a T-s diagram of the power cycle is shown in Figure 63. The numerical annotation is consistent throughout these two figures.

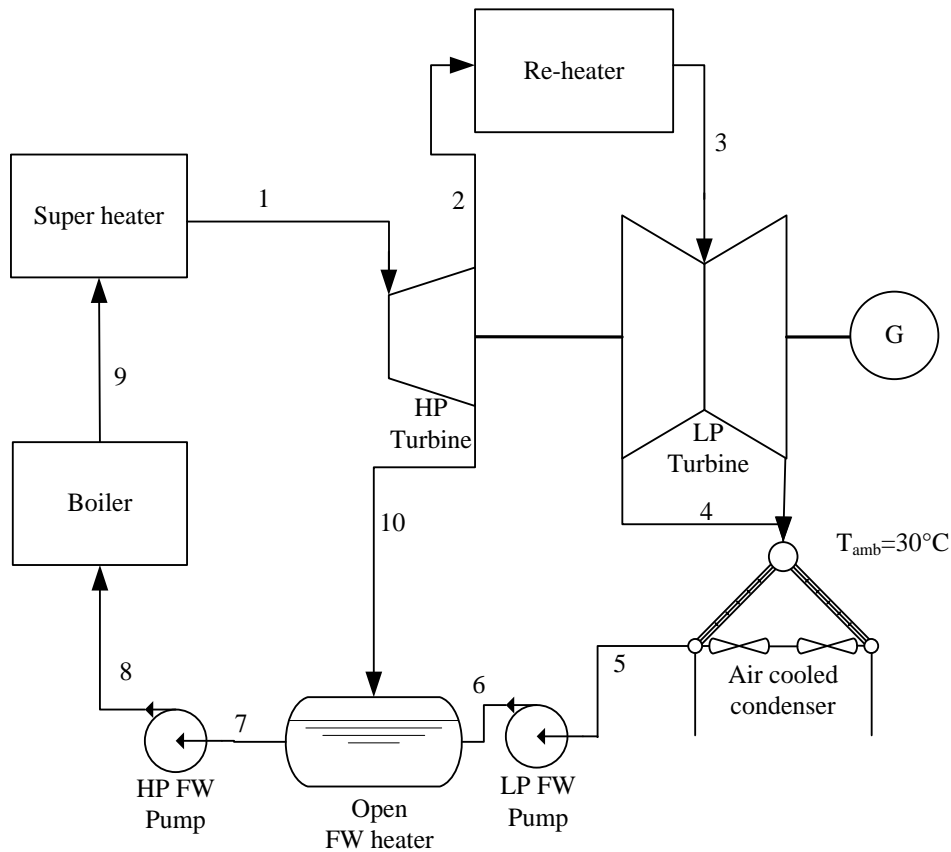


**Figure 62 - Power generation cycle**

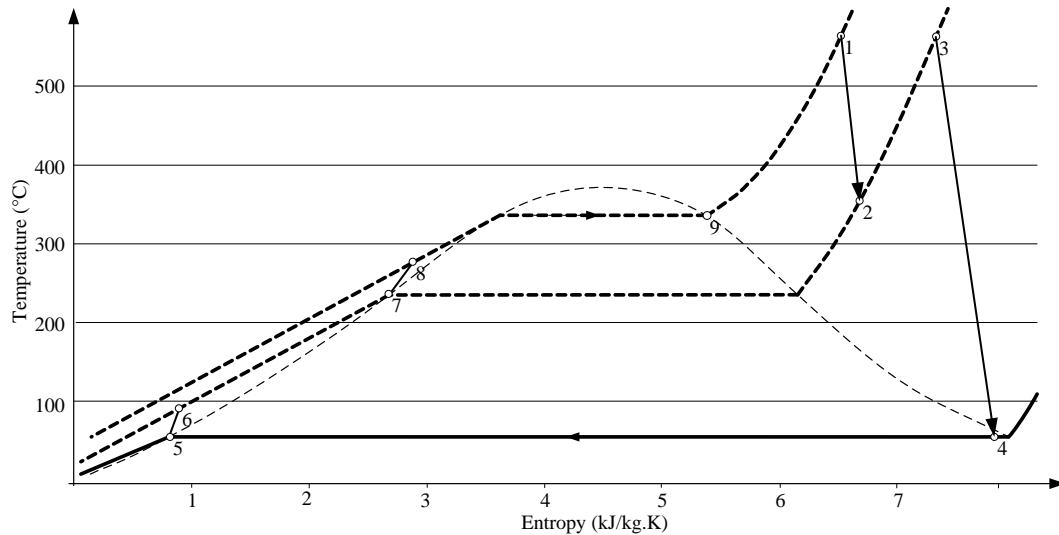


**Figure 63 - T-s diagram for the power cycle**

Flownex SE was used to provide a complete simulation environment where heat transfer, fluid mechanics and thermodynamics could be simulated simultaneously in both steady state and in transient state. To provide initial design parameters for the Flownex model, the power cycle first had to be evaluated by hand. The detailed hand calculation of the power cycle is presented in Appendix H. The energy balance of the power cycle is presented in Table 20. The overall thermal efficiency of the cycle is 38 %, which is within the expected range for such a simplified steam cycle. It must be noted that the thermal efficiencies of the components are not based on the performance of actual hardware and taken to be approximate values for these components as stated in literature (Cengel, et al., 2002) (Karassik, et al., 1985) (Johnson, 1998).

The steam generator is divided into three distinct sections:

- Boiler
- Super-heater
- Re-heater

These will be considered separately throughout. The boundary values yielded by hand calculations are shown in Table 21.

**Table 20 - Energy balance of a hypothetical power cycle**

	Mass flow (kg/s)	(MW)	Efficiency
<b>Thermal input</b>			
Boiler	93.99	151.7	
Super-heater	93.99	74.83	
Re-heater	68.01	34.01	
Total		260.54	
<b>Pump electrical input</b>			
Pump 1	68.01	0.24	0.85
Pump 2	93.99	1.48	0.85
Total		1.72	
<b>Heat removed by the condenser</b>			
Condenser	68.01	156.99	
<b>Turbine output</b>			
Turbine 1	93.99	36.39	0.87
Turbine 2	68.01	68.87	0.87
		105.26	
Generator		100	95
Overall thermal efficiency			0.38

**Table 21 - Boundary conditions and heat transfer requirements of the steam generator**

	Mass flow (kg/s)	Enthalpy change (kJ/kg)	$\dot{Q}$ (MW)	$T_{in}$ (°C)	$T_{out}$ (°C)	P(bar)
Boiler	93.99	1613.98	151.70	236.85	336.67	140
Super-heater	93.99	796.11	74.83	336.67	540	140
Re-heater	68.01	500.01	34.01	321.17	540	30

The Flownex model is built up using the hand calculations as a starting point. The Flownex model is based on exactly the same theory and assumptions as the hand calculations and thus the energy balance and the boundary conditions are the same as in Table 20 & Table 21. The details of the Flownex model are shown in Appendix I. The basic Flownex model used in the Rankine cycle is presented in Figure 64.

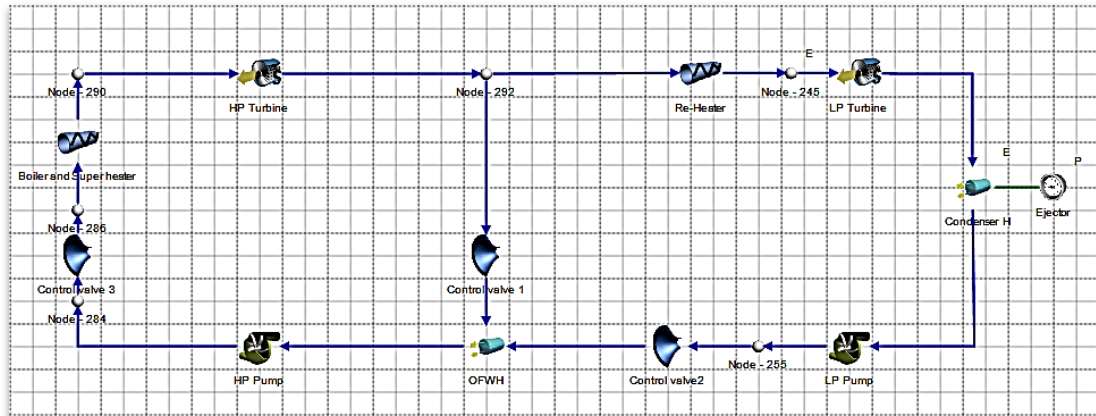


**Figure 64 - Flownex model of the Rankine Cycle**

The model shown in Figure 64 is used as a basis throughout the rest of this text because most of the design work was done with the aid of the “*Flownex designer*” tool. The designer tool uses the Newton-Raphson solution algorithm to solve a set of non-linear equations that relates to the dependent and independent variables of the flow network. The relation between the independent variables (such as orifice diameter or turbine efficiency) is set by the user, and the dependent variables (such as mass flow rate, pressure drop and flow velocity) in the designer interface. By setting goals for the dependent variables and a domain for the independent variables with initial guess values, the designer will find a solution that best suits the scenario.

## 8.2 Primary heat transfer loop

The solar thermal input of the power generating system is dependent on a number of factors mostly related to the time dependent input of the sun. The solar resource is available in a sinusoidal fashion, and has to be concentrated by the collector field and absorbed by the receiver. The collector field has its own characteristic behaviour which is highly dependent in the exact nature of the heliostats, heliostat field layout, tower height and weather conditions. Furthermore, the exact design of the receiver also has a large effect on the efficiency and characteristics of the system as a whole. Because the focus of this project is not the collector or the receiver itself, some simplifying assumptions are necessary. The aim is to obtain peak design parameters for the receiver loop that are representative of what may be encountered in a real central receiver plant.

To design the heat exchangers for the primary cooling loop the peak design heat transfer requirements are necessary. The primary heat transfer loop of the DSG concept is illustrated in Figure 65. The factors influencing both the peak heat transfer requirements and the nature of the heat exchange elements are discussed in the subsequent subsections.

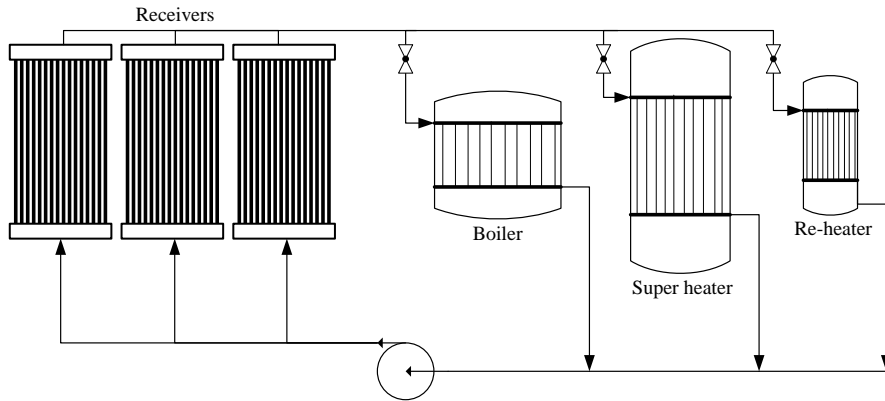


**Figure 65 - Heat exchanger configuration for the DSG concept**

### 8.2.1 Primary loop heat transfer requirements

The time dependent thermal input of the solar collector and receiver system must be considered to calculate the peak heat transfer requirements of the primary heat transfer loop of the plant. The thermal input from the collector field to the receiver is the product of the direct normal irradiation (DNI) and the collector field efficiency. The collector field's efficiency depends on the design of the field and is also time dependent. The specific design of the field is outside of the scope of this study, and the field efficiency is taken to be constant throughout the day. Consequently the time dependent profile of the thermal input can therefore be taken as the normalized DNI (Battleson, 1981) (Steine, et al., 1986) (Meduri, et al., 2013). To determine the location of the plant, a map of the South African annual DNI is presented in Figure 66, p.92.

The annual DNI is the annual sum of the DNI on that location and is measured in  $\text{kWh/m}^2$ . The map in Figure 66 indicates the best places for such a power plant. The higher the DNI, the more power is produced per square meter of the collector, which brings down the LCOE. In this project, Upington ( $28^{\circ}24'0''\text{S}$ ,  $21^{\circ}16'0''\text{E}$ ) is chosen as the location of the hypothetical plant due to high DNI, good supply of water, and the existing grid connection in the area (Fluri, 2009).

The DNI for a given location can be calculated accurately, and the Bird Clear Sky Model (Bird, et al., 1981) is taken to be the industry standard model to calculate the clear sky DNI at any given time assuming clear skies. The DNI values in Upington for four seasons are shown in Figure 67, p.92.

South Africa, Lesotho and Swaziland

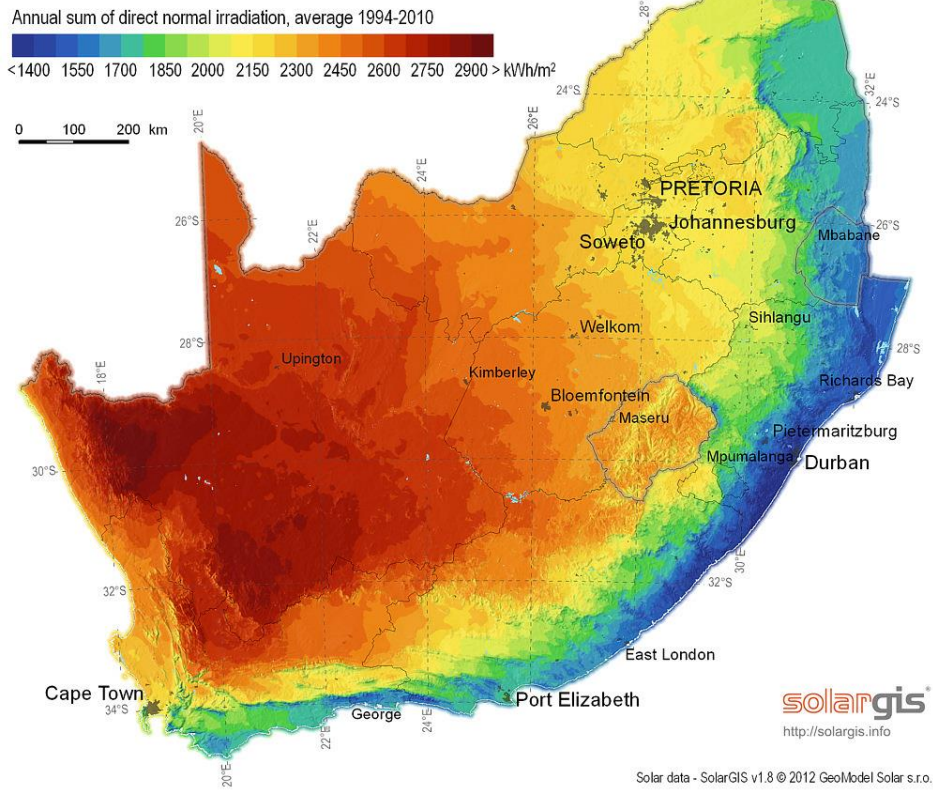


Figure 66 - Annual DNI for South Africa (Geosun)

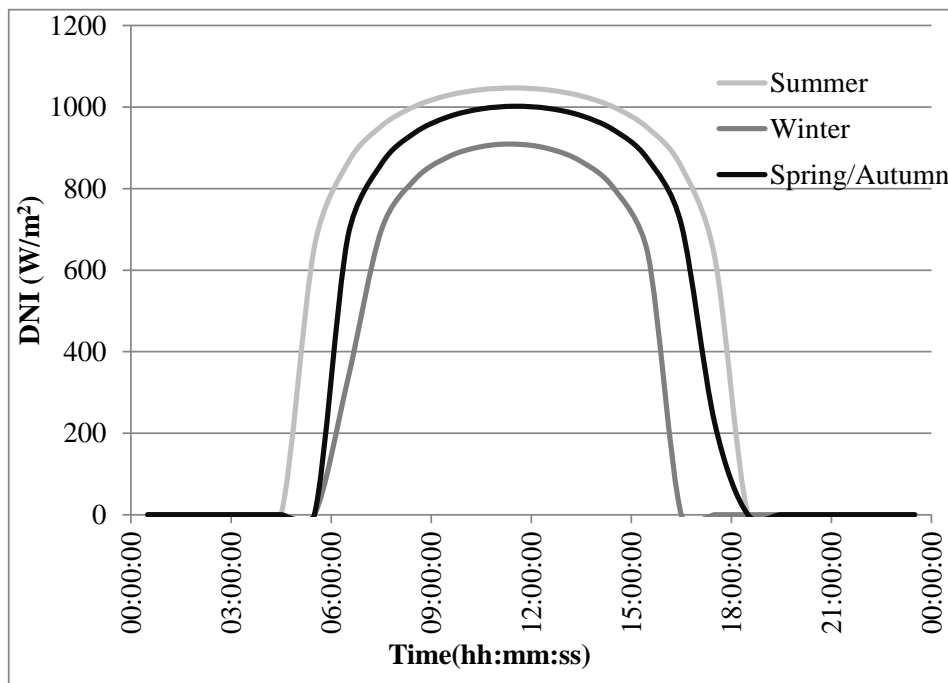
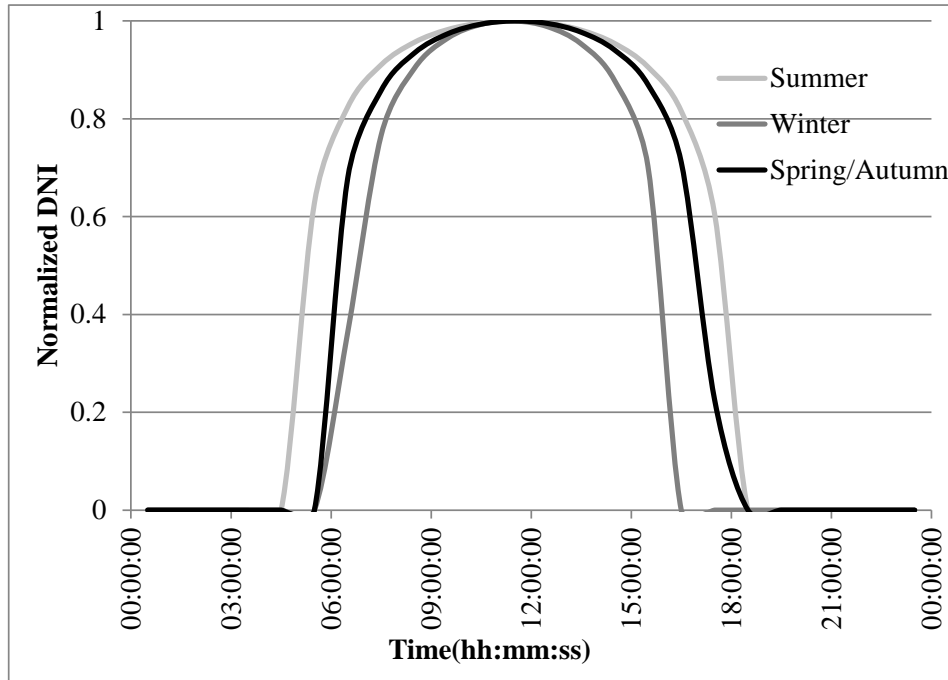


Figure 67 - Clear sky DNI for Upington



The primary heat transfer loop transports thermal energy from the receiver to the HSU and the power block. Because solar energy is time dependent, the receiver will have to have a peak working point where the receiver must absorb all the incoming radiation from the collector field. The normalized DNI dictates the time dependent “shape” of this thermal input since the assumption is based on the collector field having a constant optical efficiency throughout the day. Figure 68 presents the normalized DNI in Upington for summer, winter and spring.



**Figure 68 - Normalized DNI for the summer solstice, winter solstice and the southward equinox (spring) for Upington**

Designing the field for the winter will result in significant defocussing in summer and designing for the summer will result in excessive co-firing in the winter. A financial evaluation is required to find an optimum collector field size. To simplify the analysis, the time dependent input for the southward Equinox for 2013 (Spring – 22<sup>nd</sup> September) will be used as a basis for the time dependent thermal input,  $(D(t))$ . The primary heat transfer loop is to be sized to achieve full charge (15h) on a day with no clouds on the southward equinox. It must be noted that proper sizing of the thermal energy storage system is a complex study, and falls out of the scope of this project, and this crude assumption will have to suffice.

The receiver was sized using an energy balance of the storage system for one day illustrated in Figure 69. The heat transfer requirements to the steam generator ( $\dot{Q}_{out}$ ) is calculated in section 8.1 and is presented in Table 21. This yields a time dependent problem since the heat transfer from the primary cooling loop has a certain profile.

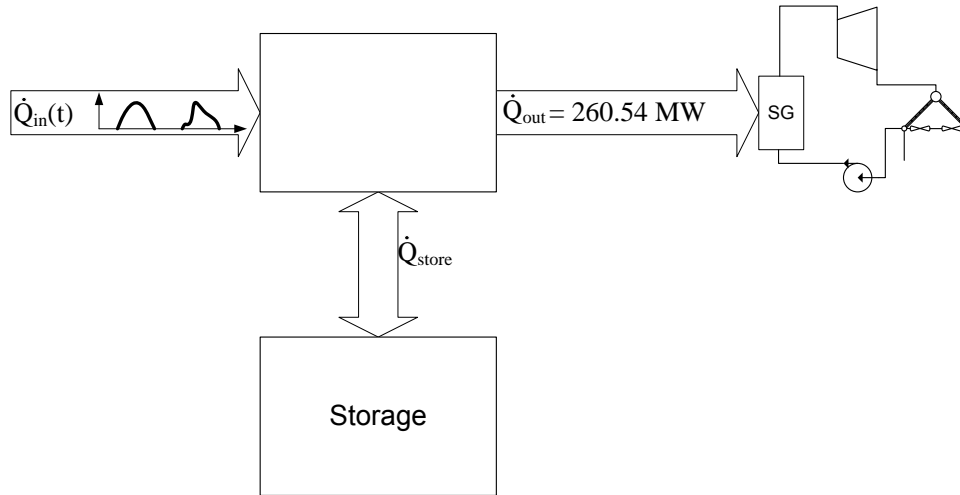


**Figure 69 - Energy balance to storage**

The heat transfer to the storage system is calculated by multiplying the normalized DNI by the peak heat transfer rate:

$$\dot{Q}_{in}(t) = \dot{Q}_{peak} D(t) \quad (8.1)$$

Where:

$$\dot{Q}_{peak} = SM \dot{Q}_{out} \quad (8.2)$$

SM is the solar multiple. The energy delivered to storage is calculated by:

$$Q_{in} = \int_{t_1}^{t_2} \dot{Q}_{in}(t) \cdot dt \quad (8.3)$$

and the energy delivered to the steam generators:

$$Q_{out} = \int_{t_1}^{t_2} \dot{Q}_{out}(t) \cdot dt \quad (8.4)$$

The size of the storage can be calculated by

$$Q_{store} = t_{store} \dot{Q}_{out} \quad (8.5)$$

The energy balance yields:

$$Q_{in} = Q_{out} + Q_{store} \quad (8.6)$$

Substituting equation 8.2 into equation 8.1 and substituting that into equation 8.6 and substituting equations 8.4 and 8.5 into equation 8.6:

$$\int_{t_1}^{t_2} SM \dot{Q}_{out} D(t) \cdot dt = \int_{t_1}^{t_2} \dot{Q}_{out}(t) \cdot dt + t_{store} \dot{Q}_{out} \quad (8.7)$$

Since  $t_{store}$  and  $\dot{Q}_{out}$  is known, the solar multiple, SM, can be calculated. The function  $D(t)$  was given by the Bird clear sky model and the integration was performed for a period of one day (since full charge is needed after one day). The resulting solar multiple is 2.73, which results in a peak heat transfer rate of 711.80 MW for the primary heat transfer loop. The time dependent energy balance is presented in Figure 70.

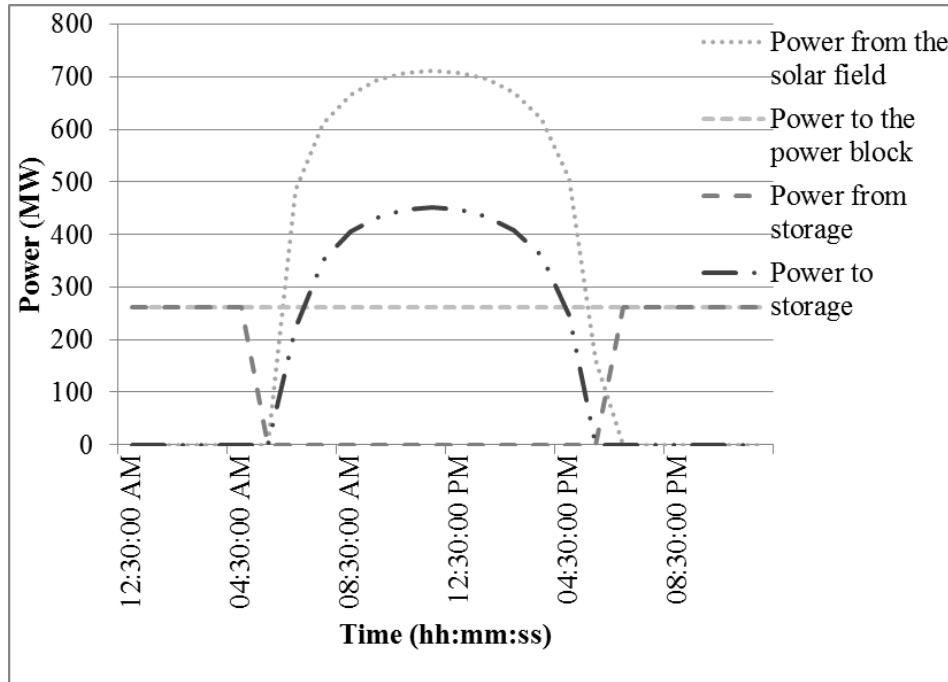


**Figure 70 - Power to and from storage**

It is possible to calculate the peak heat transfer rates to each storage section for the DSG concept by taking the ratios of the heat transfer requirements between the boiler, super- and re-heater (Table 21) and applying them to the peak heat transfer rate of the primary cooling loop. This is presented in Table 22.

Table 22 - Heat transfer requirements for the primary heat transfer loop

	$\dot{Q}_{out}$ (MW)	$\dot{Q}_{in}$ (MW)
Boiler	151.7	414.44
Super-heater	74.83	204.44
Re-heater	34.01	92.92
<b>Total</b>	<b>260.54</b>	<b>711.80</b>

### 8.2.2 Receiver sizing

The goal of designing the primary heat transfer loop is to size the heat exchangers that are imbedded into the storage system. The key components are the:

- Receiver
- PCM heat exchanger and,
- Pump

A model of each of these is required to properly simulate the primary cooling loop in Flownex. The receiver model is of secondary importance, but because it has implications on the performance of the loop, the receiver will be designed to yield reasonably representative pressure drop characteristics. The use of liquid metals has significant implications on the receiver which will become evident in the following subsections. It is one of the major advantages that liquid metals have above other HTFs. The receiver will be generic for both the DSG and the ISG concepts.

In this project a central receiver concept will be used (as illustrated in Figure 71) because it has a simpler construction and a wider field acceptance angle. An external receiver's performance increases with its capacity to absorb higher flux densities which limits radiation losses by minimizing the surface area of the receiver. The average flux density of the receiver is highly dependent on the working fluid.

Table 23 shows the typical peak flux design values for receivers utilizing various HTFs.

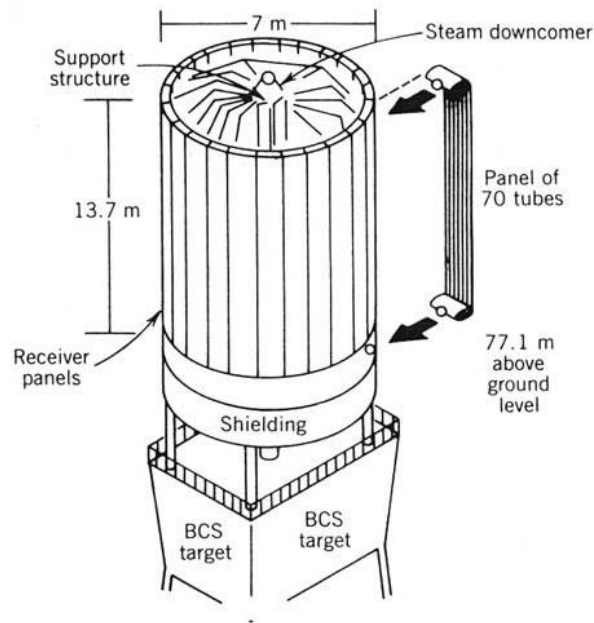


**Figure 71 - External receiver**

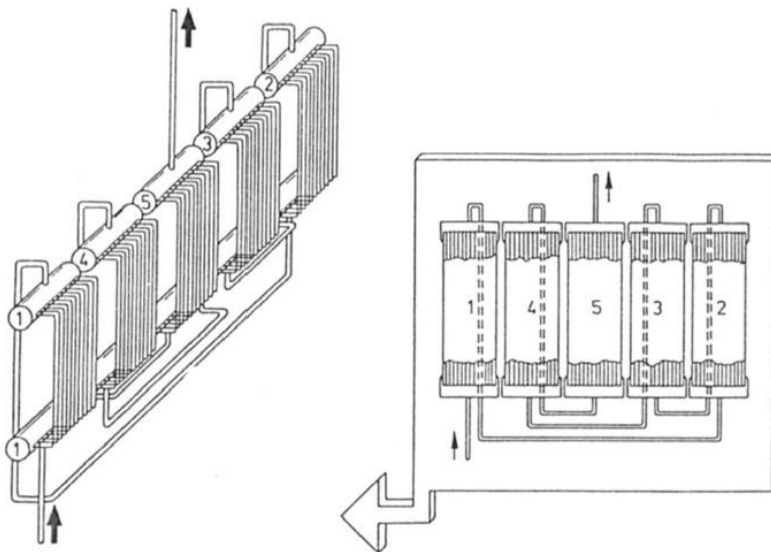
**Table 23 – Typical receiver peak flux design values (Battleson, 1981)**

Heat transfer Fluid	Designed peak flux (MW/m <sup>2</sup> )
Liquid sodium	1.5
Molten nitrate salt	0.7
Liquid water	0.7
Steam vapour	0.5
Air	0.22

It is clear that a receiver using liquid sodium would be less than half the size of a receiver using molten nitrate salt or water, reducing thermal losses by half.

Liquid sodium receivers have been tested by both SANDIA labs, and by PSA. The receiver tested at PSA could achieve a peak flux density of 2.5 MW/m<sup>2</sup> with a receiver efficiency of 90 %. (Schiel, 1988).

The construction of a liquid metal receiver is relatively simple, and is similar to water and molten salt receivers. The receiver tested at the PSA was constructed by an Italian company, Franco Tosi. It consisted of a plate of parallel pipes, with two headers. Five panels were constructed for the single receiver. A schematic of the receiver is shown in Figure 72. The panels were covered in Pyromark™ paint.

**Figure 72 - Liquid sodium receiver tested at PSA (Schiel, 1988)**

Because the dominating heat transfer characteristic of sodium is its high thermal conductivity, it is possible to generalize the attributes of a liquid sodium receiver to other liquid metals, and it is theoretically possible to construct similar receivers using other liquid metals like NaK and Lead Bismuth alloy.

The use of liquid metals as HTFs enables the construction of compact, lightweight, more efficient receivers, with simple design geometry that can operate at higher temperatures than possible with other HTFs.

For this project, a peak heat flux density of  $2.5 \text{ MW/m}^2$  (Schiel, 1988) in an external receiver will be assumed with a maximum operational temperature of  $800 \text{ }^\circ\text{C}$  due to the material limits of Inconel X750 (Special Metals Corporation, 2013). It is possible to determine the most suitable heat transfer exit temperature based on the combined thermal efficiency of the power block, storage and receiver.

As discussed in section 8.2.1, the receiver should be able to deal with  $711.80 \text{ MW}$  of heat flux. The receiver will be divided into three equally sized  $237.2 \text{ MW}$  receivers due to field limitations.

Because there are no commercial liquid metal receivers, no pressure drop and flow data available on the experimental receivers that was tested by PSA and SANDIA (Schiel, 1988), some crude assumptions will have to be made to size a receiver.

The heat transfer fluid pressure and temperature of the receiver will be found in an iterative manner using Flownex, and the wall thickness of the pipes adapted accordingly. Considering three separate receivers with uniform flux distribution (a valid assumption at noon with a properly designed field) each with a flux density of  $2.5 \text{ MW/m}^2$ , yields a surface area of  $94.91 \text{ m}^2$  for each of them. The surface area is calculated on the outer diameter of the receiver and not the surface of the physical pipes. A roughly square target is preferred for the aiming of the heliostats, and using a rounded up surface area of  $95 \text{ m}^2$  a diameter of  $5.5 \text{ m}$  and a height of  $5.5 \text{ m}$  are calculated.

The receiver is constructed of parallel tubes made of Inconel 800 coated with Pyromark™ paint. To evaluate the most suitable tube size, a mass flow rate of  $7550 \text{ kg/s}$  and an inlet temperature of  $590 \text{ }^\circ\text{C}$  is used. The exit temperature is calculated as  $692.38 \text{ }^\circ\text{C}$  using the properties presented in section 4.2. The mass flow rate of the NaK is relatively high due to the low  $C_p$  value of NaK, and therefore a low pressure drop is important to keep pumping power to a minimum. Because Inconel tube is made according to specification (Special Metals Corporation, 2013), and the pressure and temperature for the receiver are not known at this stage of the analysis, the tube wall thicknesses is taken as that of ANSI B36.19 steel tube.

The receiver is simply an array of tubes running along the circumference of the receiver with their outer wall tangential to the outer diameter of the receiver. The pressure drop was calculated for the receiver with the pre-selected conditions for each standard B36.19 tube diameter from  $1/8$  inch to  $2$  inch. Pressure drop in liquid metals flowing in tubes is calculated in the same manner as for water and other liquids (Liquid metal engineering center, 1972), and the Darcy-Weisbach (Darcy, 1857) (Weisbach, 1845) equation is used with a surface roughness of

60µm, which is typical for seamless steel tubes (Special Metals Corporation, 2013). The results are presented in Table 24 and are plotted in Figure 73.

**Table 24 - Pressure drop for various heat transfer tube diameters for the receiver**

B36.19 designation	Outside diameter (mm)	Wall thickness (s40)	Inside diameter (mm)	Pressure drop (kPa)	Pipes per receiver	Number of pipes (total)
1/8"	10.3	1.73	5.68	90656.73	1673	5019
1/4"	13.71	2.24	9.23	12130.23	1256	3768
3/8"	17.14	2.31	12.52	3767.88	1004	3012
1/2"	21.34	2.77	15.8	1706.59	806	2418
3/4"	26.67	2.87	20.93	605.80	644	1932
1"	33.4	3.38	26.64	266.81	514	1542
1 1/4 "	42.16	3.56	35.04	101.23	406	1218
1 1/2"	48.26	3.68	40.8	59.57	355	1065
2"	60.32	3.91	52.5	25.01	283	849

Smaller tube diameters are favourable for heat transfer because thinner walls can be used, a significant factor if the low thermal conductivity of Inconel is considered (Special Metals Corporation, 2013). By plotting the pressure drop versus tube diameter (Figure 73) it can be seen that 1-inch (33mm outside diameter) tube yields an acceptable 266.81 kPa pressure drop at peak flow rates.

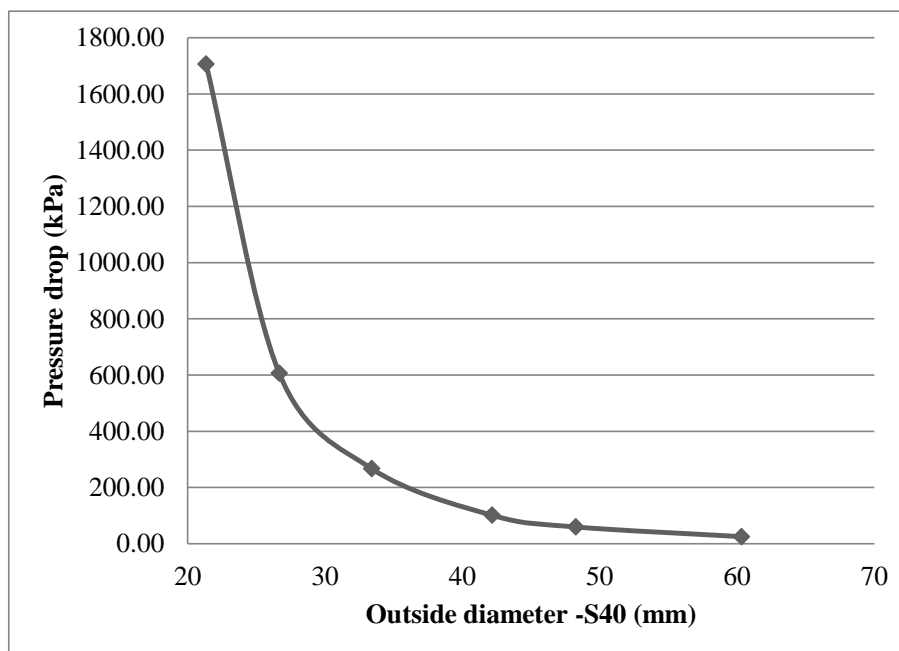


**Figure 73 - Pressure drop over receiver versus outer diameter for various B36.19 tubes**

The resulting receiver geometry and peak pressure drop characteristics are summarised in Table 25:

Total heat transfer	711.8	MW
Inlet temperature	590.0	°C
Outlet temperature	692.3	°C
Number of receivers	3	
Heat transfer per receiver	237.26	MW
Peak mass flow rate	7550	kg/s
Heat transfer fluid	NaK	
Receiver outer diameter	5.5	m
Receiver height	5.5	m
Tube outer diameter	33.4	mm
Tube wall thickness	3	mm
Pressure drop	266.80	kPa

**Table 25 - Receiver geometry and performance parameters**

The receiver is implemented into the Flownex model as a single pipe bundle with a heat source for all three receivers. The geometry is the same as in Table 25, with an elevation boundary of 100m for the bottom nodes and 105.5m for the top node to represent the height of the tower.

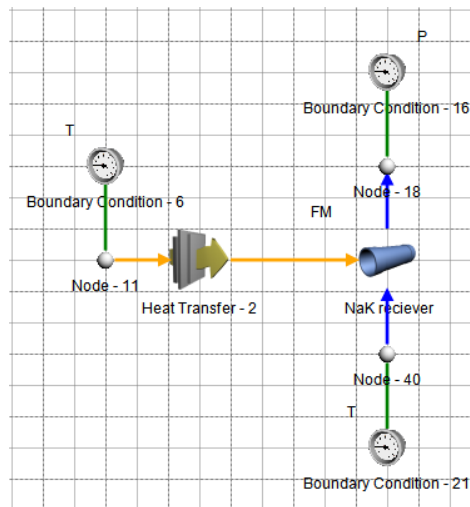


**Figure 74 – Receiver model**

### 8.3 Storage sizing

Using the heat transfer requirements determined in 8.1 (Table 21), the mass of the PCM and the volume of the storage tanks of the DSG concept is calculated and is presented in Table 26. The mass and volume of the PCM required are calculated using the properties for AlSi12 listed in Table 10, section 4.1.1. The volume of the



heat exchangers (section 8.4) and the dead volume (chapter 7) are added to the total volume of the tank. The dimensions of these tanks are presented in Table 27.

**Table 26 - Mass and volume required for 15h of thermal energy storage**

	$\dot{Q}_{out}$ (MW)	Energy storage (GJ)	Mass of PCM (Ton)	Volume (m <sup>3</sup> )	Total volume of imbedded heat exchangers (m <sup>3</sup> )	Dead volume	Total volume of the tank (m <sup>3</sup> )
Boiler	151.7	8191.80	14628.21	5714	72.13	561.25	6347.38
Super- heater	74.83	4040.82	7215.75	2819	47.66	278.07	3144.73
Re-heater	34.01	1836.54	3279.54	1281	32.42	127.40	1440.82
Total	260.54	14069.16	25123.50	9814	152.21	966.72	10932.93

**Table 27 - Size of the storage tanks**

	Boiler		Super- heater		Re-heater	
Tank diameter	36.61	m	28.23	m	18.06	m
Tank height	6	m	5	m	5	m

The height of the tanks is determined by the length of the heat exchangers, which is determined by the heat transfer requirements of both the NaK and the water/steam generators.

The ISG concept has one tank with one heat exchanger embedded into the PCM. The details of the storage tank are shown in Table 28.

**Table 28 - ISG storage sizing**

$\dot{Q}_{out}$ (MW)	260.54	MW
Energy storage (MJ)	14069.16	GJ
Mass	25123.50	Ton
Volume	9813.87	m <sup>3</sup>
Volume of heat exchanger	69.39	m <sup>3</sup>
Total volume of the tank with dead volume included	10842	m <sup>3</sup>
Height of tank	6	m
Diameter of tank	47.97	m

## 8.4 Heat exchanger sizing and modelling

Seven heat exchangers had to be sized:

- PCM – Water/steam heat exchangers for the DSG concept
  - Boiler
  - Super-heater
  - Re-heater
- NaK – PCM heat exchangers for the DSG concept
  - Boiler
  - Super-heater
  - Re-heater
- NaK – PCM heat exchangers for the ISG concept

To size the heat exchangers the extreme heat transfer parameters must be designed for and provision has to be made for process control for all intermediate conditions. As discussed in chapter 7, the solidified PCM around the heat transfer pipe adds thermal resistance to the heat exchanger and changes the heat transfer characteristics of the heat transfer surfaces. In other words, the heat exchangers have to be designed for both fully charged and nearly fully discharged conditions at nominal heat transfer rates.

As mentioned in chapter 7, the NaK and steam/water heat exchangers will be considered separately for simplification of the analysis, and this is merited by the fact that the critical design points of the steam generator in the DSG concept is during discharge only.

The basic variables of the heat exchangers in the steam generator sections include the length of the heat-transfer pipes; the number of tubes; and the tube size. A discretised model of these heat transfer surfaces is implemented in Flownex; and the model is then used to obtain the sizing of the heat transfer surfaces.

All of the heat exchanger sizing and heat transfer analysis was done in Flownex. The heat exchangers were first separately designed using the boundary conditions determined in sections 8.1 and 8.2 and was implemented as illustrated in Figure 75 below. The separate models were then incorporated into the larger Flownex model to evaluate the overall system performance parameters and to evaluate the effect on various operational conditions.

The instantaneous heat transfer model discussed in section 7.2 is used for the heat exchanger sizing. This is implemented into Flownex using a heat transfer element as shown in Figure 75. The heat transfer element can be set up to include radiation, conduction and convection of various geometries. The pipe element can be set up to determine the pipe geometry, number of parallel pipes, and problem discretization. Discretization is set up by setting the number of serial increments the pipe is divided into. The heat transfer model is also automatically discretized along the length of the pipe, and the same manner of discretization is possible with the conduction heat transfer models. The level of discretization can be set using a sensitivity analysis tool, which is used to automatically determine the

number of increments that ensures accurate results. The sensitivity analysis was set to allow a variation of no more than 0.1 % for pressure drop and heat transfer rates with decreasing increments.

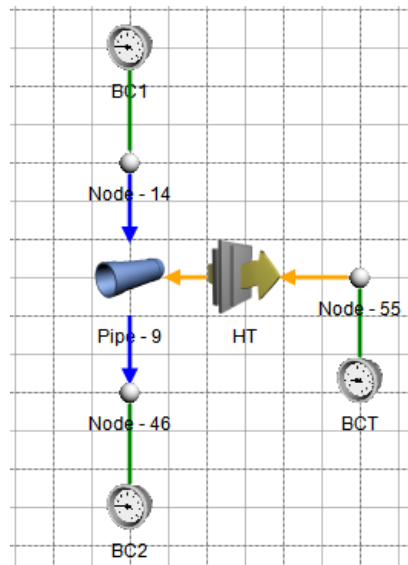


**Figure 75 – Heat transfer sizing**

The material properties of the various materials and HTFs that were incorporated into the model is summarised in Table 29, and is discussed in more detail in chapter 4.

**Table 29 – Summary of material property databases used in Flownex**

ISO 100 HTF OIL	Imported	Data imported from Table 14.
Water	Flownex library	Two phase data for all practical steam conditions according to IAPWS97 standard as discussed in section 4.3.
NaK	Imported	Data imported from functions discussed in section 4.2
AlSi12	Imported	Data imported from Table 10.
Steel	Flownex library	Material data available for 15 to 727 °C

The heat transfer coefficients on the inside of the heat transfer pipes were predicted using the correlations summarised in Table 30 below. More information on convective boiling heat transfer and liquid metal heat transfer is provided in chapter 6.

**Table 30 – Summary of correlations used in the Flownex simulations**

Single phase heat transfer for water	Gnielinski	(Gnielinski, 1975)
Two phase heat transfer for water	Steiner and Taborek	(Steiner, et al., 1992)
Pressure drop for single phase water	Darcey-Weisbach	(Darcy, 1857) (Weisbach, 1845)
Pressure drop for two phase water	Lockheart - Martenelli	(Lockheart, et al., 1949)
Heat transfer correlation for single phase liquid metal	Seban-Shimazaki	(Liquid metal engineering center, 1972)
Pressure drop for single phase liquid metal flow	Darcey-Weisbach	(Darcy, 1857) (Weisbach, 1845)

The onset of nucleate boiling, saturated boiling and Leidenfrost points are calculated automatically in Flownex (Flownex, 2011). The Leidenfrost point is where the liquid water separates from the heat transfer surface and forms a sustained vapour layer. In transition boiling, a linear extrapolation between the critical heat flux and the minimum heat flux points is used (Flownex, 2011); and for film boiling the Zuber correlation is used (Flownex, 2011).

On the PCM side of the heat transfer surfaces (the heat transfer pipes are embedded into the PCM), there is a moving boundary problem. As the storage system discharges, solidified PCM builds up around the heat transfer pipes, causing a variation in the heat transfer characteristics of the heat exchange surfaces.

The maximum diameter of the PCM build-up ( $d_o$ ), is calculated by dividing the volume of the PCM by the number of heat transfer pipes of one of the heat exchangers imbedded in it, and then calculating the distance between the sides of a hexagon of that volume. The critical design points for the heat exchanger are full charge, when the heat exchanger has no solidified PCM around it; and near full discharge where the solidification front meets the maximum diameter. In the Flownex model, the solidification front was calculated using an energy balance for transient simulations. A spread sheet was built into the Flownex model which automatically calculated the dependent variables such as  $d_o$ , storage volume and overall tank geometry based on heat exchanger geometry and storage requirements.

The heat exchangers were designed with the Flownex design tool. The Flownex design tool was set to yield the required heat transfer rates at near discharge conditions. Pressure drop was taken into account, but the pipe diameter and lengths were fixed for simplification. The diameters of all the steam pipes were set to a B36.19 1 inch S80 steam pipe for all the heat transfer surfaces. Steel was used for the heat water/steam heat exchangers, and stainless steel 306 was used for the NaK heat exchangers. The lengths of the pipes were found through a

number of design iterations that would satisfy both the NaK and the steam/water heat exchangers.

#### 8.4.1 Steam/water Heat exchangers for the DSG concept

For the plant to operate at steady conditions, the effect of the moving boundary needs to be counteracted. There is nothing that can be explicitly controlled about the energy source to the heat transfer surfaces (as in a gas-fired boiler), and the only feasible method of control is to manage the flow in the heat exchangers.

Flow boiling is a function of both convective boiling heat transfer and nucleate boiling heat transfer (Steiner, et al., 1992). To have a controllable steam generator, the convective-boiling heat transfer should be the controlling heat transfer mechanism in the heat exchanger, especially close to complete discharge.

For the boiler, the objective is to deliver saturated dry steam at the feedwater flow rate. Dry out of the boiler tubes is prevented by keeping the vapour fraction sufficiently low in the boiler itself, and this means that the flow rate through the boiler should be multiple times that of the feedwater. The process layout is shown in Figure 76 and the Flownex model of the boiler is presented in Figure 77. The model was used to determine the operational limits of the boiler circuit. The boiler circulation rate is adjusted to meet the heat transfer requirements throughout discharge. The upper and lower boiler circulation rate is presented in Table 32 along with heat transfer coefficients. The heat exchanger geometry for the boiler is presented in Table 31.

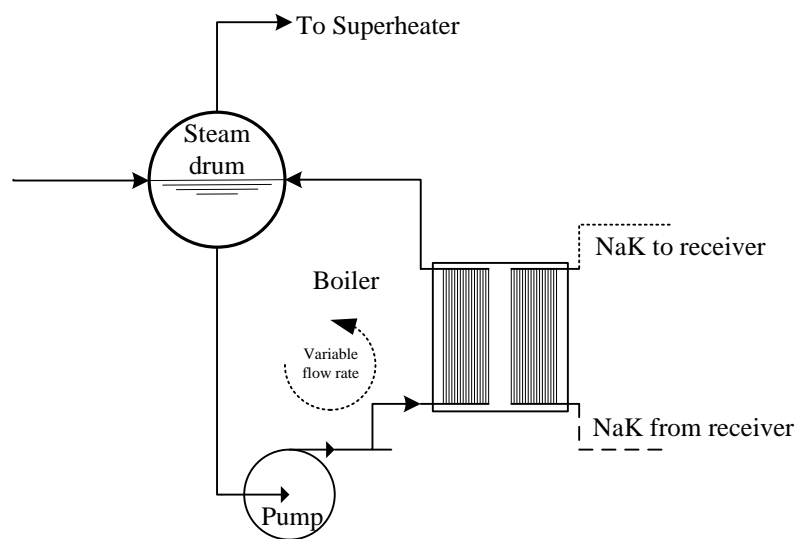


**Figure 76 - Boiler arrangement**

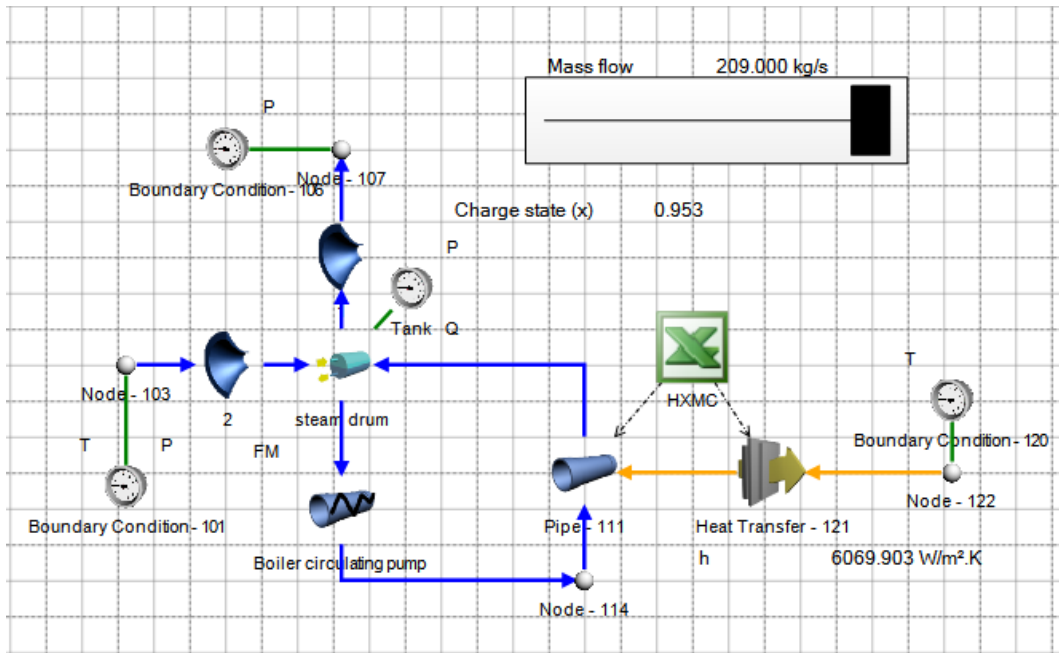


**Figure 77 – Boiler model**

Because the super-heater and re-heater operate as single phase systems, it is possible to bypass some of the steam past the re-heater or super-heater, and mix it with the superheated steam that went through the heat transfer pipes. This arrangement is illustrated in and Figure 78 and the generic Flownex model for both are presented in Figure 79. The heat exchangers for both the super-heater and re-heater were designed to deliver superheated steam with all of the steam running through the heat exchanger at the end of its charge and with steam diverted past the heat exchangers at higher charge states. The bypass rates and the average heat transfer coefficients are presented in Table 32. The heat exchanger geometry is presented in Table 31.

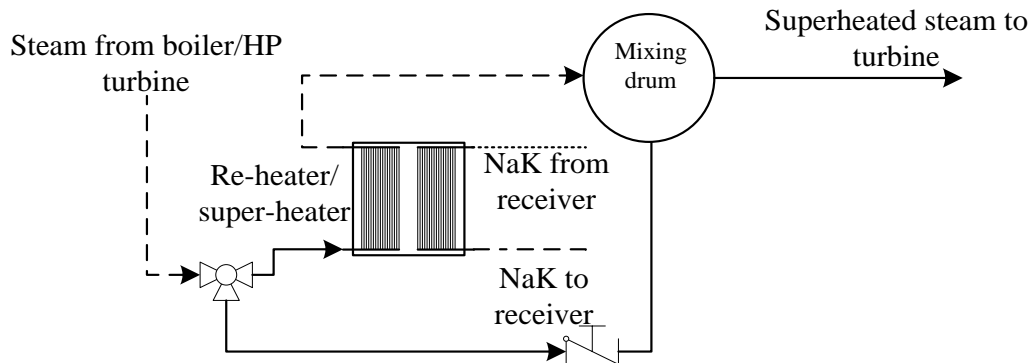


**Figure 78 - Re-heater and super-heater arrangement**

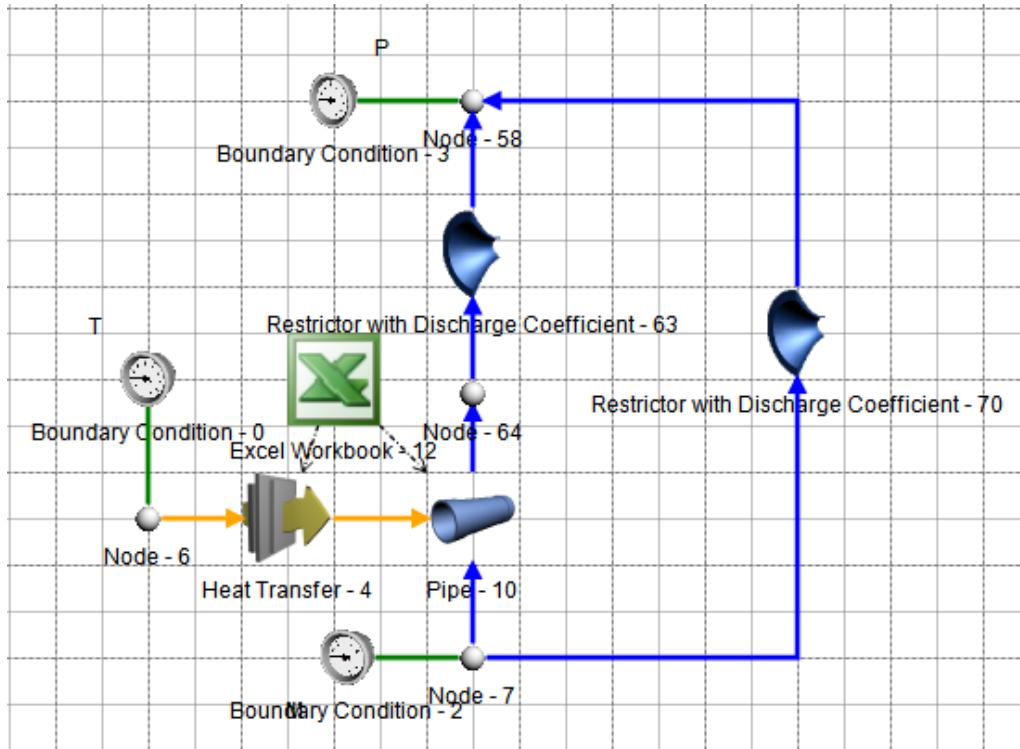


**Figure 79 – Re-heater and super-heater model**

**Table 31 – Steam water heat exchanger geometry**

	Boiler	Super-heater	Re-heater
Number of steam pipes	300	820	1000
Diameter of steam pipes	33.40 mm	33.40 mm	33.40 mm
Wall thickness	4.55 mm	4.55 mm	4.55 mm
Passes	Single	Double	Double
Length	6 m	5 m	5 m
Material	MS	MS	MS
Volume of heat exchanger	6.30 m <sup>3</sup>	14.36 m <sup>3</sup>	17.52 m <sup>3</sup>
Maximum PCM diameter, d <sub>o</sub>	2.01 m	0.66 m	0.38 m

**Table 32 – Steam/water heat exchanger control strategy**

		Full charge		Low charge	
Boiler	Boiler circulation rate	209.00	kg/s	213.00	kg/s
	Heat transfer	151.70	MW	151.70	MW
	Average convective boiling heat transfer coefficient	6069.9	W/m <sup>2</sup> .K	6937.49	W/m <sup>2</sup> .K
	$d_m$	0	m	2.01	m
Super-heater	Super-heater bypass	2.77	%	0.33	%
	Heat transfer	74.83	MW	74.83	MW
	Average convective heat transfer coefficient	2459.23	W/m <sup>2</sup> .K	2557.21	W/m <sup>2</sup> .K
	$d_m$	0	m	0.66	m
Re-heater	Re-heater bypass	9.01	%	8.22	%
	Heat transfer	34.01	MW	34.01	MW
	Average convective heat transfer coefficient	1239.27	W/m <sup>2</sup> .K	1246.03	W/m <sup>2</sup> .K
	$d_m$	0	m	0.38	m

#### 8.4.2 NaK heat exchangers for the DSG concept

The isothermal nature of the storage unit decouples the heat transfer of the steam heat exchangers from that of the NaK heat exchangers; allowing the NaK loop to be considered separately. In the DSG concept, the NaK heat exchangers have to be designed to transfer all the thermal energy from the receivers to the storage units during peak conditions. In the DSG concept the NaK heat exchangers are divided between the boiler, super-heater and re-heater. The NaK flow is diverted according to the ratios of the energy removed by the steam generator. The heat transfer requirements for each heat exchanger are shown in Table 33.

**Table 33 – NaK flow distribution**

	$\dot{Q}_{out}$ (MW)	Ratio	$\dot{Q}_{in}$ (MW)	Inlet temperature (°C)	NaK mass flow (kg/s)	NaK volume flow (m <sup>3</sup> /s)
Boiler	151.70	0.58	414.43	692.3	4396.00	6.04
Super-heater	74.83	0.29	204.43	692.3	2168.44	2.98
Re-heater	34.01	0.13	92.91	692.3	985.55	1.35



These requirements were used as boundary conditions in Flownex to size the heat exchanger. The critical design points are at maximum heat transfer rates, and close to full charge, where the layer of molten PCM is the largest. This design point was used in Flownex to size the heat exchangers. Again, for simplification, the heat exchanger pipes were kept to 1 inch S80, but are made of stainless steel 306. The length of the pipes is fixed to be the same as the length of the water/steam heat exchanger pipes.

**Table 34 – NaK heat exchanger geometry for the DSG concept**

	Boiler	Super-heater	Re-heater
Number of steam pipes	3130	1900	850
Diameter of steam pipes	33.40 mm	33.40 mm	33.40 mm
Wall thickness	4.55 mm	4.55 mm	4.55 mm
Passes	Single	Single	Single
Length	6 m	5 m	5 m
Material	SS	SS	SS
Pressure drop during peak flow	40.32 kPa	22.36 kPa	22.97 kPa
Maximum efficiency	0.93	0.93	0.93
Volume of heat exchanger	65.81 m <sup>3</sup>	33.29 m <sup>3</sup>	14.89 m <sup>3</sup>

#### 8.4.3 Heat exchangers for the ISG concept

The ISG has one NaK-PCM heat exchanger for both charging and discharging as illustrated in Figure 80. During charging all the NaK is directed through the receivers and then through the storage bank. From the storage bank the NaK will flow to the steam generator system. A liquid metal steam generator system is an extremely specialized piece of equipment and will not be dealt with in detail, as it falls outside the scope of this project. The steam generator was simulated as a pipe with a pre-set heat loss equal to the heat transfer requirements for the power cycle.

As shown in Figure 70 (section 8.2), the peak heat transfer rate from the receiver is 711.8 MW, and the heat transfer to the steam cycle is constant at 260.54 MW. Therefore, during charging the heat exchanger has to transfer 451.26 MW to the PCM, and during discharge it has to transfer 260.54 MW from the PCM to the NAK HTF.

The same receiver model used in the DSG concept was implemented in the ISG loop, and the peak receiver outlet temperature was kept at 693.45 °C for consistency. The heat exchanger length was chosen as 6m and again S80 1 inch stainless steel pipe was chosen for the heat exchanger.

The Flownex model in Figure 81 was used to size the heat exchanger and determine operational parameters.

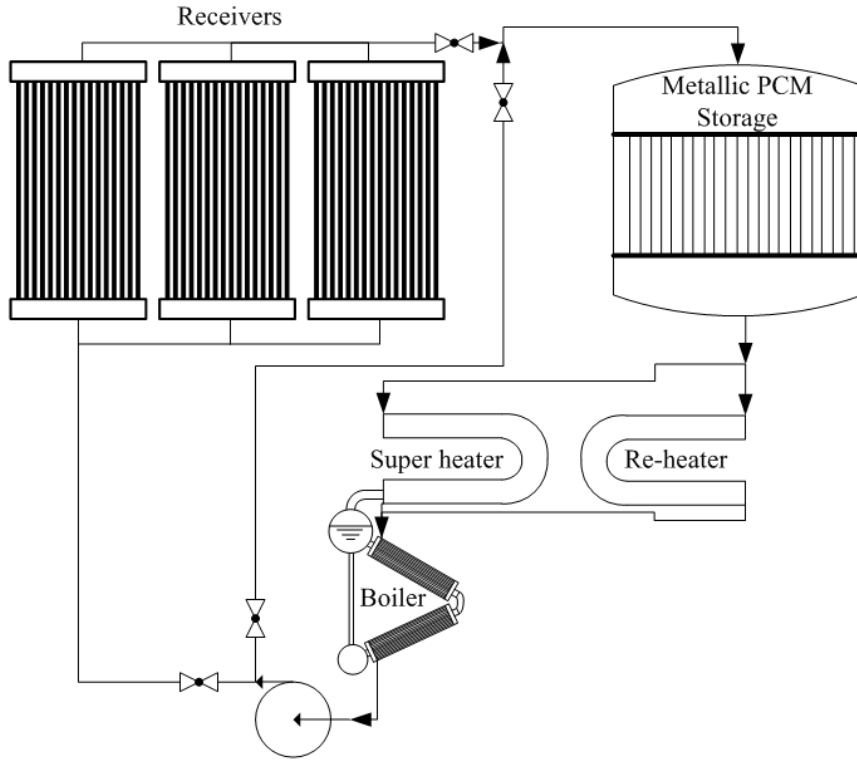


**Figure 80 – ISG heat transfer and storage**

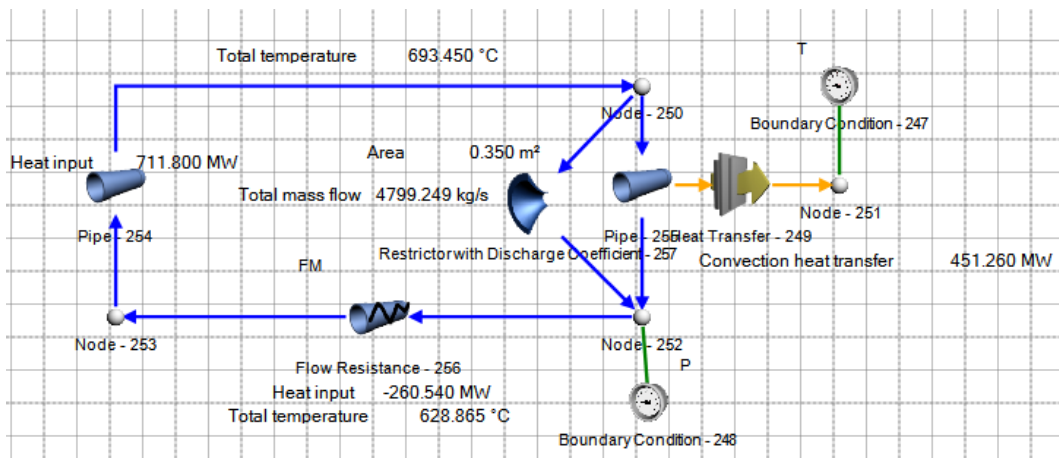


**Figure 81 - Primary cooling loop for the ISG concept**

The critical design point for the heat exchanger is charging conditions at near full charge and these conditions were used to get the design geometry presented in Table 35. The control strategies that would have to employed to control the primary cooling loop in the ISG system would be very complicated, and the design parameters of the steam generator must be known. The Flownex model can be used for these studies.

**Table 35 – NaK heat exchanger geometry, storage tank dimensions and operational parameters**

Heat exchanger geometry	
Number of steam pipes	3300
Diameter of steam pipes	33.40 mm
Wall thickness	4.55 mm
Passes	1
Length	6 m
Material	SS
Volume	112.70 m <sup>3</sup>
Tank geometry	
Height	6 m
Diameter	47.97 m
Volume	112.70 m <sup>3</sup>
d <sub>o</sub>	0.8 m
Operational parameters: Charging (Full charge)	
d <sub>m</sub>	0.8 m
NaK mass flow rate through HX	7550 kg/s
Pressure drop during peak conditions	107.51 kPa
Bypass:	0 %
Heat transfer coefficient	1405.20 kW/m <sup>2</sup> K

## 8.5 Overall model

From section 8.1 to section 8.4 all major components of the power generating cycle were designed and simulated for both the DSG and ISG concepts in separate design cases using the boundary conditions of the power cycle determined in section 8.1. The separate components could then be integrated into one single model to demonstrate the ability of Flownex to simulate an entire CSP plant.

All the components were connected together, and the model ran at nominal conditions. The entire model is centrally controlled using an Excel spreadsheet and PID control models. In this model it was assumed that the charge state and diameter of the solidified PCM is directly correlated. The charge state of the storage units and the solidification moving boundary position are calculated as shown in Figure 82.

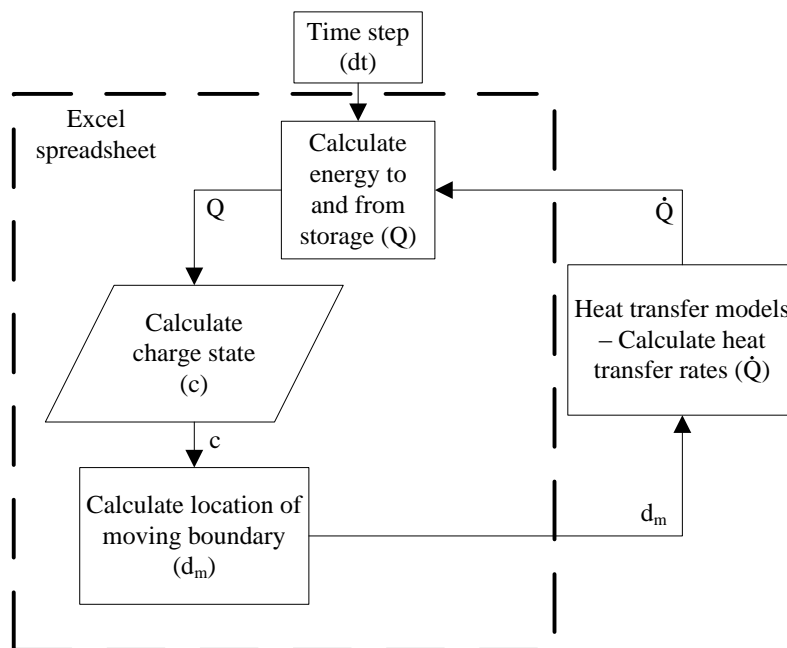


**Figure 82 – Calculation of charge state and moving boundary position**

The circulation rate of the boiler and the bypass of the re-heater and super-heater is controlled using the built in PID controller functions built into Flownex. The model could be run at nominal conditions, providing a platform for future parametric studies.

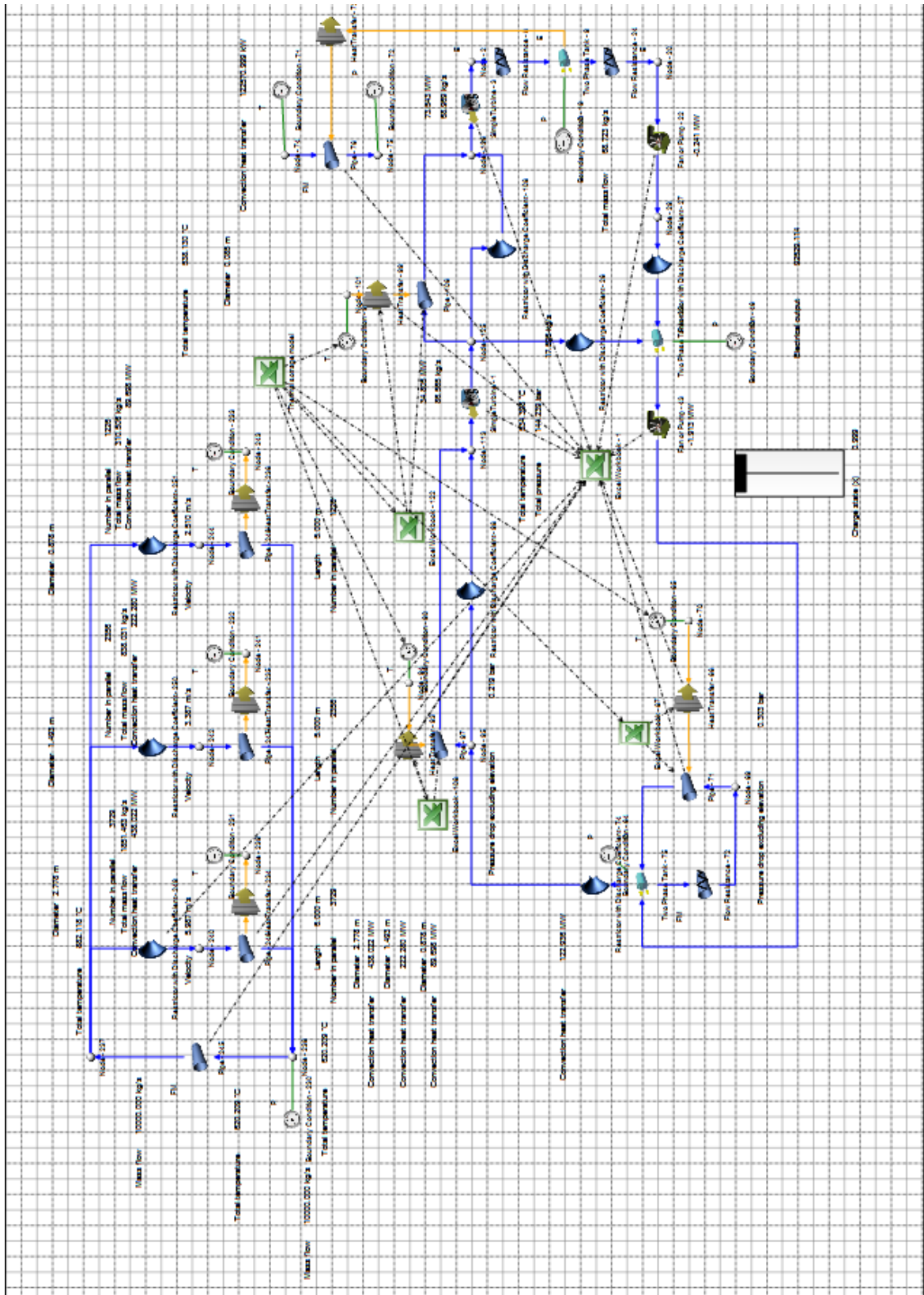


Figure 83 – Screenshot of the overall Flownex model for the DSG concept

A similar model was made for the ISG concept and is presented in Figure 84. It was possible to achieve nominal power generation values with varying charge rates and thermal input from the receiver.

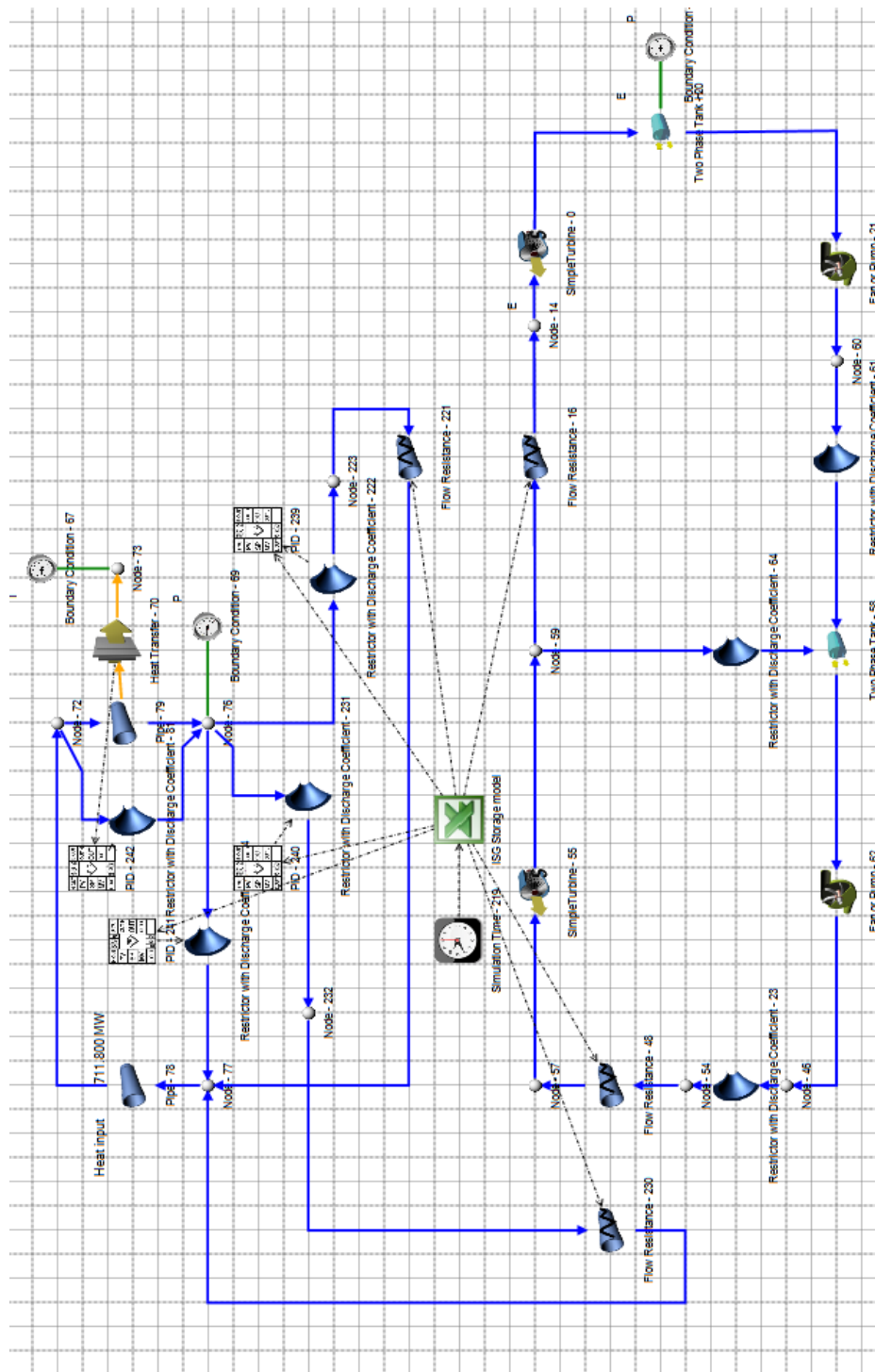


Figure 84 – Screenshot of the overall Flownex model for the ISG concept

## 8.6 Conclusion and practical considerations

In chapter 7 it was established that quasi-steady assumptions is valid for metallic PCMs such as AlSi12. To demonstrate how a metallic PCM can be used in a power plant in a TES system, a complete power plant and TES was designed and modelled in Flownex using quasi-steady heat transfer models. AlSi12 was the only PCM used. The design process yielded practical heat exchanger geometries, tank sizes and shed light on some issues concerning the use of PCMs.

### 8.6.1 Feasibility of the DSG concept

The reason the DSG concept was proposed is the uncertainty of the economic feasibility of a NaK steam generator. The DSG concept physically separates NaK and water from each other by using the PCM as a buffer. Unfortunately this adds a lot of complexity to the system.

Firstly, there is the complexity of the geometry. The two heat exchangers would have to be imbedded into the same mass of PCM, making the headers especially complicated. Additionally, the header pipes containing NaK and those containing steam would have to be in close proximity, which is also a safety risk. Add this to the unproven nature of such an assembly; this may be a risk greater than that of a NaK heat exchanger.

Since the heat source (charged PCM) cannot be controlled, the ability to run the plant at part load is limited as dry out of the boiler must be avoided. The introduction of cold HTFs (water) into a hot boiler causes boiler shock, which may cause the failure of the steel pipes of the heat exchanger (Heselton, 2005). This is unavoidable in the DSG concept if the storage system is not completely discharged before shutdown, making intermittent operation of the DSG concept impossible. Therefore the DSG concept is unfeasible for intermittent and part load operation.

The ISG concept does not have these issues, since NaK and other metallic HTFs can be kept in the heat exchangers during down time even at full charge, and the steam generation is controlled by the flow rate to the steam generator. Therefore it can be argued that the ISG concept is more suitable for CSP applications. The specific application of this concept is further discussed in chapter 10.

### 8.6.2 Thermodynamic considerations and cascaded thermal energy storage.

Entropy generation minimization is a technique to optimise a thermodynamic process by analysing irreversibilities in the system. This has been established as a research field in a book called “Entropy generation through heat and fluid flow” (Bejan, 1982). The study of entropy minimization requires the entire system to be analysed, and a model as presented in this chapter is handy in understanding these irreversibilities. Unfortunately the entropy minimization of an entire plant using PCMs is an entire study on its own, but certain principles should be taken note of.

Considering thermodynamic and heat transfer irreversibilities and the use of a single PCM as in this study highlights a core thermodynamic issue with PCMs. This is especially apparent in the boiler, where there is a big temperature gap



between the melting point of AlSi12 (577°C) and the boiling point of water in the boiler (336.67°C) This means that the energy is stored at a substantially higher temperature or “quality” than is needed.

Entropy generation with latent heat can be described by equation (8.8):

$$\Delta s = \frac{\dot{Q}}{T_m} \quad (8.8)$$

And entropy generation through sensible heat transfer can be expressed by equation (8.9):

$$\Delta s = C_{ave} \ln \frac{T_2}{T_1} \quad (8.9)$$

Where  $C_{ave}$  is the average specific heat of the working fluid,  $T_2$  is the final temperature, and  $T_1$  is the starting temperature.

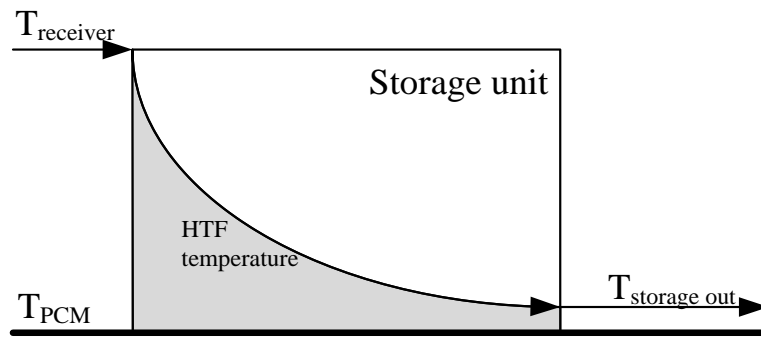
If the sum of the total entropy in the heat transfer system is taken, the entropy gain in one heat transfer fluid should ideally be the same as the entropy loss in the other heat transfer fluid or medium for the process to be reversible.

Bejan (1985) presents an analysis that assumes that the power generating cycle is an idealized Carnot cycle. The analysis was kept very generic, but the following general conclusions could be made:

- The larger the temperature difference is in heat exchange, the larger the entropy generation, and can be directly correlated.
- Multiple PCMs can be arranged in a cascaded fashion to minimize entropy generation.
- An optimal receiver temperature can be calculated based on entropy minimization.

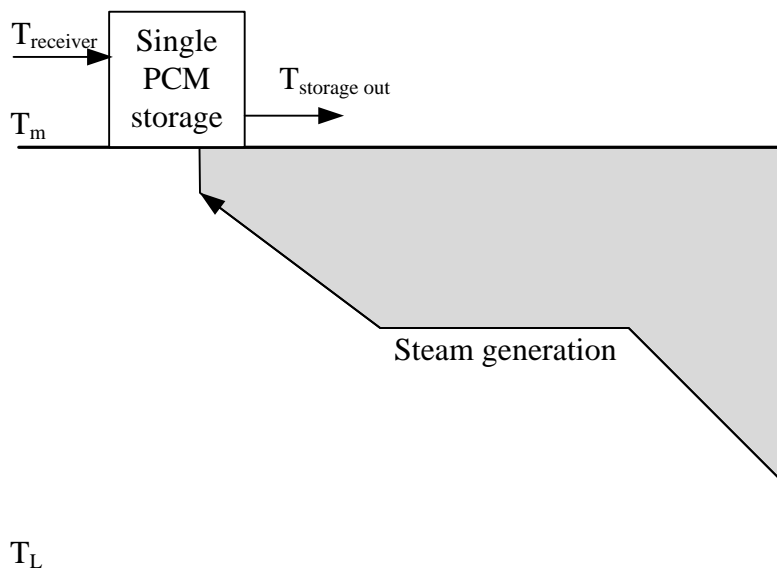
For latent heat TES, there are two heat transfer processes that contribute to entropy generation: Heat transfer between the primary cooling loop and the PCM, and heat transfer from the PCM to the working fluid of the power generation cycle. The entropy generation between the primary HTF and the PCM is illustrated in Figure 85. The entropy generation between the PCM and working fluid of the power generation cycle of various PCM storage schemes is presented in Figure 86, Figure 87 and Figure 88. The grey areas indicate the temperature gap through which heat transfer takes place; a larger temperature gap means that energy is supplied at a temperature higher than needed.





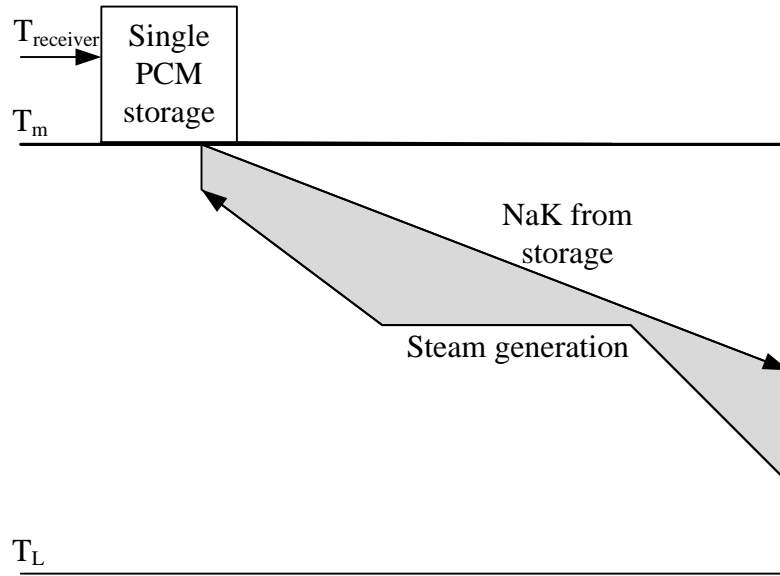
**Figure 85 - Entropy generation between the primary cooling loop and the PCM**

Figure 86 shows the single PCM DSG concept analysed in this chapter, and it is apparent that the heat transfer takes place across a large temperature gap between the boiler and the melting point of the PCM.



**Figure 86 – Single PCM storage in the DSG concept**

This situation is somewhat alleviated in the single PCM, ISG concept shown in Figure 87.



**Figure 87 – Single PCM storage in the ISG concept**

Multiple PCMs can also be used in the DSG concept as shown in Figure 88. This shows how the use of multiple PCMs can be used in a cascaded fashion to better match the steam generation process. It must also be noted that the range of metallic PCMs is limited to the availability of suitable alloys.

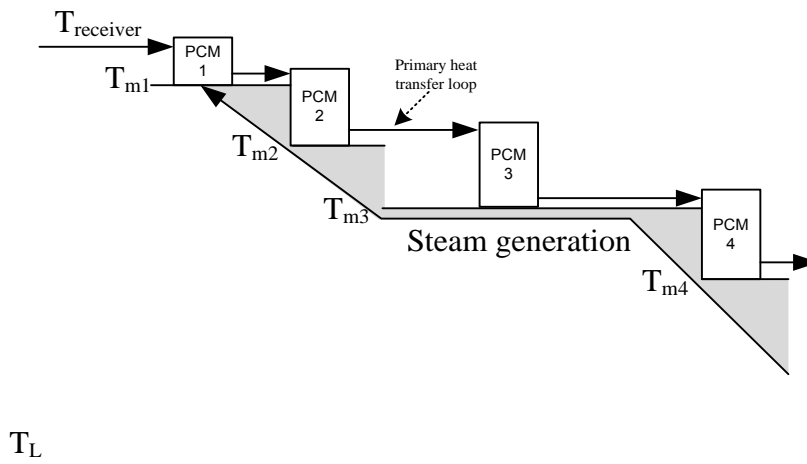


**Figure 88 – Cascaded PCMs for the DSG concept**

## 9 HIGH TEMPERATURE CORROSION OF ALSI12

During testing it was discovered that liquid aluminium alloys are extremely corrosive to most metals and metal oxides (Deqing, 2008). This came as a surprise since high temperature aluminium corrosion was never mentioned by other authors who worked on AlSi12 as a storage material (He, et al., 2001) (Li, et al., 2011) (Wang, et al., 2004). The mechanism of corrosion is diffusion of the other metal into the molten aluminium alloy (Bouayad, et al., 2003). An electron-micrograph of the interface between iron and molten aluminium is presented in Figure 89. This was the result of a sample of polished iron submerged into molten aluminium at 800 °C for 5 minutes. It is clear that the aluminium and the iron mix to form an alloy on the boundary interface, and as this process continues, the aluminium will completely dissolve the iron. The Al-Fe eutectic system is shown in Figure 90.

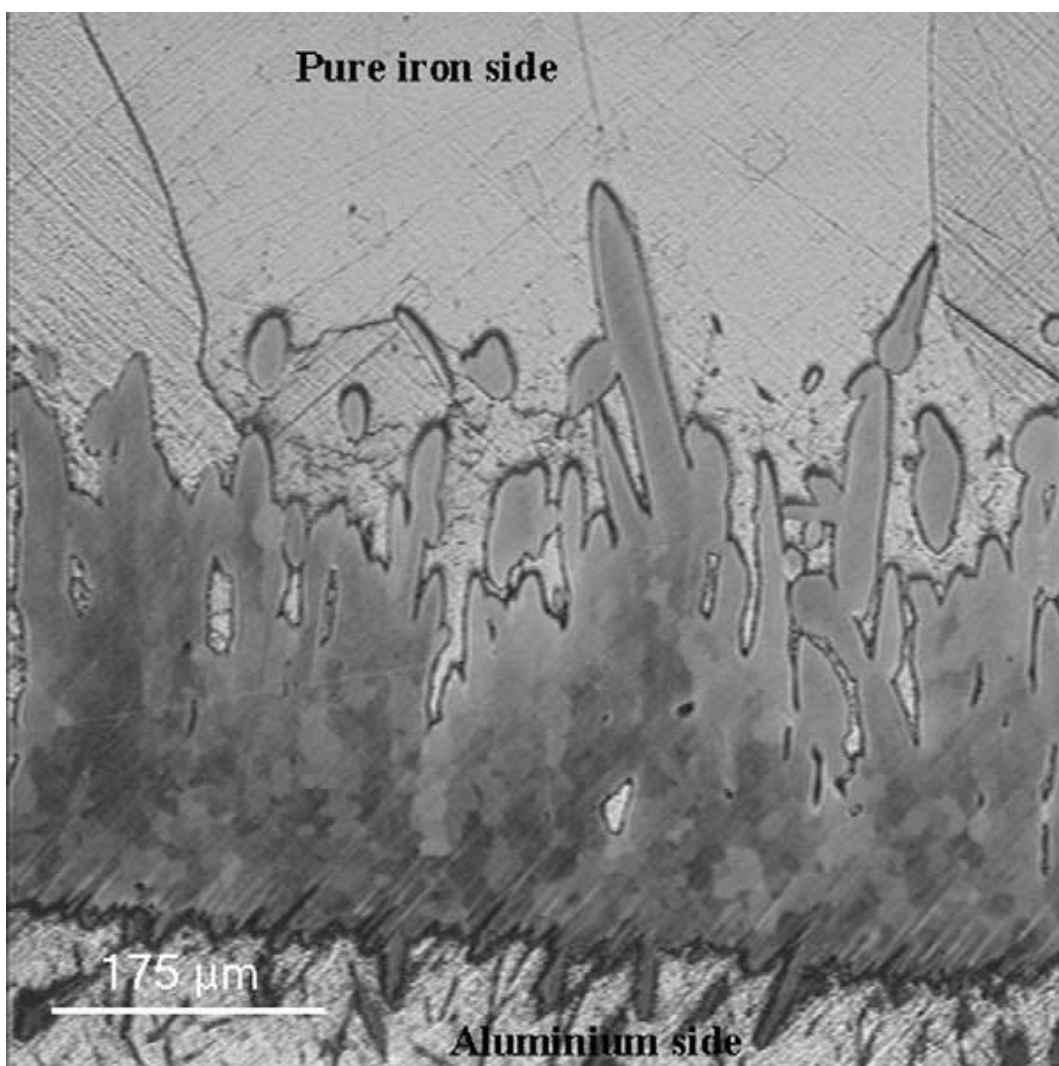


**Figure 89 - Microstructure of inter-metallic zone (Bouayad, et al., 2003)**

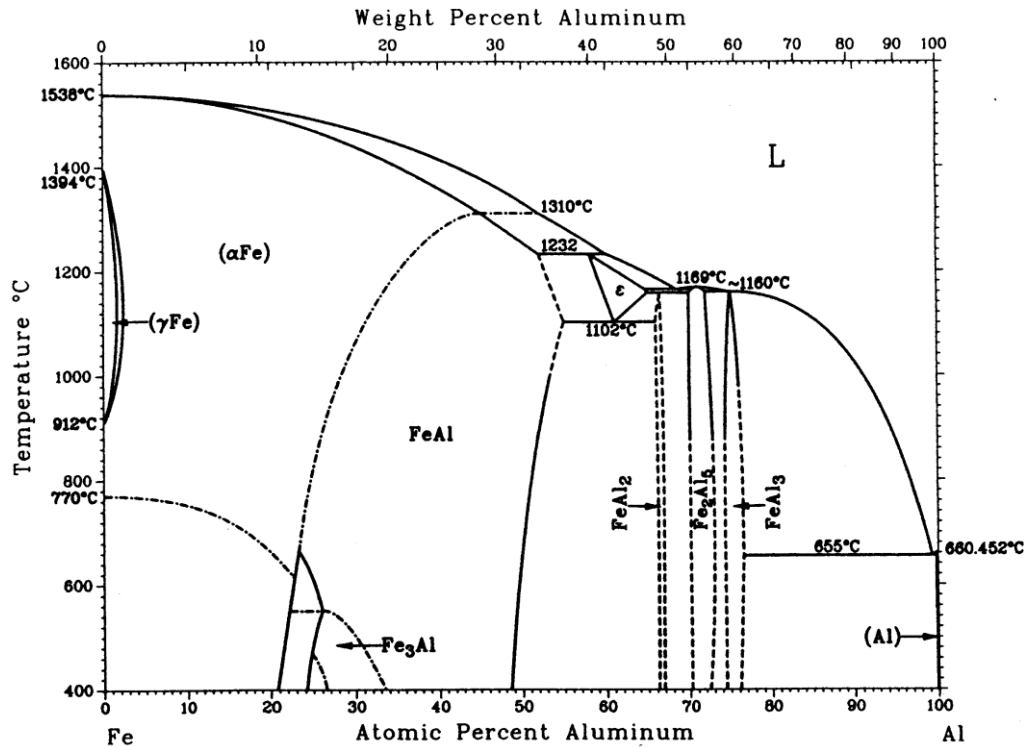


**Figure 90 - Aluminium-iron eutectic system**

All corrosion testing that could be found in literature was performed above 700 °C<sup>9</sup>, and the kinetics of the corrosive process has been measured up to 1000 °C (Bouayad, et al., 2003). The speed of the corrosion process is proportional to temperature and is influenced by the exact composition of the alloys. Unfortunately no corrosion tests could be found below 700 °C. The lowest temperature on the Al-Fe eutectic system is 660.4 °C, but the effect of a lower melting point Al-Si eutectic system in the presence of iron could not be found. Regardless, the risk of a rupturing storage vessel merited an immediate halt to the testing in the steel cylinder which has been used in this project.

In practice there are several corrosion resistant materials that have been researched. Ceramic materials like; aluminosilicate, refractories, AlN, Al<sub>2</sub>O<sub>3</sub>, Si<sub>3</sub>N<sub>4</sub>, TiB<sub>2</sub> and sialons (Yan, 2001) (Jensen, et al., 2008). Unfortunately ceramics are brittle and expensive, and are not well suited for a containment vessel or a heat exchanger. Boronized carbon steel showed fair resistance to corrosion, but it is not corrosion proof, and therefore it is not well suited for long term hardware (Tsipas, et al., 1998). The only feasible corrosion protection that could be found was the surface treatment of steel by first hot dipping the steel into molten aluminium at elevated temperatures to form a layer of bonded aluminium-iron alloy, and then to oxidize the surface of the aluminium (Deqing, et al., 2003). Figure 91 shows an

<sup>9</sup> (Deqing, 2008) (Bouayad, et al., 2003) (Deqing, et al., 2003)

electron micrograph of surface treated steel that has been exposed to molten aluminium at 750 °C for 250 hours. It showed excellent corrosion resistance. Unfortunately this was only a limited experimental run, and further testing is needed regarding the stability and the toughness of the Al<sub>2</sub>O<sub>3</sub> layer that is giving the corrosion resistance.

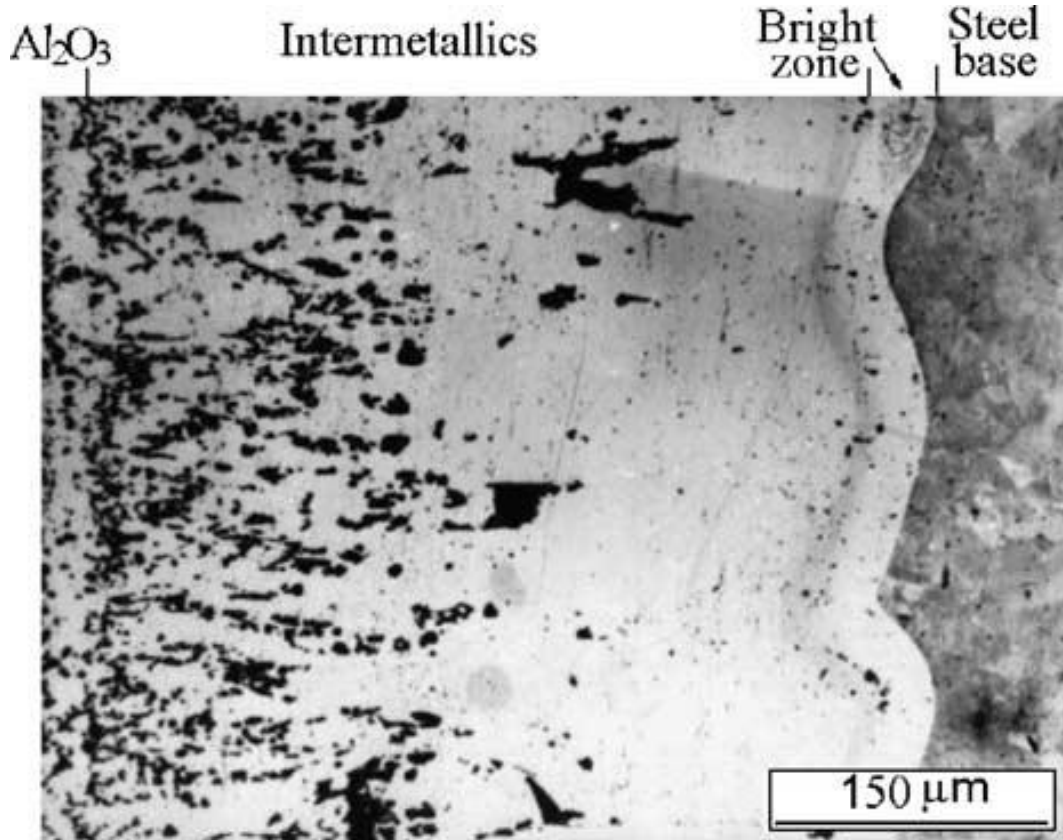


**Figure 91 - Electron-micrograph of a surface treated steel sample after corrosion testing (Deqing, et al., 2003)**

Further research is required into the corrosive effects of AlSi12 and other PCMs on ferrous alloys and methods to provide corrosion protection to these alloys. The aluminized steel with the oxide layer seems to be a promising technique, but requires further development and validation for long term use in a large storage system.

## 10 TECHNO-ECONOMIC FEASIBILITY

The economic feasibility of the storage system is dependent on:

- Cost of storage materials
- Cost of the containment vessel
- Cost implications in the rest of the system:
  - Savings on heliostats
  - Cost of the power block

Two-tank molten salt storage is used as a benchmark for cost, as this is the current state of the art. According to a leading salt producer, SQM, eutectic nitrate salt mixture (60 % NaNO<sub>3</sub> and 40 % KNO<sub>3</sub>), delivered to a South African port costs 830US\$ per metric ton (SQM, 2013). The material cost of salt storage is calculated and presented in Table 36 as 7.57 US\$/kWh. Additionally, the cost of a two tank molten salt storage system is estimated as 22US\$/kWh on top of material costs (Kolb, et al., 2011).

**Table 36 – Material cost of eutectic nitrate salt**

Cold storage point	240 °C
Maximum operating temperature	565 °C
Specific heat capacity	1.21 kJ/kg.K
Cost	830 US\$/ton
Storage capacity	109.59 kWh/ton
Storage cost	7.57 US\$/kWh

No indication of the cost of liquid metal heat transfer equipment, pumps and steam generators could be found. Looking at liquid metal technology, austenitic stainless steels offers adequate corrosion resistance to alkali metals, where corrosion protection for other liquid metals such as lead bismuth eutectic is more complex (Liquid metal engineering center, 1972).

The ISG concept requires a water-NaK steam generator. This technology has been proven in the nuclear industry, and has been implemented in some power plants since 1980, like the BN-600 reactor in Zerechny Sverdlovsk Oblast, Russia. The BN-600 reactor has a good safety record, and larger reactors are under construction (World Nuclear News, 2012). The heat transfer equipment, steam generators, corrosion protection and operation in a solar power plant would be very similar to that of a nuclear power plant, but with less risk because there is no nuclear power. Close examination of NaK and Sodium design and handling protocols would suggest that hardware would not be more complicated than molten salt systems, even though a higher degree of safety is required (Liquid metal engineering center, 1972). However, it is not possible to extrapolate cost data for liquid metal cooling from the nuclear industry to CSP, since the nuclear systems have much more stringent safety requirements, and liquid metal cooling would have to be specifically designed for CSP. In this cost analysis it is assumed that the use of NaK would not directly impact the LCOE.

The corrosion protection discussed in chapter 9 does not appear to add significant additional costs to a CSP system as the corrosion protection only involves the hot dipping of the heat exchanger pipes and the oxidation of the surface. It is assumed that the containment structures would cost the same as those used in molten salt storage. Consequently 22 US\$/kWh will be added to the cost of the PCM to serve as a comparison of overall storage system cost. This is a crude assumption, but can only be improved if a more detailed study is done.

The material price of AlSi12 is 22.5 R/kg (Zimalco, 2013). At an exchange rate of 11.01 US\$/R, this relates to 2.04 US\$/kg. The cost of the other alloys had to be calculated based on the prices of the constituents of the alloys which is summarised in Table 37.

**Table 37 – Constituent metal prices**

	Cost (US\$/ton)	Source
Aluminium	1671	(InvestmentMine, 2014)
Antimony	9200	(InvestmentMine, 2014)
Calcium	2950	(Alibaba, 2014)
Copper	7174	(InvestmentMine, 2014)
Magnesium	2850	(InvestmentMine, 2014)
Silicon	2100	(Alibaba, 2014)

The cost of a number of metallic PCMs from Table 46 (Appendix A) is presented in Table 38 below. Copper alloys were ignored because of the high cost and low heat of fusion of these copper alloys. The material cost of these alloys has been plotted against temperature in Figure 92.

**Table 38 – Material cost of a select number of metallic PCMs**

	°C	kJ/kg	US\$/ton	US\$/kWh
Si56Mg44	946	757	2430.00	11.56
Si49Mg30Ca21	865	305	2503.50	29.55
Mg47Si38Zn15	800	314	2438.40	27.96
Mg84Ca16	790	272	2866.00	37.93
Al	660	321	1671.00	19.28
Al88Si12	577	560	2043.60	13.14
Mg34.6Al65.4	497	285	2078.93	26.26
Al86.4Si9.4Sb4.2	497	471	2027.54	15.50
Al59Mg35Zn6	443	310	2103.75	24.43
Zn96Al4	381	138	1992.60	51.98
Mg46.3Zn53.7	340	185	2396.77	46.64



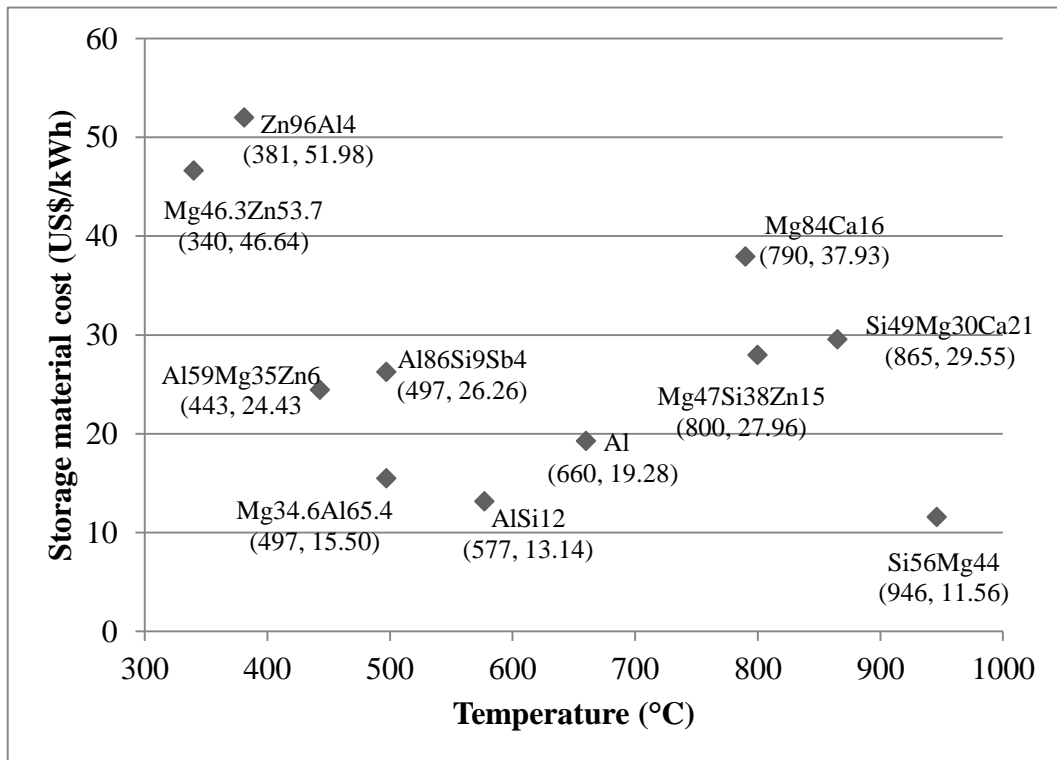


**Figure 92 – Material cost of metallic PCMs versus melting temperature.**

Table 39 shows the estimated cost of storage when tanks and heat exchangers are added to the material cost.

**Table 39 – Overall cost estimates of metallic PCMs**

	°C	Estimated overall system cost (US\$/kWh)	% Increase in cost
Nitrate salt	565	30	0.00
Si56Mg44	946	33.99	13.30
Al88Si12	577	35.57	18.57
Al86.4Si9.4Sb4.2	497	37.93	26.43
Al	660	42.58	41.93
Al159Mg35Zn6	443	46.86	56.20
Mg34.6Al65.4	497	48.69	62.30
Mg47Si38Zn15	800	50.39	67.97
Si49Mg30Ca21	865	51.98	73.27
Mg84Ca16	790	60.36	101.20
Mg46.3Zn53.7	340	69.07	130.23
Zn96Al4	381	74.41	148.03



All of the metallic PCMs considered here are more expensive than solar salt in its current form, though some of them are only marginally more expensive. The impact that metallic PCMs have on the entire CSP plant needs to be considered in terms of LCOE reduction. To make a reasonable estimation, the current cost breakdown as outlined by Kolb, et al. (2011) (Table 1, p4) will be used as a basis for analysis.

Another aspect that needs consideration is the fact that these metallic PCMs are only some of the eutectic systems that have been investigated, and it is very possible that there may be many more alloys that are even better suited as PCMs. This is discussed in section 11.3. Generally the aluminium, silicon, magnesium and zinc alloys seem to offer great prospective PCMs because of their low cost, high thermal conductivity and high heat of fusion. It is reasonable to expect that a range of new metallic PCMs will be Aluminium-Silicon based alloys. Therefore the estimated total price of AlSi12 storage will be used in the cost analysis (33.99 US\$/kWh).

As metallic PCMs are generally more expensive than salts, it is only merited with the use of a supercritical or an ultra-supercritical steam cycles. Live steam conditions of 27MPa/600 °C and a 60MPa/620 °C re-heat are normal for supercritical steam cycles (Cziesla, et al., 2009). The typical thermal efficiency of such a supercritical steam cycle can be between 45 % and 49 % depending on the cooling system used. Assuming a 45 % thermal efficiency for a supercritical power block (Cziesla, et al., 2009), the cost savings on the heliostat field and storage system can be calculated. A 45 % thermal efficiency is a 7 % improvement on the 38 % thermal efficiency of current subcritical power cycles, this is a 15.56 % reduction in energy consumption. This means 15.56 % less heliostats and storage material. The installation cost of a modern supercritical steam cycle is 2 % more expensive than a subcritical steam cycle (Bugge, et al., 2006).

The reduction of LCOE was based on the projected 2013 cost breakdown of power tower technology by Power tower technology roadmap and cost reduction plan (Kolb, et al., 2011). They calculated a LCOE of 16.5 US\$ cents per kWh for 2013 on a 100 MW<sub>e</sub> plant with 9 hours of storage. The cost breakdown was presented in Table 1, p4. In Table 40 below, the effect of such an increase of thermal efficiency on LCOE is shown, and it shows that a 2.96 % cost reduction is possible with the use of a supercritical steam cycle and metallic PCMs (Kolb, et al., 2011).

**Table 40 – Predicted reduction in LCOE**

Cost breakdown of LCOE (All costs)	Current cost breakdown	Breakdown of 2013 LCOE US\$c	Effect of storage cost increase	Effect of supercritical steam cycle	Breakdown of cost with metal PCM storage US\$c
Heliostats:	22.10 %	3.65	0.00 %	-15.56 %	3.08
Indirect costs:	20.80 %	3.43	0.00 %	0.00 %	3.43
Operations and maintenance:	12.10 %	2.00	0.00 %	0.00 %	2.00
Power plant:	12.10 %	2.00	0.00 %	2.00 %	2.04
Receiver:	10.10 %	1.67	0.00 %	0.00 %	1.67
Tax:	8.10 %	1.34	0.00 %	0.00 %	1.34
Storage:	7.40 %	1.22	18.75 %	-15.56 %	1.26
Balance of plant:	4.00 %	0.66	0.00 %	0.00 %	0.66
Site cost:	2.00 %	0.33	0.00 %	0.00 %	0.33
Tower:	1.30 %	0.21	0.00 %	0.00 %	0.21
Total:		<u>16.51</u>			<u>16.02</u>
Effect on LCOE:					<b>-2.96 %</b>

Consequently, the use of metallic phase change materials offers a prospective cost reduction. Unfortunately the 2.96 % that has been calculated is a crude estimation at best, but it shows that the use of metallic phase change materials does enable the use of a supercritical steam cycle, which in itself is the only aspect that reduces LCOE.

An aspect that needs to be considered is the role of a CSP plant. In the current environment, CSP has most value to add as a peaking solution. Unfortunately subcritical steam cycles offer greater flexibility when it comes to transient conditions than supercritical steam cycles (Heselton, 2005). So it can be argued that metallic PCM storage with supercritical steam power cycles will most probably only be beneficial if the CSP plant is designed to deliver base load power. For base load power to be feasible, the DOE target of 6 US\$ cents per kWh must be achieved. According to the Power Tower roadmap and cost reduction plan (Kolb, et al., 2011) this would require extensive cost reduction on all aspects of the plant, including storage and heat transfer equipment. This might make metallic PCMs and liquid metal heat transfer unfeasible for the whole plant, since it is more expensive than molten nitrate salt storage.

The use of two tank molten nitrate salt storage in conjunction with cascaded PCMs could offer a thermal energy storage solution that offers high temperature storage, while minimizing entropy generation. Such an arrangement is illustrated in Figure 93, with a T-s diagram in Figure 94.

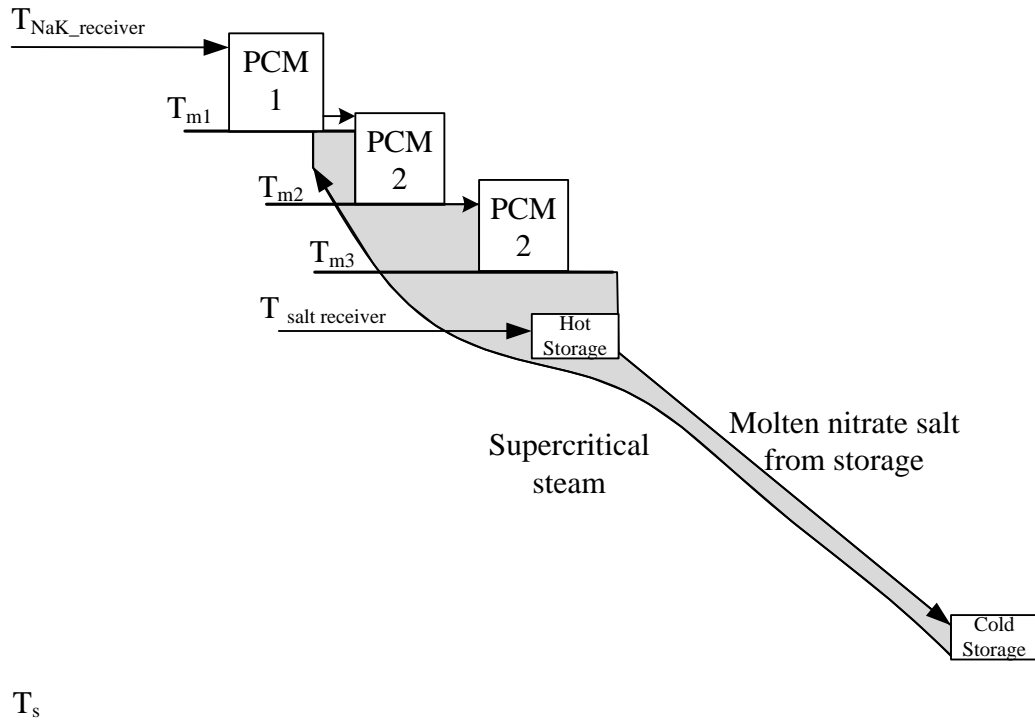


**Figure 93 – Single metallic PCM storage to enable supercritical steam**

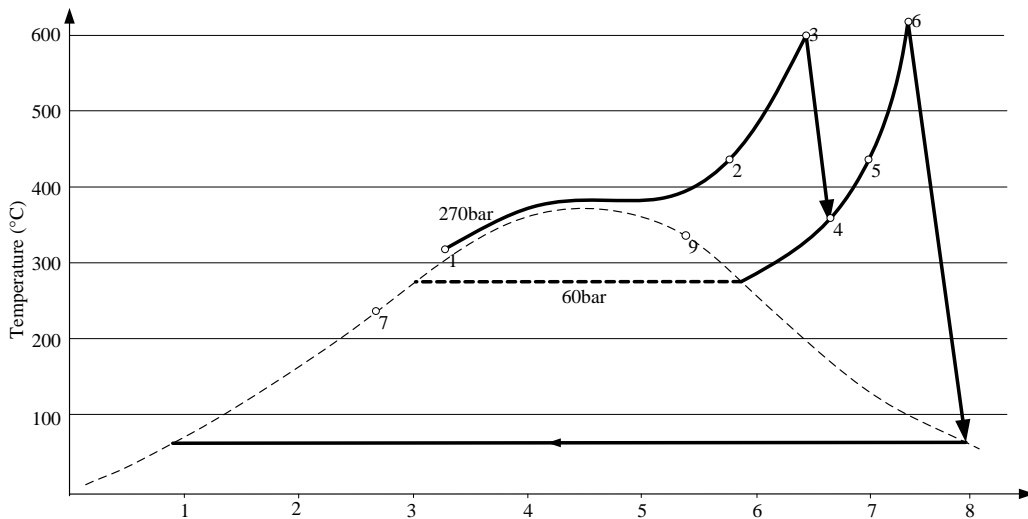


**Figure 94 – T-s diagram of a supercritical steam cycle for combined storage**

To evaluate this idea, the Lüen Ultra-supercritical steam power plant is used as a basis (Cziesla, et al., 2009). The assumption is made that the molten nitrate salt storage will only be able to heat the steam up to 540°C, and that the metallic PCM

storage will heat the steam up to the temperature required by the power cycle. The steam conditions at the points marketed on the T-S diagram in Figure 94 is presented in Table 41. The enthalpy differences across heat exchangers are also calculated, and it is shown that the heat transfer from molten nitrate salt to the power cycle is 2373.58 kJ/kg, and the heat transfer from metallic PCM to the power cycle is 164.63 kJ/kg. Therefore only 13.10 % of the energy is supplied by metallic PCM storage, and 86.9 % of the storage is two-tank molten nitrate salt storage.

**Table 41 – Enthalpy of steam in a supercritical steam generator**

			Enthalpy: (kJ/kg)	Heating provided by salt storage: (kJ/kg)	Heating provided by metallic PCM storage (kJ/kg)
(1)	Feedwater conditions	270 bar/ 310 °C	1381.50	1899.74	193.26
(2)	Exit of salt steam generator:	270 bar/ 540 °C	3281.24		
(3)	Live steam conditions:	270 bar/ 600 °C	3474.50	473.84	164.63
(4)	HP turbine outlet conditions:	60bar/ 350 °C	3043.43		
(5)	Exit of salt re- heater:	60 bar/ 540 °C	3517.27	164.63	164.63
(6)	Re-heat steam conditions:	60 bar/ 610 °C	3681.90		
				2373.58	357.89

Thus, most of the storage will be done using tried and tested, low cost two-tank molten nitrate salt storage, and the only value addition is done by replacing 13.10 % of the storage capacity with metallic PCM storage to facilitate the use of a supercritical steam cycle. Such an implementation would require the use of both a salt receiver and a liquid metal receiver, and the full cost implications are still not well understood.

## 11 FUTURE WORK

This project is considered a first step towards higher thermal energy storage in metallic PCMs and a number of future studies are needed before a conclusive decision could be made on the feasibility of latent heat storage in metallic PCMs. This section outlines a number of future research projects that will be needed for future developments.

### 11.1 Axial conduction and CFD models

In this project a simplifying assumption was made by ignoring the effects of axial conduction within the solidifying PCM and not considering the simultaneous charging and discharging of two heat exchangers in one melt. This was done to focus on the validity of the Stefan condition applied to metallic PCMs. This would require CFD techniques, which fell outside the scope of this project.

Axial conduction would be especially important in instances where there is a large variation of heat transfer rates along the length of the heat exchanger. Therefore it needs to be taken into consideration in all applications where the heat transfer fluid's bulk mean temperature is close to that of the PCM melting point and there is a significant difference between the inlet and outlet temperature of the heat transfer fluid.

### 11.2 Material testing

In chapter 4 it became clear that there is a shortage of high temperature material properties close to the melting point of AlSi12. Some assumptions proved to be valid, but high temperature materials testing must be performed on a selection of prospective metallic PCMs. The most important PCMs are:

- Si56Mg44
- AlSi12 (LM6)
- Al86.4Si9.4Sb4.2
- Al
- Al59Mg35Zn6
- Mg34.6Al65.4
- Mg47Si38Zn15

These are the most cost effective metallic PCMs, and cover a range of temperatures.

The material properties should be measured close to the melting point of the alloy, in both the liquid and solid phase. The following properties should be known:

- Melting point
- Heat of fusion
- Sub-cooling
- Thermal conductivity
- Specific heat capacity

- Density
- Coefficient of expansion
- Expansion on at phase change

The melting point, heat of fusion, sub-cooling and specific heat capacity can all be measured using a DSC machine with vacuum capabilities, as sample oxidation severely affects the DSC measurements even with nitrogen cover. Furthermore, the use of a DSC curve would be useful in CFD simulation of solidification process.

The cyclic stability of the metallic PCM should also be evaluated by cycling a sample through its melting point for about 8000 times, which will be equal to a bit more than 20 years of operation. Other aspects affecting the stability of the storage material should also be investigated.

### **11.3 More alloys and investigation into hyper-eutectics**

The use of hyper-eutectic alloys should also be investigated. Material stability may be prohibitive, but if it is possible to overcome cyclic stability, hyper-eutectic alloys will be able to provide thermal energy storage at design temperatures, which will be a great advantage from an exergetic point of view.

Furthermore it is likely that there are more alloys that offer higher heats of fusion at other melting temperatures that might be more suitable for thermal energy storage than those identified in this project (Birchenall, et al., 1979).

### **11.4 High temperature corrosion resistance, heat exchangers and containment**

Much work is still needed on corrosion resistance against molten metals. The methods discussed in chapter 9 had limited testing, and long term corrosion resistance must still be verified. The oxidation of aluminized steel is the most promising corrosion protection method, but the longevity of the oxide layer through thermal cycles needs to be verified, and the industrial application of this corrosion resistance need more research.

### **11.5 The use of liquid metals in CSP**

The use of NaK, sodium and other liquid metals as HTFs is well known in the nuclear industry and its advantages in CSP is very clear. Safety, design and material handling protocol are well established in the nuclear industry, but will need to be adapted for CSP to reduce the cost. A detailed study is required on the application of liquid metal heat transfer to CSP. The main questions regarding liquid metal heat transfer in CSP is economic feasibility and safety. This includes the use of LBE, NaK and sodium.

### **11.6 Analysis of a combined molten salt storage system with metallic PCM storage**

The concept of combining two-tank molten nitrate salt storage and metallic PCM in a cascaded fashion is new. This may be a key to the implementation of supercritical steam power cycles into CSP to deliver base load power. This concept must be investigated further and an in-depth techno-economic study needs to be performed. Most likely the concept will require two receivers, one salt, and another for liquid metal.

### **11.7 Optimisation through entropy minimization**

In section 8.6.2 the importance of entropy minimization is highlighted. A detailed study of metallic PCM storage and entropy minimization should be done. The Flownex model developed in chapter 8 can be used as a base to work from.

## 12 CONCLUSION

The current state of the art thermal energy storage is two tank molten salt. This has a maximum operational temperature of 565 °C, limited largely by the thermal properties of nitrate salts. This limits the source temperature of the power cycle, and bounds the power cycle to a subcritical steam cycle of which the maximum thermal efficiency is 36 to 40 %. Higher efficiency power cycles (like supercritical steam) offer significant reductions in the levelised cost of electricity (LCOE), but these power cycles require higher source temperatures than currently possible with conventional two tank molten salt storage.

Phase change materials (PCMs) offer higher temperature energy storage than possible with sensible heat storage. Metallic PCMs have thermal properties that are more favourable than those of non-metallic phase change materials, with high thermal conductivity and low sub-cooling being the most significant. The central topic and contribution of this project was to evaluate the feasibility of metallic PCMs as storage materials that could increase the maximum possible thermal energy storage temperature to enable higher efficiency power generation. The application of metallic PCMs in concentrating solar power is a novel idea, and the feasibility of metallic PCMs had to be evaluated.

Key to the implementation of metallic PCMs are high temperature HTFs. Liquid metals are the only heat transfer fluids (apart from gasses) that can operate at temperatures suitable for supercritical steam and thermal energy storage (TES) in metallic PCMs. Liquid metal receivers can absorb solar flux densities more than twice those possible with other heat transfer fluids. This results in compact, high efficiency receivers, which is extremely advantageous at high temperatures. Additionally, the eutectic sodium-potassium alloy (NaK) has a melting point of -12.8 °C which means that there is no need for trace heating in the primary heat transfer loop. This significantly increases safety in the liquid metal system, as it is possible to drain the heat transfer loop with no risk of pipe blockage. For this reason, NaK was chosen as the heat transfer fluid used in this study.

To evaluate the idea of using liquid metal HTFs and metallic PCMs together, two storage concepts have been developed. Aluminium-Silicon (AlSi12) was identified as an ideal metallic PCM for research and the analytical work was based on concepts employing both NaK and AlSi12, one where steam is generated directly from the PCM and another where the steam generation is done using a NaK-water heat exchanger.

Core to the analysis of latent heat thermal energy storage is the moving boundary heat transfer problem in a cylindrical coordinate system, associated with the solidification and melting of a PCM around a cylindrical pipe. Through an experiment it was found that the Stefan condition holds true for AlSi12, which allows analysis by quasi steady heat transfer assumptions. This allowed for the development of a discretised transient model using an enthalpy tracking method to predict the movement of a moving boundary. Because the Stefan condition is met, an instantaneous heat transfer analysis can be done using a standard resistance



model on the moving boundary to calculate heat transfer rates. This is especially convenient for heat exchanger sizing.

A prototype thermal energy storage unit was built, and it was used to validate the assumptions made regarding the moving boundary heat transfer problem. It was possible to predict the movement of the moving boundary and it was shown that the Stefan condition holds true even for very high temperature gradients between the coolant and the PCM. Furthermore, it was shown that instantaneous heat transfer calculations could be used to design the heat transfer surfaces in such a storage unit.

It must be noted that the effect of axial conduction was ignored, and only radial conduction was considered in this model. The effect of axial conduction will have to be analysed in detail using CFD techniques and thus fell outside the scope of this project.

To demonstrate and evaluate the concept, a Flownex model was built based on a subcritical steam power cycle. The thermodynamic model of the power generating cycle yielded boundary conditions which were used for the sizing of the heat exchangers in the storage system and steam generators. An integrated model of the storage system, primary heat transfer loop and the power block yielded a model that can be used in future studies.

The evaluation of the concepts highlighted that the DSG concept had a number of issues relating to entropy generation, practical implementation, process control and start-up and shutdown procedures. The ISG concept proved more favourable in many respects, but requires a liquid metal-water heat exchanger. If NaK or sodium were used as a primary HTF, the safety and cost of the steam generator may be prohibitive, and requires further investigation. Alternative metallic HTFs such as eutectic lead-bismuth alloy (LBE) may also offer solutions, especially in applications where the plant is used for base load energy production.

One of the key problems with the use of latent heat thermal energy storage is the fact that isothermal storage is responsible for entropy generation. Heat transfer between sensible heat and latent heat inherently yields some entropy generation, both in the primary heat transfer loop, and towards the working fluid of the power cycle. The use of cascaded PCMs can minimize entropy generation. This is a topic that needs further investigation.

During a techno economic evaluation, it was determined that metallic PCMs will add value to a CSP plant by enabling the use of supercritical steam power cycles. However, this is only significant if the DOE target for LCOE of 6US\$/kWh is reached for the entire plant, which will allow CSP to compete for base load generation. To reach this target cost reduction will have to be performed on the entire plant, and the use of high temperature storage will only form one part of the cost reduction solution.

The benefit of using metallic PCMs on their own is apparent, but storage costs can further be reduced by using metallic PCM storage in conjunction with traditional two tank molten nitrate salt storage, as only 13.10 % of the storage needs to be at

temperatures above that of the two tank molten salt storage. This also has benefits from an entropy minimization point of view. Pure aluminium, eutectic magnesium-aluminium alloy, eutectic aluminium-silicon alloy and eutectic silicon-magnesium alloy seem to be promising metallic PCMs, although more metallic PCMs need to be identified to enable cascaded PCMs across a greater temperature range and at smaller increments for entropy minimization.

Furthermore, aluminium and aluminium alloys are highly corrosive, and appropriate corrosion protection needs to be developed for industrial applications. Oxidation of aluminized steel surfaces appears to be a viable corrosion protection technique, but the application of this technique and the longevity of the corrosion resistance still need more investigation.

The use of liquid metal HTFs in CSP also need further investigation, as it is central to the development of high temperature thermal energy storage. Experience gained from the implementation of liquid metals in the nuclear industry will serve as a good basis, but the application to CSP needs to be fully understood, and cost reduction needs to be kept in mind.

### 13 REFERENCES

- Achenbach, T.** 2011. *Development of an edge module for open volumetric receiver for the use of the radiation at the receiver boundary region* [Conference] // SolarPACES. - Granada
- Adinberg, R., Zvegilsky, D. & Epstein, M.** 2010 *Heat transfer efficient thermal energy storage for steam generation* [Journal] // Energy conversion management, 51 pp. 9-15.
- Agyenim, F. Hewitt, N. Eames, P. & Smyth, M.** 2009. *A review of materials, heat transfer and phase change problem formulation for latent heat thermal energy storage systems (LHTESS)* [Journal] // Renewable and sustainable energy reviews. 14(2) pp. 615-628
- Alibaba.com** [Online]. Available: <http://www.alibaba.com/>. – [12 February 2014]
- Allen, K.G. Kröger, D.G. & Fluri, T.P.** 2009. *Thermal energy storage in a rock bed* [Conference] // ISES. - Johannesburg : ISES
- Battleson, K.W.** 1981. *Solar Power Tower Design Guide: Solar thermal central receiver power systems, a source of electricity and/or process heat* [Report] : Design guide. - : Sandia national labs - Albuquerque
- Bejan, A.** 1982. *Entropy generation through heat and fluid flow* [Book]. - New York : Wiley
- Bejan, A.** 1995. *Entropy generation minimization* [Book]. - Boca Raton : CRC press
- Bejan, A.** 1996. *Method of entropy generation minimization, or modelling and optimization based on combined heat transfer and thermodynamics* [Journal] // Revue Generale de Thermique. 35. pp. 637-646.
- Birchenall, C. E. & Reichman A.F.** 1979. *Heat storage in Eutectic Alloys* [Journal]. - Delaware : Metallurgical Transactions A, Vol 11 A.
- Bird, R.E. & Hulstrom, R.L.** 1981. *Simplified Clear Sky Model for Direct and Diffuse Insolation on Horizontal Surfaces* [Report] : Technical Report No. SERI/TR-642-761. – NREL - Golden (CO)
- Bouayad, A. Gerometta & C. Belkebir, A.** 2003. Kinetic interactions between solid iron and molten aluminium [Journal] // Materials Science and Engineering. - A363, pp.53-61/
- Brandes, E.A. & Brook G.B.** 1998. *Smithells Metals Reference Book (7th Edition)* [Book]. - Oxford : Butterworth-Heinemann.
- Bugge, J. Kjaer, S. & Blum, R.** 2006. *High-efficiency coal-fired power plants development and perspectives* [Journal] // Energy 31. pp. 1437-1445
- Burch S D [et al.].** 1996. *Applications and benefits of catalytic converter thermal management* [Conference] // SAE Fuels & Lubricants spring meeting. - Dearborn,(MI) : SAE.

- Cengel, Y.A. & Boles, M.A.** 2002. *Thermodynamics: an engineering approach - fourth edition* [Book]. - New York : McGraw-Hill.
- Cengel, Y.A.** 2003. *Heat transfer - A practical approach* [Book]. - New York : Mc Graw Hill.
- Chambadal, P.** 1957. Les centrales nucléaires [Journal] // Armand Colin. pp.1-58.
- Coastal Chemical** 2011. *Hitec Solar Salt* [Report] Houston : Coastal Chemical .
- Coastal Chemical** 2012. *Hitec heat transfer salt* [Report] Houston : Coastal Chemical .
- Cziesla, F. Bewerunge, J. & Senzel, A.** 2009. *Lünen – state of the art supercritical steam power plant under construction* [Conference] // POWER-GEN Europe 2009, Cologne.
- Darcy, H.** 1857. *Recherches Experimentales Relatives au Mouvement de L'Eau dans les Tuyaux* [Book]. - Paris : Mallet-Bachelier
- Deqing, W.** 2008. *Phase evolution of an aluminized steel by oxidation treatment* [Journal]. - Dalian : Applied Surface Science, 2008. – 254 pp.3026–3032.
- Deqing, W. Ziyuan, S. & Longjiang, Z.** 2003. *A liquid aluminium corrosion resistance surface on steel substrate* [Journal] // Applied Surface Science. - 214pp. 304-311.
- Dostal, V. Driscoll, M.J. & Hejzlar, P.** 2004. *A Supercritical carbon dioxide cycle for next generation nuclear reactors* [Report] : PhD Thesis. - Boston : MIT.
- Dow chemical company.** 2001. *Product information: Dowtherm A - Synthetic organic heat transfer fluid*, [Report] Dow chemical company
- Eck, M [et al.]** 2011. *Direct steam generation in parabolic troughs at 500degC- First results of the REAL-DISS project* [Conference] // SolarPACES - Granada
- Flownex** 2011. *Flownex theory manual* [Book]. - Pretoria : Flownex,
- Fluri, T.P.** 2009. The potential of concentrating solar power in South Africa [Journal] // Energy Policy (37). pp. 5075-5080.
- Geosun Africa** [Online]. Available: [geosun.co.za](http://geosun.co.za). [29 August 2013]
- Getling, A.V.** 1998. *Rayleigh-Benard Convection: Structures & Dynamics* [Book]. - London: World Scientific Publishing.
- Gil A [et al.]** 2010. *State of the art on high temperature thermal energy storage for power generation. Part 1 - Concepts, materials and modellization* [Journal]. - Lleida : Renewable and Sustainable Energy Reviews, 14, pp.1364-1381.
- Gnielinski, V.** 1975. Neue Gleichungen Für den Wärme- und den Stoffübergang in turbulente durchströmten Rohren und Kanälen [Journal] // Forschung im Ingenieurwesen A. 41(1) pp 8-16.

- Hall A, Ambrosini A & Ho C.** 2012. *Solar Selective Coatings for Concentrating Solar Power Central Receivers* [Journal] // Advanced materials and processes. pp. 28-32.
- He, Q. and Zhang, W.** 2001 A study on latent heat storage exchangers with the high-temperature phase-change material [Journal]. - Wuhan : International journal of energy research. pp. 25-30.
- Herring, D.H.** 2010. *Oil Quenching* [Report]. Illinois : The Herring group, Inc.
- Herrmann, U. Geyer, M. & Kearney, D.** 2006 *Overview on thermal storage systems* // Workshop on Thermal Storage for Trough Power Plants: FLABEG Solar International GmbH.
- Heselton, K.** 2005. *Boiler Operator's Handbook* [Book]. - Lilburn: Fairmont Press,
- Hoshi, A. [et al.]** 2005. *Screening of high melting point phase change materials (PCM) in solar thermal concentration technology based CLFR* [Journal] // Solar Energy 79. pp. 332-339
- Hummon, M. & Denholm, P.** 2012. *Simulating the value of concentrating solar power with thermal energy storage in a production cost model* [Report]: Technical report. - Denver : NREL
- International Energy Agency** 2010. *Technology Roadmap* [Report] / IEA. - Paris : IEA
- InvestmentMine.** [Online]. Available: <http://www.infomine.com> – [12 February 2014]
- Jensen, M.S. [et al.].** 2008. *Degradation of TiB<sub>2</sub> ceramics in liquid aluminium* [Journal] // Journal of the European Ceramic Society (28). pp. 3155-3164.
- Johnson, W.R.** 1998. *The Handbook of Fluid Mechanics* [Book]. - Heidelberg : CRC Press LLC
- Kakac, S. & Yener, Y.** 1993 *Heat conduction* [Book]. - Washington : Taylor & Francis
- Karassik, I.J. [et al.]** 1985. *Pump handbook* [Book] New York: McGraw-Hill
- Kearney, D. Herrmann, U. & Nava, P.** 2003. *Assessment of molten salt heat transfer fluid in a parabolic trough solar field* [Journal] // Journal of solar Energy Engineering(125). pp:170-176.
- Kenisarin, M.M.** 2009. *High Temperature Phase Change Materials for Thermal Energy Storage* [Journal]. - Renewable and Sustainable Energy Reviews 14(3). pp: 955-970
- Kolb, G.J. [et al.]** 2011. *Power tower technology roadmap and cost reduction plan* [Report]. Albuquerque: Sandia national laboratories

- Kopeliovich, D.** *Heat transfer oil ISO100* [Online] Available: [http://www.substech.com/dokuwiki/doku.php?id=heat\\_transfer\\_oil\\_iso\\_100](http://www.substech.com/dokuwiki/doku.php?id=heat_transfer_oil_iso_100). [05 July 2013]
- Lai, G.Y.** 2007. *High-temperature Corrosion and Materials Applications* [Book] – New York : ASM International.
- Li, F. Hu, Y. & Zhang, R.** 2011. *The influence of heating-cooling cycles on the thermal storage performances of Al-17 wt.% Si alloy* [Journal]. - Guangdong: Advanced Materials Research. – pp: 239-242.
- Liquid metal engineering centre** 1972. *Sodium-NaK engineering handbook Vols. 1-5.* [Book]. - New York : Gordon and Breach
- Lock, G.S.** 1996. *Latent heat transfer: An introduction to fundamentals* [Book]. - Oxford : Oxford Science Publication,
- Lockheart, R.W. & Martenelli, R.C.** 1949. *Proposed Correlation of Data for Isothermal heat transfer in phase change* [Journal] // Chem. Eng. Prog. (45), pp: 34-48
- Matbase** Matbase [Online] Available - <http://www.matbase.com/>. [9 September 2013]
- Medrano, M. [et al.]** 2010. *State of the art on high-temperature thermal energy storage for power generation. Part 2 - Case studies* [Journal]. - Renewable and Sustainable Energy Reviews14, pp. 1382-1401
- Meduri, P. K. Hannemann, C.R. & Pacheco, J.E.** 2013. *Performance characterization and operation of e-solar's sierra sun tower power tower plant* [Conference] // Las Vegas: Solar PACES.
- Michels, H. & Pitz-Paal, R.** 2007. *Cascaded latent heat storage for parabolic trough solar power plants* [Journal] // Solar Energy. - 81. - pp. 829-837.
- Mondolfo, L.F.** 1976. *Aluminium Alloys: Structures and properties* [Book]. - London : Butter Worths
- Munn, G.** Information on the properties of AlSi12 [Interview]. - 14 February 2013.
- Murray, J.L. and McAlister, A. J.** 1984. *The Al-Si (Aluminium-Silicon) system* [Journal] // Bulletin of alloy phase diagrams pp. 74-84.
- Novikov, I.I.** 1958. *The Efficiency of Atomic Power Stations* [Journal] // Journal Nuclear Energy II. pp. 125–128.
- Schiel, W.J.** 1988. *Testing and external sodium receiver up to heat fluxes of 2.5MW/m<sup>2</sup>: Results and conclusions from the IEA-SSPS high flux experiment conducted at the central receiver system of the Plataforma Solar de Almeria* [Journal] // Solar Energy (41) pp. 255-265.
- Siemens** 2010. *Steam turbines for CSP plants* [Brochure] - Erlangen: Siemens AG

- Special Metals Corporation** *Special metals* [Online] Available - [www.specialmetals.com](http://www.specialmetals.com). [14 November 2013]
- SPX HT-5--200GPM Tester** [Online] Available - <http://www.spx.com/en/power-team/pd-ht-series/> [3 November 2013]
- SQM Contact sustainability SQM** [Interview]. - 5 September 2013.
- Steine, W.B. and Harringan, R.W.** 1986. *Power from the sun* [Book]. - New York : John Wiley and sons, Inc.
- Steiner,D.I. and Taborek, J.** 1992. *Flow Boiling Heat Transfer in Vertical Tubes Correlated by an Asymptotic Model* [Journal] // Heat Transfer Engineering 13(2)
- Stoddard, L. Abiecunas, J. & O'Connell, R.** 2006. *Economic, Energy, and Environmental Benefits of Concentrating Solar Power in California* [Report] Subcontract Report. - Battelle: NREL.
- Sun, J.Q. [et al.]** 2007. *Thermal Reliability Test of Al-34%Mg-6%Zn Alloy as Latent Heat Storage Material and Corrosion of Metal With Respect to Thermal Cycling* [Journal] // Energy Conversion Management (48). pp. 619-624.
- Tamme,R. Laing, D. & Steinmann, W.D.** 2004. *Advanced thermal energy storage technology for parabolic trough* [Journal] // Journal of solar energy engineering . 126(2) pp. 109-125.
- Tamme. R.** 2007. *Energy storage for direct steam solar power* [Conference] // The DISTOR Project. Consortium–objective–achievements. DISTOR dissemination workshop. Energy storage for direct steam solar power plants : Almeria, Spain.
- Technical ceramics** Ceramic formers spec sheet. - Capetown [5 December 2013]
- Technical Glass.** Superwool 607 HT. [Online] Available <http://www.goodfellow.com/corporate/news/2011/Superwool-607-HT-Goodfellow-UK-Sept-2011.pdf> [ 01 September 2011]
- Tenekedjiev N [et al.]** 1995. *Microstructure and thermal analysis of strontium-treated aluminium-silicon alloys* [Book]. - Des Plaines : American foundrymen's Society, Inc.
- Thome, J.R. Kattan, N and Ould Didi, M. B.** 2002. *Prediction of two-phase pressure gradients of refrigerants in horizontal tubes* [Journal] // International Journal of Refrigeration 25(7). pp. 935-947.
- Torresol Energy** Newspaper library [Online] Available [http://www.torresolenergy.com/EPORTAL\\_DOCS/GENERAL/SENERV2/DOC-cw524d4f94e5bff/gemasolar-celebrates-its-second-anniversary-with-an-excellent-operational-record.pdf](http://www.torresolenergy.com/EPORTAL_DOCS/GENERAL/SENERV2/DOC-cw524d4f94e5bff/gemasolar-celebrates-its-second-anniversary-with-an-excellent-operational-record.pdf). [ 26 September 2013]
- Tsipas, D.N. [et al.]** 1998. *Degradation behaviour of boronized carbon and high alloy steels* [Journal] // Material Letters (37). pp. 128-131.



- U.S. Energy Information Administration** 2012. *Annual Energy Outlook 2012 - with Projections to 2035* [Report] : Independent report. Washington : U.S. Energy Information Administration,
- Voller, V. and Cross, M.** 1980 *Accurate solutions of moving boundary problems using the enthalpy method* [Journal] // International journal of heat and mass transfer (24). pp. 545-556.
- Voller, V. and Swaminathan, C.R.** 1992. *A general enthalpy method for modelling solidification process* [Journal] // Metallurgical transactions B (23B). pp. 651-664.
- Wagner, W. [et al.]** 1997. *The IAPWS Industrial Formulation 1997 for the thermodynamic properties of water and steam* [Journal] // Journal of Engineering for Gas Turbines and Power (122) - pp. 150-182.
- Wang, X. [et al.]** 2004. *Experimental research on a kind of novel high temperature phase change storage heater* [Journal]. - Beijing: Energy conversion and management.
- Weisbach, J.** 1845. *Lehrbuch der Ingenieur- und Maschinen-Mechanik* [Book]. - Braunschweig : Paris.
- World Nuclear News** *Large fast reactor approved for Beloyarsk* [Online]. Available : <http://www.world-nuclear-news.org/NN-large-fast-reactor-approved-for-Beloyarsk-2706124.html>. 27 June 2012
- Yan, M.** 2001. *Durability of materials in molten aluminium alloys* [Journal] // Journal of materials science (36). pp. 285-295.
- Zimalco** *Delivery of unit* [Invoice]. - 17 January 2013.



## APPENDIX A CANDIDATE PHASE CHANGE MATERIALS

Table 42 – Carbonates (Kenisarin, 2009)

Material	T <sub>m</sub> (°C)	λ (J/g)
Na <sub>2</sub> CO <sub>3</sub> (6.4)–85.8NaOH–7.8NaCl	282	316
Li <sub>2</sub> CO <sub>3</sub> (32.1)–34.5K <sub>2</sub> CO <sub>3</sub> –33.4Na <sub>2</sub> CO <sub>3</sub>	397	276
Li <sub>2</sub> CO <sub>3</sub> (47)–53K <sub>2</sub> CO <sub>3</sub>	488	342
Li <sub>2</sub> CO <sub>3</sub> (47)–53K <sub>2</sub> CO <sub>3</sub>	491	321
Li <sub>2</sub> CO <sub>3</sub> (44)–56Na <sub>2</sub> CO <sub>3</sub>	496	370
Li <sub>2</sub> CO <sub>3</sub> (28)–72K <sub>2</sub> CO <sub>3</sub>	498	263
Li <sub>2</sub> CO <sub>3</sub> (28.5)–71.5K <sub>2</sub> CO <sub>3</sub>	498	316
Li <sub>2</sub> CO <sub>3</sub> (44.3)–55.7Na <sub>2</sub> CO <sub>3</sub>	498	393
Li <sub>2</sub> CO <sub>3</sub> (35)–65K <sub>2</sub> CO <sub>3</sub>	505	344
NaBr(43)–2NaF–55Na <sub>2</sub> MoO <sub>4</sub>	506	241
K <sub>2</sub> CO <sub>3</sub> (62)–17NaF–21KCl	520	274
Li <sub>2</sub> SO <sub>4</sub> (59.8)–36.7Li <sub>2</sub> MoO <sub>4</sub> –3.5CaMoO <sub>4</sub>	538	406
Li <sub>2</sub> CO <sub>3</sub> (20)–60Na <sub>2</sub> CO <sub>3</sub> –20K <sub>2</sub> CO <sub>3</sub>	550	283
KBr(60)–40KF	576	315
KBr(65)–35K <sub>2</sub> MoO <sub>4</sub>	625	91
Li <sub>2</sub> SO <sub>4</sub> (82)–11.44CaSO <sub>4</sub> –6.56CaMoO <sub>4</sub>	680	207
K <sub>2</sub> CO <sub>3</sub> (47.8)–52.2K <sub>2</sub> CO <sub>3</sub>	710	176
K <sub>2</sub> CO <sub>3</sub> (50)–50Na <sub>2</sub> CO <sub>3</sub>	710	163
K <sub>2</sub> CO <sub>3</sub> (51)–49Na <sub>2</sub> CO <sub>3</sub>	710	163

Table 43 – Hydroxides (Kenisarin, 2009)

Material	T <sub>m</sub> (°C)	λ (J/g)
NaOH(50)–50KOH	169	202
LiOH(30)–70NaOH	210	278
NaOH(20)–80NaNO <sub>2</sub>	230	206
NaOH(73)–27NaNO <sub>2</sub>	237	249
NaOH(78.1)–3.6NaCl–18.3NaNO <sub>3</sub>	242	242
NaOH(28)–72NaNO <sub>3</sub>	246	182
NaOH(55.6)–4.2NaCl–40.2NaNO <sub>3</sub>	247	213
NaOH(81.5)–18.5NaNO <sub>3</sub>	256	251
LiOH(63)–37LiCl	264	437
NaOH(59)–41NaNO <sub>3</sub>	266	278
NaOH(59)–41NaNO <sub>3</sub>	266	221
LiOH(65.5)–34.5LiCl	274	339
LiOH(62)–36.5LiCl–1.5KCl	282	300
NaOH(85.8)–7.8NaCl–6.4Na <sub>2</sub> CO <sub>3</sub>	282	316
NaOH(88.3)–5.3NaCl–6.4Na <sub>2</sub> CO <sub>3</sub>	282	279
NaOH(87.3)–6.1NaCl–6.6Na <sub>2</sub> CO <sub>3</sub>	291	283
NaOH(77.2)–16.2NaCl–6.6Na <sub>2</sub> CO <sub>3</sub>	318	290

Table 44 – Chlorides (Kenisarin, 2009)

Material	T <sub>m</sub> (°C)	λ (J/g)
LiCl(59.15)–40.85Ca(NO <sub>3</sub> ) <sub>2</sub>	270	167
NaCl(7.8)–85.8NaOH–6.4NaCO <sub>3</sub>	282	316
LiCl(54.2)–6.4BaCl <sub>2</sub> –39.4KCl	320	170
LiCl(47.4–47.7)–(46.8–47.0)KCl–(3.2–3.4)LiCO <sub>3</sub> –(2.1–2.4)LiF	340	375
LiCl(58)–42KCl	348	170
KCl(28.7)–45MnCl <sub>2</sub> –26.3NaCl	350	215
LiCl(23.4–24.2)–(24.8–25.3)LiVO <sub>3</sub> –(27.1–27.6)Li <sub>2</sub> MoO <sub>4</sub> –(17.3–17.8)Li <sub>2</sub> SO <sub>4</sub> –(6.1–6.2)LiF	360	284
NaCl(22.5–26.5)–(18.5–22.5)KCl–(57.0–53.0)MgCl <sub>2</sub>	385	405
KCl(21.6)–45.4MgCl <sub>2</sub> –33.0NaCl	385	284
KCl(45.5)–34.5MnCl <sub>2</sub> –20NaCl	390	230
KCl(20)–50MgCl <sub>2</sub> –30NaCl	396	291
KCl(37.7)–37.3MnCl <sub>2</sub> –25NaCl	400	235
NaCl(56)–44MgCl <sub>2</sub>	430	320
KCl(54)–46ZnCl <sub>2</sub>	432	218
KCl(61)–39MgCl <sub>2</sub>	435	351
NaCl(56.2)–43.8MgCl <sub>2</sub>	442	325
LiCl(58.5)–23.6Li <sub>2</sub> SO <sub>4</sub> –17.9Li <sub>2</sub> MoO <sub>4</sub>	445	327
KCl(36)–64MnCl <sub>2</sub>	448	236
LiCl(49.0)–12.75Li <sub>2</sub> SO <sub>4</sub> –38.25LiVO <sub>3</sub>	449	450
KCl(35)–65MnCl <sub>2</sub>	450	237
NaCl(60)–40MgCl <sub>2</sub>	450	328
NaCl(48)–52MgCl <sub>2</sub>	450	430
CaCl <sub>2</sub> (47.6)–8.1KCl–41.3NaCl–2.9NaF	460	231
CaCl <sub>2</sub> (41.6)–2.2KCl–8.8MgCl <sub>2</sub> –47.4NaCl	460	245
CaCl <sub>2</sub> (50)–7.25KCl–42.75NaCl	465	245
KCl(36)–64MgCl <sub>2</sub>	470	388
BaCl <sub>2</sub> (8.7)–52.3KCl–18.2MgCl <sub>2</sub> –20.7NaCl	475	248
BaCl <sub>2</sub> (13.1)–16.9CaCl <sub>2</sub> –47.3KCl–22.7NaCl	478	208
BaCl <sub>2</sub> (9.3)–22.2CaCl <sub>2</sub> –42.7KCl–25.8NaCl	479	217
LiCl(69.5)–26.5LiF–4MgF <sub>2</sub>	484	157
KCl(25)–27CaCl <sub>2</sub> –48MgCl <sub>2</sub>	487	342
CaCl <sub>2</sub> (50)–1.5CaF <sub>2</sub> –48.5NaF	490	264
CaCl <sub>2</sub> (52.3–55)–(45–47.2)NaCl	500	239
NaCl(33)–67CaCl <sub>2</sub>	500	281
CaCl <sub>2</sub> (66)–5KCl–29NaCl	504	279
SrCl <sub>2</sub> (68)–13KCl–19NaCl	504	223
NaCl(5)–40NaBr–55Na <sub>2</sub> MoO <sub>4</sub>	524	215
KCl(40)–23KF–37K <sub>2</sub> CO <sub>3</sub>	528	283
MgCl <sub>2</sub> (37)–63SrCl <sub>2</sub>	535	239
KCl(28)–19NaCl–53BaCl <sub>2</sub>	542	221
KCl(24)–47BaCl <sub>2</sub> –29CaCl <sub>2</sub>	551	219
NaCl(952)–48NiCl <sub>2</sub>	573	558
LiCl(94.5)–5.5MgF <sub>2</sub>	573	131
NaCl(38.5)–23NaBr–38.5Na <sub>2</sub> MoO <sub>4</sub>	612	168
CaCl(38.5)–11CaSO <sub>4</sub> –4CaMoO <sub>4</sub>	673	224

**Table 45 – Fluorides (Kenisarin, 2009)**

<b>Material</b>	<b>T<sub>m</sub> (°C)</b>	<b>λ (J/g)</b>
NaF(5)–87NaNO <sub>3</sub> –8NaCl	288	224
LiF(7.0)–41.5LiCl–16.4LiVO <sub>3</sub> –35.1Li <sub>2</sub> CrO <sub>4</sub>	340	177
LiF(16.2)–51.5LiCl–16.2Li <sub>2</sub> SO <sub>4</sub> –16.2Li <sub>2</sub> MoO <sub>4</sub>	402	291
LiF(17.6–17.7)–(33.2–33.8) KF–(40.0–40.4) KCO <sub>4</sub> –(8.6–8.7) KCl <sup>a</sup>	422	412
LiF(20)–80LiOH	427	1163
LiF(25.0)–43.8LiVO <sub>3</sub> –14.8Li <sub>2</sub> SO <sub>4</sub> –16.5Li <sub>2</sub> MoO <sub>4</sub>	428	260
LiF(80)–20LiOH	430	528
LiF(45.7)–1.8BaF <sub>2</sub> –41.2KF–11.3NaF	438	332
LiF(42.5–45.5)–(41.0–43.0) KF–(10.7–11.5) NaF–(2.8–3.0) KCl	440	682
LiF(27.1)–11.9NaF–55.1KF–5.9MgF <sub>2</sub> <sup>a</sup>	449	699
LiF(29.2)–11.7NaF–59.1KF <sup>a</sup>	454	414
LiF(46.5)–42KF–11.5–NaF	454	325
Li(29)–12NaF–59KF <sup>a</sup>	463	442
LiF(73.6)–26.4LiCl	485	403
KF(50)–50LiCl	487	344
LiF(33)–67KF <sup>a</sup>	493	458
LiF(18.0)–53.0LiVO <sub>3</sub> –29.0Li <sub>2</sub> MoO <sub>4</sub>	493	297
NaF(20.1)–79.9ZrF <sub>4</sub> <sup>a</sup>	510	255
NaF(17)–21KCl–62K <sub>2</sub> CO <sub>3</sub> <sup>a</sup>	520	274
KF(23)–40KCl–37K <sub>2</sub> CO <sub>3</sub> <sup>a</sup>	528	283
LiF(36.1)–34NaF–18.5CaF <sub>2</sub> –3.3BaF <sub>2</sub> –8.1BaMoO <sub>4</sub>	536	653
KF(40)–60KBr	576	315
LiF(25.67–25.76)–(36.45–36.57)NaF–(27.0–27.25) CaF <sub>2</sub> –(10.63–10.67)MgF <sub>2</sub> <sup>a</sup>	593	510
KF(55)–45KCl	605	407
LiF(35.2)–38.3NaF–26.5CaF <sub>2</sub>	615	636
LiF(52)–35NaF–13CaF <sub>2</sub>	615	640
Li(46)–44NaF–10MgF <sub>2</sub>	632	858
NaF(27)–73NaBr	642	360
LiF(34.51–34.79)–(37.25–37.6)MgF <sub>2</sub> –(24.5–25.0)CaF <sub>2</sub> –(3.21–3.31)NaF	651	460
LiF(60)–40NaF	652	816
NaF(33.5)–66.5NaCl	675	572
LiF(62)–19NaF–19MgF <sub>2</sub>	693	690
LiF(70)–30MgF <sub>2</sub>	728	520
NaF(65)–23CaF <sub>2</sub> –12MgF <sub>2</sub>	743	568
LiF(67)–33MgF <sub>2</sub>	746	947
LiF(74)–13KF–13MgF <sub>2</sub>	749	860
LiF(80)–20CeF <sub>3</sub>	756	500
LiF(81.5)–19.5CaF <sub>2</sub>	769	820
KF(85)–15CaF <sub>2</sub>	780	440
KF(85)–15MgF <sub>2</sub>	790	520
NaF(64)–20MgF <sub>2</sub> –16KF	804	650
NaF(62.5)–22.5MgF <sub>2</sub> –15KF	809	543
NaF(68)–32CaF <sub>2</sub>	810	600
NaF(75)–25MgF <sub>2</sub>	832	627
CaF <sub>2</sub> (49)–41.4CaSO <sub>4</sub> –9.6CaMoO <sub>4</sub>	943	237

**Table 46 – Metals (Kenisarin, 2009)**

<b>Material</b>	<b>T<sub>m</sub> (°C)</b>	<b>λ (J/g)</b>
Cu(83)–10P–7Si	840	92
Cu(74)–19Zn–7Si	765	125
Cu (91)–9P	715	134
96Zn–4Al	381	138
Mg(55)–28–17Zn	400	146
Zn(49)–45Cu–6Mg	703	176
Mg(52)–25Cu–23Ca	453	184
46.3Mg–53.7Zn	340	185
Cu(80)–20Si	803	197
Zn <sub>2</sub> Mg	588	230
Mg <sub>2</sub> Cu	841	243
Mg(60)–25Cu–15Zn	452	254
Mg(84)–16Ca	790	272
34.65Mg–65.35Al	497	285
Al(54)–22Cu–18Mg–6Zn	520	305
Si(49)–30Mg–21Ca	865	305
Al(59)–35Mg–6Zn	443	310
Mg(47)–38Si–15Zn	800	314
64.3–34.0Cu–1.7Sb	545	331
68.5Al–5.0Si–26.5Cu	525	364
60.8Al–33.2Cu–6.0Mg	506	365
60.8Al–33.2Cu–6.0Mg	506	365
Cu(69)–17Zn–14P	720	368
66.92Al–33.08Cu	548	372
64.1Al–5.2Si–28Cu–2.2Mg	507	374
46.3Al–4.6Si–49.1Cu	571	406
Cu(56)–27Si–17Mg	770	420
Al(65)–30Cu–5Si	571	422
86.4Al–9.4Si–4.2Sb	471	471
83.14Al–11.7Si–5.16Mg	555	485
87.76Al–12.24Si	557	498
Si(56)–44Mg	946	757

**Table 47 – Nitrates (Kenisarin, 2009)**

<b>Material</b>	<b>T<sub>m</sub> (°C)</b>	<b>λ (J/g)</b>
LiNO <sub>3</sub> (29)–17NaNO <sub>3</sub> –49.4KNO <sub>3</sub> –4.6Sr(NO <sub>3</sub> ) <sub>2</sub> a	105	110
LiNO <sub>3</sub> (33)–67KNO <sub>3</sub> <sup>a</sup>	133	170
LiNO <sub>3</sub> (31.7)–68.3KNO <sub>3</sub> <sup>a</sup>	135	136
KNO <sub>3</sub> (53)–40NaNO <sub>2</sub> –7NaNO <sub>3</sub> <sup>a</sup>	142	80
LiNO <sub>3</sub> (55.4)–4.5NaNO <sub>3</sub> –40.1KCl <sup>a</sup>	160	266
LiNO <sub>3</sub> (58.1)–41.9KCl <sup>a</sup>	166	272
LiNO <sub>3</sub> (47.9)–1.4LiCl–50.7NaNO <sub>3</sub> <sup>a</sup>	180	265
LiNO <sub>3</sub> 57)–43NaNO <sub>3</sub> <sup>a</sup>	193	248
LiNO <sub>3</sub> (49)–51NaNO <sub>3</sub> <sup>a</sup>	194	265
LiNO <sub>3</sub> (45)–47NaNO <sub>3</sub> –8Sr(NO <sub>3</sub> ) <sub>2</sub> <sup>a</sup>	200	199
LiNO <sub>3</sub> (87)–13NaCl <sup>a</sup>	208	369
KNO <sub>3</sub> (54)–46NaNO <sub>3</sub> <sup>a</sup>	222	100
NaNO <sub>3</sub> (54)–46KNO <sub>3</sub>	222	117
NaNO <sub>3</sub> (70)–30NaOH	247	158
LiNO <sub>3</sub> (97.4)–2.6Ba(NO <sub>3</sub> ) <sub>2</sub>	253	368
NaNO <sub>3</sub> (86.3)–8.4NaCl–5.3Na <sub>2</sub> SO <sub>4</sub>	287	177

**APPENDIX B PROPERTIES OF NAK<sup>10</sup>**

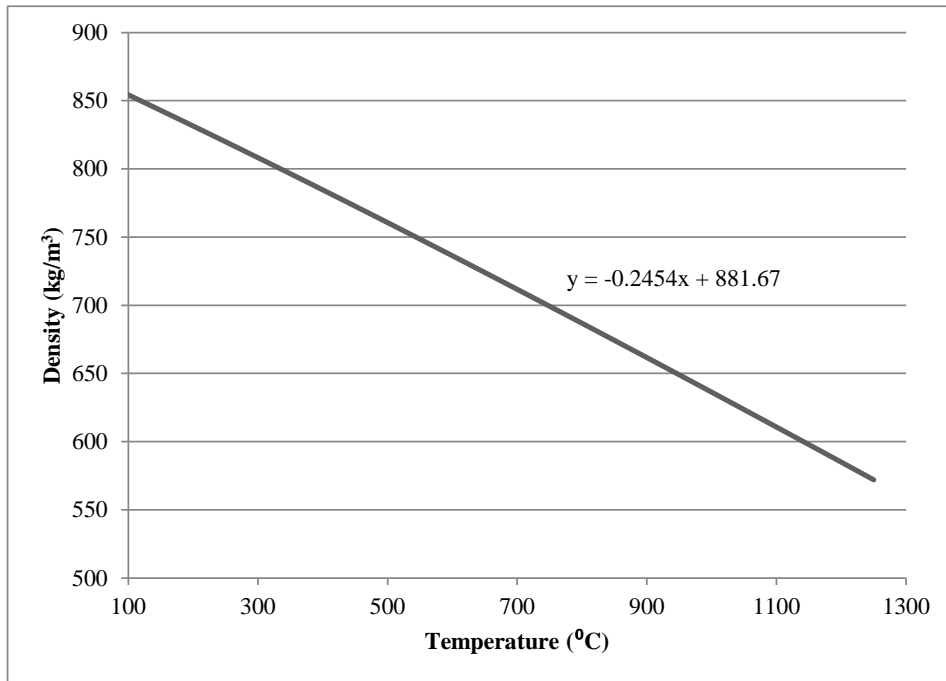


**Figure 95 - Density of eutectic NaK**

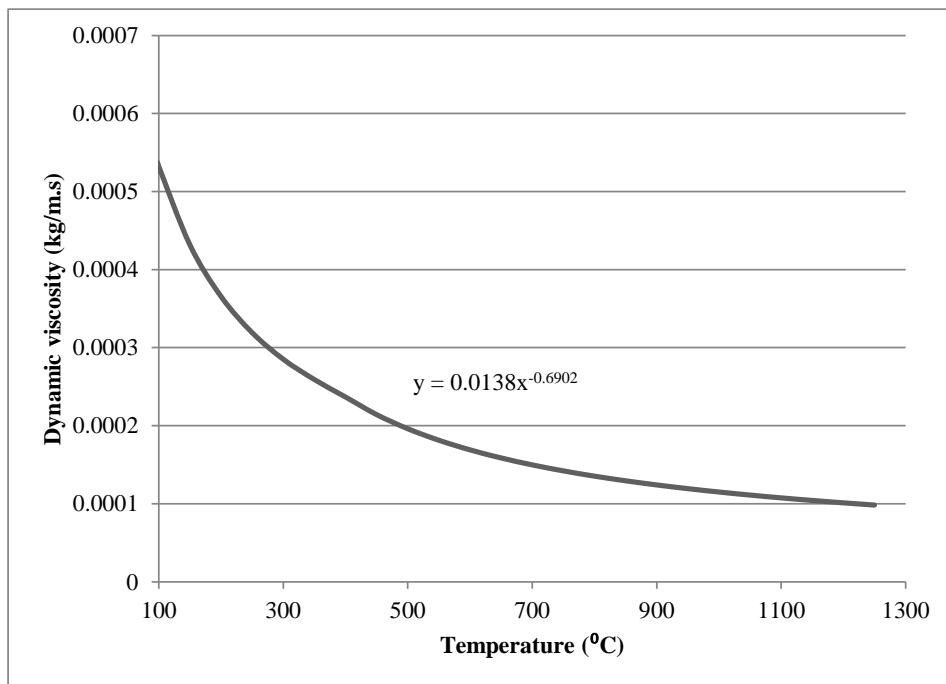


**Figure 96 - Dynamic viscosity of NaK**

<sup>10</sup> (Liquid metal engineering center, 1972)

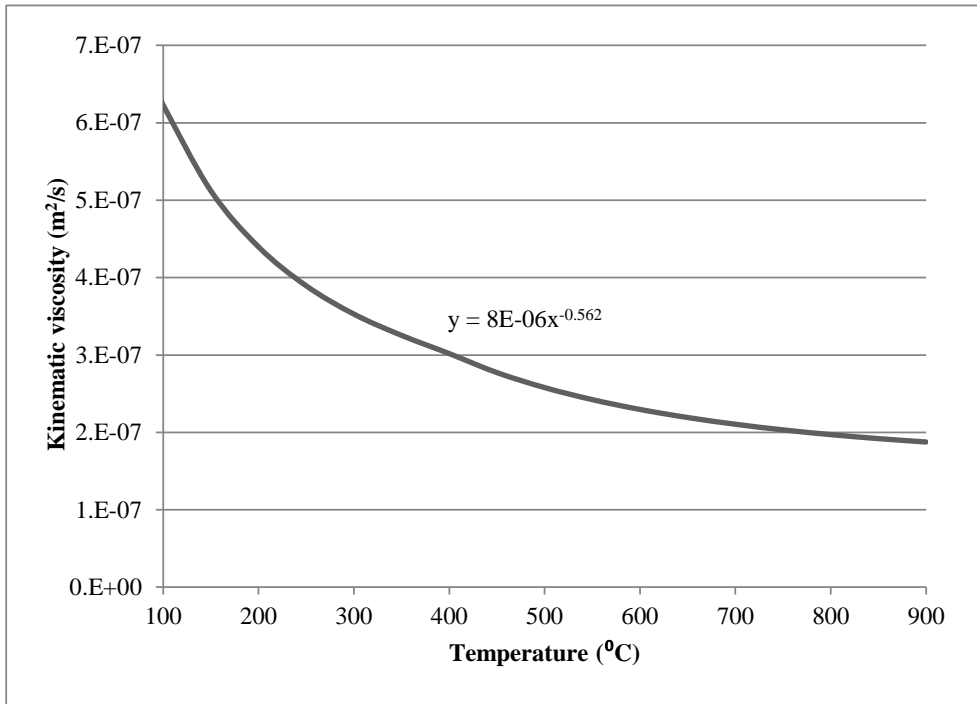


**Figure 97 - Kinematic viscosity of eutectic NaK**

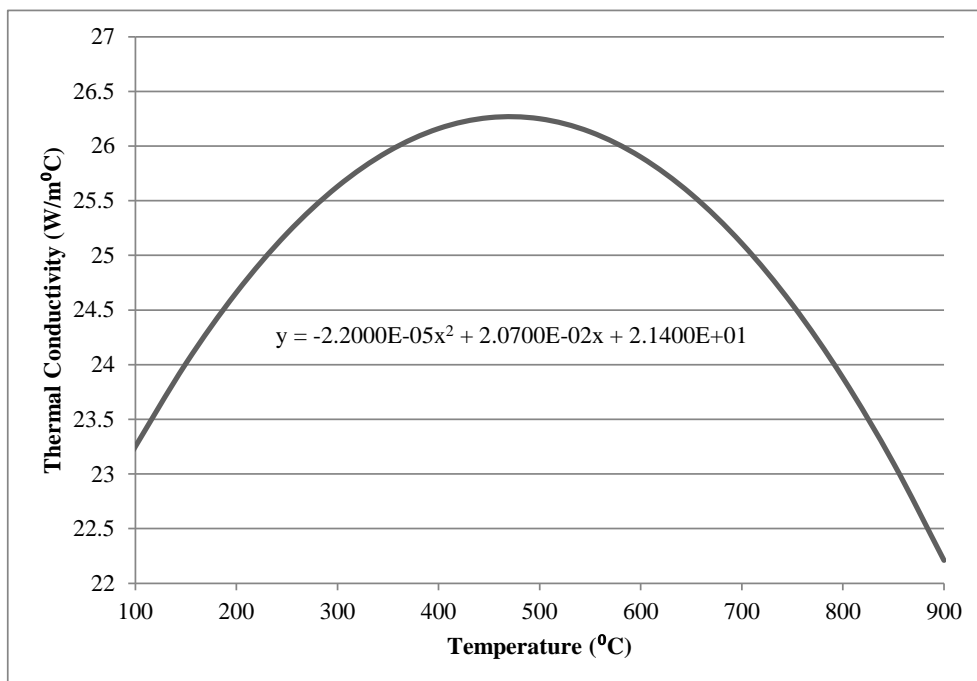


**Figure 98 - Thermal conductivity of eutectic NaK**

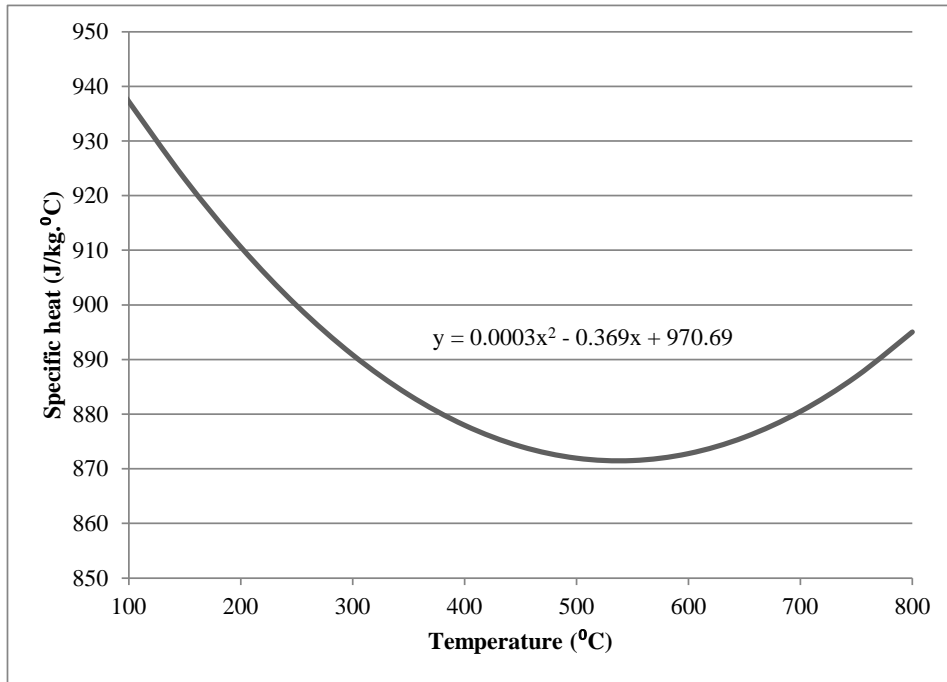


**Figure 99 - Specific heat of eutectic NaK**

### APPENDIX C DERIVATION OF THE STEFAN NUMBER

This section presents the derivation of the Stefan number as presented in Lock (1996):

Consider a phase change problem where a phase change material is being frozen by removing heat from a surface at  $Y = 0$ . The initial temperature of the material is  $T_\infty$ , the melting point is  $T_i$  and the temperature of the surface at  $Y=0$  is  $T_0$ . This is shown in figure 100.

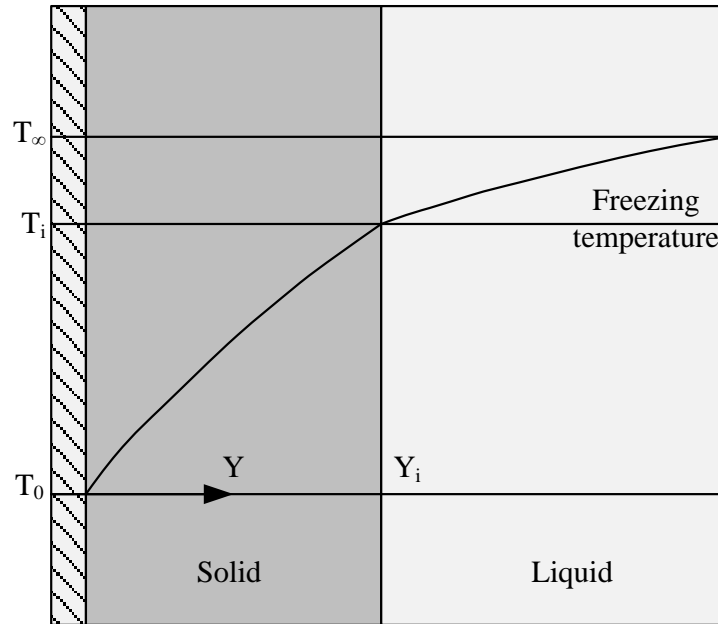


**Figure 100 - Temperature profiles during one-dimensional freezing of a liquid initially at  $T_\infty$**

The conduction in the solid region can be described as:

$$\frac{\partial T_S}{\partial t} = k_s \frac{\partial^2 T_S}{\partial Y_S^2} \quad (\text{C.1})$$

$$0 < Y < Y_i$$

And similarly for the liquid:

$$\frac{\partial T_L}{\partial t} = k_s \frac{\partial^2 T_L}{\partial Y_L^2} \quad (\text{C.2})$$

$$Y_i < Y$$

And the interface boundary can be described as:

$$\lambda \rho_s \frac{dY_i}{dt} = k_s \left( \frac{\partial T_S}{\partial Y} \right) - k_L \left( \frac{\partial T_L}{\partial Y} \right) \quad (\text{C.3})$$



$$Y = Y_i$$

Assuming  $T_\infty > T_i$ , that all the material was molten at  $t=0$ , and that the surface temperature is suddenly lowered to a fixed value of  $T_0 < T_i$ . From Figure 100 it is clear that some scales are implied in the liquid ( $T_i < T_L < T_\infty$ ), solid ( $T_0 < T_S < T_i$ ) and a dimensional scale ( $0 < Y_S < Y_i$ ). By designation the scale of a variable by a superscript  $c$ , we take:

$$\begin{aligned}\theta_L^c &= T_\infty - T_i \\ \theta_S^c &= T_i - T_0\end{aligned}\tag{C.4}$$

And

$$Y_S^c = Y_i$$

as difference scales. The remaining scales are unknown;  $t^c$ ,  $Y_i^c$  and  $Y_L^c$ .  $Y_i^c$  is the scale that will yield the position of the solidification interface. Assuming the liquid is all at the melting point ( $T_\infty = T_i$ ), this negates the conductivity of the liquid phase and removes equation C.2 and simplifies the interface equation, C.3, that may be re-written after introducing the following normalized values:

$$\begin{aligned}\phi_s &= \frac{T - T_0}{\theta_S^c} \\ y_s &= \frac{Y_S}{Y_S^c} \\ \tau &= \frac{t}{t^c} \\ \xi &= \frac{Y_i}{Y_i^c}\end{aligned}\tag{C.5}$$

By taking  $Y_S^c = Y_i^c$  (as implied by equation C.4), and substituting it into the deduced interface equation (C.3), the following equation is obtained:

$$\frac{d\xi}{d\tau} = \left[ \frac{k_S \theta_S^c t^c}{\lambda \rho_S (Y_i^c)^2} \right] \left( \frac{\partial \phi_S}{\partial y_S} \right)_i\tag{C.6}$$

The expression in square brackets is a non-dimensional term of which the magnitude depends on the unknown scales  $t^c$  and  $Y_i^c$ . The magnitude of this term is not arbitrary because the derivatives of the equation, being normalized, are expected to be of the order one. The only way equation C.6 can be satisfied in general is if

$$\frac{k_S \theta_S^c t^c}{\lambda \rho_S (Y_i^c)^2} = O(1).\tag{C.7}$$

This is a qualitative relationship between  $t^c$  and  $Y_i^c$ . By simply taking the right hand side as 1, equation C.7 is converted into a quantitative relation.

By substituting the normalized variables (C.5) into equation C.1, the following equation can be found:

$$\left[ \frac{(Y_i^c)^2}{k_s t^c} \right] \frac{\partial \phi_s}{\partial \tau} = \frac{\partial^2 \phi_s}{\partial y_s^2} \quad (\text{C.8})$$

Again the expression in the square brackets is a non-dimensional term and is reminiscent of a reciprocal Fourier number, but has no meaning unless the length and time scales are known. Equation 7 yields this, and can be re arranged to:

$$Ste_s = \frac{C_p \theta_s^c}{\lambda} = \frac{C_p (T_i - T_0)}{\lambda} \quad (\text{C.9})$$


The Stefan number of the solid layer is effectively the ratio of the sensible and latent heat. Hence,

$$Ste_s \frac{\partial \phi_s}{\partial \tau} = \frac{\partial^2 \phi_s}{\partial y_s^2} \quad (\text{C.9})$$

In essence the Stefan number determines the relative importance of the left side of equation C.9. When the  $Ste \ll 1$ , the transient term may be neglected, conduction is then essentially the same as in steady conditions.

**APPENDIX D EXPERIMENTAL DESIGN**

**D.1 Certificates of analysis and calibration**



**ZIMALCO**  
 Zimco Aluminium Company - Reg. No. 1947/025245/07  
 A Division of Zimco Group (Pty) Ltd

### Certificate of Analysis

**T F Design**

Date of Delivery: 2013/09/09

Delivery Note No.:

Shipment No:

Batch No.: 1IH013 Mass Delivered: 408


Material: 6763306 - LM6 + Sr Certificate Number: 35661

---

### Analysis Performed

Element	Unit	Result
Cu	%	0.01
Mg	%	0.01
Si	%	12.89
Fe	%	0.54
Mn	%	0.08
Ni	%	0.01
Zn	%	0.02
Ti	%	0.09
Pb	%	<0.01
Sn	%	<0.01
Sr	ppm	293

Remarks



Chief Chemist

ISO9001:2008 and OHSAS18001:2007 - Supplier of Supral Aluminium Alloys, Master Alloys and Supramex Aluminium Powder

**Figure 101 - Chemical analysis of aluminium alloy cast into the test section**


	7 Warming Avenue Springbok 812, Springbok Post 8119 P.O. Box 1208, Beaufort West 8000 South Africa T: 041 818 8000 F: 041 232 8353	47 Bunting Crescent Looi Street, Cape Town 7728 P.O. Box 24118, Looi Street, Cape Town 7719 South Africa E: 021 7527962 F: 021 752 8899	Document Title: Document Type: Document No: Rev Date: Rev Desc: Approved By:	Sensor Quality Inspection Certificate Document Type: Document No: Rev Date: Rev Desc: Approved By:																				
<b>Sensor - Quality Inspection Certificate</b>																								
<b>Instructions</b>																								
1. Inspection Certificate to be filled in by the Sensor Department's Quality Officer 2. Quality officer should refer to UFS-QCC-000017 (Rev 01) if unsure regarding inspection 3. Management should be informed of all defects. 4. A signed copy of inspection certificate to be attached to Jobcard			<table border="1" style="width:100%; border-collapse: collapse; font-size: 8px;"> <thead> <tr> <th colspan="2">Quantities</th> <th rowspan="2">Quantity to inspect</th> </tr> <tr> <th>From</th> <th>To</th> </tr> </thead> <tbody> <tr> <td>1</td> <td>3</td> <td>All (100%)</td> </tr> <tr> <td>5</td> <td>10</td> <td>3 off</td> </tr> <tr> <td>10</td> <td>60</td> <td>6 off</td> </tr> <tr> <td>50</td> <td>100</td> <td>10 off</td> </tr> <tr> <td>100 +</td> <td>100</td> <td>15 off</td> </tr> </tbody> </table>		Quantities		Quantity to inspect	From	To	1	3	All (100%)	5	10	3 off	10	60	6 off	50	100	10 off	100 +	100	15 off
Quantities		Quantity to inspect																						
From	To																							
1	3	All (100%)																						
5	10	3 off																						
10	60	6 off																						
50	100	10 off																						
100 +	100	15 off																						
Customer: <u>Univ of Stellenbosch</u>		Job Number: <u>247631/1</u>																						
Date Of Inspection: <u>25/6/13</u>		Drawing/Part No: <u>4stc15-KS1U</u>																						
Sensor type:	<u>K</u>																							
Stem Length:	<u>30</u>																							
Stem Diameter:	<u>4.76</u>																							
Termination Type:	<u>Cable</u>																							
Mounting Type:	<u>✓</u>																							
Cable Option:	<u>st/Beaded</u>																							
Cable Length:	<u>5000</u>																							
Grounded or Ungrounded:	<u>Ungrounded</u>																							
Please tick the appropriate box																								
1. Is all Weld in a good condition?	<input checked="" type="checkbox"/>	YES	<input type="checkbox"/>	NO																				
2. Is there any Mechanical defects on the sensor? (Tick Appropriate box)	<input type="checkbox"/>	YES	<input checked="" type="checkbox"/>	NO																				
3. Is Colour Coding & Polarity according to Thermocouple Ref chart?	<input checked="" type="checkbox"/>	YES	<input type="checkbox"/>	NO																				
4. Has label details been check and is it acceptable?	<input checked="" type="checkbox"/>	YES	<input type="checkbox"/>	NO																				
5. Is Sensor response time to 118 °C below the max upper limit of 3 minutes?	<input checked="" type="checkbox"/>	YES	<input type="checkbox"/>	NO																				
6. Is insulation of ungrounded sensors higher than 1000ms at 100V?	<input checked="" type="checkbox"/>	YES	<input type="checkbox"/>	NO																				
7. Does the Sensors Temperature reading at 120°C fall within specified tolerance? Refer to Tolerance chart	<input checked="" type="checkbox"/>	YES	<input type="checkbox"/>	NO																				
8. Is Jobcard and drawing, if applicable, updated and correct?	<input checked="" type="checkbox"/>	YES	<input type="checkbox"/>	NO																				
9. Is the Quality of sensor acceptable?	<input checked="" type="checkbox"/>	YES	<input type="checkbox"/>	NO																				
Remarks: <u>No label P.c not working</u>																								
QA Inspector:	<u>[Signature]</u>	Signed:	<u>[Signature]</u>	Date: <u>25/6/13</u>																				

Figure 102 - Certification of compliance for K-type thermocouples

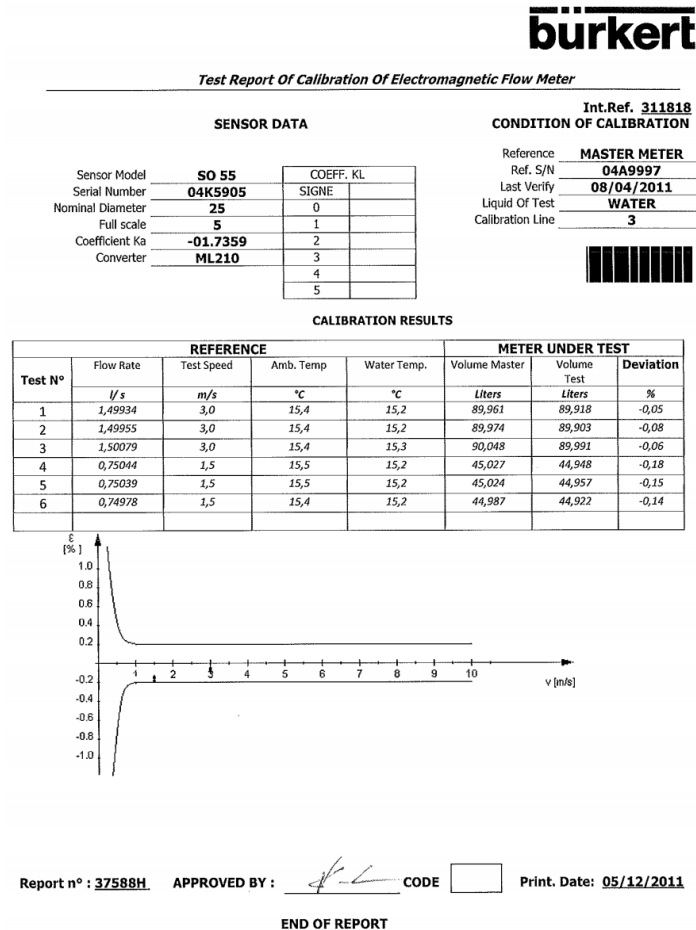


Figure 103 - Calibration certificate - water flow meter

## D.2 Laminar flow meter design detail

In preliminary design stages of the experimental setup, oil flow rates between 0.1 and 2 kg/s were considered. The flow meter was built from a 6m long 2 inch S10 seamless stainless steel pipe. Using equations 7.28 and 7.29 the design parameters of the flow meter was evaluated; which is presented in Table 48. The critical design geometry of the laminar flow meter is presented in Table 49.

**Table 48 - Design parameters of the laminar flow meter**

	<b>Min</b>		<b>Max</b>	
Mass flow rate	0.10	kg/s	2.00	kg/s
Volumetric flow rate	1.12E-04	m <sup>3</sup> /s	2.25E-03	m <sup>3</sup> /s
Flow velocity	0.05	m/s	1.04	m/s
Reynolds number	75.69		1513.87	
Entrance length	0.20	m	3.97	m
Pressure drop	19.31	Pa	386.15	Pa
<b>Constants</b>				
Kinematic viscosity	3.60E-05	m <sup>2</sup> /s		
Density	890	kg/m <sup>3</sup>		
Length	1	m		
Diameter	47.8	mm		
Temperature	40	°C		

**Table 49 - Laminar flow meter critical geometry**

Internal diameter	47.8	mm
Entrance length	4	m
Distance between the pressure taps	1.000	m

Furthermore, the flow meter is insulated using an evacuated annulus around the central pipe. The reason for this is that the flow meter is highly dependent on the viscosity of the fluid, which is strongly influenced by the temperature, especially at lower temperatures. The annulus vacuum is held by a vacuum pump for the duration of the experiment. The gap between the inner and the outer pipe is held through star shaped spacers placed throughout the length of the pipe. A drawing of the flow meter is presented in Figure 104.

The pressure difference between the pressure taps is measured using an Endress+Hauser Deltabar S PMD75 pressure transducer. The transducer was calibrated using a Betz micromanometer; the calibration curve is shown in Figure 105. The viscosity of the ISO 100 heat transfer oil was independently tested according to the ASTM D 445 specification, and the certificate of analysis is presented in Figure 106. The results of the viscosity test are shown in Figure 107

and is presented with a curve fit. The Dynamic viscosity is presented in Figure 108.

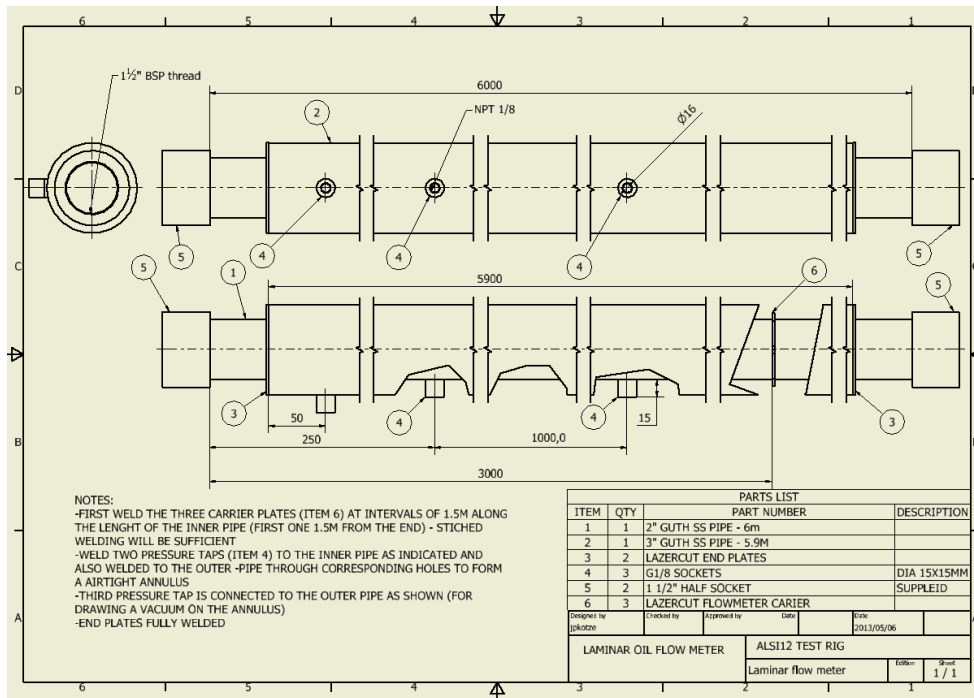


Figure 104 - Laminar flow meter drawing

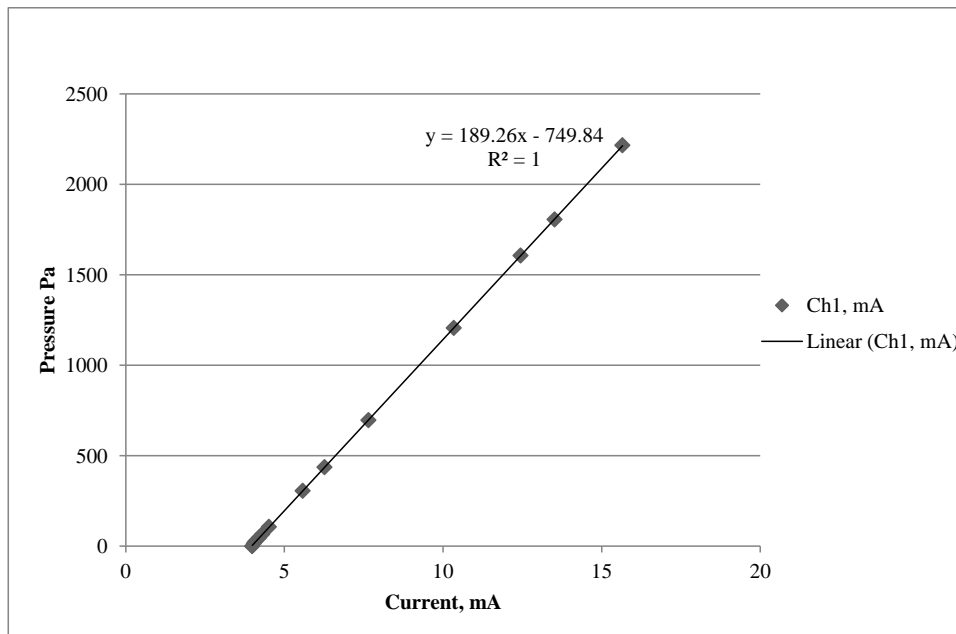


Figure 105 - Calibration curve for the Endress+Hauser Deltabar S PMD75 pressure transducer

# J. MULLER

LABORATORIES (PTY) LTD  
Reg. No. 1980/004037/07  
 ANALYTICAL CHEMISTS

P.O. BOX 511  
 PAARDEN EILAND 7420  
 REP. OF SOUTH AFRICA  
 TELEPHONE: 27-021-5118301/2  
 FAX: 27-021-5103800  
 E-mail: [jmlabs@iafrica.com](mailto:jmlabs@iafrica.com)

Our Ref LN305205-U001-05

OFFICE & LABORATORIES AT:  
 30 MARINE DRIVE  
 PAARDEN EILAND 7405  
 REP. OF SOUTH AFRICA

Date of Issue: 31 MAY 2013

## Certificate of Analysis

PAGE 1 OF 1

**This is to certify that** the sample listed below was analysed

**SUBMITTED BY:** STELLENBOSCH UNIVERSITY  
 PRIVATE BAG X1  
 MATIELAND  
 7602  
**ATTENTION:** JOHAN KOTZÉ

**SAMPLE TYPE:** OIL (x1)  
**SAMPLE MARKS:** NIL

**DATE SAMPLE RECEIVED:** 28 MAY 2013  
**DATE ANALYSIS STARTED:** 30 MAY 2013  
**DATE ANALYSIS COMPLETED:** 31 MAY 2013

Analysis relates only to the sample/s tested:  
Analysis gave:

ASTM D 445	Kinematic Viscosity @ 20°C	mm <sup>2</sup> /s	299
ASTM D 445	Kinematic Viscosity @ 30°C	mm <sup>2</sup> /s	153
ASTM D 445	Kinematic Viscosity @ 40°C	mm <sup>2</sup> /s	91
ASTM D 445	Kinematic Viscosity @ 50°C	mm <sup>2</sup> /s	54
ASTM D 445	Kinematic Viscosity @ 60°C	mm <sup>2</sup> /s	36
ASTM D 445	Kinematic Viscosity @ 70°C	mm <sup>2</sup> /s	33
ASTM D 445	Kinematic Viscosity @ 80°C	mm <sup>2</sup> /s	21

  
 RP ANALYST  
 J JOHNSON

  
 LABORATORY MANAGER  
 U SHUTTLEWORTH

**J. MULLER LABORATORIES (PTY) LTD DIRECTOR: B.M. JOHNSON**  
 THIS CERTIFICATE/REPORT SHALL NOT BE REPRODUCED EXCEPT IN FULL  
 WITHOUT PRIOR WRITTEN CONSENT OF J. MULLER LABORATORIES (PTY) LTD.  
 CONDITIONS OF ISSUE ATTACHED

**Figure 106 - Kinematic viscosity of the ISO 100 heat transfer oil**



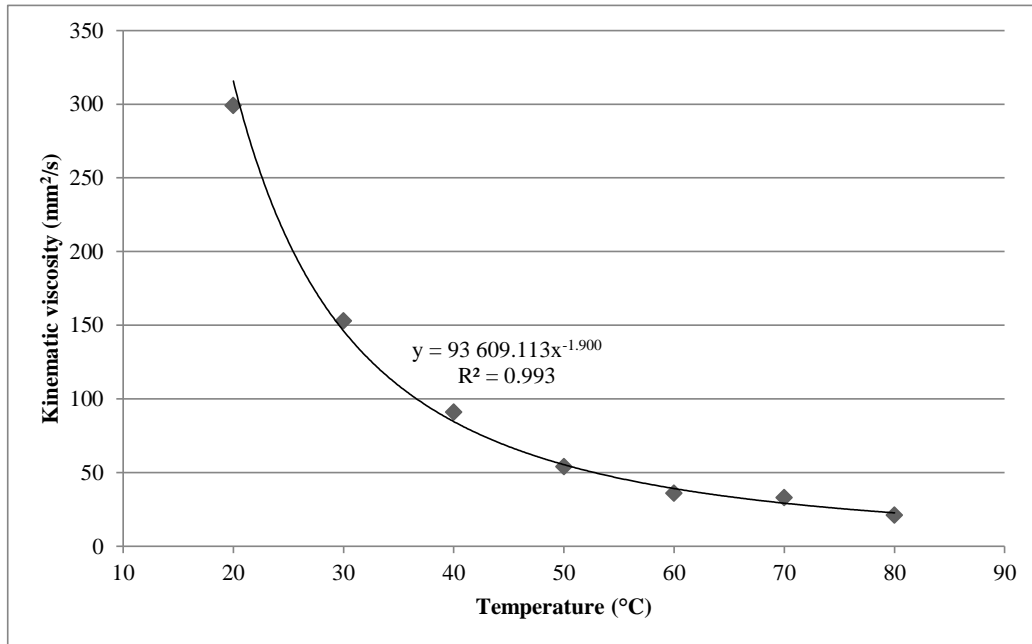


**Figure 107 - Kinematic viscosity of ISO 100 oil as a function of temperature**

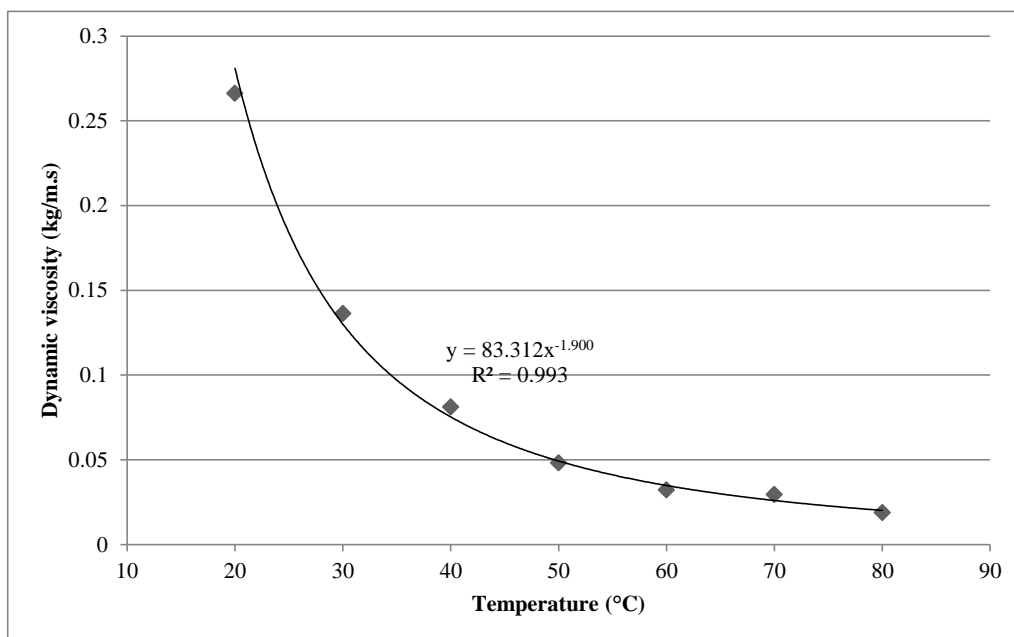


**Figure 108 - Dynamic viscosity of ISO100 oil as a function of temperature**

The Flow meter was initially calibrated against a SPX In-line hydraulic tester. It has flow measurement scale of 0 to 200 l/min and an accuracy of 2 % of full scale (SPX, 2013). The flow meter was connected in series with the hydraulic tester, and the flow rate was adjusted using the tester’s valve. The resulting calibration curve is shown in Figure 109. The calibration was done at an oil temperature of 42.5°C.

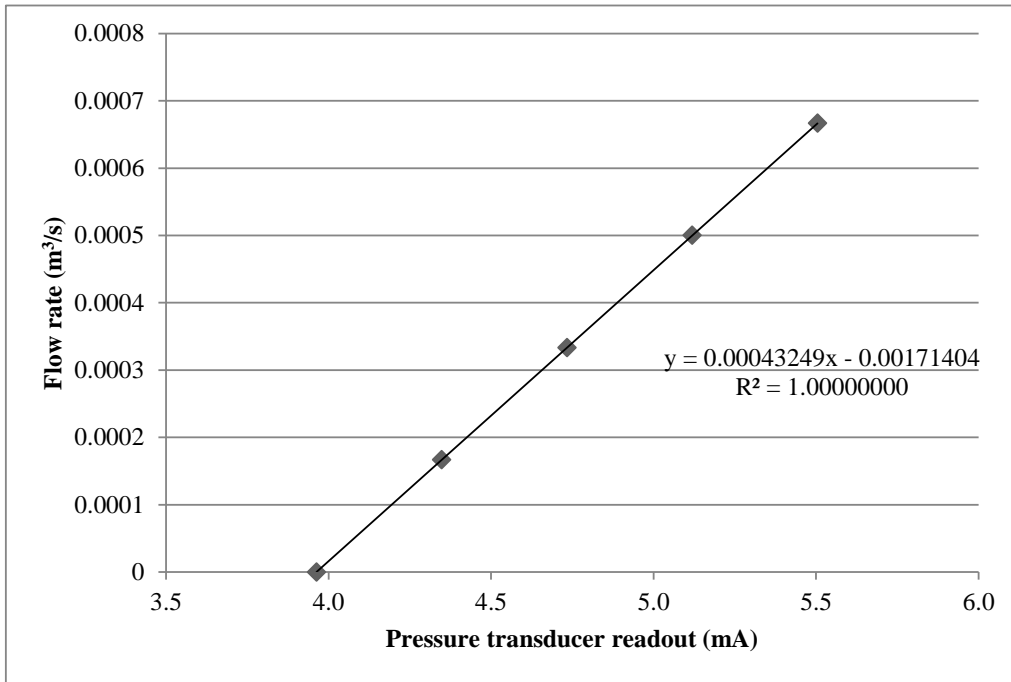


**Figure 109 - Calibration curve for the flow meter at 42.5°C**

## APPENDIX E PREDICTION OF THERMAL LOSSES OF THE TEST SECTION

The heat losses from the surface of the cladding is both convective and radiation. The outer surface of the cladding will be treated as a single smooth polished stainless steel cylinder. Only these surfaces will be considered because of the radial nature of the problem. The geometry, emissivity ambient temperature and surface temperature are presented in 7.4.3.

**Table 50 – Geometry, properties and conditions for heat loss estimation**

Diameter	0.48 m
Length	1.29 m
Surface area	1.93 m <sup>2</sup>
Emissivity	0.17
Ambient temperature (T <sub>amb</sub> )	18.00 °C
Surface temperature (T <sub>s</sub> )	49 °C

The natural convective heat transfer coefficient on the surface can be calculated like that of a vertical plane wall if equation E.1 is met. (Cengel, 2003).

$$D \geq \frac{35L}{Gr_L^{1/4}} \quad \text{E.1}$$

The Grashof number was evaluated at the film temperature, which is the average between the ambient and the surface temperatures. The surface temperature of the cladding was measured at 224 °C and the ambient temperature was measured at 18°C. The properties of air at the film temperature (121 °C) are presented in Table 51:

**Table 51 – Air properties at 121°C**

$\nu$	2.52E-05	m <sup>2</sup> /s
$\beta$	0.00254	
$\alpha$	3.57E-05	m <sup>2</sup> /s
k	0.03374	W/m.K
Pr	0.7041	

The Grashof number is  $1.23 \times 10^{10}$ . Substituting the Grashof number into equation E.1, yields a right-hand side value of 0.121m, satisfying the condition. Thus, the convection can be taken as that of a vertical plane wall. The Rayleigh number is  $8.65 \times 10^9$ , yielding a Nusselt number of  $1.8 \times 10^2$ , and this translates to a heat transfer coefficient, h, of 5.28 W/(m<sup>2</sup>.K). Using equation E2, the heat transfer through natural convection is calculated as 1876.25W

$$\dot{Q}_{Conv} = hA(T_s - T_{amb}) \quad (E.2)$$

The radiation heat transfer is calculated using equation E.3 with the properties listed in Table 50. The radiation heat transfer is calculated as 1586.07W.

$$\dot{Q}_{Rad} = \varepsilon A_s \sigma (T_s^4 - T_{amb}^4) \quad (E.3)$$

This yields total thermal losses of 3462.42W.

## APPENDIX F HEAT TRANSFER MEASUREMENTS

### F.1 Measurement of heat transfer from PCM to Oil

The heat transfer was measured using the 0-20mA output from the flow meter installation as discussed in Appendix D, and the temperature measurements at the inlet and outlet of the test section.

To calculate the mass flow rate:

- The pressure drop in the laminar flow meter was calculated using the calibration curve in presented in Figure 105.
- The volume flow rate was calculated using equation 7.28.
- The mass flow rate was calculated using the properties listed in Table 14
- The heat transfer rates was derived using the temperature difference across the inlet and the outlet of the test section, and the  $C_p$  value listed in Table 14.

The resulting heat transfer rates for the experiment is presented in Figure 110.

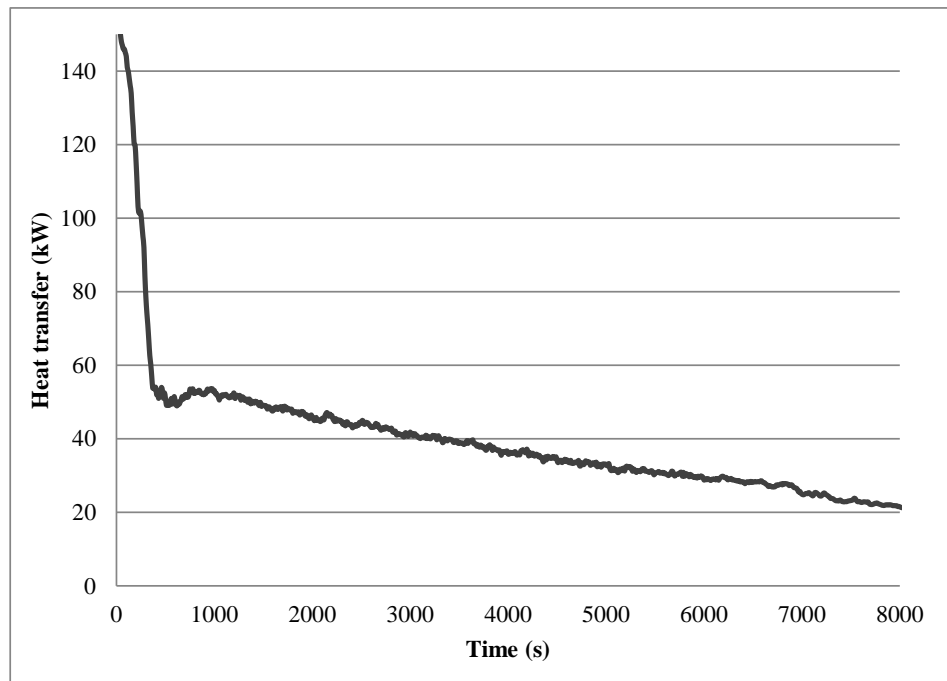


**Figure 110 - Heat transfer rates from PCM to oil**

Notice that the heat transfer rates begin very high, at about 150 kW, but rapidly drops down to 50kW, where it slowly decreases with time to below 20kW. This initial phase of high heat transfer rates corresponds to the sensible discharge of the PCM as discussed in section 7.5.

## F.2 Measurement of heat transfer from Oil to Water

The water mass flow rates were given directly by the Bürkert SO55 flow meter, and it was possible to determine the heat transfer using the inlet and outlet temperatures. The water properties of the IAPWS industrial formulation 1997 were used. The resulting heat transfer rates are presented in Figure 111.

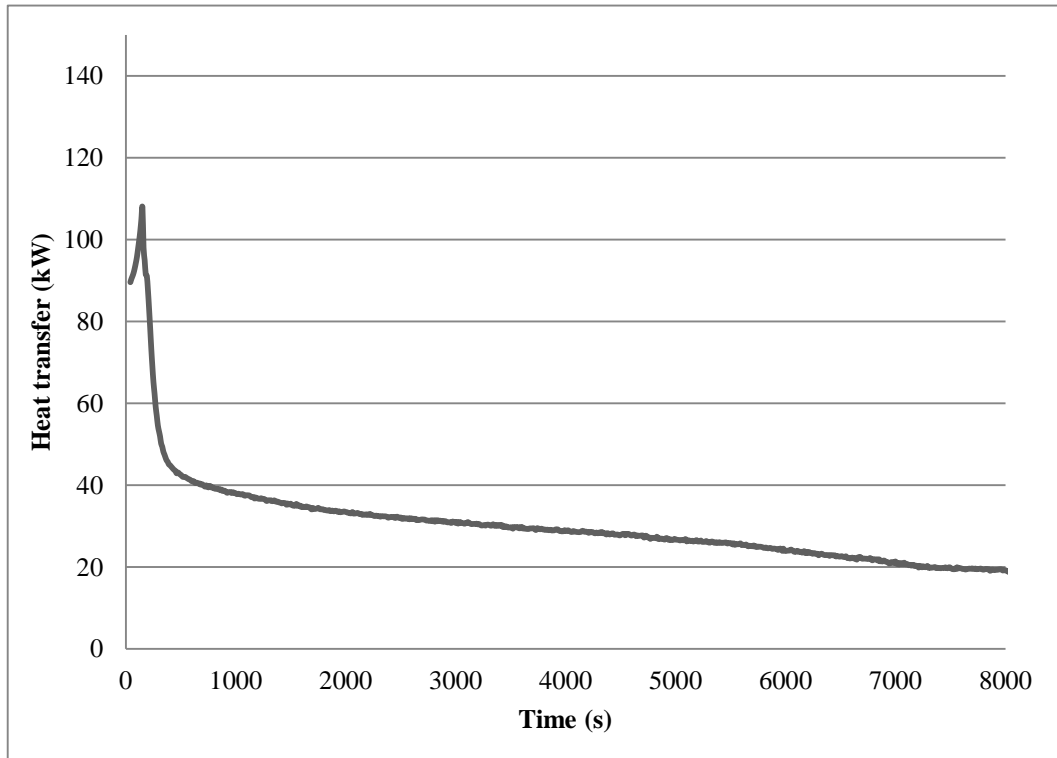


Figure 111 - Heat transfer from oil to water

**APPENDIX G SIMULATION CODE**

```

clear %clear memory
clc %clear screen% Geometrical Constants
%declare global variables

d_pi=0.024; %inner pipe diameter (m)
d_i=0.032; %outer pipe diameter(m)
d_o=0.398; %outer pipe diameter/outer diameter of hexagonal element(m)
L=1.289; %lenth of test section (m)

r_pi=d_pi/2;
r_i=d_i/2;
r_o=d_o/2;

Material properties:
% PCM : AlSi12
T_m=577; %melting point of PCM (degC)
H_f=560000; %heat of fusion (J/kg)

%solis
roh_PCMS=2560; %density around melting point 2700 (kg/m^3)
k_PCMS=160; %thermal conductivity (W/mK)
C_PCMS=2560; %Specific heat capacity of PCM (J/kgK)

%liquid
roh_PCML=2560; %density around melting point 2700 (kg/m^3)
k_PCML=160; %thermal conductivity (W/mK)
C_PCML=1741; %Specific heat capacity of PCM (J/kgK)

%Mildsteel
roh_MS=7854; %density around melting point 2700 (kg/m^3)
k_MS=36.2; %thermal conductivity (W/mK)
C_MS=685; %Specific heat capacity of steel (J/kgK)

%Insert into array
k=[k_MS,k_PCMS,k_PCML];
roh=[roh_MS,roh_PCMS,roh_PCML];
Cp=[C_MS,C_PCMS,C_PCML];
alpha=[(k_MS/(roh_MS*C_MS)),(k_PCMS/(roh_PCMS*C_PCMS)),(k_PCML/(roh_PCML*C_PCML))];
%calculation constants
dr=0.001;
dt=0.001;
SimT=3; %hours
%calculate number of increments
nr=((r_o)-(r_pi))/(dr);
nt=SimT*60*60/dt;
%set up propertie matricies
r=r_pi:dr:r_o; %create a size matrix
T=ones(1,nr); %create temperature matrix
E=ones(1,nr); %create
S=ones(1,nr); %state
Q=ones(1,nr+1); %state
M=ones(1,nr); %Mass

V=ones(1,nr);% create volume matrix
init=ones(1,nr)*630;
T(1,:)=init;
R=zeros(1,nr); %resistance in elements
READOUT=zeros(9,(SimT*3600)/(10));
%READOUTTime=10:10:(SimT*3600/10);
READOUT(1,:)=10:10:(SimT*3600);

```

```

#####boundary Interfaces#####
n_i=5;
S(1,1:(n_i-1))=0;
%flags
W=1; %flag to show the solidification thing
TN=1; %flag the time stamp
%initialize properties matrices
for j=1:nr
    %Volumes
    if j==1
        V(1,j)=L*pi*((r(1,j)+dr/2)^2-r(1,j)^2);
    else
        V(1,j)=L*pi*((r(1,j)+dr/2)^2-(r(1,j)-dr/2)^2);
    end
    %resistances
    if j<n_i
        m=1;
        R(j)=log((r(j+1))/r(j))/(2*pi()*L*k(m));
    elseif j>=n_i
        m=2;
        R(j)=log((r(j+1))/r(j))/(2*pi()*L*k(m));
    end
end
R_conv=1/(2*pi()*r(1))*L*h_oil);

%enthalpy cutoffs for ALSI12

Tm1=575;
Tm2=577;

H1=0;
H2=Cp(2)*Tm1;
H3=H2+H_f;

A=(H3-H2)/(Tm2-Tm1);
Ti=630;
%mass matrix
for j=1:nr
    if j<n_i
        m=1;
        M(j)=V(j)*roh(m);

    elseif j>=n_i
        m=3;
        M(j)=V(j)*roh(m);
    end
end
%energy matrix
for j=1:nr
    if j<n_i
        m=1;
        E(j)=Ti*Cp(m)*M(j);
    elseif j>=n_i
        if Ti<Tm1
            H=Ti*Cp(2);
            E(j)=H*M(j);
        elseif Ti>Tm2
            H=H3+Cp(3)*(Ti-Tm2);
            E(j)=H*M(j);
        end
    end
end
HC=E./M;

for i=1:nt
    time=i*dt; %generate time stamp for readout

    %heat flow between elemnets
    for j=1:nr+1
        if j==1

```



```

        if time<40
            Q(j)=0;
        else
            Q(j)=1236*(-7.4465170001*log(time)+91.9651158219);
        end
    elseif j<nr+1
        Q(j)=(T(j)-T(j-1))/R(j-1);
    elseif j==nr+1
        Q(j)=-3462.42;
    end
end
end

%energy balance on the elements
for j=1:nr
    E(j)=E(j)+dt*(Q(j+1)-Q(j));
end
%assign temperatures to nodes
H=E./M;
for j=1:nr

    if j<n_i
        T(j)=H(j)/Cp(1);
    else
        if H(j)<H2

            T(j)=H(j)/Cp(2);
            S(j)=0;
        elseif H(j)<H3

            T(j)=Tm1+H(j)/A-H2/A;
            S(j)=2;
        elseif H(j)>=H3
            T(j)=Tm2+(H(j)-H3)/Cp(3); % need to be fixed
            S(j)=1;
        end
    end
end

end

for j=1:nr
    if T(j)>Tm1
        POS1=r(j);
        break
    end
end

for j=1:nr
    w=nr+1-j;
    if T(w)>Tm1
        POS2=r(w);
        break
    end
end

end

%log the results
if time==(TN*10)
    READOUT(2,TN)=T(25);
    READOUT(3,TN)=T(50);
    READOUT(4,TN)=T(75);
    READOUT(5,TN)=T(100);
    READOUT(6,TN)=T(125);
    READOUT(7,TN)=T(150);
    READOUT(8,TN)=T(180);
    READOUT(9,TN)=T(185);
    READOUT(10,TN)=T(187);
    READOUT(11,TN)=Q(1)/1000;
end

```

```
READOUT (12, TN) = Q (nr+1) ;  
READOUT (13, TN) = POS1 ;  
READOUT (14, TN) = POS2 ;  
READOUT (15, TN) = T (19) ;  
READOUT (16, TN) = T (70) ;  
READOUT (17, TN) = T (79) ;  
READOUT (18, TN) = T (124) ;  
READOUT (19, TN) = T (169) ;
```

```
TN=TN+1
```

```
end
```

```
end
```

## APPENDIX H THERMODYNAMIC ANALYSIS OF THE STEAM CYCLE

The generating cycle is a regular steam Rankine cycle with the following properties:

- 100 MW electrical output;
- base load operation;
- 540 °C, 140 bar superheat;
- 540 °C, 30 bar re-heat;
- one open-feed water heater supplied from the high-pressure turbine outlet; and
- Air-cooled condenser (ACC) with a condenser pressure of 0.15 bar with an air temperature of 30 °C

The steam cycle is represented by the process diagram in Figure 112 below. The numerical annotation on Figure 112 will be used throughout the analysis.

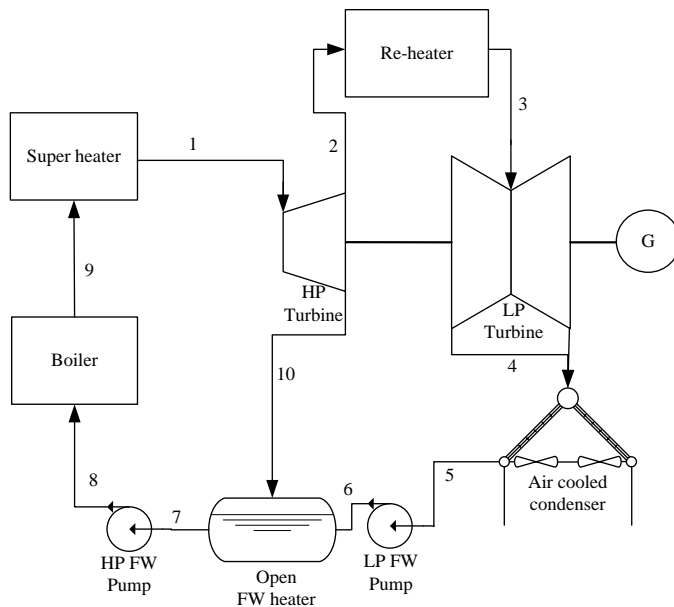


**Figure 112 - Steam Rankine cycle**

*Assumptions:*

- Steady state operation
- Kinetic and potential energy changes are negligible
- Pressure drop through the piping is negligible
- The thermal efficiencies of the various components in the Rankine cycle are shown in Table 52.

Component:	Isentropic
------------	------------

	Efficiency
HP Turbine efficiency:	87%
IP&LP Turbine efficiency:	87%
Pump 1 efficiency	85%
Pump 2 efficiency	85%
Generator efficiency	95%

**Table 52 - Component efficiencies for the steam Rankine cycle**

The T-S diagram is presented in Figure 113,

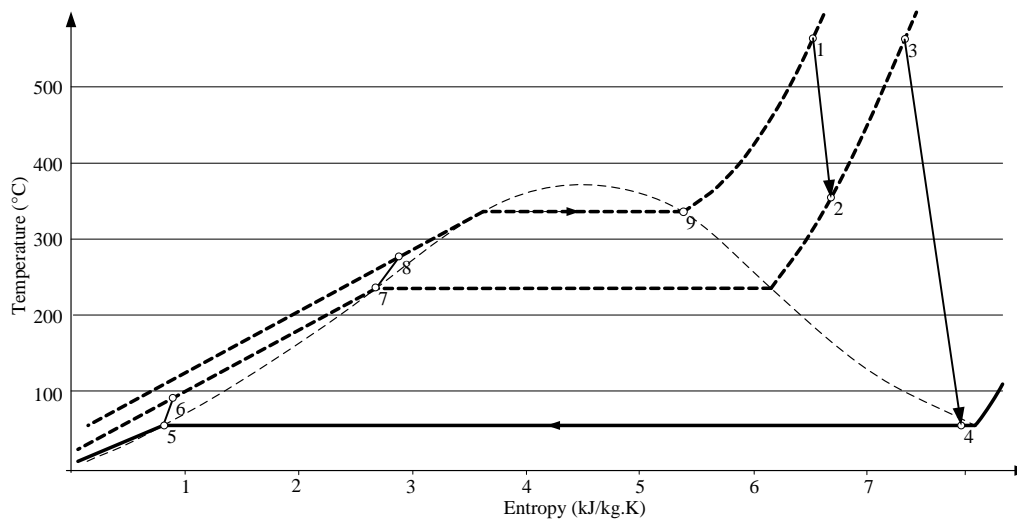


**Figure 113 - T-S diagram for the Rankine steam cycle**

**Steam conditions:**

<i>State 1:</i>	Specified	$P_1 = 140 \text{ bar}$ $T_1 = 540 \text{ }^\circ\text{C}$ $h_1 = 3434.20 \text{ kJ/kg}$ $s_1 = 6.53 \text{ kJ/kgK}$ $\rho_1 = 41.10 \text{ kg/m}^3$
<i>State 3:</i>	Specified	$P_3 = 30 \text{ bar}$ $T_3 = 540 \text{ }^\circ\text{C}$ $h_3 = 3547.04 \text{ kJ/kg}$ $s_3 = 7.35 \text{ kJ/kgK}$ $\rho_3 = 8.147 \text{ kg/m}^3$
<i>State 5:</i>	Saturated liquid of known pressure (0.15 bar)	$P_5 = 0.15 \text{ bar}$ $T_5 = 53.97 \text{ }^\circ\text{C}$ $h_5 = 225.94 \text{ kJ/kg}$

		$s_5 = 0.755 \text{ kJ/kgK}$ $\rho_5 = 986.16 \text{ kg/m}^3$
<i>State 7:</i>	Saturated liquid of a known pressure (30 bar)	$P_7 = 30 \text{ bar}$ $T_7 = 53.97 \text{ }^\circ\text{C}$ $h_7 = 1008.37 \text{ kJ/kg}$ $s_7 = 2.65 \text{ kJ/kgK}$ $\rho_7 = 821.89 \text{ kg/m}^3$
<i>State 9:</i>	Saturated steam of a known pressure (140 bar)	$P_9 = 140 \text{ bar}$ $T_9 = 336.67 \text{ }^\circ\text{C}$ $h_9 = 2638.09 \text{ kJ/kg}$ $s_9 = 5.37 \text{ kJ/kgK}$ $\rho_9 = 87.04 \text{ kg/m}^3$
<i>State 2</i>	$s_{2s}=s_1=6.53 \text{ kJ/kgK}$ using $s_{2s} \rightarrow h_{2s} = 2989.19 \text{ kJ/kg}$ $h_2=h_1-\eta_t(h_1-h_{2s})$ $h_2=3047.04 \text{ kJ/kg}$ $h_2 \text{ \& } P_2 \rightarrow T_2 = 321.17 \text{ }^\circ\text{C}$	$P_2 = 30 \text{ bar}$ $T_2 = 321.17 \text{ }^\circ\text{C}$ $h_2 = 3047.04 \text{ kJ/kg}$ $s_2 = 6.63 \text{ kJ/kgK}$ $\rho_2 = 11.73 \text{ kg/m}^3$
<i>State 10</i>	State 10 = State 2	$P_2 = 30 \text{ bar}$ $T_2 = 321.17 \text{ }^\circ\text{C}$ $h_2 = 3047.04 \text{ kJ/kg}$ $s_2 = 6.63 \text{ kJ/kgK}$ $\rho_2 = 11.73 \text{ kg/m}^3$
<i>State 4</i>	$s_{4s}=s_3=7.35 \text{ kJ/kgK}$ $s_g=8.01 \text{ kJ/kgK}$ $s_f=0.75 \text{ kJ/kgK}$ $s_{fg}=7.25 \text{ kJ/kgK}$ $x_{4s} = (s_{4s} - s_{\text{sat.liq}@0.15 \text{ bar}})/s_{fg}=0.909$ $h_{4s}=h_f + x_{4s}h_{fg}=2383.05 \text{ kJ/kg}$ $h_4=h_3-\eta_t(h_3-h_{4s})= 2534.3 \text{ kJ/kg}$ $x_4=(h_4-h_f)/h_{fg}=0.97$ $s_4= s_f + x_4s_{fg} = 7.81 \text{ kJ/kgK}$	$P_4 = 0.15 \text{ bar}$ $T_4 = 53.97 \text{ }^\circ\text{C}$ $h_4 = 2534.36 \text{ kJ/kg}$ $s_4 = 7.35 \text{ kJ/kgK}$ $\rho_4 = 0.0998 \text{ kg/m}^3$ $x_4=0.97$
<i>State 6</i>	$w_{\text{pump1.in}}=[v_5(P_6-P_5)]/\eta_{\text{pump1}} = 3.56$	$P_6 = 30 \text{ bar}$

	kJ/kg	$T_6 = 54.21 \text{ }^\circ\text{C}$
	$h_6 = h_5 + w_{\text{pump1.in}} = 229.40 \text{ kJ/kg}$	$h_6 = 229.59 \text{ kJ/kg}$
	from $h_6$ & $P_6$ : all other properties	$s_6 = 2.64 \text{ kJ/kgK}$
		$\rho_6 = 987.34 \text{ kg/m}^3$
<i>State 8</i>	$w_{\text{pump2.in}} = [v_7(P_8 - P_7)] / \eta_{\text{pump2}} = 15.75 \text{ kJ/kg}$	$P_8 = 140 \text{ bar}$
	$h_8 = h_7 + w_{\text{pump2.in}} = 1024.11 \text{ kJ/kg}$	$T_8 = 336.67 \text{ }^\circ\text{C}$
	from $h_8$ & $P_8$ : all other properties	$h_8 = 1024.11 \text{ kJ/kg}$
		$s_8 = 5.373 \text{ kJ/kgK}$
		$\rho_8 = 828.43 \text{ kg/m}^3$
<i>Steam bleed flow rate at condition 10</i>	Let $y$ be the fraction of steam bled off at the end of the HP turbine. Then:	$y = 0.28$
	$\dot{E}_{in} = \dot{E}_{out}$	
	$yh_{10} - (1 - y)h_6 = h_7$	
<i>Mass flow rate</i>	The specified electrical power output is 100 MW. Taking the thermal efficiency of the generator yields that the turbines must produce 105.3 MW. By doing a basic energy balance on the power cycle the mass flow rate can be calculated.	$\dot{m} = 93.99 \text{ kg/s}$
	$\dot{Q}_{gen} = \dot{Q}_{turbines} - \dot{Q}_{pumps}$	
	$100000 = \dot{m}((h_1 - h_2) - (h_8 - h_7)) - \dot{m}(1 - y)(h_3 - h_4) - (h_6 - h_7)$	
	This yields:	
	$\dot{m} = 93.99 \text{ kg/s}$	

A basic energy balance is presented in Table 53.

	Mass flow (kg/s)	$\dot{Q}$ (MW)
Turbine 1	93.99	36.39
Turbine 2	68.01	68.87
		<u>105.26</u>
Pump 1	68.01	0.24
Pump 2	93.99	1.48
		<u>1.72</u>
Boiler	93.99	151.70
Super-heater	93.99	74.83
Re-heater	68.01	34.01
		<u>260.54</u>
Thermal efficiency		0.38

**Table 53 - Energy balance of hypothetical power cycle**

The boundary conditions and the heat transfer requirements for the steam generator is presented in Table 54.

	Mass flow (kg/s)	Enthalpy change (kJ/kg)	$\dot{Q}$ (MW)	$T_{in}$ (°C)	$T_{out}$ (°C)	P(bar)
Boiler	93.99	1613.98	151.70	236.85	336.67	140
Super- heater	93.99	796.11	74.83	336.67	540	140
Re-heater	68.01	500.01	34.01	321.17	540	30

**Table 54 - Boundary conditions and heat transfer requirements of the steam generator**

## APPENDIX I FLOWNEX MODEL

The Flownex model is used to aid in the design of the storage system and the heat exchange equipment. To obtain boundary conditions for the design of the storage system and the heat exchangers, the power cycle discussed in section 8.1 and the boundary conditions developed in appendix H is was used as starting point for the Flownex model.

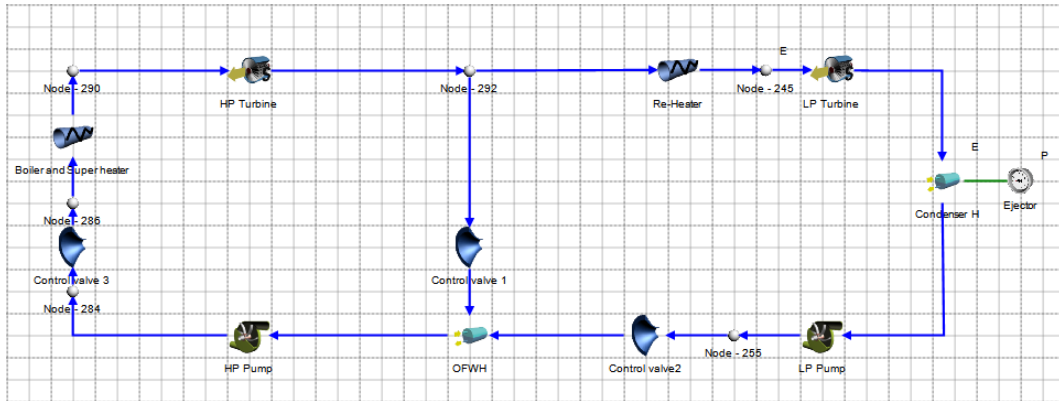


**Figure 114 - Flownex model of the steam Rankine cycle**

The model is shown in Figure 114. The model was built using the designer tool to fine-tune the component settings to match the conditions of the Rankine cycle presented in section 8.1. The designer tool uses the Newton-Raphson solution algorithm to solve a set of non-linear equations. The relation between the independent variables (such as orifice diameter or turbine efficiency) is set by the user, and the dependent variables (such as mass flow rate, pressure drop and flow velocity) in the designer interface. Using a set of boundary conditions, the Rankine cycle is built up from the inlet of the HP turbine and worked around until the entire power generating cycle is a closed loop, running both as a steady state model or a transient state model.

The turbines were modelled with the *SimpleTurbine* component because the performance curves of a real turbine could not be obtained, nor does the purpose of this model merit the level of detail. The simple turbine only takes a constant isentropic efficiency of the turbine into account. This is in contrast with the “*Turbine*” component, which takes the performance curves to calculate the working point of the turbine depending on shaft speed and steam conditions. The settings of the high pressure (HP) turbine model are shown in Figure 115. As with all the components discussed henceforth, the settings and work points of the components was found using the “*Designer tool*”.



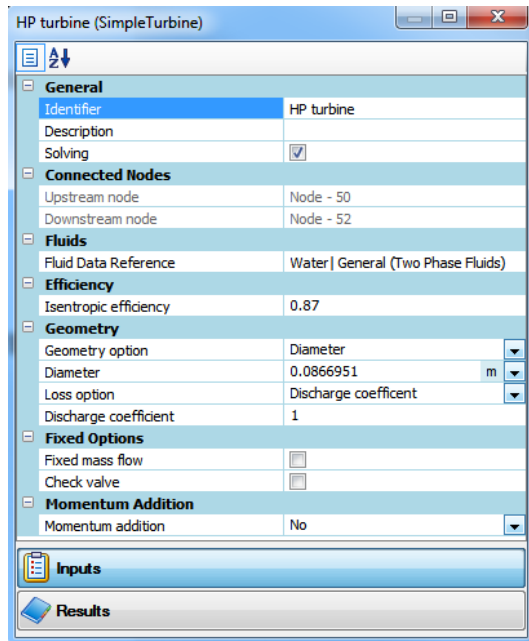


**Figure 115 - HP turbine settings**

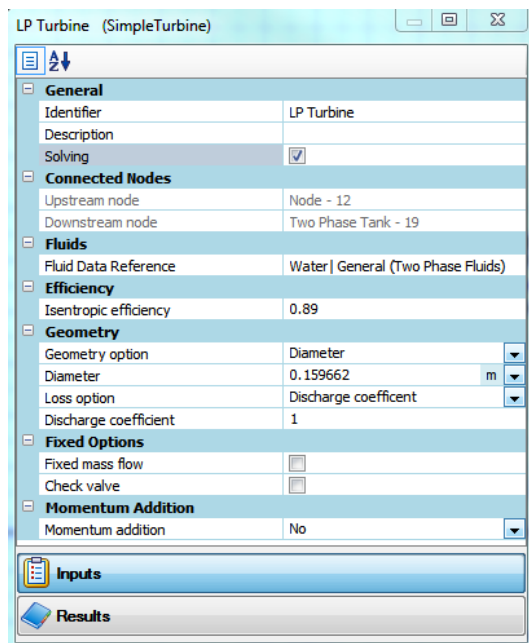


**Figure 116 - LP turbine settings**

The pumps were simulated by the “Fan or Pump” component. The fan model is based on a pump chart. Because the feedwater pumps are hypothetical, custom pumping curves had to be made up. Simple three point pump charts were constructed around the desired working points, specified by the hand analysis in appendix H. The pump chart for the low pressure pump is shown in Figure 117 and the HP pump chart is shown in Figure 118.

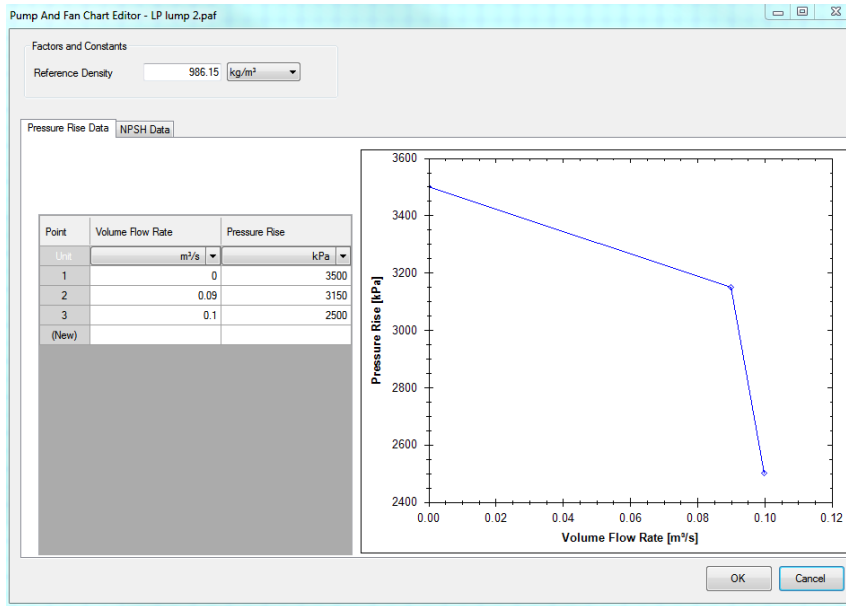


**Figure 117 - LP Pump chart**

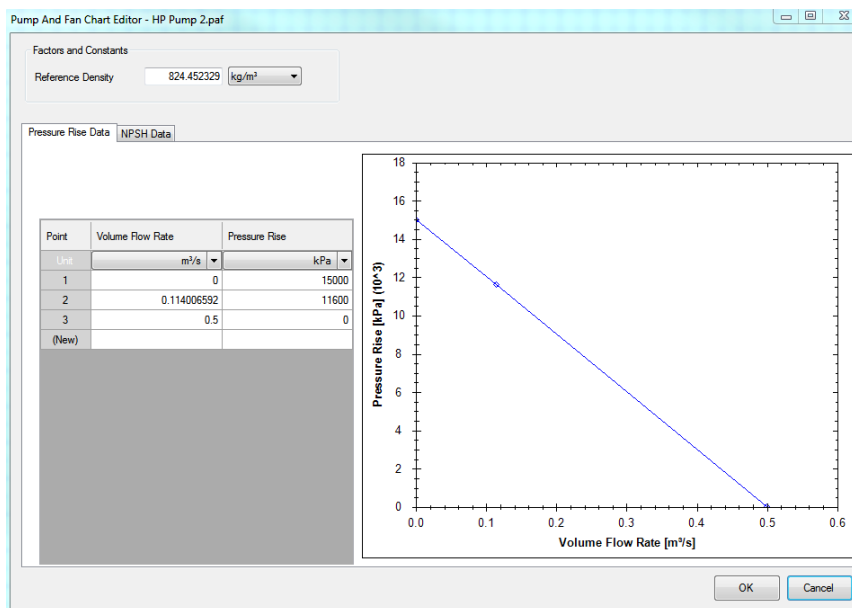


**Figure 118 - HP pump chart**

Both the open feed water heater and the condenser are modelled using a “Two phase tank” component. The “two phase tank” is essentially a node with a volume and a geometry where the level of the tank is determined by the quality ( $x$ ) of the two phase fluid in the tank. The height of the outlets to interfacing components (such as pumps) determines if they receive saturated liquid or saturated steam. Both were modelled as cylindrical drums with a diameter of 1m, and a length of 3m with flat ends standing vertically. The outlets were set to be at the bottom of the tank as to only allow saturated water to flow from the node.

The flow of turbine bleed steam to the open feed-water heater OFWH is controlled so that the level of the OFWH is kept at 1.5m ( $x=0.5$ ). Similarly, the heat extracted from the condenser is also controlled by changing the heat removed from the condenser. The condenser pressure is normally controlled by an ejector. The ejector is simulated by placing a pressure boundary value on the condenser.

The flow rates are controlled by “*restrictor with discharge coefficient*” components. The discharge coefficient in all three is set to 1, the number in parallel is also set to 1 and the cross-sectional diameter was determined by using the “*Designer*” tool. The diameter of the restrictor that feed the OFWH was set to allow 25.98kg/s through (as in the hand calculations). Its diameter is 0.146m.

The restrictors after both pumps have been set up by the “*Designer*” as to have the pumps remain at their designed working point. The restrictor after the LP pump was set using the area function, and was set on 0.001986 m<sup>2</sup>, and that of the HP pump was set on 0.065707m on the diameter setting.

Heat input was initially given by the “*Custom losses*” components. Both of them had their losses set to zero, but the heat input was added as calculated by hand.

This model runs both in steady state and transient state, and is used as the basis to add on and design the proper heat exchange and storage equipment.